The Dissertation Committee for Christopher James Thibodeaux Certifies that this is the approved version of the following dissertation:

Mechanistic Studies of Two Enzymes that Employ Common Coenzymes in Uncommon Ways

Committee:

Hung-wen Liu, Supervisor

Eric Anslyn

Walter Fast

Kenneth A. Johnson

Christian P. Whitman

Mechanistic Studies of Two Enzymes that Employ Common Coenzymes in Uncommon Ways

by

Christopher James Thibodeaux, B.S.

Dissertation

Presented to the Faculty of the Graduate School of

The University of Texas at Austin

in Partial Fulfillment

of the Requirements

for the Degree of

Doctor of Philosophy

The University of Texas at Austin

August, 2010

Dedication

To all whom have made significant contributions to my life:

I am eternally grateful.

Acknowledgements

First and foremost, I would like to thank Dr. Liu for providing me with the opportunity to work at the cutting edge of biochemical research, and for allowing me the freedom to explore and develop my scientific interests. In addition, I would like to thank the numerous other members of the Liu group (both past and present) for their helpful insights, stimulating conversations, and jovial personalities. They have all helped to immeasurably enrich my experience as a graduate student, and I would consider myself lucky to ever have another group of coworkers as friendly and as helpful as they all have been. Special thanks need to be attributed to Drs. Mark Ruszczycky, Chad Melançon, Yasushi Ogasawara, and Svetlana Borisova for their helpful suggestions and discussions at various points throughout my research, to Dr. Steven Mansoorabadi for performing the DFT calculations and for the many interesting conversations we have had over the years, and to Mr. Wei-chen Chang for continually supplying me with a variety of useful compounds that have been instrumental in the completion of this work. I would also like to thank Dr. Yung-nan Liu, Miss Sun He, and Miss Meilan Wu for assisting me with some of the molecular cloning and protein purification, Dr. Zhihua Tao for constructing several of the ACC deaminase mutants, and to Steve Sorey in the NMR facility for his assistance in collecting some of the NMR data.

Finally, none of this would have been possible (or worthwhile) without the support of my family, especially my wife and parents.

Mechanistic Studies of Two Enzymes that Employ Common Coenzymes in Uncommon Ways

Christopher James Thibodeaux, Ph.D.

The University of Texas at Austin, 2010

Supervisor: Hung-wen Liu

Enzymes are biological catalysts which greatly accelerate the rates of chemical reactions, oftentimes by many orders of magnitude over the uncatalyzed reaction. The remarkable catalytic rate enhancement afforded by enzymes derives ultimately from the structure and chemical properties of the enzyme active sites, which allow enzymes to selectively bind to their substrates and to stabilize high energy chemical species and unstable intermediates along the reaction coordinate. To enhance their catalytic ability, many enzymes have also evolved to require coenzymes for optimal activity. These coenzymes often provide chemical functionality and reactivity that are not accessible by the twenty canonical amino acids and, hence, coenzymes serve to greatly enhance the diversity of chemical reactions that can be mediated by enzymes. The work described in this dissertation focuses on mechanistic studies of two enzymes that use common coenzymes in unusual ways. In the first section of this work, studies will focus on the type II isopentenyl diphosphate:dimethylallyl diphosphate isomerase (IDI-2), an essential enzyme in isoprenoid biosynthesis that employs a flavin mononucleotide (FMN)

coenzyme for catalysis. In most biological systems, flavin coenzymes mediate electron transfer reactions. However, the IDI-2 catalyzed reaction involves no net redox change, raising questions as to the role of the flavin in the chemical mechanism. The chemical mechanism of IDI-2 will be interrogated with a combination of spectroscopic studies and biochemical techniques. Our studies suggest that the flavin coenzyme of IDI-2 may employ a novel mode of flavin-dependent catalysis involving acid/base chemistry. In the second section of this dissertation, attention will be focused on elucidating the chemical mechanism of 1-aminocyclopropane-1-carboxylate deaminase (ACCD), an enzyme that plays a role in regulating the production of the potent plant hormone, ethylene. ACCD is a pyridoxal-5′-phosphate (PLP)-dependent enzyme that catalyzes a C-C bond cleavage event that is unique among the catalytic cycles of PLP-dependent enzymes. Altogether, our mechanistic studies of IDI-2 and ACCD help to illustrate the catalytic diversity of common coenzymes, and demonstrate that some enzymes have evolved to exploit readily available coenzymes for atypical reactions.

Table of Contents

List of Abbreviations: AATase, aspartate aminotransferase; α-KB, 2-keto-1-butanoic acid; ACC, 1-aminocyclopropane-1-carboxylic aicd; ACCD, 1-aminocyclopropane-1-carboxylate deaminase; ACP, 1-aminocyclopropane-1-phosphonate; ATP, adenosine triphosphate; CAPS, *N*-cyclohexyl-3-aminopropanesulfonic acid; CAPSO, 3-(cyclohexylamino)-2-hydroxy-1-propanesulfonic acid; DMAPP, dimethylallyl pyrophosphate; DNA, deoxyribonucleic acid; DTT, dithiothreitol; EPPS, 4-(2-hydroxyethyl)piperazine-1-propanesulfonic acid; EPR, electron paramagnetic resonance; FAD, flavin adenine dinucleotide; FMN, flavin mononucleotide; FPP, farnesyl pyrophosphate; GPP, geranyl pyrophosphate; HMP, hydroxyl-*N*-methylpiperidine; IDI, isopentenyl diphosphate:dimethylallyl diphosphate isomerase; HEPES, 4-(2-hydroxyethyl)-1-piperizineethanesulfonic acid; IPP, isopentenyl pyrophosphate; IPTG, isopropyl β-D-thiogalactopyranoside; KIE, kinetic isotope effect; LB, Luria-Bertani; LBHB, low barrier hydrogen bond; LDH, L-lactate dehydrogenase; LFER, linear free energy relationship; MEP, methyl erythritol phosphate; MES, 2-(*N*-morpholino)ethanesulfonic acid; MOPS, 3-(*N*-morpholino)propanesulfonic acid; MSR, mean square residual of the fit; NADH, nicotinamide adenine dinucleotide (reduced form); NADPH, nicotinamide adenine dinucleotide phosphate (reduced form); NMR, nuclear magnetic resonance; NTA, nitrilotriacetic acid; PCR, polymerase chain reaction; PLP, pyridoxal-5′-phosphate; PPi, pyrophosphate; SAM, *S*-adenosyl-L-methionine; SDS-PAGE, sodium dodecyl sulfate polyacrylamide gel electrophoresis; SET, single electron transfer; SKIE, solvent kinetic isotope effect; SHMTase, serine hydroxymethyltransferase; TAPS, *N*-tris(hydroxymethyl)methyl-3-

aminopropanesulfonic acid; UDP, uridine diphosphate; wt, wild type; ZPE, zero point energy

Chapter 1: The Essential Role of Isopentenyl Diphosphate:Dimethylallyl Diphosphate Isomerases in Isoprenoid Biosynthesis

1.1 Background

Isoprenoids (or terpenoids) constitute one of the largest and most structurally diverse classes of natural products that are found in all living systems. Collectively, isoprenoids serve diverse biological roles as vitamin precursors, hormones, photosynthetic pigments, electron transport mediators, antibiotics, and as anchors for membrane-associated proteins (*1*). A few examples of isoprenoids (Figure 1.1) include the anticancer agent taxol (**1**), *β*-carotene (**2**, the precursor to vitamin A), the mammalian and plant hormones cholesterol (**3**) and abscisic acid (**4**), respectively, the phytol side chain of chlorophyll (**5**), the pharmaceutical preservative, camphor (**6**), and coenzyme Q (**7**) – an essential component of the mitochondrial electron transport chain required for oxidative phosphorylation and ATP biosynthesis.

1.2 Biosynthesis of Isoprene Units

Despite the large number of naturally occurring isoprenoid compounds, all isoprenoids are derived from the two ubiquitous isoprene starter units, isopentenyl pyrophosphate (IPP, **8**) and dimethylallyl pyrophosphate (DMAPP, **9**, see Scheme 1.1). To date, two pathways for the biosynthesis of IPP and DMAPP have been identified: the mevalonate pathway and the non-mevalonate or methylerythritol phosphate (MEP) pathway. The mevalonate pathway was first discovered in the 1950's (*1-5*) and is the

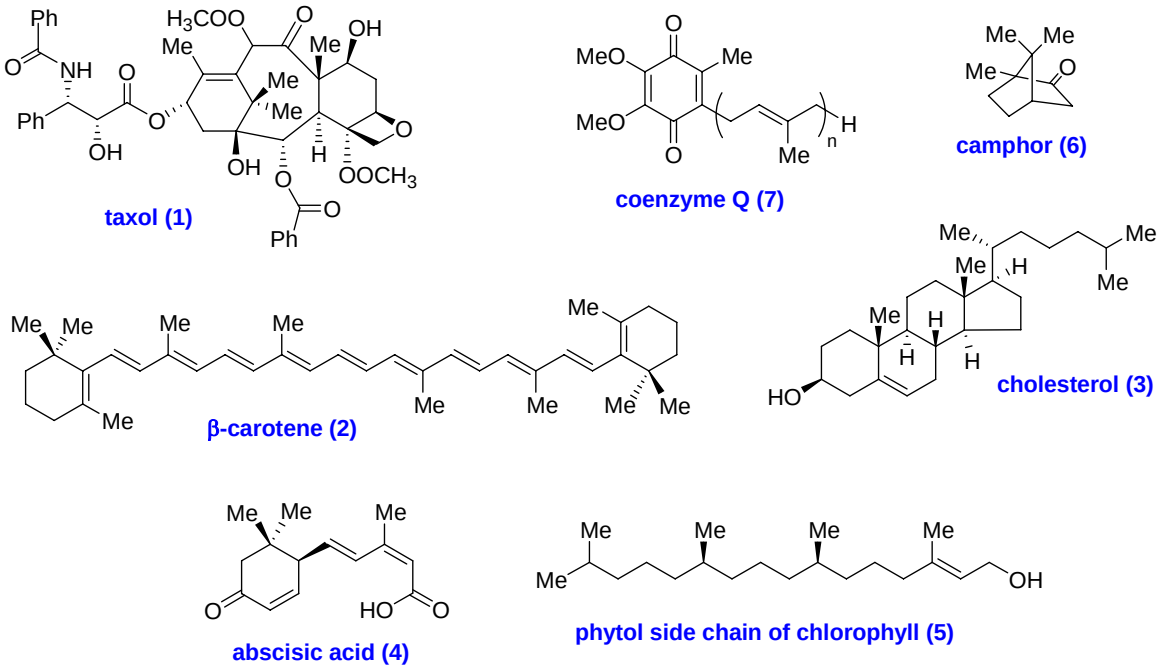

Figure 1.1: Representative Isoprenoids

pathway employed by eukaryotes, archaea, and some bacteria. The MEP pathway was only recently discovered and is present in the chloroplasts of plants, algae, and in most bacteria (*6, 7*). The MEP pathway has generated considerable interest because none of the biosynthetic enzymes present in this pathway have homologues in humans, making each enzyme a potential drug target (*8, 9*).

The mevalonate pathway (Scheme 1.1, reviewed in (*1, 5*)) begins with the condensation of two molecules of acetyl-CoA (**10**) catalyzed by acetyl-CoA acyltransferase (also known as thiolase) to form **11**, which is then condensed with a third molecule of **10** by 3-hydroxy-3-methyl-glutaryl (HMG)-CoA synthase to form HMG-CoA, **12**. In the following step, HMG-CoA is reduced by two molecules of NADPH to

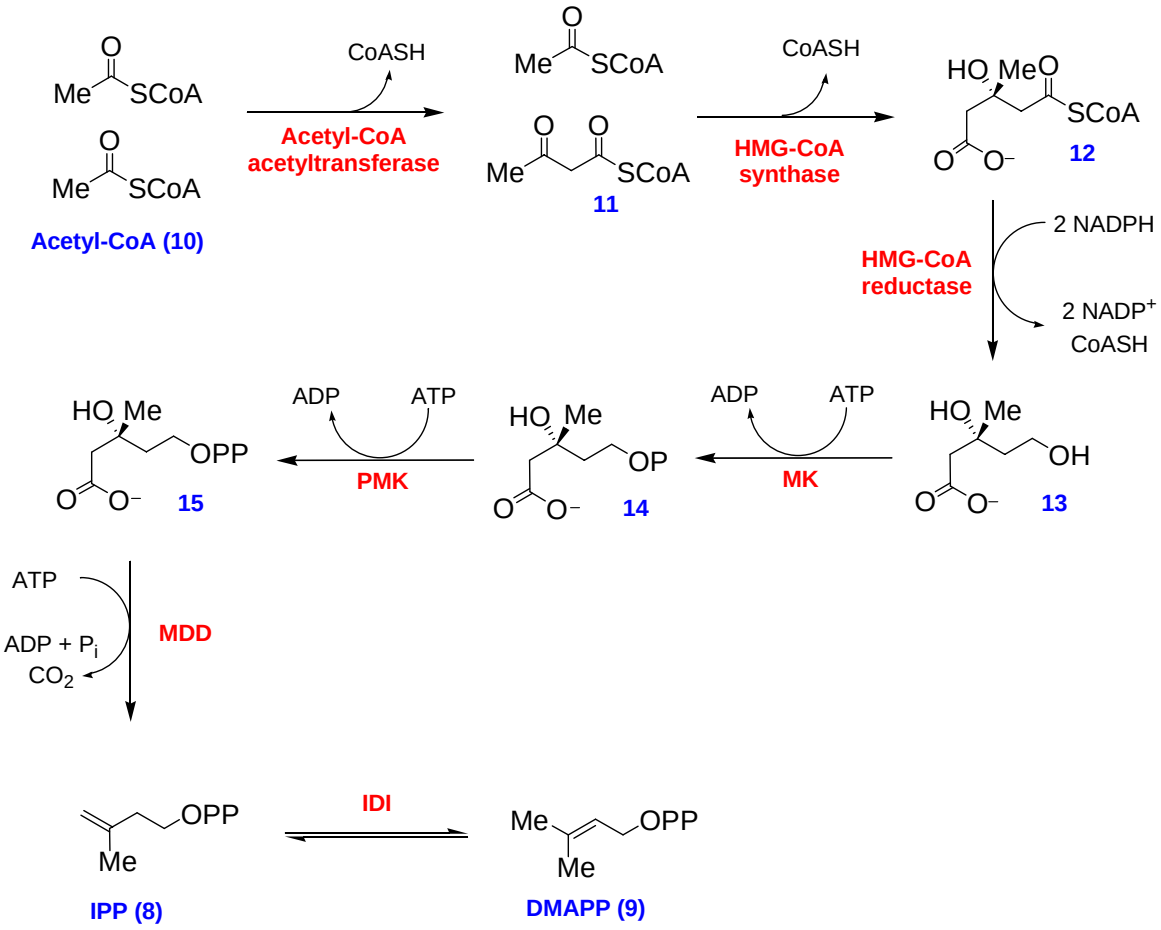

Scheme 1.1: Mevalonate pathway for isoprenoid biosynthesis

form the 4e^- reduced product, mevalonate (**13**) by HMG-CoA reductase (*10*). The conversion of **12** to **13** is the committed step in isoprenoid biosynthesis, and HMG-CoA reductase has been successfully inhibited by a group of drugs termed statins (such as Lipitor and lovastatin) that serve to lower cholesterol levels in the serum (*11*). The next two steps in the pathway involve successive ATP-dependent phosphorylations of mevalonate and mevalonate-5-phosphate (**14**) by mevalonate kinase (MK) and phosphomevalonate kinase (PMK), respectively (*12*), to form mevalonate-5-diphosphate

(**15**). This compound is then converted into IPP (**8**) by an ATP-dependent decarboxylation catalyzed by mevalonate diphosphate decarboxylase (*13-15*). The mevalonate pathway for isoprenoid biosynthesis is completed by the conversion of IPP into DMAPP (**9**) by an isopentenyl diphosphate:dimethylallyl diphosphate isomerase (or IDI (*16*)).

The more recently discovered methylerythritol phosphate (MEP) pathway for isoprenoid biosynthesis (*6, 17-19*) is initiated by the condensation of pyruvate (**16**) with glyceraldehyde-3-phosphate (G3P, **17**) to form 1-deoxy-D-xylulose-5-phosphate (DXP, **18**, Scheme 1.2), which also serves as an intermediate in thiamin and pyridoxol biosynthesis in *E. coli* (*18*). In the committed step to isoprenoid biosynthesis by the MEP pathway, DXP is then converted by DXP-reductoisomerase (DXR) into 2-*C*-methyl-D-erythritol-4-phosphate (MEP, **19**). From **19**, cytidylylation by IspD leads to **20** (*20, 21*), ATP-dependent phosphorylation by IspE yields **21** (*22, 23*), and cyclization by IspF yields **22** (*24, 25*). In the final two steps of the MEP pathway, the [4Fe-4S] cluster containing enzymes IspG and IspH respectively catalyze the 2e- reduction of **22** to give **23** (*26, 27*), and the 2e- reduction of **23** to give a mixture of IPP and DMAPP (*28-30*). As both IPP and DMAPP are generated in the final step, organisms that rely on the MEP pathway for the biosynthesis of their isoprenoids do not require an IDI activity.

1.3 Chain Elongation in Isoprenoid Biosynthesis

Following the biosynthesis of the IPP and DMAPP isoprene units by either the mevalonate or MEP pathway, isoprenoid chain elongation is then required to synthesize

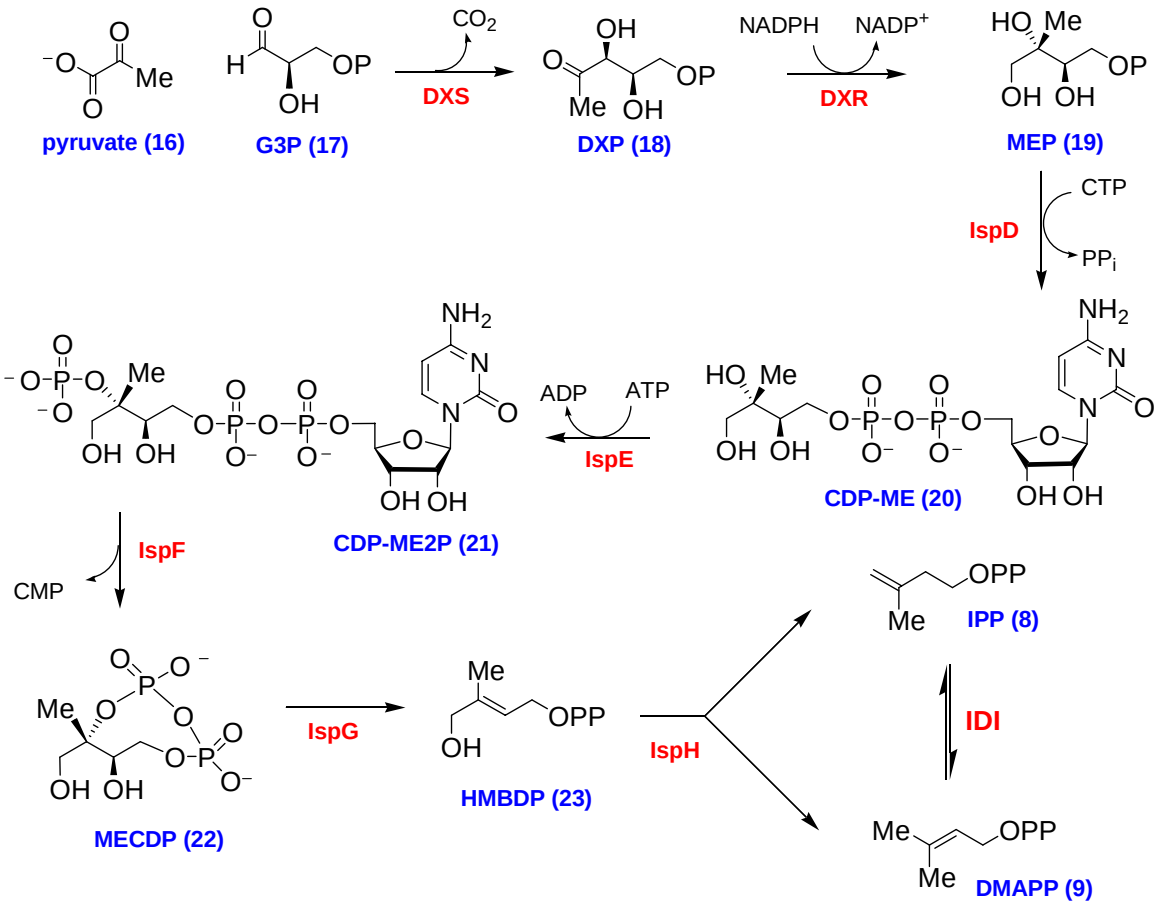

Scheme 1.2: Methylerythritol phosphate (MEP) pathway for isoprenoid biosynthesis

the majority of isoprenoid compounds made by cells (Scheme 1.3). Chain elongation is generally initiated by the condensation of IPP and DMAPP by a farnesyl pyrophosphate (FPP) synthase, which belongs to a group of enzymes called prenyltransferases that collectively share similar structures and catalytic mechanisms (*31-33*). The chemical mechanism of FPP synthase involves an electrophilic alkylation reaction that proceeds in three distinct steps (Scheme 1.4). In the initial step, the C-O bond of the allylic

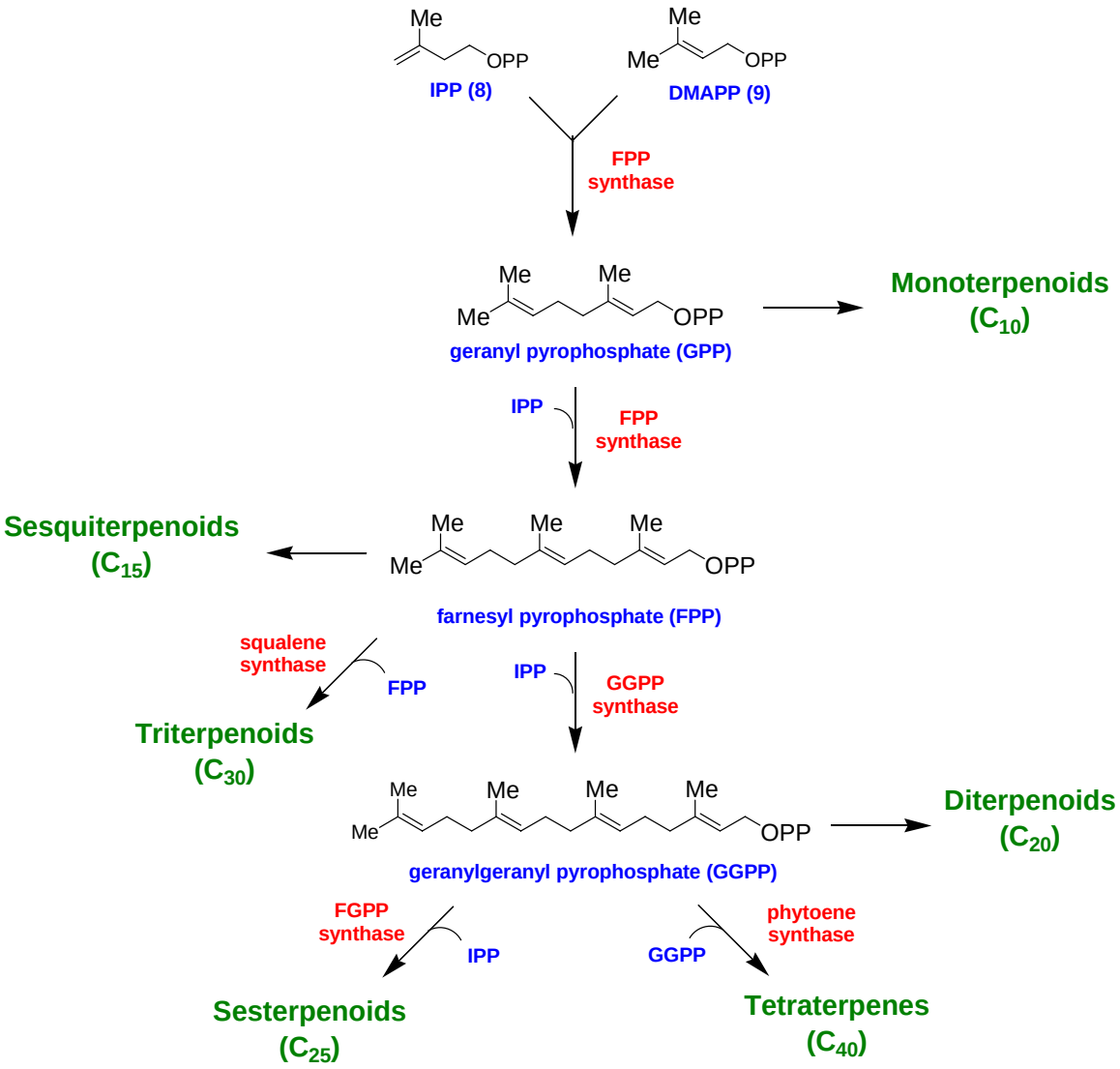

Scheme 1.3: Chain elongation in isoprenoid biosynthesis

pyrophosphate substrate (DMAPP) is broken in S_N1 fashion, forming a tight ion pair between the allylic cation and the PPi leaving group (*34-36*). Next, the C3-C4 bond of IPP is alkylated by the allylic cation to form a tertiary carbocation intermediate, **24**, (*37, 38*) that can then be stereospecifically deprotonated (*33*) to generate GPP (**25**). In a similar manner, GPP can also be extended to FPP (**26**) by FPP synthase, except that in

this second reaction, the allylic pyrophosphate substrate is now GPP, and the product of the reaction is FPP. As the FPP synthase-catalyzed reaction illustrates, each subsequent round of isoprenoid elongation introduces a new allylic pyrophosphate moiety into the product that is then poised for another round of extension/condensation to generate most of the higher-order isoprenoids (Scheme 1.3). Slight variations in the active site architecture of prenyltransferases govern the double bond stereochemistry and the chain length of the substrates that are accepted.

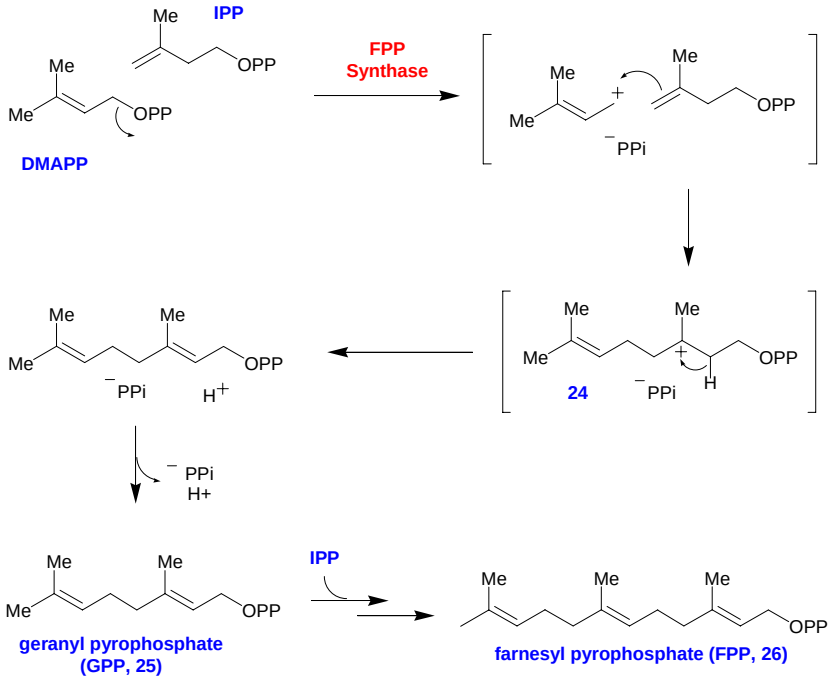

Scheme 1.4: Putative chemical mechanism for farnesyl pyrophosphate synthase

1.4 Isopentenyl Diphosphate:Dimethylallyl Diphosphate Isomerase (IDI)

As discussed in the previous section, the initiation of long chain isoprenoids requires the presence of DMAPP, as this compound serves as the initial allylic pyrophosphate substrate that alkylates the IPP starter unit. Following the first

condensation between IPP and DMAPP to form GPP, longer chain isoprenoids can be generated using IPP as the extender unit. Because at least some DMAPP must be present to initiate long chain isoprenoid biosynthesis, organisms that rely on the mevalonate pathway (Scheme 1.1) for the production of their isoprene units require an isopentenyl diphosphate:dimethylallyl diphosphate isomerase (IDI) activity to generate DMAPP. In contrast, organisms that use the MEP pathway (Scheme 1.2) do not require an IDI activity, because both IPP and DMAPP are generated in the final step of the pathway. IDI enzymes exist in two evolutionarily distinct forms, termed type I IDI (IDI-1) and type II IDI (IDI-2). IDI-1 requires divalent metal ions for catalysis and employs general acid/base chemistry provided by amino acid functional groups in the active site to catalyze the net 1,3-proton addition/elimination reaction. IDI-2 requires a reduced flavin coenzyme in addition to divalent metal ions for catalysis, and its mechanism is poorly understood.

1.5 Mechanistic studies of IDI-1

IDI-1 enzyme activity was initially discovered by Lynen and co-workers during their attempts to understand squalene biosynthesis in baker's yeast (*16, 39*). Shortly thereafter, preliminary mechanistic studies were carried out with partially purified IDI-1 from several sources (*40-42*). These studies established that the reaction requires divalent metal ions (Mg^{2+}) for activity and that a cysteine residue is likely important in catalysis (*40*). In addition, these studies helped to define the stereochemical course of the reaction (summarized in Scheme 1.5). Using tritium exchange experiments, solvent-

derived ^{3}H was incorporated into C2 of IPP but not into C2 of DMAPP, suggesting that protonation/deprotonation at C2 is stereospecific. Subsequent studies demonstrated that the *pro R* H is removed from C2 of IPP during turnover (*41*). In addition, solvent-derived ^{3}H was incorporated into the C4 olefinic position of IPP and into one of the C4 methyl groups of DMAPP (*40*). Subsequent studies demonstrated that protonation at C4 of IPP occurs at the *re* face of the double bond, and leads to incorporation of solvent protons into the (*E*)-methyl group of DMAPP (*42, 43*). Based on these studies, the stereochemical course of the IDI-1 reaction was suggested to be an antarafacial 1,3-proton addition/elimination (*42*). Interestingly, using D_2O exchange experiments and ^{1}H-NMR analysis of IDI-1 reaction mixtures, Poulter and co-workers demonstrated that all of the hydrogens in both IPP and DMAPP (except those at C1) could be slowly exchanged by an IDI-1-catalyzed process (Scheme 1.5). This result suggests that the IDI-1 active site does not rigidly control the stereochemistry of the requisite proton transfers during turnover. Likely explanations for this lack of stereo- and regioselectivity are the presence of alternative acid/base groups in the enzyme active site and/or the presence of different IPP/DMAPP binding modes.

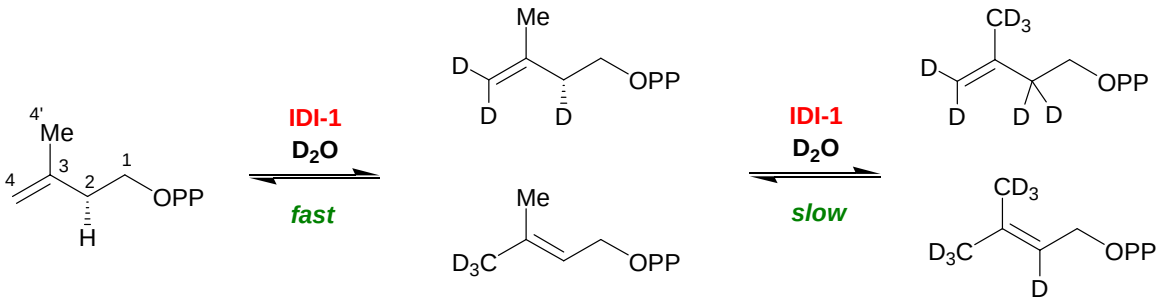

Scheme 1.5: Stereochemistry of IDI-1 catalyzed reaction

Subsequent kinetic and inhibition studies provided support for an IDI-1 chemical mechanism involving either a 3° carbocation intermediate, or a transition state with carbocation character (*40, 44, 45*). Most notably, kinetic studies using (*Z*)-CF_3-DMAPP (**27**, Scheme 1.6) as the substrate indicated a decrease in activity of ~ 10^6 (*44*), which is very similar to the ~ 10^7 decrease in the solvolysis rate of the corresponding methanesulfonate compound (**28**), which presumably proceeds via S_N1 chemistry and an allylic carbocation intermediate (*34*). Thus, it appears that the intermediate (or transition state) in the IDI-1 catalyzed reaction is characterized by a substantial degree of cationic character. In addition, 2-(dimethylamino)ethyl pyrophosphate (NIPP, **29**) was designed as a mimic for the putative 3° substrate carbocation intermediate and was found to be a slow, tight binding inhibitor of IDI-1 with a 10-100 pM binding affinity – 4 to 5 orders of magnitude tighter than IPP or DMAPP binding (*44, 45*). Upon denaturation of IDI-1, NIPP was released into solution, indicating that the inhibition is due to a non-covalent interaction with the active site of IDI-1.

More recent biochemical and structural studies have further helped to elucidate the chemical mechanism of IDI-1 (Scheme 1.7). X-ray crystallographic analysis revealed that the native enzyme contains a Zn^{2+} ion coordinated with an octahedral geometry to an unusual His_3Glu_2 pocket (*46, 47*). In addition to the Zn^{2+} ion, a Mg^{2+} ion is bound between the pyrophosphate moiety of the substrate and the enzyme (*46*). A combination of site directed mutagenesis and studies with various electrophilically activated IPP and DMAPP analogues have identified Cys67, Glu116, and Tyr104 (*E. coli* numbering) as important catalytic residues (*48-50*). In the co-crystal structures of IDI-1 in complex with

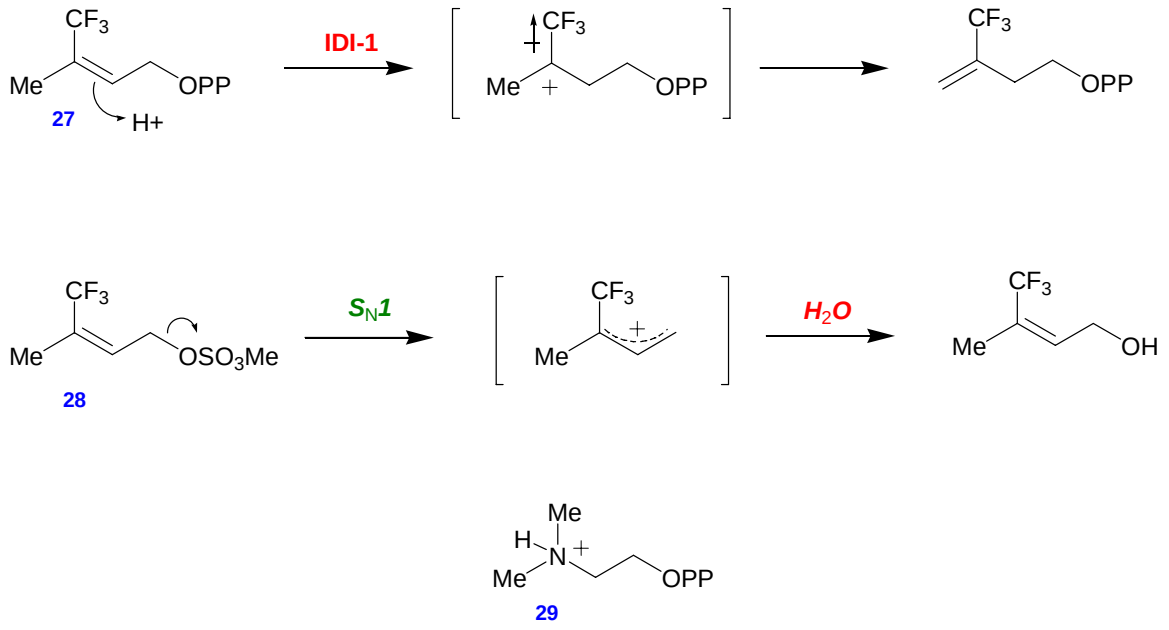

Scheme 1.6: Substrate analogues and inhibitors suggest presence of electron-deficient intermediate during IDI-1 catalysis

various inhibitors, these amino acids are arranged on opposite sides of the inhibitor and appear to be positioned appropriately for acid/base catalysis (*50, 51*). The carboxylate side chain of Glu116 coordinates to the Zn ion, hydrogen bonds to Tyr104, and is oriented towards the protonated ammounim moiety of NIPP in the co-crystal structure. In addition, mutation of Glu116 leads to a drastic decrease in activity and Glu116 can be covalently modified by several electrophilic inhibitors. Because of these observations, Glu116 is believed to be one of the residues involved in acid/base catalysis, perhaps with the assistance of Tyr104, a residue that is also required for activity (*50*). The thiol side chain of Cys67 is positioned on the opposite side of the bound inhibitor, away from the Glu116-Tyr104 dyad, and is believed to be the other acid/base group. This is consistent

with the inactivity of C67A and C67S mutants (*49*) and the observation that C67 forms thioether linkages with several inhibitiors in the co-crystal structure (*50*). In addition, the nearby aromatic Trp161 residue could help to stabilize an electron deficient intermediate (or transition state) through cation-π interactions.

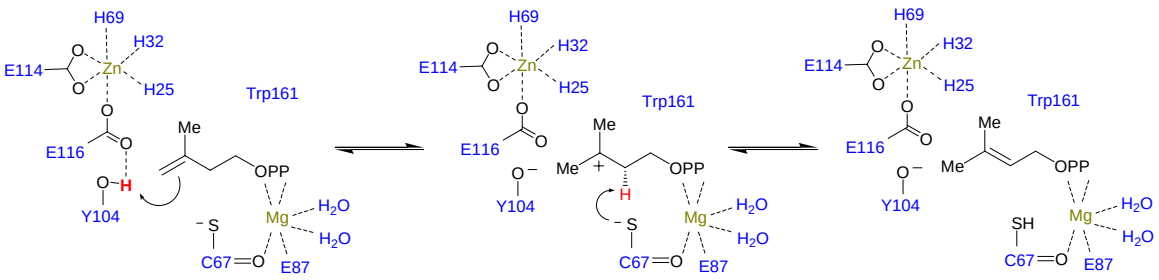

Scheme 1.7: Putative chemical mechanism for *E. coli* IDI-1

Despite the fact that IDI-1 has been subjected to intense mechanistic studies over the years, the exact nature of the allylic-1,3-isomerization remains mysterious and it is still unclear whether the mechanism proceeds via a concerted transition state, or through a 3° carbocation intermediate. Even though 3° carbocation intermediates are highly reactive species, there are multiple precedents for their existence in reactions catalyzed by isoprenoid biosynthetic enzymes, most notably in the prenyl transferase (*32*) and terpenoid cyclase families of enzymes (*52*). Additional insight into the nature of the allylic 1,3-isomerization catalyzed by IDI was provided by Richard and co-workers in their model studies of the stepwise, acid-catalyzed isomerization of 4-(4-methoxyphenyl)-2-methyl-1-butene (**30**, Scheme 1.8) in a mixture of

H_2O:trifluoroethanol (80:20% v/v) at pH 7.0 (*53, 54*). Estimates of the rate constants for the decay of the carbocation intermediate (**31**) to **30** and **32**, were derived from measurements of the kinetic partitioning of **31** to form the various products (**30**, **32**, and **33**) and from previously measured rate constants for the trapping of tertiary carbocations by solvent molecules (*54*). Based on comparison of the rate constants for the IDI-catalyzed isomerization (k_{cat}) and the uncatalyzed reaction (k_{non} = 4.7 x 10^{-11} s^{-1}, determined form the rate constants in Scheme 1.8), they calculated that IDI lowers the overall energetic barrier to the 1,3-allylic isomerization by 16 kcal/mol. A large portion of the ensuing catalytic rate enhancement (k_{cat}/k_{non} ~ 10^{11}) is likely achieved by electrostatic stabilization of the cationic intermediate/transition state by the IDI active site. From this data, the authors speculate that the IDI-1 catalyzed reaction likely involves a concerted proton addition/elimination. First, the fact that reaction of the carbocation intermediate (**31**) with solvent is > 50 fold faster than solvent deprotonation of **31** (to **32**), suggests that if IDI-1 catalyzes a stepwise transformation, then the cationic intermediate cannot be accessible to water molecules, because IDI-1 does not catalyze hydration of IPP/DMAPP (*43*). Alternatively, if IDI-1 catalyzes a concerted allylic 1,3-isomerization, a carbocation intermediate would never be formed. Furthermore, they argue that because the barriers to deprotonation of **31** are already very small, that there is little intrinsic advantage to general acid catalysis to form a 3° carbocation. This is in contrast to the step-wise mechanisms for enzymes that catalyze reversible α-deprotonation of carbonyl compounds via enolate intermediates, where there is a large intrinsic advantage to general base catalysis. Because of these reasons, they favor a

concerted protonation/deprotonation mechanism for IDI-1. However, to date, no conclusive experimental evidence to distinguish among these mechanistic possibilities for IDI-1 has been reported.

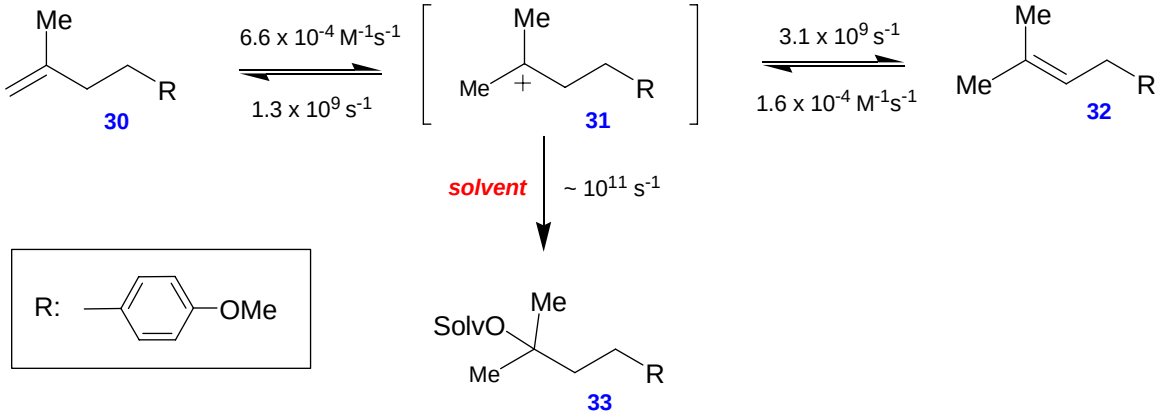

Scheme 1.8: Model studies of the stepwise, acid-catalyzed 1,3-allylic isomerization of **30** in H_2O:TFE (80:20 %v/v)

1.6 Identification and Initial Characterization of IDI-2

In 2001, Kuzuyama, Seto, and co-workers identified a phylogenetically distinct IDI during their studies of isoprenoid biosynthesis in *Streptomyces* sp. strain CL190 (*55*). Upon identifying and sequencing the gene cluster encoding the mevalonate pathway enzymes, no *idi1* gene was found. However, an open reading frame of unknown function (*orfD*) was subsequently shown to encode an IDI enzyme. Interestingly, in addition to divalent metal ions, this isomerase also required flavin mononucleotide (FMN) and a

reducing agent (NADPH) for activity. Due to its distinct gene sequence and unique coenzyme requirements, OrfD was subsequently dubbed IDI-2. They also demonstrated that the *Streptomyces idi2* gene could complement the *idi1*$^-$ mutation in *E. coli*, suggesting that catalyzing the isomerization of IPP to DMAPP is indeed the physiological function of IDI-2.

Subsequent biochemical studies indicated that the *pro S* hydride of NADPH is transferred to the IDI-2 bound oxidized FMN (FMN_{ox}) to reduce the flavin to its $2e^-$ reduced state (Scheme 1.9), suggesting that NADPH is likely the physiological reductant and that it binds to IDI-2 in a specific orientation (*56*). Interestingly, additional investigation into the requirement of IDI-2 for NADPH indicated that only catalytic quantities of NADPH were required to activate IDI-2:FMN_{ox}, after which the enzyme remained competent for multiple turnovers (*56, 57*). This result suggests that there is no net redox change in the flavin after completion of each catalytic cycle, which is consistent with the redox neutral allylic-1,3-isomerization reaction that is being catalyzed. Using deuterated IPP analogues (Scheme 1.9), it was shown that, like IDI-1, IDI-2 catalyzes the stereospecific removal of the *pro-R* hydrogen from C2 of IPP during turnover (*58*). Deuterium exchange studies revealed that the olefinic and the *pro-R* C2 protons of IPP are exchanged with solvent deuterium, and that deuterium is selectively incorporated into the (*E*)-methyl group of DMAPP (*59*). Interestingly, IDI-2 appears to be much more stereoselective with respect to the location of solvent deuterium incorporation into IPP and DMAPP than its IDI-1 counterpart, as no protons were

exchanged for deuterium at any of the other carbon atoms of IPP or DMAPP upon extended incubation with IDI-2 in D_2O.

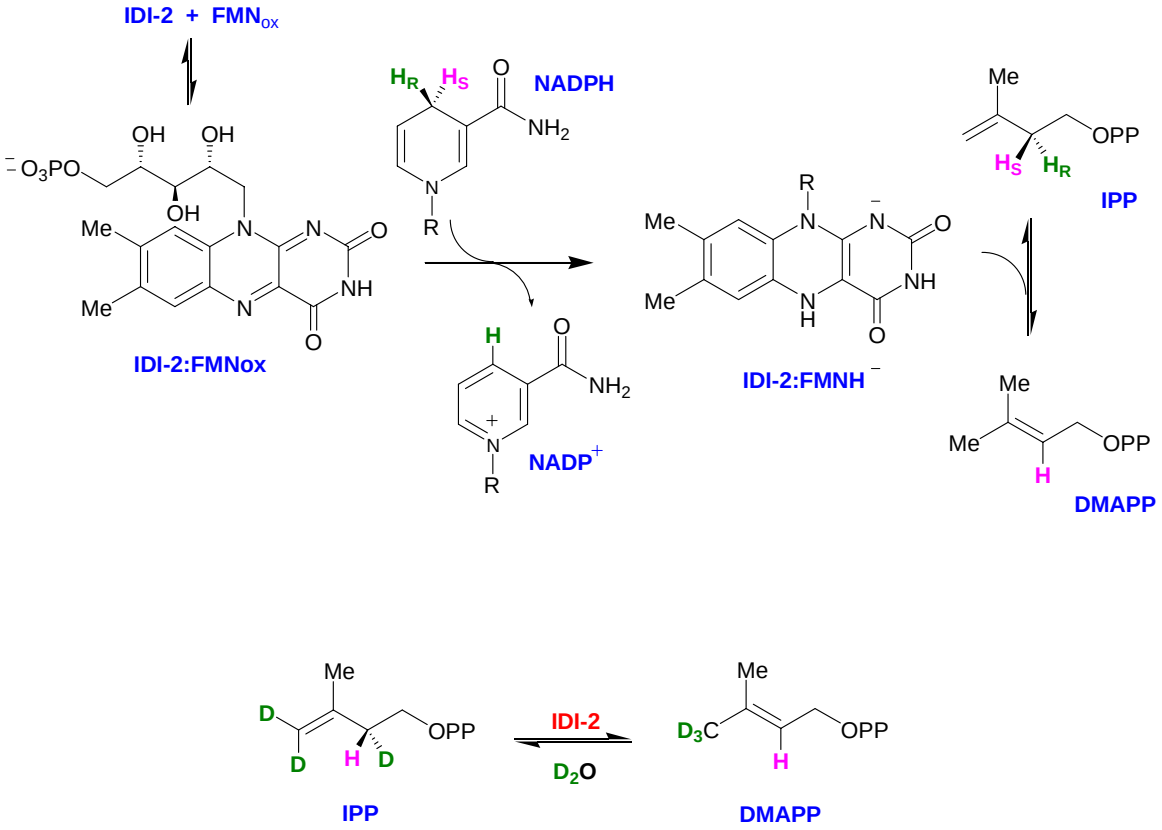

Scheme 1.9: General properties of IDI-2 catalyzed reaction

The first X-ray crystal structures of IDI-2 revealed that the enzyme adopts a TIM-barrel fold (*60, 61*), which is structurally distinct from the α/β fold adopted by IDI-1 (*51*). When the crystals of IDI-2 were soaked with FMN_{ox}, the binding site for the coenzyme could be readily identified (Figure 1.2). Several interactions between conserved amino acid residues and the flavin include putative hydrogen bonds between Thr67, Ser95,

Lys187, and His149 (*S. aureus* numbering) with the N5, C4=O, N1, and C2=O groups of the flavin, respectively. In these initial structural studies, the authors were unable to co-

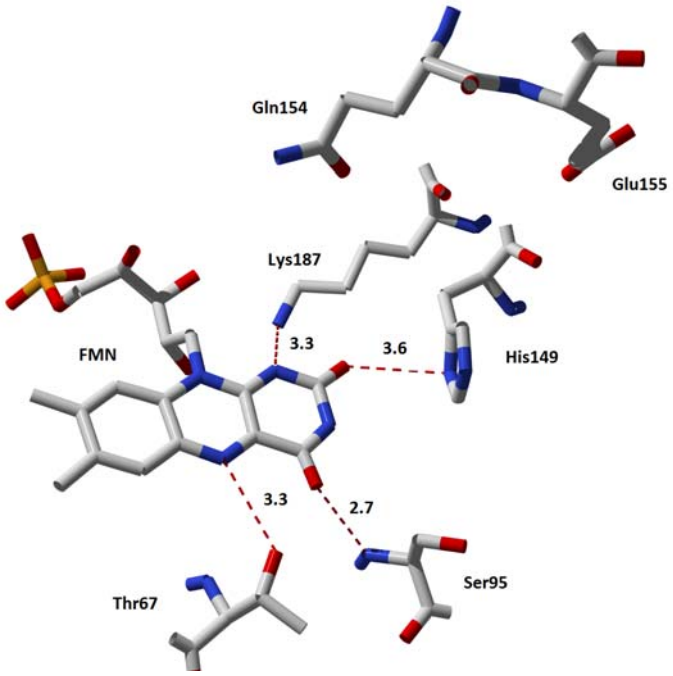

Figure 1.2: FMN binding site of IDI-2 from *Bacillus subtilis*, with distances shown in Å

cyrstalize IDI-2:FMN with IPP and/or Mg^{2+}, and they also did not report structures with the reduced coenzyme bound. Phylogenetic analysis indicated that IDI-2 is distantly related to the α-hydroxy acid dehydrogenases, a superfamily of FMN-dependent enzymes that also adopt TIM-barrel folds (*7*). Interestingly, IDI-2 enzymes lack the set of conserved catalytic amino acids residues present in the α-hydroxy acid dehydrogenases, indicating mechanistic divergence. This is not surprising, as these dehydrogenases typically employ an oxidized flavin for the 2*e*- oxidation of the hydroxyl group α to the

carboxyl group in their respective substrates (Scheme 1.10), while IDI-2 uses a reduced flavin to catalyze a redox neutral isomerization. Instead, IDI-2 enzymes contain a different set of strictly conserved residues in the direct vicinity of the FMN (including His149, Gln154, and Glu155) in addition to other absolutely conserved residues in the *N*-terminal portion of the enzyme, which exhibits a greater extent of amino acid sequence divergence from the α-hydroxy acid dehydrogenases than the *C*-terminal domain (which adopts the TIM-barrel fold in both classes of enzymes).

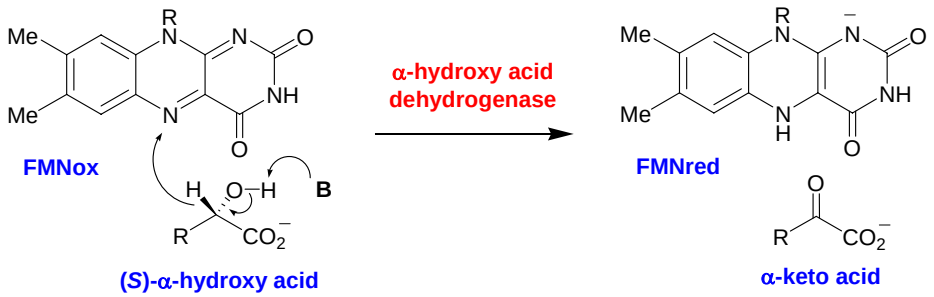

Scheme 1.10: A typical reaction catalyzed by members of the (*S*)-α-hydroxy acid dehydrogenase enzyme superfamily

1.7 Flavoenzymes that Catalyze reactions with no Net Redox Change

The structures of the common flavin coenzymes used in biological systems in their various oxidation and ionization states (**34** - **38**) are shown in Figure 1.3. Most flavoenzymes employ either the flavin mononucleotide (FMN) or flavin adenine dinucleotide (FAD) form of the coenzyme. While flavins typically transfer electrons

(either 1*e*- or 2*e*-) or activate the singlet form of molecular oxygen (O_2) for oxygen insertion into substrates in biological systems, they are chemically diverse coenzymes

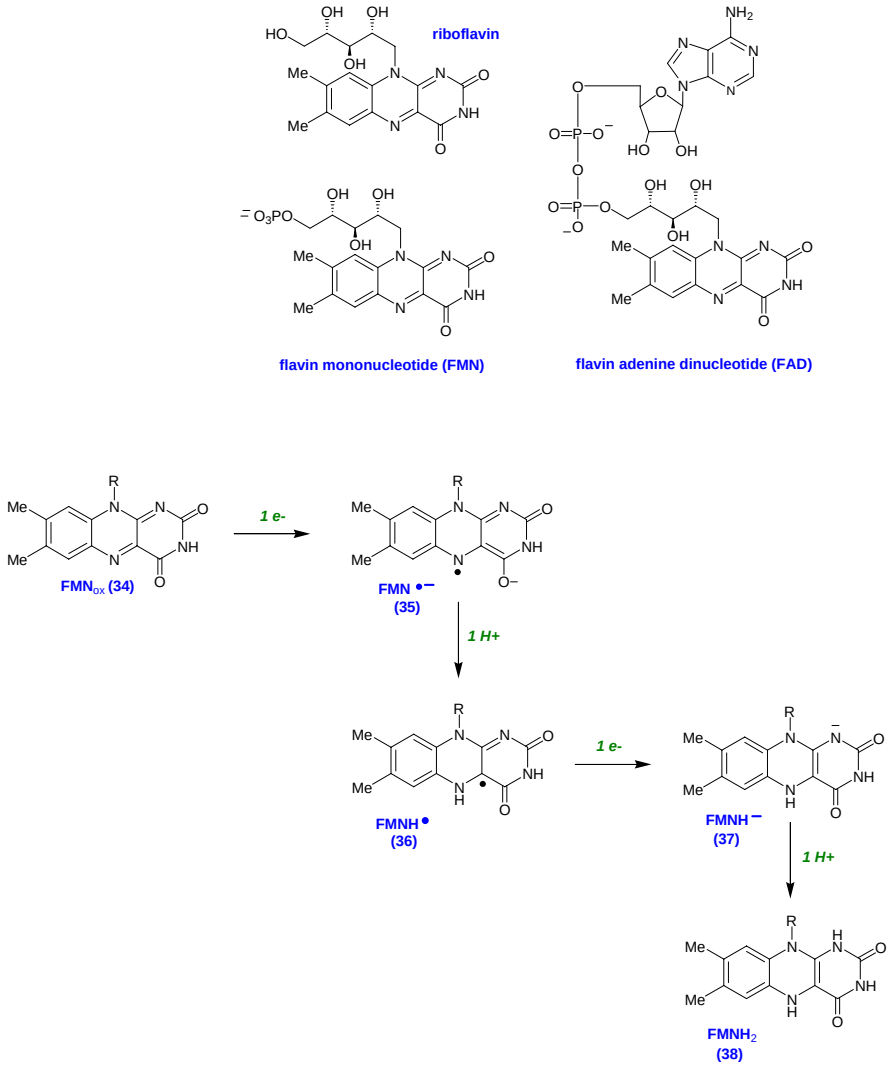

Figure 1.3: Biologically relevant protonation and redox states of flavin coenzymes

that are known to catalyze numerous types of reactions (*62*). The involvement of flavin coenzymes in reactions that involve no net redox change (such as the IDI-2 catalyzed

reaction) is unusual, but is not without precedent (*63*). Several examples of enzymes which employ flavins in unusual manners are highlighted below.

5-Hydroxyvaleryl CoA dehydratase (HVCD) catalyzes the dehydration of 5-hydroxyvaleryl-CoA (**39**, Scheme 1.11) to pent-4-enoyl-CoA (**40**) during the fermentation of proline by certain anaerobic bacteria (*64*), and it requires an oxidized FAD coenzyme for activity (*65*). The reaction is initiated by C2 deprotonation and transfer of a hydride equivalent from C3 of **39** to the N5 position of FAD_{ox} to generate the 2*e*- reduced flavin and the unsaturated intermediate (**41**). This transformation is reminiscent of the first step in the reactions catalyzed by the acyl-CoA dehydrogenases (*66*), which are close structural homologues of HVCD. The oxidation of the substrate C2-C3 bond is thought to activate the C4 proton of **41**, enabling dehydration across the C4-C5 bond to proceed via acid/base catalysis. The hydride equivalent is then transferred from the reduced flavin back to C3 of the dehydrated intermediate (**42**) to generate product (**40**). Thus, the reaction catalyzed by HVCD appears to involve a cryptic 2*e*-transfer cycle.

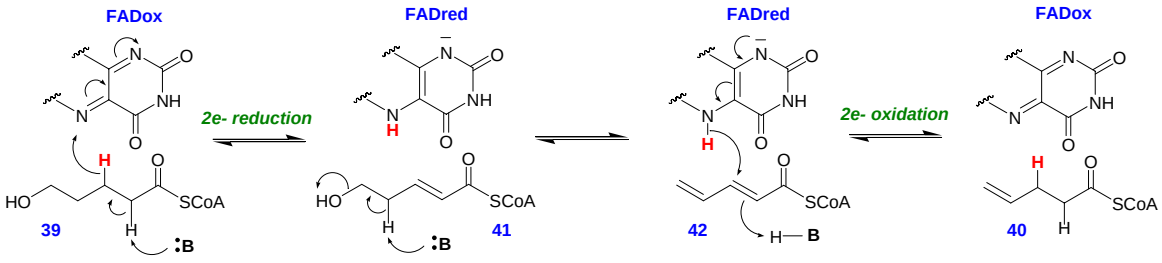

Scheme 1.11: Putatuve chemical mechanism for HVCD

DNA photolyases are critical FAD-dependent enzymes in bacteria that repair thymidine dimers formed between adjacent thymidine residues in DNA. These dimers are formed by UV radiation and they must be repaired prior to replication of the bacterial genome, or mutations can be stably incorporated into the chromosome. Extensive structural, biochemical, and computational studies on DNA photolyases (reviewed in (*67*)) have provided considerable insight into the catalytic mechanism of this interesting flavoenzyme (Scheme 1.12). First, light in the 300-450 nm range is absorbed by an antenna pigment (either 5,10-methenyl-tetrahydrofolylpolyglutamate or 7,8-didemethyl-8-hydroxy-5-carba-5-deaza-riboflavin), which non-radiatively transfers this energy to the $FADH^-$ coenzyme of DNA photolyase. The excited FADH- then pumps an electron into the thymidine dimer (**43**), giving the neutral semiquinone (FMNH•) and a substrate ketyl radical intermediate (**44**), which undergoes a series of intramolecular rearrangements to repair the dimer. An electron is then transferred back to FMNH• to regenerate the resting form of the enzyme and to complete the catalytic cycle. Support for the existence of the kinetically competent radical pair comes from time-resolved EPR and pulse radiolysis spectroscopic studies (*67*). Thus, like 5-hydroxyvaleryl-CoA dehydratase, the flavin coenzyme of DNA photolyases catalyzes a cryptic redox cycle, where there is no net change in the redox state of the flavin after catalysis.

Another interesting and unique mode of flavoenzyme catalysis that does not involve a net change in the redox state of the flavin is observed in the reaction catalyzed by UDP-galactopyranose mutase (UGM), an FAD-dependent enzyme that contracts the sugar ring of UDP-galactopyranose (UDP-Gal*p*, **45**) to its furanose form (UDP-Gal*f*, **46**)

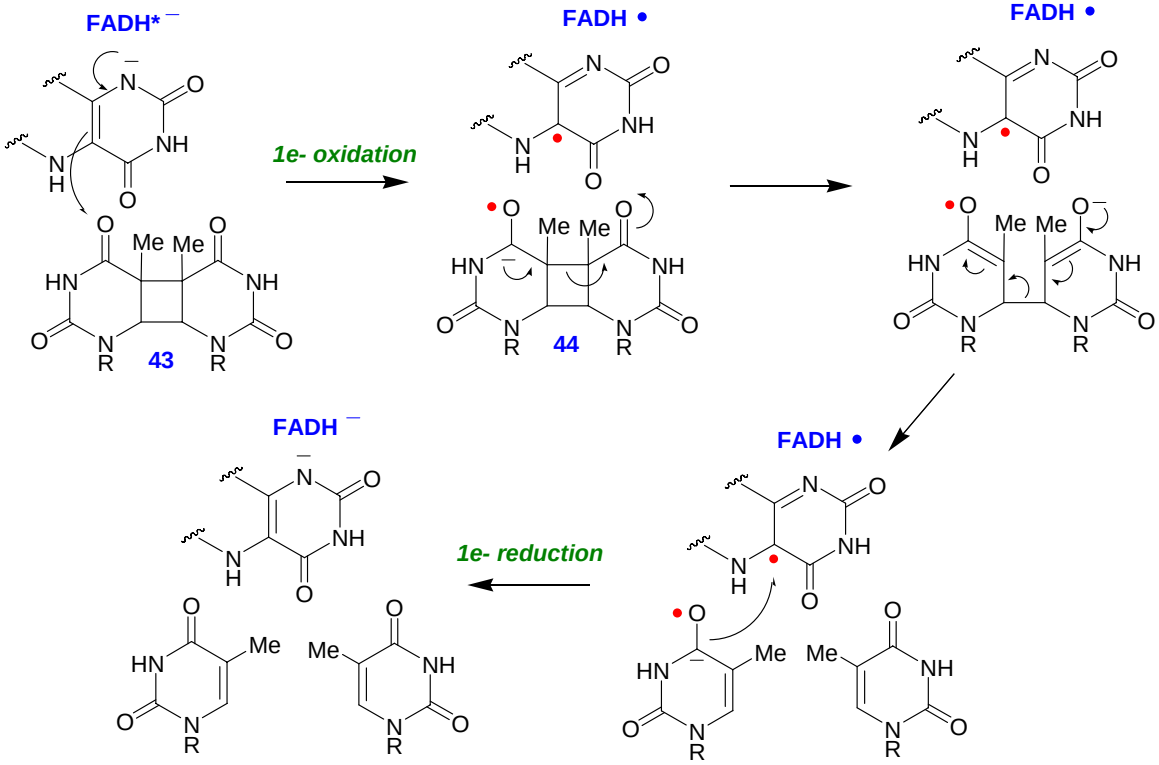

Scheme 1.12: Putative chemical mechanism for DNA photolyase

during the biosynthesis of bacterial cell surface polysaccharides (Scheme 1.13). Like IDI-2, the catalytic cycle of UGM begins with the reduced form of the coenzyme. The initial step in the chemical mechanism involves expulsion of the UDP moiety from UDP-Gal*p* and nucleophilic attack by the flavin to form **47**. This could be achieved either through S_N1-type chemistry via an oxocarbenium ion intermediate or by direct nucleophilic attack of the reduced FAD on the anomeric carbon (S_N2-type mechanism). Formation of the iminum species (**48**) concomitant with opening of the pyranose ring could enable cyclization (**48** → **49**) to form the furanose ring by nucleophilic attack of the C4□ hydroxyl moiety on the anomeric carbon. Support for the formation of the

iminium species (**48**) in the UGM catalytic cycle was obtained when the reaction mixture was quenched with $NaCNBH_3$ and analyzed by mass spectrometry. Under these conditions, the reduced N5-alkyl flavin adduct (**50**) was detected (*68*). In addition, structural studies of UGM in complex with UDP-Gal*p* indicate that the N5 atom of the

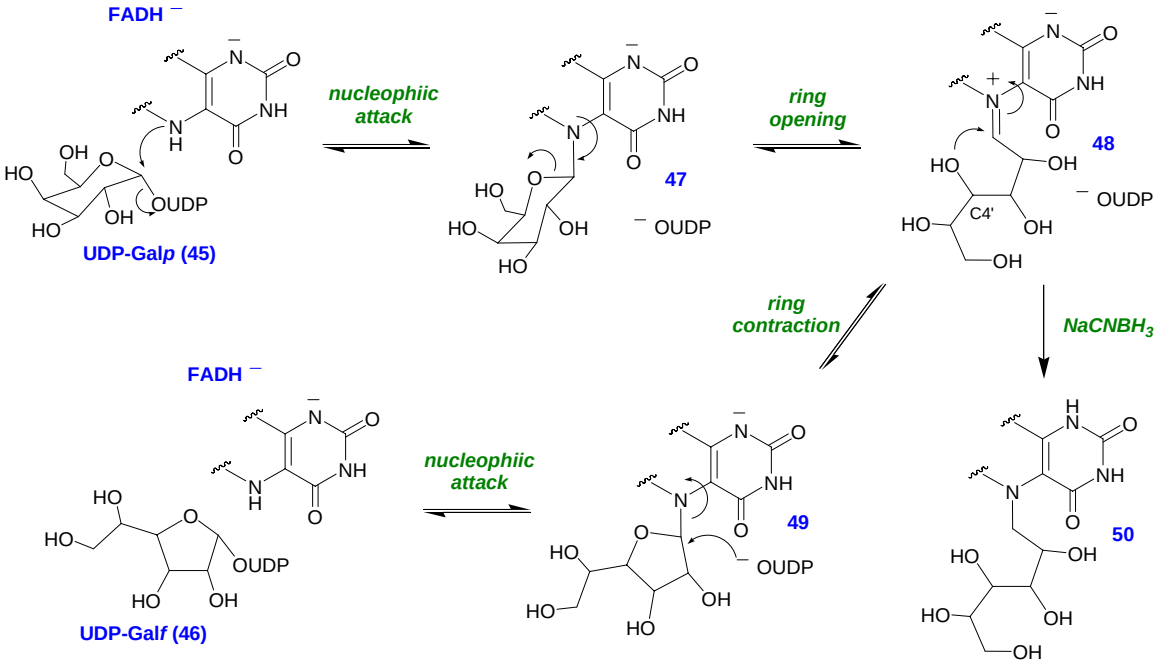

Scheme 1.13: Putative chemical mechanism for UGM

reduced FAD is in close proximity to the anomeric carbon, and appears to be positioned suitably for covalent catalysis (*69, 70*). Thus, in contrast to the proposed mechanisms for 5-hydroxyvaleryl-CoA dehydratase and DNA photolyase, the putative chemical mechanism for UGM does not appear to involve the formal transfer of reducing equivalents between the flavin and the substrate.

As a final example, the FMN-dependent enzyme chorismate synthase (CS) catalyzes the anti-1,4-elimination of the 3-phosphate group and unactivated C6 *pro-R* proton from 5-enolpyruvyl-3-shikimate phosphate (EPSP, **51**, Scheme 1.14), forming chorismate (**52**) in the final step of the shikimate biosynthetic pathway. The resting form

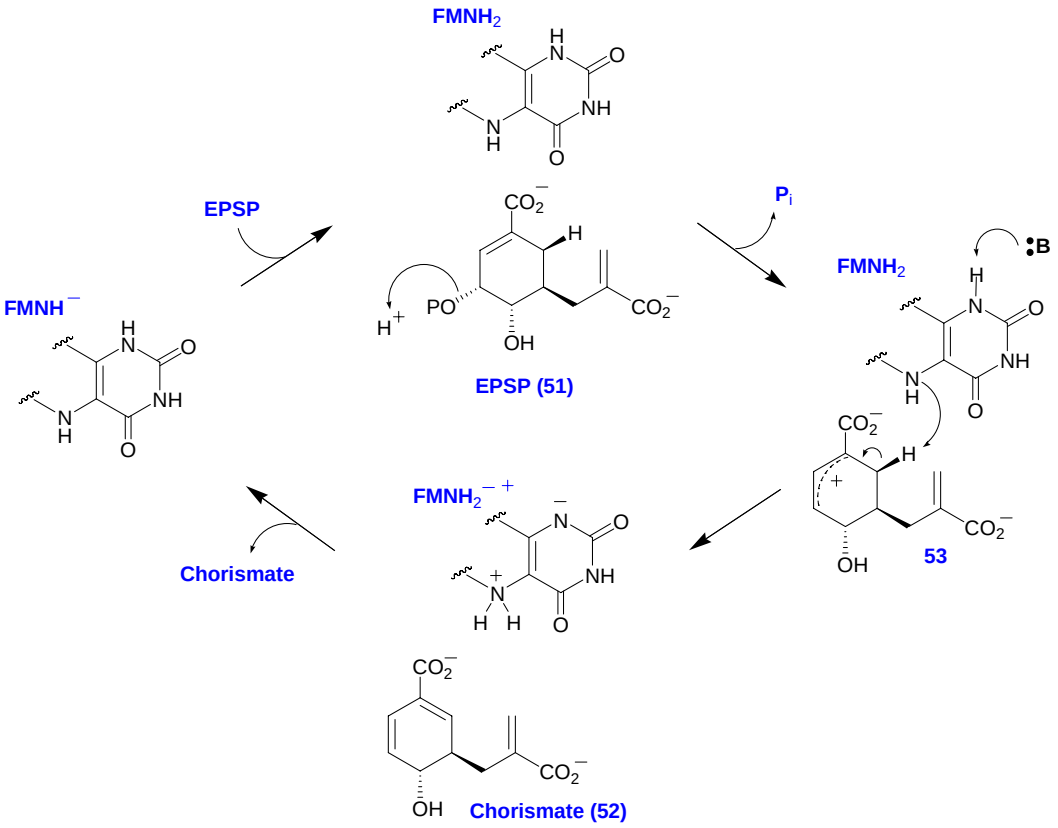

Scheme 1.14: Putative chemical mechanism for chorismate synthase

of the enzyme binds to the anionic reduced form of FMN (FMNH-), but upon EPSP binding, a large conformational change leads to the accumulation of the neutral reduced form of the flavin ($FMNH_2$) (*71-74*). Structural and mutagenesis studies have demonstrated that EPSP stacks on top of the isoalloxazine moiety of the flavin, and that a conserved His residue may be responsible for protonating FMNH- at the N1 atom upon

EPSP binding (*75, 76*). Transient kinetic experiments, kinetic isotope effect measurements, and studies with fluorinated EPSP substrate analogues are all consistent with a chemical mechanism where phosphate elimination (facilitated by a conserved His residue) precedes deprotonation in a stepwise reaction via an electron deficient intermediate, **53** (*74, 77-80*). The exact function of the $FMNH_2$ intermediate in the chemical transformation is still unclear, but the X-ray crystal structure suggests that the N5 atom of the flavin is in the direct vicinity of the *pro-R* C6 proton of the substrate and, as such, could assist in deprotonation of the carbocation intermediate. Thus, in the case of CS, the reduced FMN might be serving as an acid/base catalyst.

1.8 Mechanistic Considerations for IDI-2

The unusual mechanisms observed in the flavoenzymes discussed above illustrate the catalytic versatility of flavin coenzymes. In light of these studies, several potential chemical mechanisms involving the flavin can be envisioned for the redox neutral allylic-1,3-isomerization catalyzed by IDI-2 (Scheme 1.15). The first possibility is that the flavin serves a structural role, helping to keep the active site of IDI-2 folded into a catalytically competent conformation. This sort of role for flavins has been observed in the acetolactate synthases (*81*), but is inconsistent with the observation that IDI-2 reconstituted with FMN_{ox} is inactive (*55*). Furthermore, the reduced form of 5-deaza-FMN (**54**, Scheme 1.15A), whose binding affinity to IDI-2 is very similar to that of FMN, does not support catalysis (*56, 82*). This latter observation also seems to be at odds with a simple electrostatic stabilization mode of FMN catalysis (Scheme 1.15B),

unless the putative electrostatic stabilization of the carbocation intermediate (**55**) depends strongly on the N5 atom of the reduced flavin. A cryptic 2*e*- transfer mechanism (Scheme 1.15C), as has been proposed for 5-hydroxyvaleryl-CoA dehydratase, also seems unlikely for IDI-2 because hydride transfer to and protonation of IPP would generate the fully saturated isoprenoid intermediate (**56**), which would need to be deprotonated ($pK_a \sim 50$) and oxidized to complete the catalytic cycle.

Alternatively, if a cryptic single electron transfer mechanism is operative (Scheme 1.15D), single electron transfer (SET) from FMNH- could be coupled to protonation at C4 of IPP to generate the FMNH•/substrate radical (**57**) pair. Deprotonation at C2 of the radical intermediate and electron transfer to FMNH• would complete the catalytic cycle. This mechanism would require the assistance of active site amino acid residues to facilitate the protonation/deprotonation steps. Interestingly, the SET mechanism seems to be consistent with the observation that IDI-2 reconstituted with reduced 1-deaza-FMN (**58**, Scheme 1.15A - an analogue that is capable of SET reactions (*83, 84*)) supports wild type levels of IDI-2 catalysis (*56*), while IDI-2 reconstituted with 5-deaza-FMN (**54**, an analogue that is only capable of concerted 2*e*- transfers (*84, 85*)) is inactive (*56, 82*). Furthermore, redox titrations and photoreduction experiments of the IDI-2-bound flavin in the presence of IPP revealed the thermodynamic stabilization of FMNH• in the presence of IPP (*56, 86*). While it is not exactly clear what catalytic advantage a SET mechanism for IDI-2 catalysis would afford, these results nevertheless suggest that the IDI-2 active site is at least capable of accommodating a neutral semiquinone and, thus, an isomerization mechanism involving SET can not be excluded.

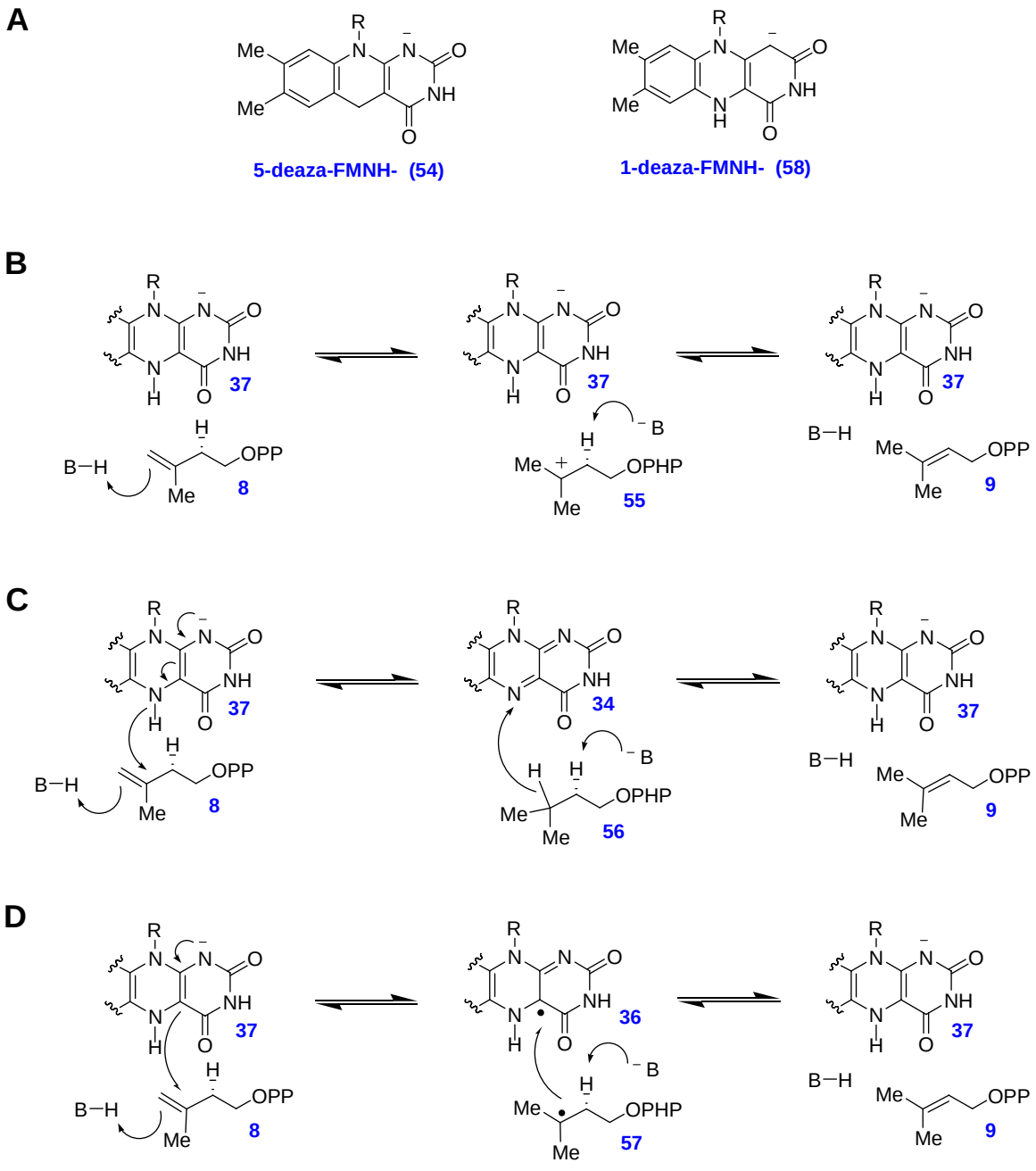

Scheme 1.15: Mechanistic possibilities for IDI-2 catalysis

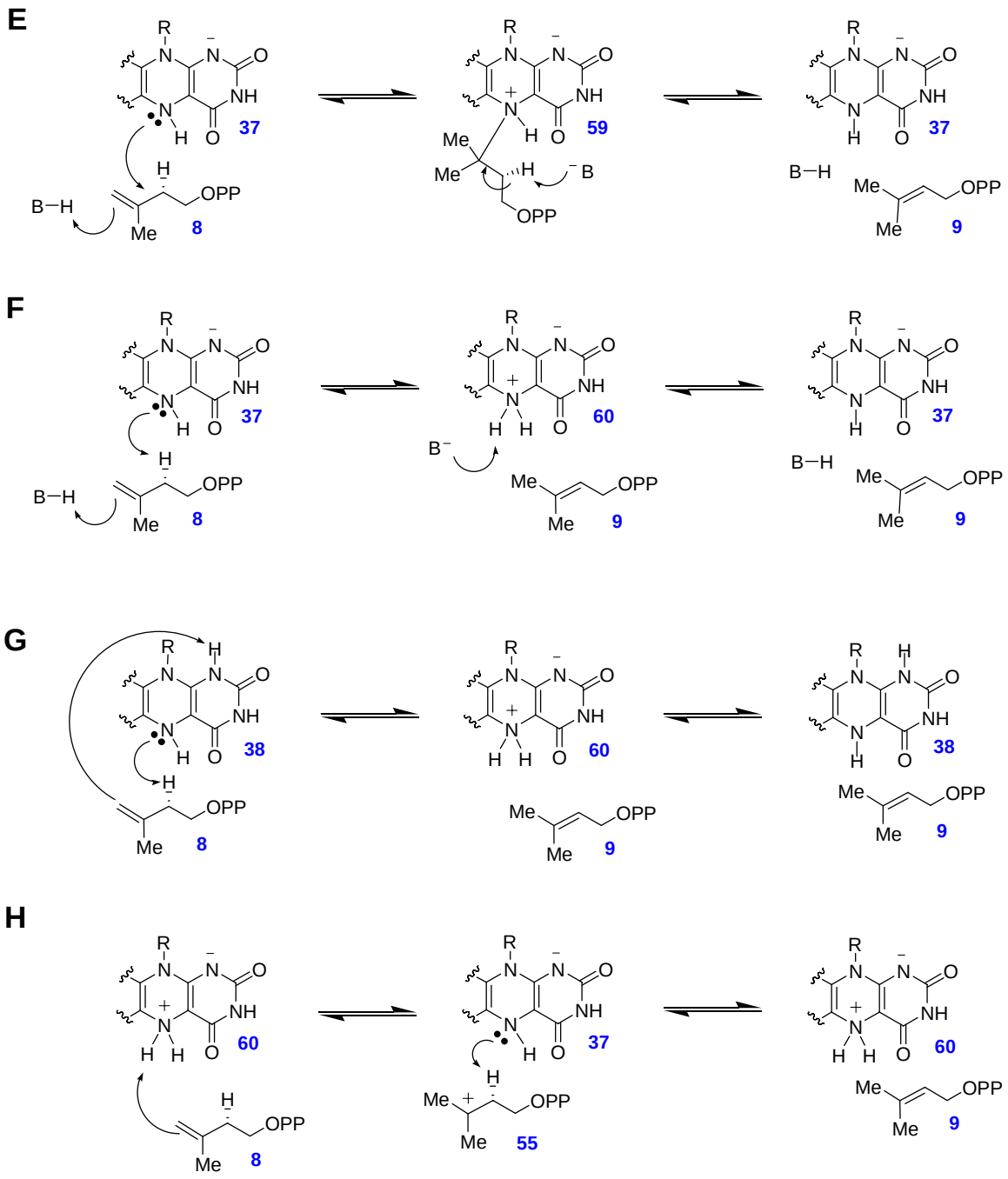

Scheme 1.15 (continued)

In contrast to the structural, electrostatic, and redox modes of FMN-dependent catalysis, IDI-2 could employ the reduced flavin as a covalent catalyst (Scheme 1.15E), similar to the UGM-catalyzed reaction. While the IDI-2 reaction differs from the UGM reaction in that there is no leaving group expelled in the nucleophilic attack step, nucleophilic addition by the N5 atom of reduced FMN to C3 of IPP/DMAPP could help to drive protonation by neutralizing the development of positive charge on the substrate in the transition state for protonation. Furthermore, the zwitterionic reduced flavin species (**59**) that would result from alkylation of FMNH- at N5 has recently been suggested to be a physiologically accessible species within enzyme active sites (*87*). Deprotonation of the adduct (**59**) and elimination of the reduced flavin would complete the catalytic cycle. A final possibility is that the reduced flavin participates directly in the acid/base chemistry steps, either serving as a general base with the assistance of amino acid residues to fulfill the general acid role (Scheme 1.15F), or by catalyzing both the protonation and deprotonation steps via $FMNH_2$ (**38**) or its zwitterionic tautomer, **60** (Scheme1.15G and H, respectively).

1.9 Thesis Statement

Isopentenyl diphosphate:dimethylallyl diphosphate isomerases (IDI) catalyze an essential reaction during the early stages of isoprenoid biosynthesis – generating the allylic diphosphate substrate (DMAPP) that is required for initiation of long chain isoprenoid biosynthesis. Two structurally and mechanistically distinct IDI enzymes have been discovered in nature. The type I enzymes (IDI-1) require only divalent metal ions

for catalysis and they use acid/base chemistry supplied by active site amino acid residues to catalyze the allylic-1,3-isomerization of IPP to DMAPP. The more recently discovered IDI-2 catalyzes an identical chemical transformation, but requires a reduced flavin mononucleotide (FMN) coenzyme in addition to divalent metal ions for catalysis. Thus, IDI-2 employs a flavin coenzyme to catalyze a reaction that involves no net change in the oxidation/reduction state of its substrates. The overall goal of our studies on this enzyme is to define the general mechanistic principles of IDI-2 catalysis from *Staphylococcus aureus*, in hopes of identifying the role of the coenzyme in this unusual flavin-dependent reaction. This information could eventually assist in the development of inhibitors for IDI-2, which is not present in human cells, but is essential for the survival of several human pathogens including *S. aureus* (*7*).

Chapter 2: Spectroscopic, Biochemical, and Computational Studies of the IDI-2 Bound Flavin Intermediate

2.1 Introduction

Flavin coenzymes exhibit fairly distinct spectroscopic characteristics in their various redox and protonation states. Thus, clues to the chemical mechanism of IDI-2 should be obtainable from the identity of the IDI-2-bound flavin intermediate(s) that are present in the resting state of the enzyme and that form during turnover. In this chapter, we investigate the spectroscopic properties of the IDI-2 bound FMN under various conditions using UV-visible absorption and electron paramagnetic resonance (EPR) spectroscopies. In addition, X-ray crystallographic studies of IDI-2 enzymes (*60, 61, 88, 89*) and multiple amino acid sequence alignments of IDI-2 enzymes from several sources (*7*) were used to identify conserved active site amino acid residues that could potentially modulate the spectroscopic properties of the IDI-2 bound flavin in the presence and absence of IPP. Several of these amino acid residues were mutated and the spectroscopic properties of the mutant enzymes are investigated. Finally, time-dependent DFT calculations are used to assess how various feautures of the IDI-2 active site may contribute to the UV-visible absorption spectrum of the flavin intermediate that forms upon IPP binding. Overall, these studies help to define the chemical mechanism for IDI-2 catalysis and set the stage for the more detailed kinetic and mechanistic analyses of the IDI-2 catalyzed reaction performed in Chapters 3 and 4.

2.2 Methods

***2.2.1 Site-directed mutagenesis of the wt idi2 gene from Staphylococcus aureus*:** For generation of the K186A, H149A, T67A, and Q154N mutant enzymes, the *idi2* gene from *S. aureus* encoded in the pQES plasmid (a generous gift from Prof. Hauro Seto, Tokyo University of Agriculture) was used as the template and pairs of complementary primers (see Table 2.1 for primer sequences) were used to replace the Gln154, Lys186, Thr67 and His149 codons of the wt *idi2* gene by site directed mutagenesis. Primers were ordered from either Sigma (St. Louis, MO.) or IDT (Coralville, IA.). The mutagenic PCR reactions were conducted as recommended by the QuikChange mutagenesis protocol (Stratagene, La Jolla, CA.). Following the mutagenic PCR reactions, parental plasmid DNA was digested with Dpn1 for 3 h at 37 °C and a small portion of the reaction mixture was used to transform *E. coli* XL10 cells. Transformants were selected on agar containing 100 μg/mL ampicilin. Mutant plasmids were isolated from 5 mL overnight cultures of these transformants (grown in LB) using a Quiagen plasmid miniprep kit, and the sequence of the mutated *idi2* gene was verified by DNA sequencing conducted by the Institute for Cellular and Molecular Biology core facilities at the University of Texas, Austin. After the sequences of the mutant pQES constructs had been verified, they were used to transform *E. coli* M15[pRep4] cells for protein expression.

2.2.2 Transformation of E. coli M15[pRep4] cells with IDI-2/pQES constructs: *E. coli* M15[pRep4] cells were transformed with the appropriate pQES expression plasmid

(encoding the desired IDI-2 construct). The transformation procedure was carried out as follows: 50 ng of the appropriate pQES construct was incubated with 50 μL of chemically competent *E. coli* M15[pRep4] on ice for 30 min. The mixtures were heat shocked at 42 °C for 45 sec in a water bath, incubated on ice for an additional 2 min, and supplemented with 1 mL of LB broth. Transformation cultures were grown at 37 °C for 45 min in a water bath with constant shaking. A 100 μL aliquot of the transformation culture was then added onto an LB-agarose plate supplemented with 100 μg/mL ampicilin and 30 μg/mL kanamycin. Plates were incubated at 37 °C overnight to generate clonal populations of *E. coli* M15[pRep4] cells harboring the desired IDI-2/pQES expression construct.

Mutant	**Primer**	**Primer sequence**
Q154N	Forward	5′-CAAATCCATGTTAATTCTCCT**AAC**GAATTAGTTATGCCTGAAGGG
	Reverse	5′-CCCTTCAGGCATAACTAATTC**GTT**AGGAGAATTAACATGGATTTG
T67A	Forward	5′GGCCTTTATATTAATGCAATG**G**CGGGTGGTAGCGAGTGGACGAAA
	Reverse	5′TTTCGTCCACTCGCTACCACCCG**C**CATTGCATTAATATAAACCGG
K186A	Forward	5′TATCTGTTCCAGTCATTATA**GCG**GAAGTTGGATTTGGTATGAG
	Reverse	5′CTCATACCAAATCCAACTTC**CGC**TATAATGACTGGAACAGATA
H149A	Forward	5′CTTGAGGCACAACGCTTACAAATCGCGGTTAATTCTCCTCAAGAATTAGTT
	Reverse	5′AACTAATTCTTGAGGAGAATTAACCGCGATTTGTAACGCTTGTGCCTCAAG

Table 2.1: Primer sequences for site-directed mutagenesis of the wt *idi2* gene from *S. aureus*. The mutated sequenece is highlighted in bold.

2.2.3 Over-expression of IDI-2 and its mutants: All IDI-2 constructs were expressed as *N*-His_6 fusion proteins as described below. A 30 mL starter culture of LB (supplemented with 100 μg/mL amp and 30 μg/mL kan) was inoculated with a single clonal population of *E. coli* M15[pRep4] cells transformed with the desired IDI-2 expression construct. The starter culture was grown overnight at 37 °C with constant shaking. For large scale protein expression, 6 L of LB (also supplemented with amp and kan) were each inoculated with 5 mL of the overnight starter culture, grown at 37 °C with constant shaking until OD_{600} = 0.3. At this point, IPTG was added to a final concentration of 250 μM, the temperature was lowered to 25 °C, and the cultures were grown for an additional 24 h. Cells were harvested by centrifugation at 8000*g* for 10 min at 4 °C and stored at -80 °C until protein purification.

2.2.4 Purification of IDI-2 and its mutants: Frozen *E. coli* M15[pRep4] cell pellets were thawed on ice and re-suspended in 100 mL of lysis buffer containing 50 mM Na_2HPO_4, 300 mM NaCl, 10 mM imidazole, 1 mg/mL lysozyme and 10% glycerol (pH 7.5). Cells were sonicated using 12 x 20 sec bursts. Cell debris was removed by centrifuging the sonicated samples at 20,000*g* for 30 min at 4 °C. Following centrifugation, the supernatant was mixed with ~ 15 mL of Ni-NTA resin (Qiagen) that had been previously washed with lysis buffer, and incubated at 4 °C for 1 h. This mixture was then loaded onto a column at 4 °C and the flow through was collected. The column was washed with 150 mL of wash buffer (50 mM Na_2HPO_4, 300 mM NaCl, 20 mM imidazole, 10% glycerol, pH 7.5) and the His-tagged IDI-2 constructs were then

eluted with elution buffer (50 mM Na_2HPO_4, 300 mM NaCl, 250 mM imidazole, 10% glycerol, pH 7.5). Fractions containing the recombinant IDI-2 (screened by SDS-PAGE) were pooled, concentrated to ~ 7 mL and dialyzed against 6 L of storage buffer (50 mM Na_2HPO_4, 300 mM NaCl, 10 % glycerol, pH 7.5) at 4 °C. Following dialysis, aliquots of the protein were flash frozen in liquid nitrogen and stored at – 80 °C until use.

2.2.5 UV-visible absorption spectroscopy of wt IDI-2: To examine the absorption properties of the IDI-2-bound FMN in its oxidized, reduced, semiquinone, and IPP bound states, anaerobic reaction mixtures containing 150 μM IDI-2, 80 μM FMN, 5 mM $MgCl_2$, 1 mM DTT, and 2 mM IPP (when present) in 100 mM HEPES (pH 7.0) were prepared in a glove box (Coy Laboratory Products, Grass Lake, MI) under an atmosphere of 5:95% H_2:N_2. All UV-visible absorbance spectra were recorded at 25 °C in quartz cuvettes unless otherwise stated. The enzyme solution was degassed by 40 cycles of vacuum followed by purging with argon. All other solutions were purged with argon for 10 min. After mixing all of the reaction components together in the glove box, the UV-visible absorption spectrum of the enzyme in the oxidized state was recorded. This sample was then photoreduced for 2 min with a Kodak slide projector and the spectrum of the reduced sample was recorded. Following photoreduction, IPP was added to a final concentration of 2 mM to determine the spectrum of the flavin intermediate. To generate the flavin semiquinone, IPP (2 mM) was pre-incubated with oxidized IDI-2 prior to a 2 min photoreduction.

UV-visible absorption spectra were also recorded for IDI-2 reconstituted with 1-deazaFMN and 5-deazaFMN in the presence and absence of IPP (*90*). For 5-deazaFMN, 80 μM oxidized coenzyme (K_d = 16 μM (*56*)) was incubated with 100 μM IDI-2 in 50 mM potassium phosphate buffer (pH 7.0), and the reaction was photoreduced as described above. For the incubation containg 1-deazaFMN, coenzyme and enzyme concentrations were increased to 150 and 200 μM, respectively, to account for the weaker binding of 1-deazaFMN$_{ox}$ (K_d = 97 μM (*56*)). In addition, we could not photoreduce the IDI-2 bound 1-deazaFMN. Instead, the coenzyme was chemically reduced with 50 mM $Na_2S_2O_4$. After recording spectra for the reduced states, 1 mM IPP was added and the absorption spectra of the IPP-bound states were recorded. The absorption spectra were corrected for the presence of the native FMN that copurifies with IDI-2 by difference spectroscopy.

2.2.6 EPR analysis of IDI-2 bound flavin semiquinone: Reactions for EPR analysis were prepared in a Coy Laboratories anaerobic chamber using degassed buffers. Reactions containing 250 μM IDI-2, 200 μM FMN, 5 mM $MgCl_2$, and 2 mM IPP in 100 mM HEPES (pH 7.0) were photoreduced for 2 min to generate the semiquinone using a Kodak slide projector, and were then transferred into EPR tubes and flash frozen in isopentane cooled in a dewar of liquid N_2. Samples were stored in liquid N_2 until EPR analysis. For the sample prepared in D_2O, IDI-2 storage buffer was exchanged with deuterated storage buffer (100 mM TAPS, 10% glycerol, pD 8.0) using a Microcon centrifugal filtration device (Millipore, Bedford, MA.) with a 30 kDa MW cutoff. Stock solutions of FMN, $MgCl_2$, IPP, and HEPES were also prepared in D_2O. Several rounds

of dissolving in D_2O, followed by lyophilization were carried out to remove as much of the protium as possible. Deuterated buffers were then degassed and transferred to the glove box for sample preparation. X-band EPR spectra were recorded at liquid N_2 temperatures (-77 °K) with a Bruker EMX EPR spectrometer (Billerica, MA). A total of 50 scans (with a sweep time of 163 sec/scan) were recorded for each sample over a 120 G region centered at 3355 G. The spectra were acquired with the following instrument parameters: microwave frequency = 9.420 GHz, microwave power = 50 μW**,** receiver gain = 5.02 x 10^5, modulation frequency = 100 kHz, and modulation amplitude = 4.00 G.

2.2.7 Comparison of flavin intermediate absorbance at pH 8.0 to free $FMNH_2$ absorbacne at pH 4.0: All incubations contained 50 μM FMN, 20 mM $Na_2S_2O_4$, and 5 mM $MgCl_2$ in 100 mM potassium phosphate buffer. For the spectra of free, reduced FMN, the pH of the phosphate buffer was adjusted to pH 4.0 to record the spectrum of the neutral reduced FMN ($FMNH_2$) or to pH 8.0 to record the spectrum of the anionic reduced FMN (FMNH-). For the spectra of the IDI-2 bound reduced FMN, an IDI-2 concentration of 120 μM was used. Under these conditions, the majority of the 50 μM reduced FMN should be enzyme bound (K_d = 12 μM (*56*)) in the presence and absence of IPP. The pH of the phosphate buffer was adjusted to 8.0 and spectra were recorded in the absence and presence of 2 mM IPP (a saturating IPP concentration at pH 8.0). All absorbance spectra were recorded at 25 °C in quartz cuvettes.

2.2.8 pH-dependence of flavin intermediate absorbance: Incubations contained 70 μM IDI-1, 200 μM FMN, 20 mM $Na_2S_2O_4$, 5 mM IPP (when present), 5 mM $MgCl_2$, 1 mM DTT, and 100 mM buffer. The buffers used were HEPES (pH 7.0), TAPS (pH 8.0 and 9.0), and CAPS (pH 10.0). UV-visible absorbance spectra were recorded 2 min after mixing all of the components together, which provides sufficient time for the flavin intermediate to reach its equilibrium level under these conditions. The difference spectra were calculated by subtraction of the absorption spectrum of the sample lacking IPP from the spectrum of the sample containing IPP at each different pH.

2.2.9 UV-visible absorption spectroscopy of IDI-2 mutant enzymes: Incubations were prepared under anaerobic conditons in the glove box as described above and each reaction contained 150 μM enzyme, 75 μM FMN, 2 mM IPP (when present), 5 mM $MgCl_2$, and 1 mM DTT in 100 mM TAPS, pH 8.0. Samples were photoreduced for 1 min in the glove box using a Kodak slide projector and the spectrum of the photoreduced enzymes were recorded. Following addition of 2 mM IPP to the photoreduced samples, the reactions were incubated for 2 min prior to recording the absorption spectra of the IPP-bound state.

2.2.10 DFT calculations: The UV-visible spectra of putative flavin intermediates in the catalytic cycle of IDI-2 were calculated with time-dependent density functional theory (TD-DFT) using *Gaussian 98* (*91*) by Dr. Steven Mansoorabadi, a post-doctoral associate in our lab. Full or partial geometry optimizations (which utilized the available

crystallographic data to fix the positions of heavy atoms (*89*)) were performed using Becke-style 3-parameter DFT with the Lee-Yang-Parr correlation functional (B3LYP) and Pople's polarized double-ζ 6-31G* basis set. The first ten low-lying excited-states were then calculated using the optimized geometries and the same B3LYP/6-31G* scheme. For some of the calculations, the effects of solvent water were included using the polarizable continuum model (PCM). The UV-visible spectra were then reconstructed using Gaussian line-shapes and the calculated excitation energies and oscillator strengths

2.3 Results and Discussion

***2.3.1 Characterization of the IDI-2 bound semiquinone*:** Preliminary characterization studies of IDI-2 by Dr. William Kittleman (a former member of our group) suggested that IDI-2 was capable of thermodynamically stabilizing a neutral FMN semiquinone (FMNH•, Scheme 2.1) in the presence of IPP in photoreduction and redox titration experiments (*56, 92*). He found that if IDI-2:FMN_{ox} was reduced in the absence of IPP, then the flavin was reduced directly to its $2e^-$ reduced state. However, if IDI-2:FMN_{ox} was reduced in the presence of IPP, then a species with UV-visible absorbance consistent with a neutral semiquinone formed. This data suggests that IPP binding to the oxidized enzyme alters the $1e^-$ redox potentials of the flavin, allowing the thermodynamic stabilization of FMNH•. This, in conjunction with his findings that 5-deaza-FMN (an obligate $2e^-$ donor/acceptor) was inactive, whereas 1-deaza-FMN (which is capable of

mediating both $1e^-$ and $2e^-$ transfers) supported IDI-2 catalysis (*56*), provided initial support for an IDI-2 mechanism involving single electron transfer (Scheme 2.1).

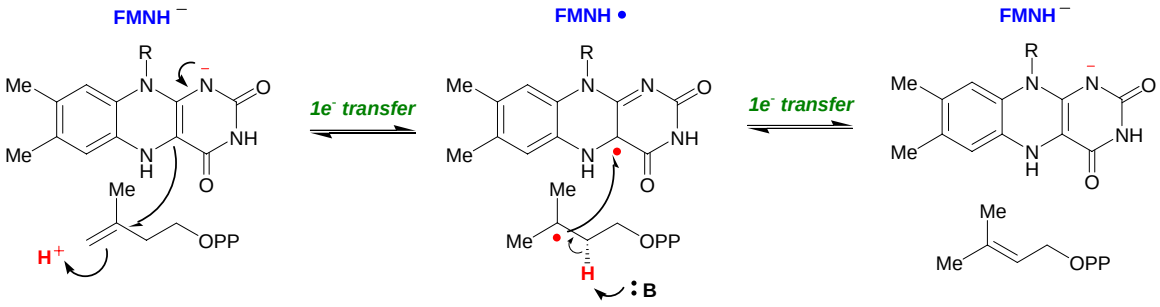

Scheme 2.1: Single electron transfer mechanism for IDI-2, showing formation of a neutral semiquinone/substrate radical pair.

If single electron transfer occurs between the flavin and the isoprene substrate, then a FMNH•/substrate radical pair should form at some point along the reaction coordinate for isomerization. To test for the presence of the FMNH•/substrate radical pair predicted by this mechanism, we analyzed the EPR spectra of anaerobic IDI-2:FMN:IPP mixtures. Consistent with the previous photoreduction studies (*56*), substantial quantities of a neutral semiquinone formed when IDI-2:FMN_{ox} was incubated with IPP prior to photoreduction (Figure 2.1). Two samples were prepared in this manner, one in H_2O buffer and one in D_2O buffer. These samples were then flash frozen in liquid nitrogen in the glove box, and analyzed by X-band EPR spectroscopy (Figure 2.2). The *g*-value of the isotropic paramagnetic species detected in these studies (g = 2.00) is consistent with an organic radical, most likely the neutral flavin semiquinone observed by UV-visible abosorption spectroscopy in Figure 2.1 (*93*). In D_2O, the line

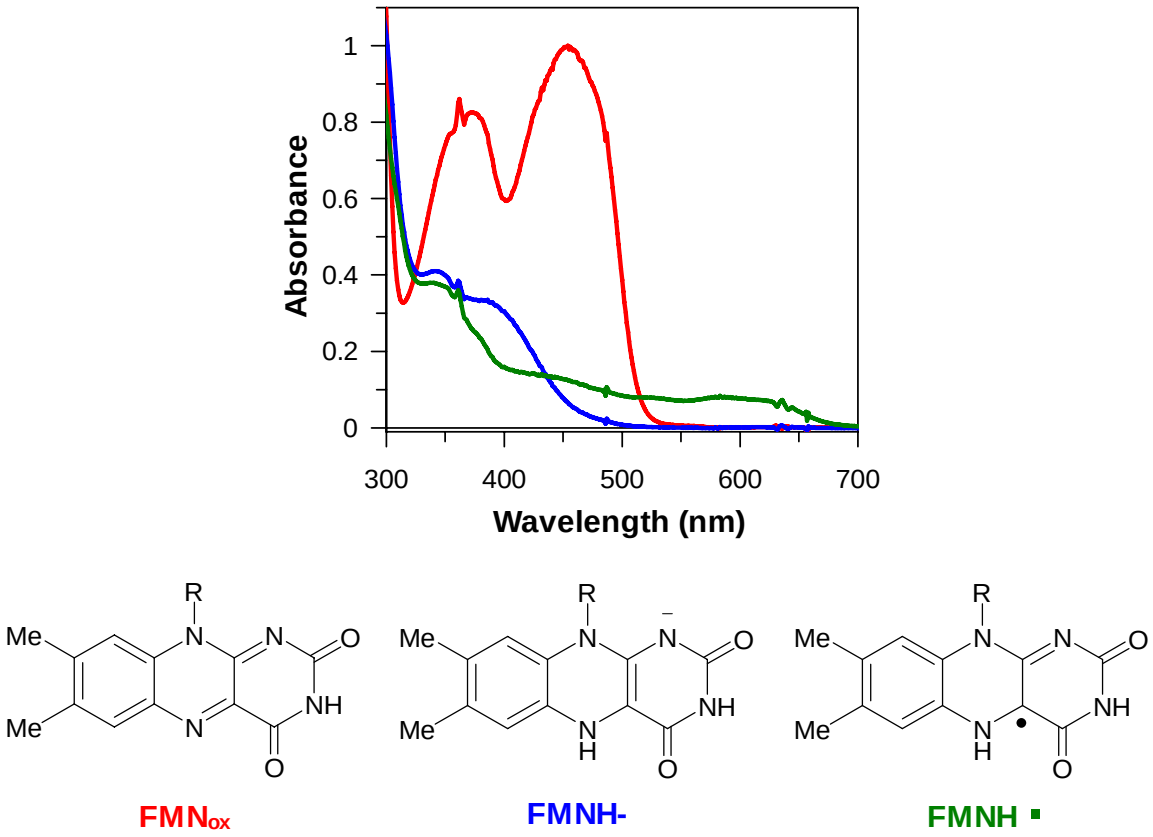

Figure 2.1: UV-visible absorption spectra of IDI-2:FMN in the oxidized (FMN_{ox}, red), photoreduced ($FMNH^-$, blue), and semiquinone (FMNH•, green) states in HEPES buffer at pH 7.0. The semiquinone form of the enzyme was generated by photoreduction of a mixture containing IDI-2:FMN_{ox} and IPP as described in the Methods section. The chemical species giving rise to the observed absorption spectra are also shown.

width of the signal narrows from 20 to 15 G, suggesting that a substantial portion of the unpaired electron spin on the flavin semiquinone is localized at N5, where the unpaired electron spin can be coupled to the nuclear spin of the proton at N5 through hyperfine interactions. This hypefine coupling leads to broadening of the spectral line width in H_2O and is consistent with the paramagnetic species being a neutral semiquinone, with the N5 atom of the flavin protonated. Anionic semiquinones (see **35** in Figure 1.3) have

the N5 atom deprotonated and exhibit EPR line widths of ~ 15 G in both H_2O and D_2O. The small peaks at the ends of the EPR spectra in Figure 2.2 are likely due to a hyperfine interaction between the unpaired electron spin and ^{14}N nuclei of the flavin, whose triplet spin states splits the semiquinone signal into three components. As the sample is moved into D_2O, some of the signal broadening is removed and the ^{14}N hyperfine interactions become more pronounced.

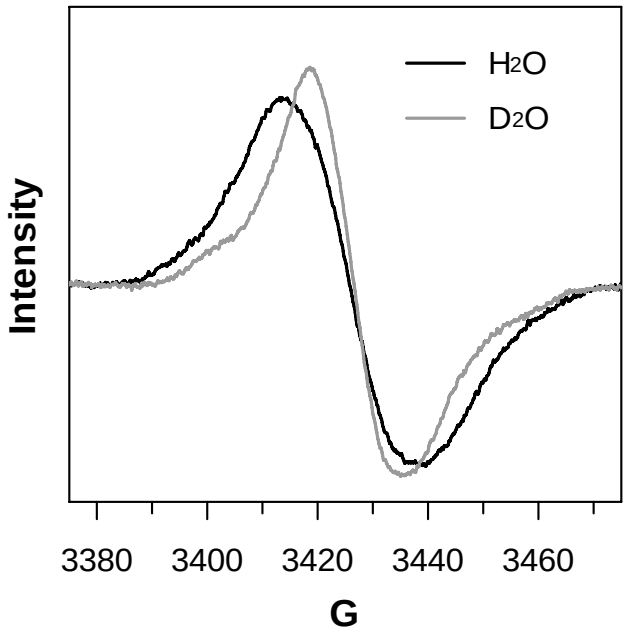

Figure 2.2: X-band EPR spectra of the IDI-2 bound semiquinone in protiated and deuterated buffer at pL 7.0. The line width of the isotropic organic radical signal (g = 2.00) narrows from 20 to 15 G in D_2O. This combined with the ^{14}N hyperfine couplings observed on the extremities of the spectrum suggest the organic radical species is a neutral FMN semiquinone (FMNH•).

Importantly, the unpaired electron spin of FMNH• in our samples appears to be magnetically isolated, and no zero-field splitting of the signal was observable. This

suggests that there is no substrate-based radical in close proximity to the FMNH• whose unpaired electron spin is coupled with the electron spin of FMNH•. We also prepared samples where IDI-2:FMN_{ox} was reduced (either by photoreduction or with NADPH or $Na_2S_2O_4$) prior to the addition of substrate, but no semiquinone could be detected by absorbance spectroscopy (*90*). Trace amounts of a magnetically isolated FMNH• (quantified to be < 1% of the IDI-2 concentration) could be detected in EPR studies of these samples (*90*). The trace amounts of FMNH• in these samples is likely attributable to a slight amount of O_2 contamination.

2.3.2 A flavin intermediate forms upon IPP binding: When IDI-2:FMN_{ox} is photoreduced under anaerobic conditions to its active $2e^-$ reduced state, the absorption spectrum of the resulting flavin species is consistent with an anionic, reduced FMN ($FMNH^-$), where the N1 atom of the flavin is ionized (Figure 2.3) (*90, 92, 94*). This IDI-2:$FMNH^-$ species has a λ_{max} at 350 nm and a shoulder at about 390 nm. The pK_a of the N1 atom of reduced FMN is 6.7 in free solution (*95, 96*), suggesting that apo IDI-2 likely binds to the anionic form of the reduced coenzyme under physiological conditions. When these anaerobic samples were exposed to O_2, the flavin re-oxidized, suggesting that the photoreduction procedure employed in these studies does not damage the flavin (data not shown). Upon binding to a saturating concentration of IPP (or DMAPP), absorption bands appear at 325 nm and ~ 435 nm. The spectrum of this flavin intermediate resembles the neutral reduced flavin ($FMNH_2$) that forms in some flavoproteins and which typically have λ_{max} values ranging from 390 – 450 nm (*71, 74, 94, 97*). A similar

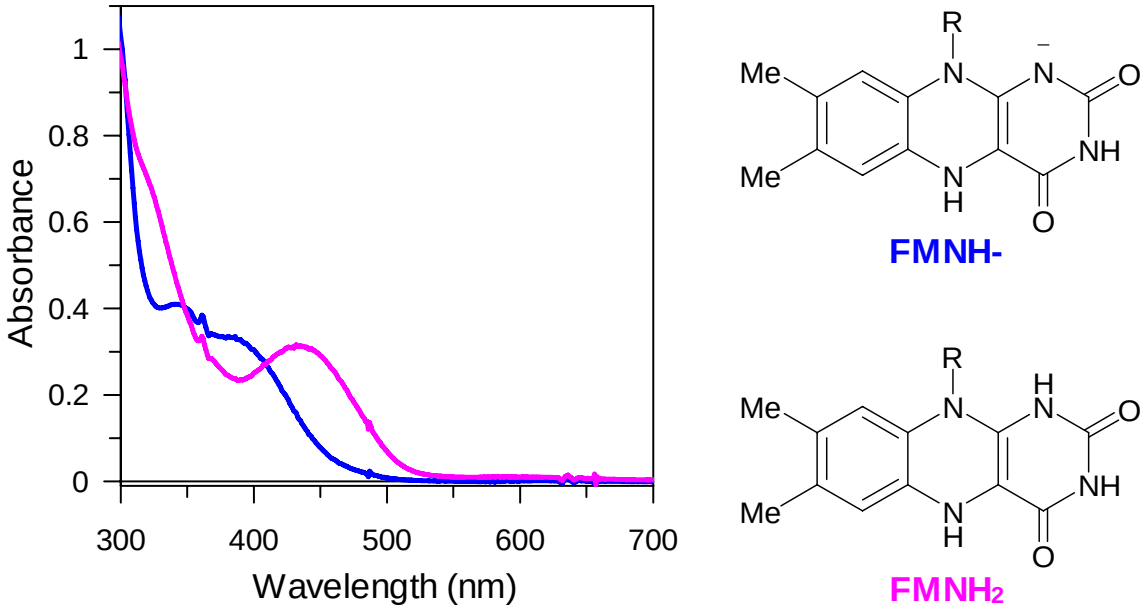

Figure 2.3: UV-visible absorption spectra of IDI-2 bound to reduced FMN in the absence (blue) and presence (fuchsia) of IPP in HEPES buffer, pH 7.0, and initial assignment of the flavin species as FMNH- and $FMNH_2$, respectively (*90, 92*).

IDI-2 bound flavin species is also observed in reaction mixtures containing NADPH or $Na_2S_2O_4$ as the reducing agent in the presence of IPP (*90*). In these samples, however, absorbance changes at wavelengths < 400 nm cannot be assessed due to the absorption of both reducing agents in this region. Initial support for the assignment of the flavin intermediate as $FMNH_2$ was also provided by analyzing the absorption spectra of IDI-2 reconstituted with reduced 1-deaza and 5-deaza-FMN analogues (Figure 2.4) (*90*). Based on comparison of the IDI-2 bound deaza-FMN spectra with spectra of the free deaza-FMN analogues at different pH (*83, 85, 98*), both coenzymes appear to be converted from their anionic into their neutral forms upon IPP binding.

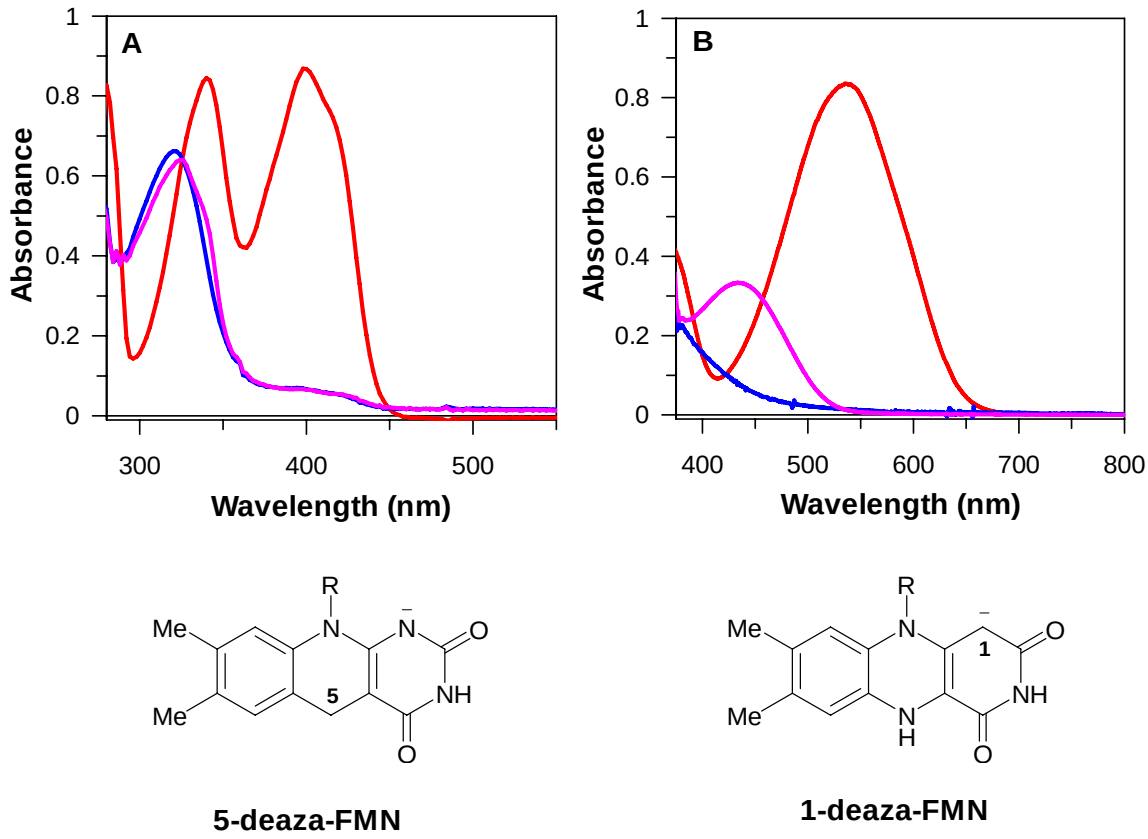

Figure 2.4: UV-visible absorption spectra of IDI-2 reconstituted with 5-deaza-FMN (A) and 1-deaza-FMN (B) in the oxidized (red), reduced (blue), and IPP-bound (fuchsia) states in HEPES buffer, pH 7.0 (*90*). The IDI-2 bound 5-deaza-FMN in panel A was photoreduced, while the IDI-2 bound 1-deaza-FMN in panel B was chemically reduced with sodium dithionite. The structures of 5- and 1-deaza-FMN in their anionic $2e^-$ reduced states are also shown.

2.3.3 Spectroscopic comparison of the IDI-2 bound FMN intermediate to free $FMNH_2$:

To gain additional insight into the identity of the FMN intermediate, we compared the absorbance changes in IDI-2:$FMNH^-$ upon IPP binding at pH 8.0 to absorbance changes in free $FMNH^-$ as the pH is reduced from 8.0 to 4.0 (Figure 2.5). We predicted that, if the FMN species that forms upon IPP binding to IDI-2:$FMNH^-$ at pH 8.0 is indeed an

$FMNH_2$ species, then the absorbance changes in the flavin chromophore should be similar to those observed when reduced flavin is moved from pH 8.0 to pH 4.0 (where the reduced FMN should be in the $FMNH^-$ and $FMNH_2$ forms, respectively). While the absorbance spectra in the two experiments are qualitatively very similar in the 400-500 nm range (Figure 2.5A and B), the difference spectra reveal subtle differences (Figure 2.5C). Namely, the maximal absorbance change of the flavin intermediate that forms upon IPP binding to IDI-2:$FMNH^-$ at pH 8.0 is red shifted (λ_{max} = 455 nm) and is more intense than the maximal absorbance change in the free flavin when the pH is reduced (λ_{max} = 425 nm).

One possible explanation for these observations is that the IDI-2 bound flavin intermediate is indeed an $FMNH_2$ species with slightly altered absorbance properties relative to free $FMNH_2$ in solution. These differences may be the result of the different local environments of free $FMNH_2$ in solution and $FMNH_2$ bound to the active site of IDI-2. Alternatively, the IDI-2 intermediate may be something other than $FMNH_2$, such as an anionic $FMNH^-$ species, whose isoalloxazine ring conformation or local protein environment changes significantly relative to the IDI-2:$FMNH^-$ resting form upon IPP binding.

Similar absorption changes to those seen in IDI-2:$FMNH^-$ upon IPP binding (as in Figure 2.3) have been observed with several flavodoxins when the pH is lowered. At a first glance, this appears to suggest that protonation of $FMNH^-$ is responsible for the absorbance changes observed in flavodoxin. In the case of flavodoxins, however, the pH-dependence of the UV-visible absorbance of the $FMNH^-$ coenzyme is believed to be due

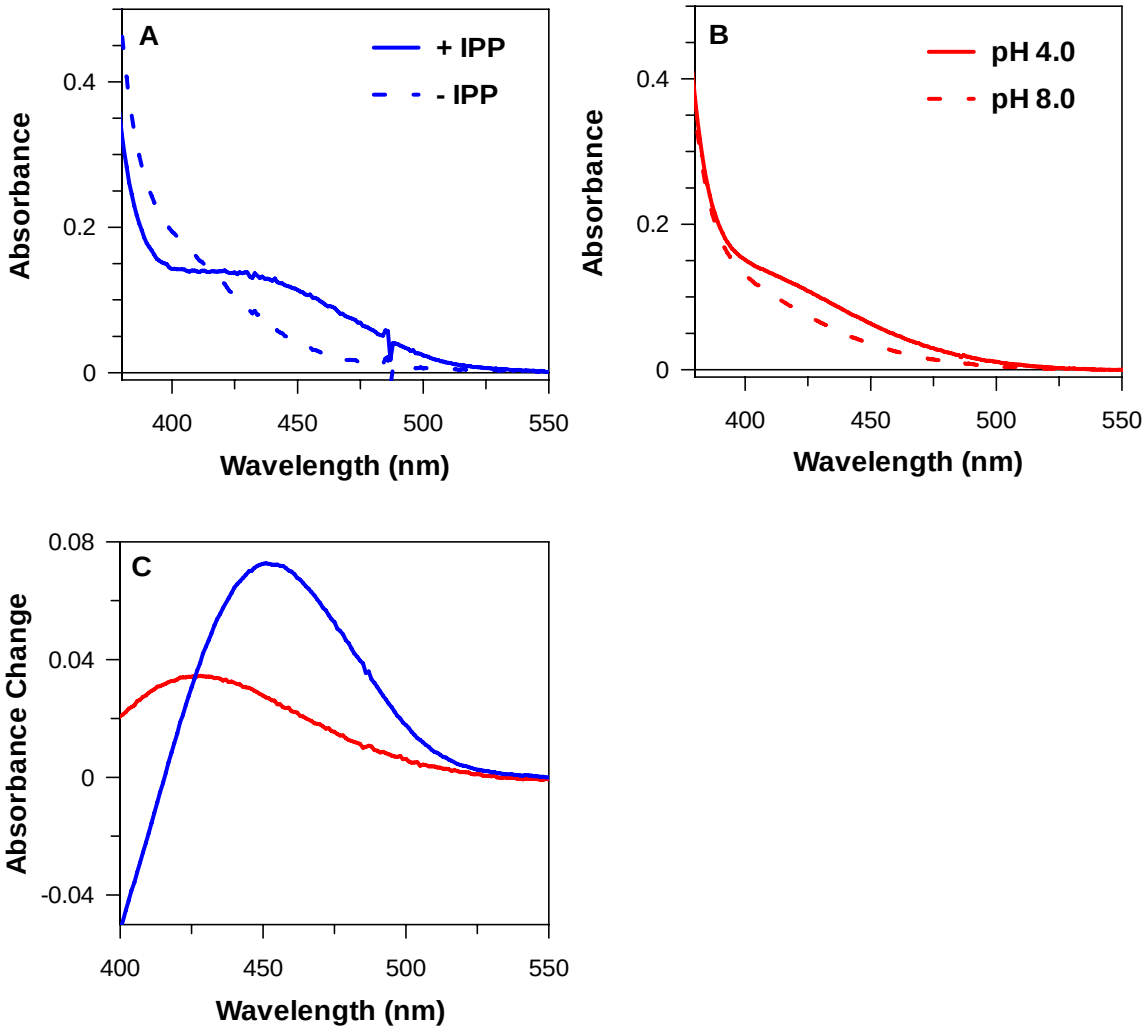

Figure 2.5: UV-visible absorption spectra of reduced IDI-2:FMN in the presence and absence of IPP at pH 8.0 (A) and reduced FMN free in solution at pH 4.0 and 8.0 (B). For the difference spectra shown in (C), the spectrum of IDI-2:FMN was subtracted from that of IDI-2:FMN:IPP (blue curve) and the spectrum of free FMN at pH 8.0 was subtracted from the spectrum taken at pH 4.0 (red curve).

either to an alteration in the active site environment around the $FMNH^-$ or to a conformational change in the flavin, rather than to protonation of the N1 atom of the anionic coenzyme (*99*). This conclusion is supported by NMR and structural studies of

flavodoxins, which show that the N1C2=O region of flavodoxin-bound, reduced FMN remains in the anionic form across a broad pH range (*95, 99-101*), presumably due to steric constraints to N1 protonation imposed by an active site glycine residue (*102*). The ability of flavodoxins to maintain reduced FMN in its anionic form is thought to be critical for lowering the redox potential of these enzymes, allowing them to serve as the reductant for a variety of biochemical reactions within cells. By analogy, a similar change in the conformation of the IDI-2 active site or in the $FMNH^-$ itself, could potentially result in an altered absorption spectrum for IDI-2:$FMNH^-$ upon IPP binding.

In line with this possibility, both structural and kinetic studies have provided evidence that an enzyme conformational change may accompany IPP binding. The K_d for reduced FMN binding to IDI-2 is 12 μM in mixtures containing only IDI-2 and reduced FMN (*56*). In contrast, in the presence of IPP, the amount of FMN required to saturate steady state activity was found to be roughly equivalent to the 50 nM enzyme concentration used in the assay (*56*). This data suggests that FMN binding in the ternary IDI-2:FMN:IPP complex is much tighter than binding in the IDI-2:FMN complex, and implies that a conformational change may occur upon IPP binding (*90*). More direct evidence for a conformational change has been provided by X-ray crystallographic studies. In the absence of IPP or pyrophosphate, a short *N*-terminal region of IDI-2 is not ordered in the crystal structures, leaving the active site accessible to the bulk solvent (*60, 61*). However, in the presence of IPP or pyrophosphate, this *N*-terminal region makes several contacts with the pyrophosphate moiety and effectively closes off the active site

(*88, 89*). Thus, it is possible that this putative conformational change leads to an alteration of the absorbance properties of $FMNH^-$ without protonating the N1 atom.

2.3.4 pH-dependence of flavin intermediate absorption: Intrigued by the results in the previous section, we decided to test whether the UV-visible absorption spectrum of the IDI-2:FMN:IPP complex changed as a function of pH. If the flavin intermediate in the IDI-2:FMN:IPP complex is an $FMNH_2$ species, and if the proton at N1 in this complex is freely exchangeable with bulk solvent, then it is possible that the FMN may ionize at higher pH, which should lead to a corresponding change in the absorbance spectrum of the IDI-2 bound coenzyme. To test for this, we prepared two reduced IDI-2:FMN samples (one lacking IPP and one containing a saturating IPP concentration) at several different pH values over the pH range 7.0 - 10.0. Difference spectra were generated for each pair of samples at each pH to examine the pH-dependence of the λ_{max} and intensity of the absorbance change in the reduced FMN coenzyme (Figure 2.6). These data show that, while there is a slight decrease in the intensity of the absorbance change at higher pH, a substantial amount of the intermediate is still present at pH 10.0. If the logarithm of the concentration of the flavin intermediate is plotted versus pH, it is clear that there is no substantial decrease in the levels of the intermediate, as would be expected if $FMNH_2$ was ionizing at higher pH. In addition, there appear to be no shifts in the λ_{max} of the absorbance change, suggesting that the same flavin species is forming upon IPP binding across the pH range tested. These data suggest that if the flavin intermediate that forms upon IPP binding is $FMNH_2$, then the IDI-2 active site is capable of elevating the pK_a of

reduced FMN from 6.7 in free solution to a value > 10.0 in the IDI-2:$FMNH_2$:IPP complex. Alternatively, the intermediate could be an anionic reduced flavin with slightly altered absorbance properties relative to IDI-2:$FMNH^-$, that remains ionized when bound to the IDI-2:FMN:IPP complex from pH 7.0 – 10.0.

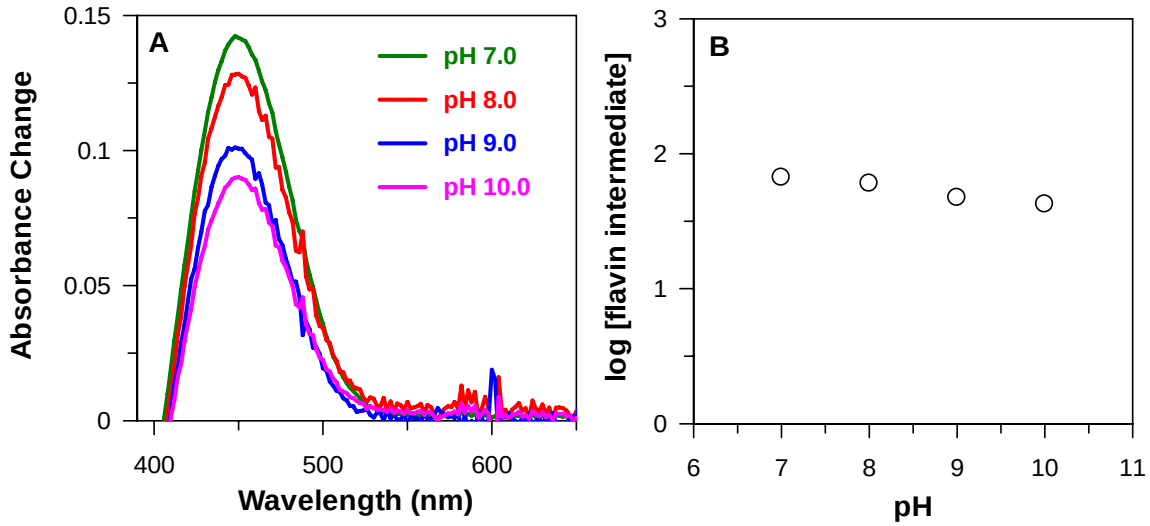

Figure 2.6: The pH-dependence of steady state flavin intermediate concentration. Incubations contained 70 μM IDI-1, 200 μM FMN, 20 mM $Na_2S_2O_4$, 5 mM IPP (when present), 5 mM $MgCl_2$, 1 mM DTT, and 100 mM buffer. The buffers used were HEPES (pH 7.0), TAPS (pH 8.0 and 9.0), and CAPS (pH 10.0). UV-visible absorption spectra were recorded 2 min after mixing all of the components together, which provides sufficient time for the flavin intermediate to reach its equilibrium level under these conditions. The difference spectra in panel A were calculated by subtraction of the absorption spectrum of the sample lacking IPP from the spectrum of the sample containing IPP at the indicated pH. Panel B shows the pH dependence of the flavin intermediate concentration, estimated from its $\Delta\varepsilon_{440} = 2100\ M^{-1}cm^{-1}$ (see Chapter 3).

2.3.5 Absorption properties of IDI-2 mutant enzymes: X-ray crystallographic analysis of IDI-2 from several sources suggest that the conserved active site residues His149 and Lys186 (*S. aureus* numbering) could potentially be involved in protonating $FMNH^-$ upon IPP binding (*60, 61, 88, 89*). In these crystal structures, the imidazole side chain of

His149 is ~ 3.5 Å from the C2=O moiety of the FMN and the amine group of the Lys186 side chain is ~ 3.0 Å from the N1 atom of FMN (Figure 2.7). To assess the potential involvement of these residues in $FMNH^-$ protonation upon IPP binding, we constructed and purified the H149A and K186A mutants and analyzed the absorbance properties of the photoreduced enzymes under anaerobic conditions in the presence and absence of IPP (Figure 2.8, difference spectra are shown in Figure 2.9). Upon IPP binding, these two mutant enzymes exhibit changes in the absorption properties of the flavin that are very similar to those observed with the wild type enzyme. Namely, the resting form of the flavin (λ_{max} ~ 350 nm) is converted to a species with λ_{max} values in the ~ 320 and ~ 440 nm range. These results suggest that protonation of $FMNH^-$ at N1 by either Lys186 or His149 is not likely to be responsible for the absorbance changes observed upon IPP binding. As there are no other potential amino acid candidates for protonation of the N1-C2=O moiety of $FMNH^-$ upon IPP binding revealed by the X-ray crystal structure, these results cast doubt on the assignment of the flavin intermediate as a 1,5-dihydro-$FMNH_2$ species.

In addition to Lys186 and His149, the conserved Gln154 and Thr67 residues could also potentially play a role in modulating the absorbance properties of the flavin intermediate. In the IDI-2:FMN:IPP co-crystal structure (Figure 2.7), the bound isoprenyl diphosphate substrate appears to form hydrophobic stacking interactions with the flavin (*89*). Gln154 is oriented on the opposite face of the substrate molecule relative to FMN, where it could function to help position the substrate relative to the flavin to ensure optimal catalytic rates if the flavin is somehow involved in catalysis. Thr67 is part

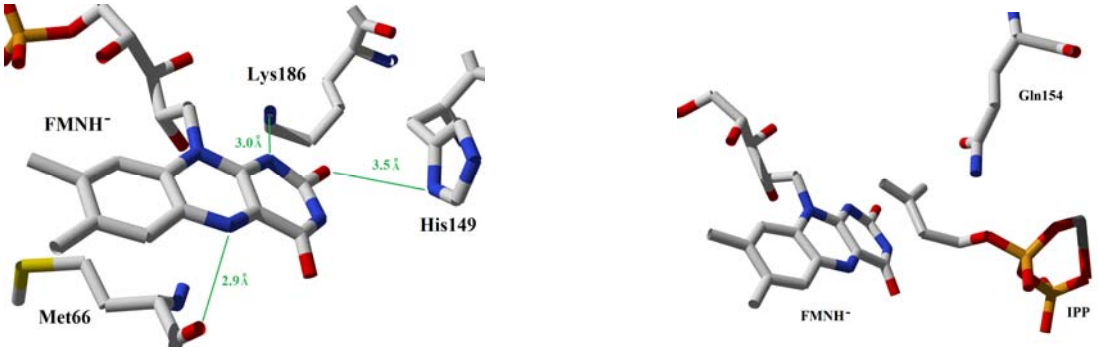

Figure 2.7: Several views of the active site of IDI-2 from *Sulfolobus shibatae* taken from the X-ray crystal structure solved by Unno et.al. (*89*). The left panel shows putative interactions between the side chains of Lys186 and His149 with the N1 and C2=O moieties of FMN, respectively, as well as a potential hydrogen bonding interaction between the backbone carbonyl of Met66 and the N5 atom of FMN. The right panel illustrates the stacking interaction between IPP and the flavin that may be mediated by the conserved Gln154 residue.

of a conserved MTGG amino acid motif and is adjacent to the Met66 residue whose backbone carbonyl appears to hydrogen bond with the N5 atom of the flavin. As neither Gln154 nor Thr67 appears to interact directly with FMN in the crystal structures, we did not initially expect there to be any drastic effects of the Q154N or T67A mutations on the absorbance properties of the flavin. Similar to the other enzymes investigated here, the resting forms of the Q154N and T67A mutants exhibit a λ_{max} near 350 nm with a shoulder at ~ 390 nm in the absence of IPP (Figure 2.8). To our surprise, the absorbance changes observed in the Q154N and T67A mutant enzymes upon IPP binding differed slightly from those observed in the wild type, K186A, and H149A enzymes (Figure 2.8 and 2.9). Most notably, in both mutants, an additional peak at ~ 360 nm is present in the spectrum of the complex with IPP (Figure 2.9). In addition, in the Q154N mutant, the λ_{max} of the absorbance change in the ~ 440 nm region is blue shifted ~ 20 nm relative to the other

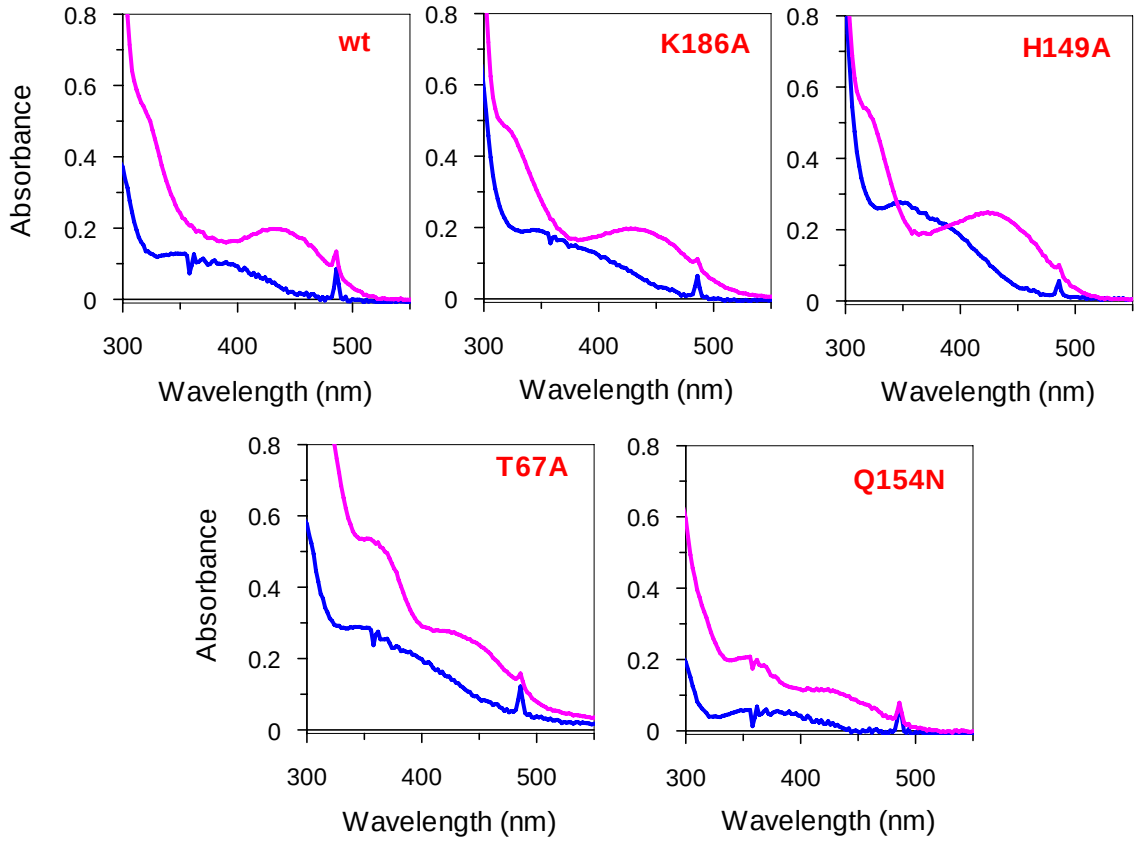

Figure 2.8: UV-visible absorption properties of wt IDI-2 and the K186A, H194A, T67A, and Q154N mutants in the presence and absence of IPP in TAPS, pH 8.0. IDI-2:FMN samples were photoreduced under anaerobic conditions to give the spectra of the resting state (blue curves). 2 mM IPP was added to the photoreduced samples to give the substrate-bound state (fuchsia curves).

mutants (Figure 2.9). The Q154N mutant is also unusual in that the intensity of the flavin absorption (both in the absence and presence of IPP) is weaker than in the other enzymes. These results suggest that even though Gln154 and Thr67 do not make direct contact with the flavin, they still have some effect on the absorption properties of the flavin. This effect may be related to the relative positioning of the reduced flavin and IPP in the fully complexed enzymes. When considered with the pH-independence of the flavin

intermediate spectrum and the spectral differences between the IDI-2 bound flavin intermediate and $FMNH_2$ in free solution, the absorbance properties of these mutant enzymes suggests that the initial assignment of the flavin intermediate as an $FMNH_2$ species (*90, 92*) may need to be reconsidered.

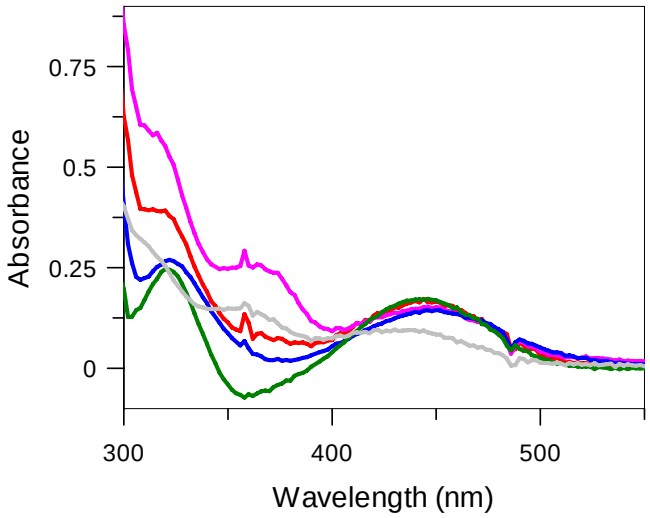

Figure 2.9: Difference spectra for the data in Figure 2.8. The spectrum recorded in the absence of IPP was subtracted from the spectrum recorded in the presence of IPP for each enzyme: wild type IDI-2 (red), K186A (blue), H149A (green), T67A (fuschia), and Q154N (gray).

2.3.6 DFT calculations provide insight into factors that govern the IDI-2 flavin intermediate absorption: To aid in our characterization of the flavin intermediate that forms upon IPP binding to reduced IDI-2:$FMNH^-$, Dr. Steven Mansoorabadi (a postdoctoral associate in our lab) calculated absorption spectra for reduced FMN under several different conditions using time-dependent DFT calculations. In these calculations, several parameters were systematically varied in order to deduce what

factors may contribute to the UV-visible absorption spectra of the IDI-2 bound reduced FMN in the presence and absence of substrate. First, the protonation state at N1 of the flavin was varied. Second, the conformation of the flavin isoalloxazine ring was either allowed to assume its lowest energy form (which was found to be relatively planar), or was fixed into the bent conformation observed in the IDI-2:FMN:IPP co-crystal structure (*89*). Third, the calculations were either performed in the gas phase (as a rough mimic of a hydrophobic active site) or in a solvent continuum. Finally, IPP (when present in the calculations) was held in close proximity to the flavin – fixed into the average position observed in the co-crystal structure. Several notable features of these calculations are summarized below.

At a first glance, it is clear that our calculations predict that the absorbance properties of the anionic reduced flavin ($FMNH^-$, Figure 2.10A) are much more sensitive to the conditions tested than the neutral reduced flavin ($FMNH_2$, Figure 2.10B). Changing the environment of planar $FMNH^-$ from a solvated environment to a hydrophobic environment leads to a red shift in the λ_{max} of the major visible absorption band from 340 → 373 nm. A similar (though slightly more drastic) red shift is seen in the major absorption band of bent $FMNH^-$ when it is moved from a polar environment into a more hydrophobic environment (384 → 462 nm). In contrast, the spectra of planar and bent $FMNH_2$ were relatively insensitive to the nature of the surrounding medium. Second, bending of $FMNH^-$ (in either the gas or aqueous phase) from a planar conformation into the conformation observed in the co-crystal structure with IPP leads to the appearance of a transition at ~ 320 nm and to a red shift of the major absorption band

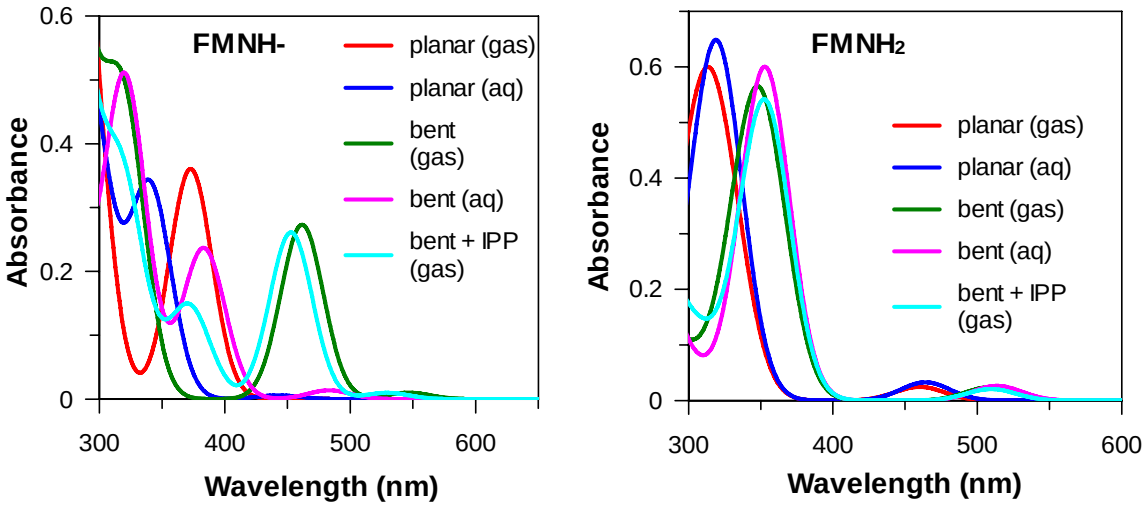

Figure 2.10: DFT calculations of the absorbance spectra of reduced FMN in its anionic (FMNH-) and neutral ($FMNH_2$) forms. Only the electronic transitions in the near UV and visible regions of the spectrum are shown. In this figure, "gas" indicates calculations carried out in the gas phase, and "aq" indicates calculations carried out in a solvent continuum. "Planar" and "bent" designate the conformation of the flavin isoalloxazine moiety. For the "planar" structures, the energy of the entire flavin molecule was minimized (this led to a planar structure) prior to calculation of the energies and probabilities of the electronic transitions. For the "bent" structures, the C, N, and O atoms of the isoalloxazine moiety were fixed to the positions observed in the crystal structure prior to energy minimization (*89*). Finally, "IPP" indicates calculations conducted with the position of IPP fixed relative to the flavin – mimicking the geometry observed in the co-crystal structure.

(from 374 → 463 nm and from 340 → 384 nm in the gas and aqueous phases, respectively). Bending of $FMNH_2$ leads to smaller red shifts (314 → 348 nm and 319 → 353 nm in the gas and aqueous phases, respectively). Finally, when IPP was held close to the bent $FMNH^-$, the major gas phase transitions (453 and ~ 320 nm) were very similar to those observed in the absence of IPP (462 and ~ 315 nm), except that an additional absorption band appeared around 370 nm. As with the change in solvent polarity and the bending of the flavin, the presence of IPP had very little effect on the electronic transition

energies of $FMNH_2$ in the UV-visible region of the spectrum. Importantly, none of the spectra calculated for $FMNH_2$ are predicted to give transitions in the 400-450 nm region of the visible spectrum, where the flavin intermediate observed upon IPP binding to reduced IDI-2:$FMNH^-$ absorbs maximally.

Comparisons between the experimentally observed spectra of reduced IDI-2:FMN in the presence and absence of IPP with selected calculated spectra are shown in Figures 2.11A and B, respectively. Prior to substrate addition, the spectrum of the reduced IDI-2:FMN complex most closely resembles calculated spectra for $FMNH^-$ under several conditions. The experimentally observed λ_{max} (345 nm) is most similar to the λ_{max} of the planar, solvated $FMNH^-$ (340 nm). According to our calculations, the shoulder at ~ 390 nm in the experimentally observed spectrum could be due to the bending of a significant fraction of the IDI-2 bound $FMNH^-$ molecules (λ_{max} = 385 nm), or to a slightly more hydrophobic environment around some of the IDI-2 bound $FMNH^-$ molecules (λ_{max} = 374 nm). These conclusions seem to be in line with the available structural data. Namely, in the absence of IPP or pyrophosphate, the active site is in an open conformation and the flavin is accessible to solvent (*60, 61*). Thus, it is reasonable to assume that the flavin may be planar and at least partially solvated in the IDI-2:$FMNH^-$ resting state. If a significant fraction of the IDI-2:$FMNH^-$ molecules exist in the closed conformation (normally observed upon IPP or pyrophosphate binding (*88, 89*)), this could lead to the shoulder observed at ~ 390 nm. Alternatively, a substantial fraction of IDI-2 bound FMNH- could exist in the bent conformation, which could also lead to the shoulder observed at ~ 390 nm in a solvated envirnoment.

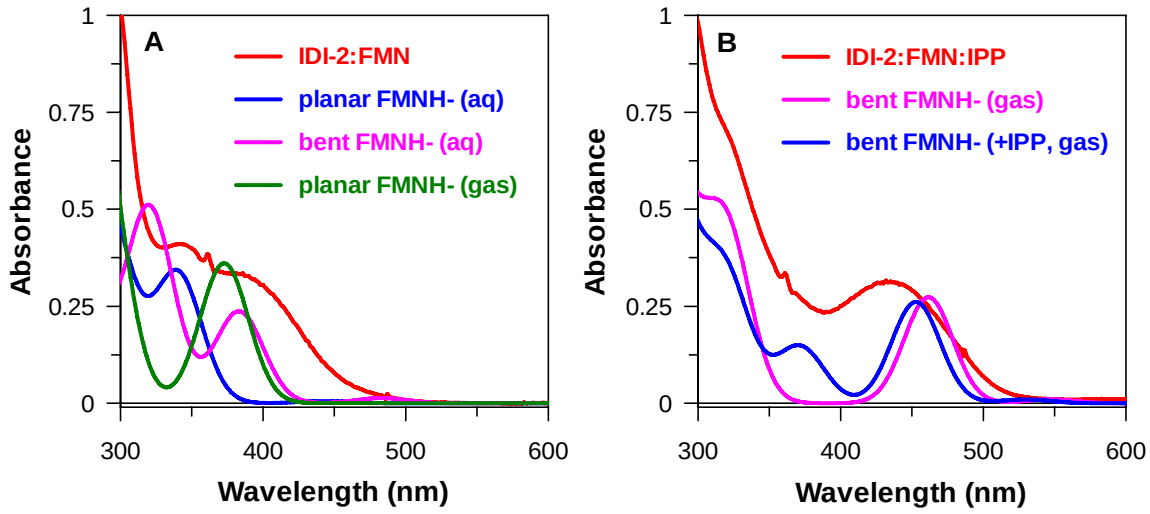

Figure 2.11: Comparison of selected calculated spectra with experimentally observed absorption spectra for reduced IDI-2:FMN in the absence (A) and presence (B) of IPP. In both panels, the experimental data is shown by the red curve.

The spectrum of the reduced IDI-2:FMN:IPP complex most closely resembles spectra calculated for bent $FMNH^-$ molecules in the gas phase (Figure 2.11B). Our calculations indicate that the bending of $FMNH^-$ from a planar structure into the conformation observed in the crystal structure induces significant changes in the spectrum of the anionic coenzyme, and leads to absorption bands (~ 320 and 450 nm) that are very similar in energy to those observed in the experimental spectra. Interestingly, the hydrophobic stacking interaction between IPP and bent $FMNH^-$ in the gas phase leads to an additional absorbance band ~ 370 nm that may also contribute to the spectrum of the experimental IDI-2:FMN:IPP complex. This putative stacking interaction could be somehow accentuated in the T67A and Q154N mutants, leading to the clearly visible absorption band at ~ 360 nm in these mutants (see Figures 2.8 and 2.9). It is also

interesting to note that the relative intensities of the ~ 320, 370, and 450 nm bands predicted from the gas phase DFT calculations of bent $FMNH^-$ in the presence of IPP appear to correlate well with the relative intensities of the absorption bands seen in the experimental spectra for the wild type IDI-2:FMN:IPP complex (Figure 2.11B).

2.4 Conclusions, Mechanistic Implications, and Future Directions

2.4.1 The flavin intermediate is most likely an FMNH- species: In order to better distinguish among the putative chemical mechanisms for IDI-2 presented in Chapter 1 (Scheme 1.15), we have conducted spectroscopic, biochemical, and computational studies to elucidate the structure and protonation state of the flavin species that are bound to IDI-2 in the presence and absence of substrate. UV-visible absorption spectroscopy of the reduced FMN coenzyme bound to IDI-2 in the presence and absence of IPP has revealed an absorbance change upon IPP binding that likely indicates formation of a distinct flavin intermediate during IDI-2 catalysis. In Chapter 3, the kinetic competence of this flavin intermediate will be verified by single-turnover stopped-flow studies. The identity of the flavin intermediate was probed with pH-variation experiments, site-directed mutagenesis, comparison of its absorbance properties to those of free reduced flavin, and computational studies. Cumulatively, our results most strongly support the assignment of the flavin intermediate as an anionic reduced FMN species ($FMNH^-$) that is deprotonated at the N1 atom of the isoalloxazine moiety.

Support for this conclusion is derived from the insensitiviy of the flavin intermediate absortption to solution pH in the range 7.0 – 10.0, a result which suggests that the IDI-2 bound flavin intermediate is likely either $FMNH^-$ or a 1,5-dihydro-$FMNH_2$ species with a substantially elevated pK_a relative to its value (6.7) in free solution. Furthermore, the differences in the absorption changes associated with protonating the free $FMNH^-$ and with binding of IPP to IDI-2:$FMNH^-$ suggest that the flavin intermediate absorption is red shifted and is more intense than the absorption of $FMNH_2$ in solution. As will be shown in Chapter 4, similar patterns of absorbance changes are also observed when IDI-2 is reconstituted with several flavin analogues. In addition, UV-visible absorption spectroscopy of several active site mutants reveals that the two most likely candidates (Lys186 and His149) for protonating the N1 position of $FMNH^-$ upon IPP binding are not required for the formation of the flavin intermediate, whose appearance in these mutant enzymes is very similar to the wt enzyme. This result indicates either that $FMNH^-$ is not protonated at N1 upon IPP binding, or that the proton needed to protonate $FMNH^-$ is derived from some other source. Our present results cannot exclude the possibility that either Lys186 or His149 protonates $FMNH^-$ in the absence of the other. Finally, time-dependent DFT calculations indicate that the absorption spectrum of $FMNH^-$ is much more sensitive than the spectrum of $FMNH_2$ to solvent polarity, bending of the flavin isoalloxazine ring system, and to hydrophobic stacking with IPP. Interestingly, these calculations suggest that bending of the flavin (to the conformation observed in the crystal structure) and desolvation of the active site can generate changes in the absorbance of $FMNH^-$ that are consistent with the experimentally observed changes

upon IPP binding to the IDI-2:$FMNH^-$ resting state. An additional contribution to the absorption spectrum of the flavin intermediate may be derived from a hydrophobic stacking interaction between $FMNH^-$ and IPP. Optimal stacking between IPP and the flavin could be facilitated in part by Gln154 and the hydrogen bond between Met66 and FMN. In support of this, the flavin intermediate in the Q154N and T67A mutant enzymes exhibited altered absorption properties relative to the wt, K186A, and H149A enzymes. Gln154 could interact directly with IPP while Thr67 could help to optimize the interaction between Met66 and FMN.

2.4.2 The protonation state of the reduced, IDI-2 bound flavin has mechanistic relevance: The feasibility of the various chemical mechanisms for IDI-2 catalysis shown in Scheme 1.15 is expected to depend upon the protonation state of the reduced flavin. Namely, mechanisms involving the reduced flavin as an electron transfer mediator, a nucelophilic or electroststic catalyst, or as an acid/base catalyst with the help of a separate amino acid derived acid/base residue are expected to employ the anionic $FMNH^-$ form of the coenzyme. Maintaining the reduced FMN in the anionic form should help to lower the redox potential of the flavin if a SET mechanism is operative (Scheme 1.15D), increase the nucleophilicity of N5 in a nucleophilic catalysis scenario (Scheme 1.15E), increase the capacity of the flavin to electrostatically stabilize a substrate carbocation (Scheme 1.15B), or ensure that the pK_a of the acid/base functional group on the flavin is within the physiological range (Scheme 1.15F). In contrast, in a mechanism where the reduced flavin provides both of the acid/base functional groups required to complete the

1,3-allylic isomerization (as in Scheme 1.15G and 1.15H), IDI-2 would be expected to stabilize a protonated form of the reduced flavin upon IPP binding. The protonation of $FMNH^-$ could occur either at N1 to form the canonical 1,5-dihydro-$FMNH_2$ tautomer (**38**, Scheme 1.15G) or at N5 to form the zwitterionic 5,5-dihydro-$FMNH_2$ tautomer (**60**, Scheme 1.15H).

To address the protonation state of the flavin intermediate more directly, we are currently employing a biosynthetic approach to synthesize uniformly ^{15}N-enriched FMN which will then be reconstituted with apo IDI-2 and analyzed by NMR spectroscopy in the presence and absence of IPP. The biosynthetic approach relies on the over-expression of *E. coli* flavodoxin (which binds FMN tightly, but non-covalently) in minimal media supplemented with $^{15}NH_4Cl$ as the sole nitrogen source. Following purification of flavodoxin with affinity chromatography, the ^{15}N-enriched FMN is resolved from the flavodoxin, purified, and reconstituted with apo IDI-2 for analysis. Previous ^{15}N-NMR studies of reduced FMN and of reduced flavoproteins have revealed that the chemical shift of the N1 atom is strongly dependent on its protonation state, with large upfield shifts in the resonance of N1 (~ 50-60 ppm) being observed upon protonation (*100, 103*). Thus, this type of analysis could provide a direct probe for assessing changes in the protonation state of N1 upon IPP binding, which should be mechanistically informative. In addition, previous work has shown that the magnitude of $^1J_{15N\text{-}1H}$ coupling constants are related to the hybridization state of the N nucleus (*104, 105*). This property of N-H bonds could be useful for assessing the role of the N5 atom of the flavin in catalysis. For example, if the flavin intermediate that is observed in IDI-2 reaction mixtures

accumulates prior to slow chemistry steps that limit the 1,3-allylic isomerization (which our kinetic studies in Chapter 3 indicate), then we expect to observe an ^{15}N-^{1}H coupling constant for N5 that is consistent with sp^3 hybridization (~72 Hz) if the N5 atom is acting as a nucleophilic or acid/base catalyst. Similar types of studies have proven useful in unraveling the structural and electronic properties of other flavoenzyme active sites (*95, 101, 103, 106-110*), and are expected to significantly advance our understanding of the role of FMN in IDI-2 catalysis.

2.4.3 Considering an isomerization involving single electron transfer: An early hypothesis for the function of the reduced IDI-2 bound FMN coenzyme was that the reduced FMN could transfer a single electron to IPP (or DMAPP) concomitant with or subsequent to double bond protonation to generate a flavin semiquinone/substrate radical pair (Scheme 2.1), that could then be converted to products by deprotonation of the substrate radical and single electron transfer back to the flavin semiquinone (*56*). This proposal was based largely on two sets of experimental observations. First, a neutral FMN semiquinone accumulated in redox titrations and in photoreduction experiments conducted in the presence of IPP. In the absence of IPP, the IDI-2 bound FMN was found to cycle directly between the $2e^-$ reduced form and the $2e^-$ oxidized form, with no thermodynamic stabilization of a semiquinone. These experiments suggested that the IDI-2 active site was at least capable of accommodating a semiquinone species in the presence of IPP. Second, IDI-2 was found to exhibit wild type levels of activity when the reduced FMN was replaced with reduced 1-deaza-FMN (*56*), whereas IDI-2 reconstituted

with reduced 5-deaza-FMN was nearly devoid of activity (*56, 82*). Based on previous studies with these FMN analogues which demonstrated that 1-deaza-FMN is capable of both $1e^-$ and $2e^-$ transfers whereas 5-deaza-FMN is only capable of $2e^-$ transfers (*84*), this data seemed to support a role for the reduced FMN coenzyme of IDI-2 in single electron transfer chemistry.

This initial mechanistic proposal for IDI-2, however, has been challenged by several more recent lines of experimental evidence (*86, 90, 92*). First, in the EPR studies reported in this Chapter, we were unable to detect an IPP/FMN semiqunone radical pair in either anaerobic, catalytically competent IDI-2 reaction mixtures or under photoreduction conditions that are known to generate large quantities of the IDI-2 bound neutral semiquinone (*90*). Similar EPR results were reported for the *Thermus thermophilus* IDI-2 enzyme by Poulter and co-workers (*92*). Second, as illustrated by the single-turnover multi-wavelength stopped flow studies performed in Chapter 3, no flavin semiquonone accumulation was detected in the pre-steady state. Thus, we were unable to detect and/or validate the kinetic competence of a semiquinone/substrate radical pair using stopped-flow absorbance spectroscopy. Together, the stopped-flow and EPR studies suggest that if the FMN semiquinone/substrate radical pair forms as part of IDI-2 turnover, then it must be a kinetically unstable intermediate that is consumed faster than it is formed in the pre-steady state, and also a thermodynamically unstable intermediate that can not be detected in reaction mxtures at chemical equilibrium because its energy is much higher than the other enzyme forms present.

Several recent studies with IPP substrate analogues conducted by Poulter and co-workers have provided strong evidence against hydrogen atom transfer mechanisms involving a transient semiquinone/substrate radical pair (*86, 111, 112*). First, alkyne and allene substrate analogues (**1** and **2**, Scheme 2.2) of IPP and DMAPP, respectively, were synthesized and found to be competitive inhibitors of IDI-2 (*112*). Gas phase computational studies of the hydrocarbon versions of **1**, **2**, IPP, and DMAPP (Scheme 2.2, **3** – **6**, respectively) indicated that the heats of reaction ($\Delta_R H$) for protonation of **3** and **4** were substantially more endothermic than $\Delta_R H$ for protonation of **5** and **6**, leading to calculated $\Delta\Delta H$ values of 14.7 and 15.3 kcal/mol for the **3**/**5** and **4**/**6** pairs, respectively. In contrast, $\Delta_R H$ for hydrogen atom transfer to **3** and **4** was slightly more exothermic than $\Delta_R H$ for hydrogen atom transfer to **5** and **6**, leading to calculated $\Delta\Delta H$ values of -2.1 and -1.8 kcal/mol for the **3**/**5** and **4**/**6** pairs, respectively. Thus, these computational results predict that there should be a substantial enthalpic barrier to the turnover of compounds **1** and **2** if IDI-2 employs a protonation/deprotonation mechanism. In contrast, compounds **1** and **2** are expected to exhibit similar reactivities as IPP and DMAPP if IDI-2 employs a mechanism involving a concerted proton coupled electron transfer. The fact that **1** and **2** are not turned over, but instead act as competitive inhibitors of IDI-2 provides support for a protonation/deprotonation mechanism and argues against a pathway involving single electron transfer.

Finally, Poulter and co-workers also demonstrated (*86, 111*) that a radical clock cyclopropyl analogue of IPP (**7**, Scheme 2.3) was converted to the corresponding DMAPP analogue (**8**) at rates similar to that for the conversion of IPP to DMAPP.

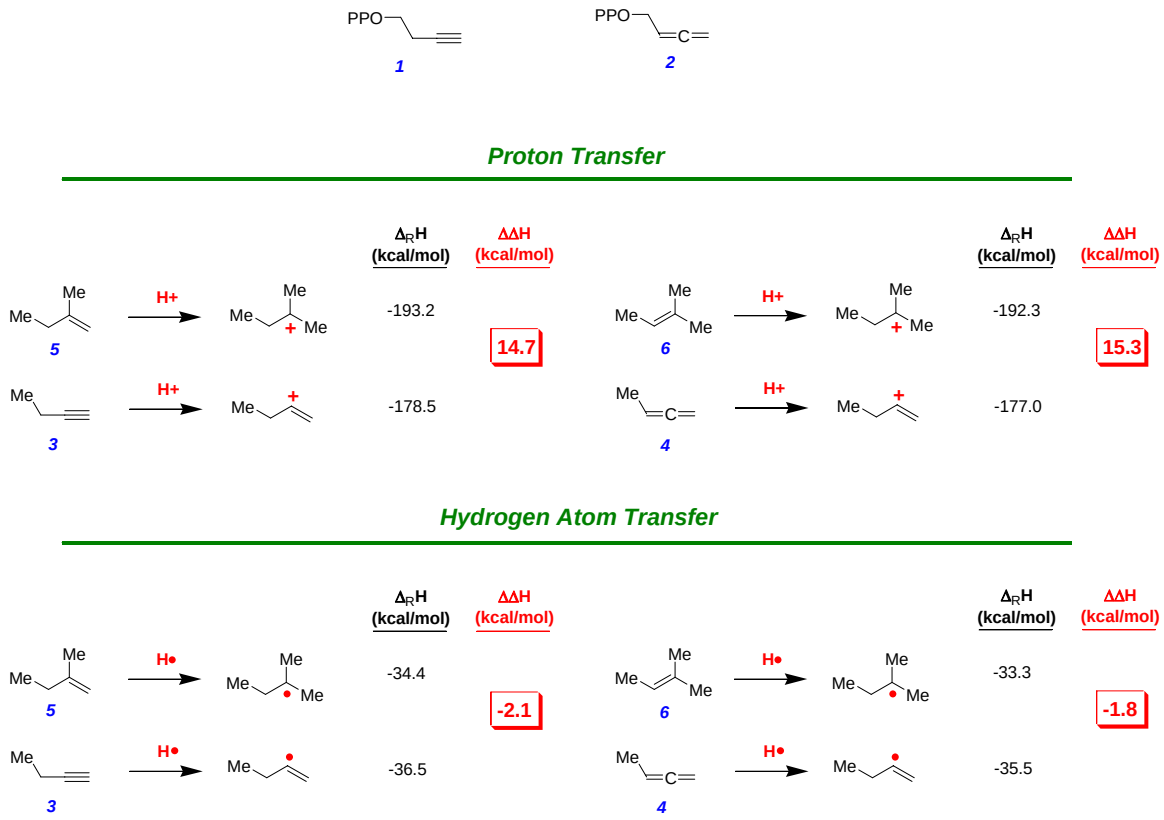

Scheme 2.2: Calculated gas phase heats of formation ($\Delta_R H$) for proton and hydrogen atom transfer to several different unsaturated hydrocarbons (*112*).

Importantly, no radical-induced fragmentation products or time-dependent IDI-2 inactivation was observed in these studies. These observations stipulate that if a catalytically competent radical pair is forming in the IDI-2 active site during turnover, then the substrate radical must be deprotonated and oxidized by $1e^-$ faster than the known rate of radical fragmentation for the cyclopropyl radical intermediate (1.3×10^8 s^{-1} (*113*)). Altogether, these more recent mechanistic studies cast doubt on an isomerization mechanism involving a cryptic single electron transfer mechanism and suggest that the

IDI-2 bound neutral semiquinone observed in potentiometric and photoreduction studies is likely an artifact of the experimental conditions.

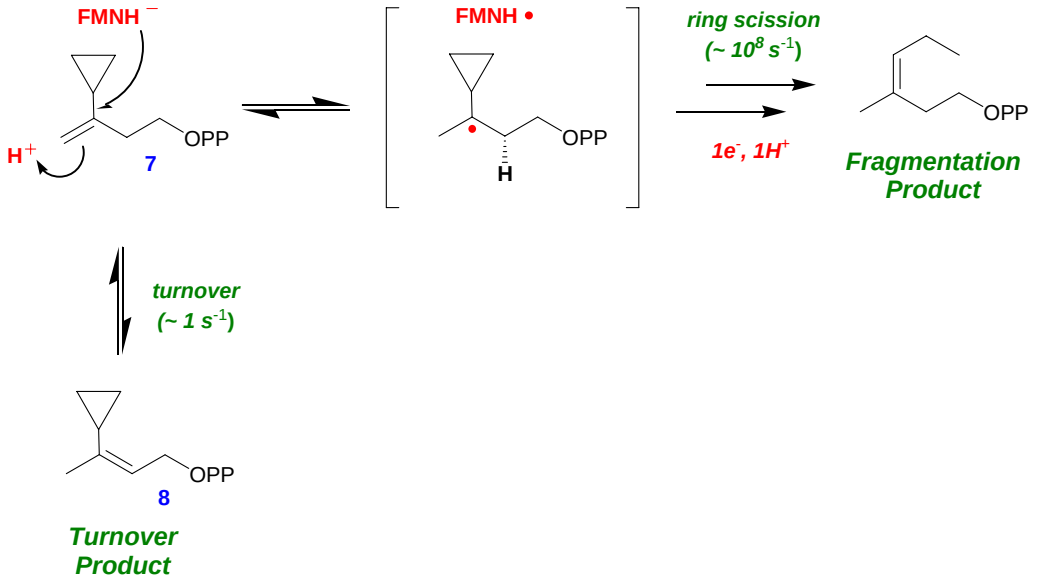

Scheme 2.3: Mechanistic studies with the cyclopropyl IPP analogue (**7**) yielded turnover product (**8**) rather than fragmentation product (*86*).

Chapter 3: Defining the Biochemical Properties of the IDI-2 Catalyzed Reaction

3.1 Introduction

In the previous chapter, we conducted a series of spectroscopic studies on the FMN coenzyme bound to IDI-2 and its mutants. These studies were aimed at characterizing the chemical nature of the flavin species present in the resting and substrate-bound forms of the enzyme, and are critical for helping to define the role of the flavin in the chemical mechanism of IDI-2 catalysis. Indeed, our spectroscopic and computational analyses suggest that the flavin intermediate is likely an anionic, reduced FMN species that could be poised for a role as a catalytic base in the IDI-2 catalyzed reaction. In this chapter, our focus will be directed towards defining the biochemical properties of IDI-2. The first key goal of this chapter is to identify and define the nature of the steps in the kinetic mechanism that limit steady state turnover. This information is critical for assessing the likelihood of acid/base catalysis in the IDI-2 catalyzed reaction and the involvement (if any) of the flavin in this process. To achieve this goal, we performed kinetic studies of IDI-2 and several of its mutant enzymes, studied the pH-dependence of the steady state kinetic parameters for the wild type enzyme, and conducted kinetic isotope effect studies to assess the possibility that proton transfers to and from the substrate limit turnover. Pre-steady state kinetic studies of the wild type enzyme were used to verify the catalytic competence of the flavin intermediate that

accumulates in the steady state and to identify the position of the rate limiting step in the kinetic mechanism relative to DMAPP formation. Finally, a minimal kinetic mechanism is proposed for the IDI-2 catalyzed reaction, and the feasibility of this mechanism is assessed using global simulations of the kinetic data. Altogether, the studies performed in this chapter provide a considerable amount of insight into the IDI-2 catalyzed reaction, and have helped to illuminate what factors govern catalysis by this unusual flavoenzyme.

3.2 Methods

***3.2.1 General*:** All reagents used in these studies were purchased from either Sigma (St. Louis, Mo.) or Fisher Scientific unless otherwise stated. The wild type and mutant IDI-2 proteins were expressed and purified as described in Chapter 2. The IPP, DMAPP, and (*R*)-[2-^{2}H]-IPP substrates were chemically synthesized by Wei-chen Chang (a graduate student in our lab) according to previously described methods (*114*). The concentrations of the IPP, (*R*)-[2-^{2}H]-IPP, and DMAPP stock solutions were determined by ^{1}H-NMR via comparison of integrated signal peak areas with those of a NaOAc internal standard. Protein concentrations were determined by the Bradford assay. All linear and non-linear regression was performed using GraFit 5.0 (Erithacus Software, Surrey, UK). All NMR spectroscopy was performed in the core facilities of the Department of Chemistry and Biochemistry at the University of Texas, Austin.

3.2.2 Determination of steady state kinetic parameters: The steady state kinetic parameters for the IDI-2 catalyzed conversion of IPP to DMAPP were determined according to a previously described assay (*55, 56*). The assay is based on the acid lability of DMAPP, which allows it to be selectively derivitized and separated from unreacted IPP. The standard assay conditions were 50 nM apo IDI-2, 20 μM FMN, 20 mM sodium dithionite, variable concentrations of [1-^{14}C]-IPP (2.0 μCi/μmol), 5 mM $MgCl_2$, 1 mM DTT, in 100 mM TAPS (pH 8.0). [1-^{14}C]-IPP was purchased from American Radiolabeled Chemicals (St. Louis, MO.). Reactions (300 μL total volume) were carried out at 27 °C under anaerobic conditions (an atmosphere of 95:5% N_2:H_2) in a glove box (Coy Laboratories, Grass Lake, MI.). All reaction components (excluding IPP) were pre-incubated at 25 °C for 10 min prior to the addition of [1-^{14}C]-IPP to initiate the reaction. At 0.5, 2.5, 4.5, 6.5, and 8.5 min, 50 μL aliquots were removed from the reaction mixture and were quenched in 200 μL of 25% HCl in MeOH at 37 °C for 10 min. Petroleum ether (1 mL, obtained from Acros, mp 60-95 °C) was added to the acid quenched time points to extract the derivitized DMAPP product. Aliquots of the organic layer (700 μL) were then added to 5 mL of BCS-NA scintillation fluid (Amersham Biosciences, Buckinghamshire, UK) and the ^{14}C content of the samples were determined with a Beckman LS-6500 liquid scintillation counter. The concentration of DMAPP at each time point was then calculated using the measured ^{14}C content of the sample and the specific activity of [1-^{14}C]-IPP used in the assay. The initial velocities of DMAPP formation at each IPP concentration were determined by linear regression, plotted against IPP concentration, and fitted with the Michaelis-Menten equation to determine the steady

state kinetic parameters. Unless otherwise stated, all steady state kinetic data for wt IDI-2 and its mutants were collected and analyzed under these conditions. For the H149A, K186A, T67A and Q154N mutant enzymes, the total enzyme concentrations were 400 nM, 1 μM, 1 μM and 7.75 μM, respectively, and the IPP concentration range was adjusted to account for the differences in the Michaelis constant (K_m) for binding IPP to these enzymes. For the studies with K186A and H149A, the specific activity of the IPP stock solution was 0.25 μCi/μmol. Control assays established that 20 μM FMN was sufficient for saturation of activity with wt IDI-2, T67A, and H149A, while 50 μM FMN was required for the K186A and Q154N enzymes (data not shown).

3.2.3 Determination of the equilibrium constant: A total of 5 reactions containing 5 mM IPP and 10 μM IDI-2 under standard assay conditions were prepared. The reactions were allowed to run for 2 h at 25 °C, at which time each reaction was quenched and the DMAPP present in the reaction mixtures was derivatized and quantified as described above. From the five replicate measurements, the equilibrium constant for the conversion of IPP to DMAPP was determined: K_{eq} = [DMAPP]/[IPP] = 1.2 ± 0.1.

3.2.4 pH-dependence of the steady state kinetic parameters: The steady state kinetic parameters for the wild type IDI-2 were also determined under the standard assay conditions at pH 6.0, 7.0, 9.0, and pH 10.0 using 100 mM MES, HEPES, TAPS, or CAPS, respectively, as the buffer. The enzyme concentration used was 100 nM at pH 6.0, 9.0, and 10.0 and was 50 nM at pH 7.0 and 8.0. In addition, control assays at pH 6.0

indicated that the concentration of Mg^{2+} needed to be increased to 50 mM to ensure full activity. The other reaction conditions were identical to those reported for the standard steady state kinetic assay in section ***3.2.2***.

3.2.5 Rapid-mix chemical quench experiments. To analyze the rate of DMAPP formation in the pre-steady state, a rapid chemical quench experiment was performed using a KinTek RFQ-3 rapid-quench-flow system (KinTek Corp., Austin, TX). The reactions were carried out at 37 °C and the conditions (after mixing) were 20 μM IDI-2, 100 μM FMN, 100 mM dithionite, 520 μM [1-^{14}C]-IPP (1.92 μCi/μmol), 5 mM $MgCl_2$, and 1 mM DTT in 100 mM HEPES, pH 7.0. One syringe contained 40 μM IDI-2, the other syringe contained 1.04 mM IPP, and both syringes contained all of the other reaction components at the concentrations indicated above. The reactants were allowed to mix for variable lengths of time (from 3 ms to 1 s) prior to quenching with a constant volume of 25% HCl in MeOH. The acid-quenched time points were derivatized and analyzed as described for the steady state kinetic assays to determine the DMAPP concentrations at each time point. The data were then normalized by the total enzyme concentration, plotted versus time, and fitted using linear regression to determine the pre-steady state rate of DMAPP formation.

3.2.6 ^{1}H-NMR assays for measuring substrate kinetic isotope effects and the rate of the reverse reaction: The substrate deuterium kinetic isotope effect on k_{cat} ($^{D}k_{cat}$) was determined by direct comparison of the initial velocities of DMAPP formation from IPP

and (*R*)-[2-^{2}H]-IPP measured under pseudo-first order conditions. To monitor the time-dependent formation of DMAPP, we employed an *in situ* NMR assay similar to that reported by Laupitz et al (*7*). The reaction mixtures (660 μL) contained 100 nM IDI-2 (200 nM for the (*R*)-[2-^{2}H]-IPP reaction), 10 mM IPP (or (*R*)-[2-^{2}H]-IPP), 20 μM FMN, 20 mM sodium dithionite, 2.0 mM sodium acetate (internal standard), 1 mM DTT, 10 mM $MgCl_2$, and 9% (v/v) D_2O in 100 mM potassium phosphate buffer (pH 8.0, 27 °C). The IPP and (*R*)-[2-^{2}H]-IPP reactions were carried out on the same day using the same batch of enzyme. Following the addition of enzyme to the solution, the sample was transferred to the NMR tube. The NMR spectrometer was locked and shimmed, and the time-dependent appearance of the (*Z*)-methyl proton resonance of DMAPP (δ = 1.66 ppm) (*7, 55, 58*) was then followed over 120 min using a Varian Unity 500 MHz NMR spectrometer. Spectra for each point in the time course were acquired over a 220 s interval using a 2 s delay between successive pulses and a 180 s time delay between successive 220 s spectra acquisition periods. The concentration of DMAPP at each time point was calculated from the integrated peak areas of the (*Z*)-methyl proton resonance at δ = 1.66 ppm by normalizing to the peak area of the 2.0 mM acetate internal standard at δ = 1.84 ppm. The initial velocity of DMAPP formation from each substrate was then determined by linear regression and $^{D}k_{cat}$ was calculated as the ratio of the initial velocities for the protiated and deuterated substrates. A similar ^{1}H-NMR assay was used to estimate k_{cat} in the reverse direction ($k_{cat,rev}$), except that the time-dependent formation of the IPP C2 proton resonance at 2.35 ppm was followed. These reactions contained

500 nM IDI-2 and 20 mM DMAPP, but were otherwise identical to the conditions used for the ^{1}H-NMR assays for IPP and (*R*)-[2-^{2}H]-IPP.

3.2.7 Solvent kinetic isotope effects: Prior to measuring the solvent kinetic isotope effects (SKIEs) on k_{cat} and k_{cat}/K_m for the wild type enzyme ($^{D_2O}k_{cat}$ and $^{D_2O}k_{cat}/K_m$), the initial velocity of DMAPP formation was screened over the pL range 7.0 – 8.5 (pL = pH or pD; pD = pH meter reading + 0.4 (*115*)) using a saturating concentration of IPP. A stock buffer solution containing FMN, DTT, and $MgCl_2$ in HEPES (pL 7.0 and 7.5) or TAPS (pL 8.0 and 8.5) was made in either H_2O or D_2O and then adjusted to the desired pL with 10 M NaOH. The final reaction mixtures contained 56.3 nM IDI-2 and 269 μM IPP (11 μCi/μmol), with all other conditions identical to those reported for the standard assay except that the experiments were conducted at 37 °C. The initial velocity at 269 μM IPP (an estimate of k_{cat}) was measured in triplicate at each pL. These studies indicated that k_{cat} appeared to be pL-independent from ~ pL 7.5 to 8.5 (*90*). Next, $^{D_2O}k_{cat}$ and $^{D_2O}k_{cat}/K_m$ were determined at pL 8.0 in 100 mM TAPS buffer using the standard assay conditions. For these studies, stock solutions of FMN, IPP, $MgCl_2$, DTT, and TAPS were individually dissolved in D_2O (99.9% D, Sigma) and were lyophilized to dryness. This process was repeated three times to exchange as many of the solvent exchangeable protons with deuterium as possible. Sodium dithionite was dissolved directly in D_2O, and wt IDI-2 (in protiated storage buffer) was diluted roughly 10,000 fold into the final assay mixtures.

3.2.8 Proton inventory studies: The initial velocity of the wt IDI-2 reaction was measured under pseudo-first order conditions using 200 μM [1-^{14}C]-IPP (2.0 μCi/μmol) at pL 8.0 with the standard assay conditions in buffers containing variable amounts of D_2O. Stock solutions of FMN, $MgCl_2$, DTT, and TAPS were individually dissolved in the appropriate water mixture (0, 20, 40, 60, 80, and 100% D_2O v/v), lyophilized to dryness, redissolved in the appropriate water mixture, and adjusted to pL 8.0. The atom fraction of deuterium (n = moles D/[moles D + moles H]) present in the final reaction mixture was corrected to account for the different molar volumes of H_2O and D_2O (18.069 and 18.134 mol/mL, respectively), the amount of NaOH that was added to adjust the pL of the stock water mixtures, and for protium derived from the enzyme and IPP stock solutions. Initial velocities were determined in triplicate in each water mixture and the data were fit with several different forms of the Gross-Butler equation (*115*). Descriptions of the Gross-Butler equation and its application to studying IDI-2 are given in the results and discussion section.

3.2.9 Viscosity effects: Viscosity effects were measured on k_{cat} for wt IDI-2 using the standard assay conditions, except that the assays contained variable concentrations of glycerol (0, 10, 15, 25, 27.5, and 30 % (w/v)) as the viscogen, and were carried out in 100 mM HEPES (pH 7.5). The initial velocity at each concentration of glycerol was determined in triplicate using 150 μM [1-^{14}C]-IPP (2.0 μCi/μmol). Under the assumption that the rates of diffusion limited reactions (such as substrate/product binding and release and large-scale enzyme conformational changes) are inversely proportional to the

viscosity of the medium (*116-118*), the data were fitted to Equation 3.1 to determine the viscosity effect on k_{cat}:

Equation 3.1

$$k_o/k_\eta = S\bullet(\eta_{rel} - 1) + 1$$

Here, η_{rel} (= η_o/η) is the relative viscosity of the solution (taken from (*119*), where η_o is the viscosity of the reference solution (water) and η is the viscosity at a given concentration of glycerol), k_o is the initial velocity (under pseudo-first order conditions) measured in buffer containing no glycerol, k_η is the initial velocity measured in buffer of relative viscosity, η_{rel}, and S is the slope of the plot (S = 1 for reactions that are 100% diffusion controlled).

3.2.10 Single-wavelength stopped flow studies: To monitor the kinetics of flavin intermediate formation and decay in the pre-steady state, the changes in IDI-2 bound flavin absorbance were monitored upon mixing with IPP, DMAPP, or (*R*)-[2-^{2}H]-IPP in a HI-TECH Scientific SF-61 Double Mixing Stopped-Flow System (London, UK) equipped with a photomultiplier detector. After mixing, reactions contained 75 μM apo IDI-2, 225 μM flavin, 20 mM dithionite, variable concentrations (from 0.02 to 2 mM) of either IPP or DMAPP, 5 mM $MgCl_2$, and 1 mM DTT in 100 mM TAPS (pH 8.0). The single turnover reactions with (*R*)-[2-^{2}H]-IPP contained 60 μM substrate and were compared directly with the reactions containing 60 μM IPP. Enzyme (150 μM) was pre-

incubated with all reaction components except substrate in one syringe. The concentration of unbound, reduced flavin in this syringe should be ~ 5 × the K_d for reduced FMN binding to *S. aureus* apo-IDI-2 (14 μM) (*56*), ensuring that the majority of the enzyme has a bound flavin molecule both before and after mixing. In support of this, no shifts in the background absorbance were observed when enzyme solution was mixed with buffer lacking IPP. Replicate injections were performed at 25 °C over 120 sec. Upon mixing, absorbance changes at 440 nm were followed using a log time scale to collect as many data points as possible in each kinetic phase of the reaction. After subtraction of the background absorbance, the time-courses were fitted with exponential equations (of the form shown in Equation 3.2) to determine the rates and amplitudes of the observed kinetic phases.

Equation 3.2:

$$A_t = \sum_{1}^{n} \left[A_n \bullet (1 - e^{-k_{obs,n} \bullet t}) \right] + C$$

Here, A_t is the absorbance change at 440 nm at time = t, A_n and $k_{obs,n}$ are the observed amplitude change and rate constant, respectively, for kinetic phase n, and C is an offset that accounts for the A_{440} change at t = 0.

3.2.11 Multi-wavelength stopped flow studies: Reactions contained 200 μM IDI-2, 400 μM FMN, 20 mM sodium dithionite, 150 μM IPP or DMAPP, 5 mM $MgCl_2$, and 1 mM

DTT in 100 mM TAPS, pH 8.0, 25 °C. Time-dependent changes in the absorption spectrum of the IDI-2 bound flavin were followed over 0.4 and 4 sec time scales using a diode array detector in place of the photomultiplier detector used for the single-wavelength stopped-flow studies.

3.2.12 Global simulation of kinetic data: The time-dependence of the pre-steady state absorbance changes in the forward and reverse direction and the steady state kinetic data were simulated with a minimal kinetic mechanism using KinTek Global Kinetic Explorer version 2.0.13 with FitSpace Explorer (KinTek Corp., Autin, TX) (*120, 121*). Descriptions of the simulated minimal mechanism and the assumptions made prior to global fitting of the data are discussed in the Results and Discussion section.

3.3 Results and Discussion

***3.3.1 Steady state kinetics*:** To determine the steady state kinetic parameters for the wt IDI-2 and its mutants, we employed the acid-lability assay developed previously by Satterwhite. This assay is based on the acid lability of DMAPP, which allows it to be selectively derivatized and isolated from unreacted IPP (Scheme 3.1). At specific time points, aliquots of the reaction mixture are removed and quenched in a concentrated solution of HCl in MeOH. The acidic conditions lead to the elimination of the pyrophosphate group of DMAPP (but not IPP), generating an allylic cation that can be quenched by solvent molecules to produce the corresponding mixture of alcohols and

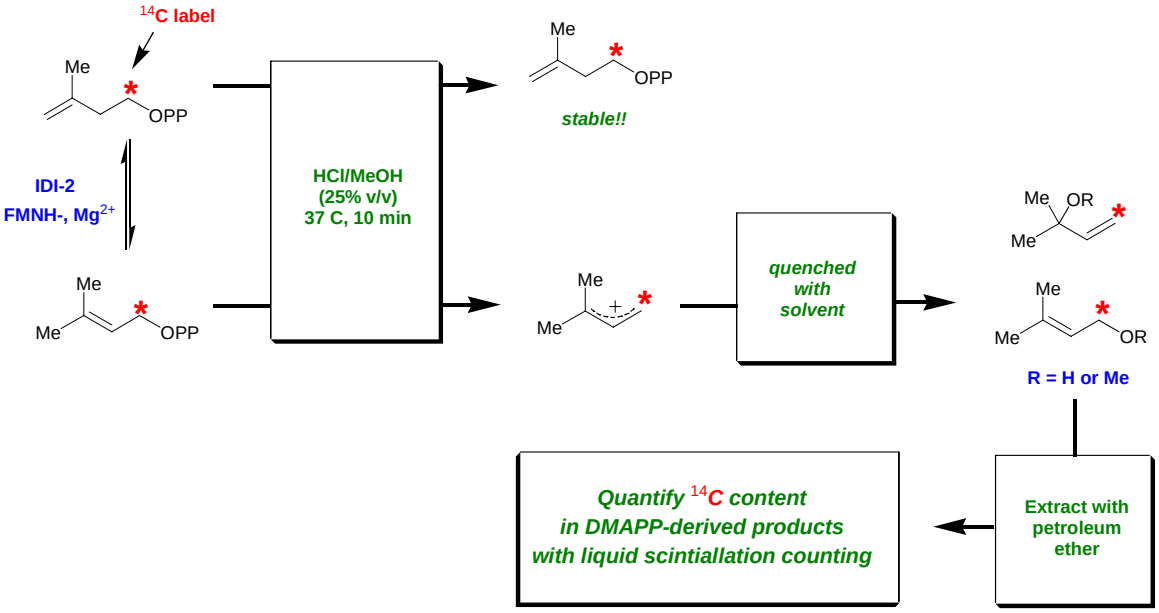

Scheme 3.1: Satterwhite assay for quantitation of ^{14}C label in DMAPP

ethers. These derivatized products of DMAPP can then be extracted from the aqueous phase using petroleum ether. The ^{14}C content of the sample can then be used, along with the specific activity of the [1-^{14}C]-IPP employed in the assay, to calculate the concentration of DMAPP at each time point.

Using this assay, the steady state kinetic parameters for the wt IDI-2 enzyme and several of its mutants were determined (Figure 3.1A and Table 3.1). The parameters for the wt enzyme (k_{cat} = 0.47 ± 0.01 s^{-1}, K_m = 9 ± 1 μM, and k_{cat}/K_m = 5.5 x 10^4 $M^{-1}s^{-1}$) compare favorably with the parameters determined for IDI-2 enzymes from several different sources (*7, 55, 56, 92*). Importantly, these previous studies also demonstrated that the IDI-2 activity does not depend critically on the method of flavin reduction, as the

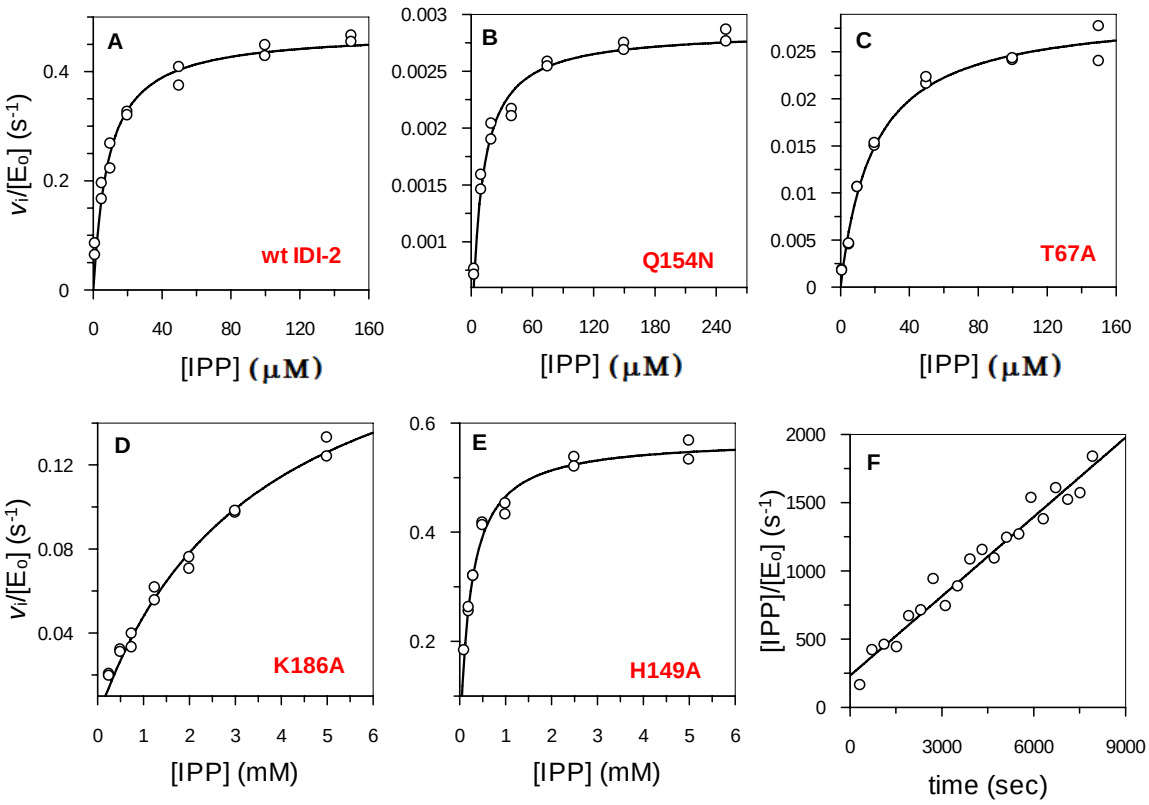

Figure 3.1: Non-linear fits of the steady state kinetic data for the wt IDI-2 (A) and its active site mutants (B – E) to the Michaelis-Menten equation. The initial velocities determined at each IPP concentration (v_i) have been normalized by the total enzyme concentration (E_o) used in the assay (0.05, 1, 7.75, 1, and 0.4 μM for wt IDI-2, T67A, Q154N, K186A, and H149A, respectively). The time-dependent formation of IPP in the reverse direction under a saturating DMAPP concentration (20 mM) is shown in panel F and was fitted with a line to estimate $k_{cat,rev} = 0.19\ s^{-1}$.

NADPH-, dithionite-, and photoreduced enzymes exhibit similar activities. Thus, dithionite was used in all of our assays to facilitate sample preparation and handling. The initial velocity for the reverse reaction with DMAPP as the substrate was also measured under pseudo-first order conditions using an ^{1}H-NMR assay to provide an estimate for $k_{cat,rev}$ of 0.19 s^{-1} (Figure 3.1F). From the Haldane relationship (K_{eq} =

$(k_{cat}/K_m)_{for}/(k_{cat}/K_m)_{rev}$ and the experimentally determined values of K_{eq} = 1.2, $(k_{cat}/K_m)_{for}$ = 5.5 x 10^4 $M^{-1}s^{-1}$, and $k_{cat,rev}$ = 0.19 s^{-1}, the $K_{m,DMAPP}$ was calculated to be 4 μM.

Enzyme	k_{cat} (s^{-1})	K_m (μM)	k_{cat}/K_m ($M^{-1}s^{-1}$)
wt IDI-2 (forward)	0.47(1)	9(1)	5.5 x 10^4
wt IDI-2 (reverse)	0.19	4*	4.8 x 10^4 *
T67A	0.029(1)	19(2)	1.5 x 10^3
Q154N	0.0029(1)	9.0(7)	3.2 x 10^2
K186A	0.21(2)	3500(500)	6.0 x 10^1
H149A	0.57(1)	230(20)	2.4 x 10^3

Table 3.1: Summary of steady state kinetic parameters for the wt IDI-2 and its mutants. Standard errors in the final digit of the parameter estimates are shown in parentheses. *Calculated from $k_{cat,rev}$, $(k_{cat}/K_m)_{for}$, and K_{eq} = 1.2 using the Haldane relationship.

Among the mutant enzymes, the H149A and K186A mutations appeared to perturb the K_m for IPP to a much greater extent than they perturbed k_{cat} (Table 3.1). Consistent with a role in substrate binding, the imidazole N atom of His149 is within ~ 4 Å from the Mg^{2+} ion that is complexed with the pyrophosphate moiety of IPP in the co-crystal structure of IDI-2 with reduced FMN and IPP (*89*). Interestingly, the primary amino group of the Lys186 side chain does not appear to be close enough to IPP in this structure to engage in direct binding interactions with the substrate. Thus, the reason for the large K_m for IPP observed for the K186A mutant is not readily apparent. Loss of Lys186 side chain may alter the stacking interactions between the flavin and IPP in the active site, or may somehow hinder the putative enzyme conformational change that

occurs upon IPP binding (dicussed in Chapter 2). Interestingly, a higher concentration of FMN was required to saturate the steady state activity of this mutant (data not shown), suggesting that the "closed" form of this enzyme:flavin:substrate complex may not be as stable. Alternatively, the loss of Lys186 may lead to unfavorable electrostatic interactions between the anionic reduced FMN resting state and the pyrophosphate moiety of IPP. Regardless of the effects of these mutations on the K_m for IPP, the similarity between the k_{cat} values of the H149A and K186A mutants and the wt enzyme clearly indicate that the Lys186 and His149 side chains are not absolutely required for the conversion of IPP to DMAPP.

In contrast to the K186A and H149A mutants, the K_m values for IPP measured for the T67A and Q154N mutants are very similar to the K_m value measured for the wt enzyme, while the k_{cat} values in both of these mutants are significantly reduced (Table 3.1). Based on the crystal structures of IDI-2 that were available at the time (*60, 61*), we initially proposed that the side chain of Thr67 could be accepting a hydrogen bond from the N5 atom of the reduced FMN, perhaps activating the N5 atom for a catalytic function in the isomerization of IPP/DMAPP double bond (*90*). When the structure for the fully complexed IDI-2 was solved, however, the side chain of Thr67 was found to be oriented away from FMN, suggesting that our initial prediction is unlikely. However, in this fully complexed structure, the backbone carbonyl group of the adjacent, conserved Met residue (M66) is within 3 Å of the N5 atom of FMN, and appears to be in position to accept a hydrogen bond from FMN. Though likely an indirect effect, the loss of activity in the T67A mutant is probably due to the disruption of the hydrogen bond between Met66 and

the N5 atom of the flavin. This result suggests that the electronic properties of the flavin in the direct vicinity of the N5 atom are likely important for catalysis. Interestingly, the co-crystal structure shows that the N5 atom of reduced FMN is ~ 3Å away from the C2 atom of the bound substrate and appears to be appropriately positioned for abstraction of the *pro R* C2 proton, which would be consistent with the observed stereospecificity of the IDI-2 catalyzed reaction (*58*).

A more drastic decrease in k_{cat} (~ 170 fold) was observed for the Q154N mutant (*122*). The side chain of Gln154 appears to be in close proximity to the substrate molecule in the co-crystal structure and is oriented toward the opposite face of the substrate as the FMN. It is possible that Q154 plays some role (along with the N5 atom of FMN) in mediating proton transfers to and from the substrate, perhaps with the assistance of a putative proton relay composed of the conserved His10 and Glu222 residues which appear to link the side chain of Gln154 to the bulk solvent via a hydrogen bonding network. Finally, preliminary studies of the Q154A mutant (data not shown) suggest an even more drastic decrease in k_{cat} (~ 900 fold), lending credence to the idea that the chemical properties of the amide side chains of Gln and Asn are somehow important for catalysis.

3.3.2 pH-dependence of the steady state kinetic parameters: To test for the presence of acid/base catalysis in IDI-2 and to identify active site groups that could be involved in general acid/base catalysis, we studied the pH-dependence of the steady state kinetics for wt IDI-2 (Figure 3.2 and Table 3.2). The data show that k_{cat} is relatively independent of

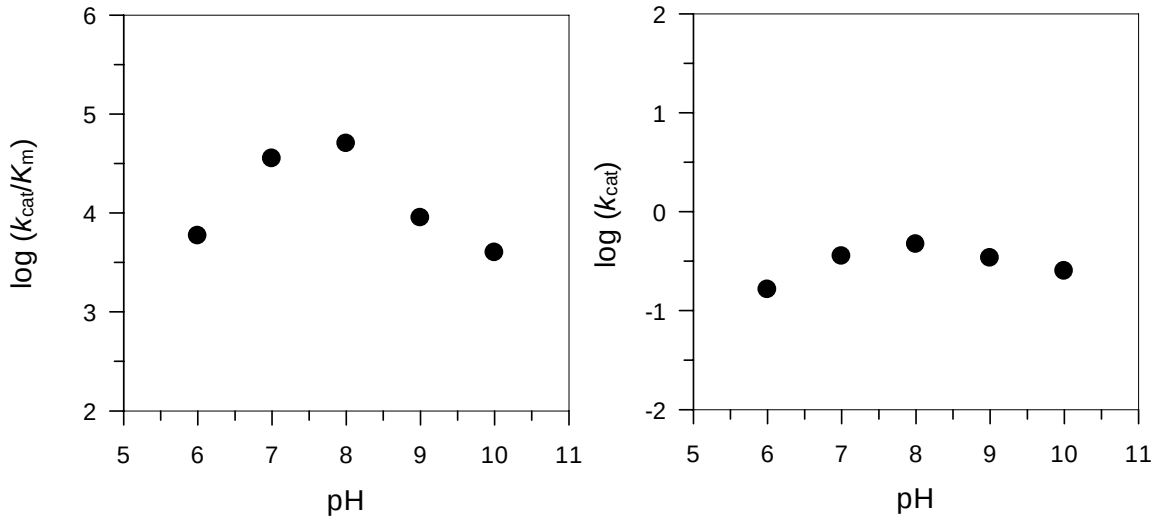

Figure 3.2: pH-dependence of k_{cat}/K_m (A) and k_{cat} (B) for the wt IDI-2 catalyzed reaction.

pH	k_{cat} (s^{-1})	K_m (μM)	k_{cat}/K_m ($M^{-1}s^{-1}$)
6.0	0.164(1)	28(1)	5.9×10^3
7.0	0.35(1)	10(1)	3.5×10^4
8.0	0.47(1)	9(1)	5.5×10^4
9.0	0.34(1)	38(2)	9.0×10^3
10.0	0.25(1)	59(15)	4.2×10^3

Table 3.2: Summary of the pH-dependence of the steady state kinetic parameters for the wt IDI-2.

pH, which suggests that either acid/base chemistry is not limiting the rate of steady state turnover, or that both enzyme and substrate must be correctly protonated for substrate binding and catalysis. There were slight decreases in k_{cat} at the pH extremes, but the magnitude of the slopes of the acidic and basic limbs of the k_{cat}-pH profile (~ +0.3 and ~ -0.15, respectively) are clearly less than 1. Thus, this data fails to provide direct evidence

for general acid/base catalysis in the wt IDI-2, but does not rule it out. It is interesting to note that the slight decrease in k_{cat} at pH 10.0 (53% of the k_{cat} measured at pH 8.0) appears to be very similar to the slight decrease in the equilibrium levels of the flavin intermediate at pH 10.0 (69% of the levels seen at pH 8.0, see Figure 2.6). Thus, there appears to be a correlation between the equilibrium concentration of the flavin intermediate and the maximum rate of steady state turnover.

In contrast, the k_{cat}/K_m parameter clearly decreases with slopes ~ 1 at both high and low pH as the K_m for IPP gets larger. We did not conduct a thorough analysis to identify the ionizable groups responsible for substrate binding. However, control assays indicated that the 20 μM FMN concentration used in these assays was sufficient to saturate IDI-2 activity across the pH range tested (data not shown). Thus, the ionization controlling the acidic limb of the k_{cat}/K_m-pH profile (pK_a ~ 6.5) is not likely to be the reduced FMN (pK_a 6.7 in solution). His149 or Glu155, both of which serve as ligands to the Mg^{2+} ion are potential candidtes for the residue responsible for controlling the acidic limb of the profile. The residue responsible for controlling the basic limb of the k_{cat}/K_m-pH profile (pK_a ~ 8.5) may be Lys186. This conclusion would be in line with the perturbation in $K_{m,IPP}$ measured for the K186A mutant (Table 3.1). As mentioned above, however, Lys186 does not appear to make direct contact with IPP. Thus, the effect of this residue on IPP binding could stem from steric and/or electronic effects of the Lys186 side chain on the active site environment. Another potential candidate for the acidic and basic groups in the k_{cat}/K_m-pH profile is the pyrophosphate moiety of IPP, whose 2nd and 3rd ionization constants should be ~ 6.0 – 6.5, and 8.5 – 9.0, based on comparison to the

acid dissociation constants reported for other diphosphates (*123*). If this is the case, it would suggest that IPP^{2-} forms a complex with Mg^{2+} in the physiological pH range and binds to the enzyme in a charge neutral state (Scheme 3.2). Below pH 6, IPP^{1-} would not be able to bind Mg^{2+} as tightly, but increasing the concentration of Mg^{2+} could help to pull the IPP in solution towards the IPP-Mg complex according to Le Chatelier's principle. This is consistent with the preliminary observation that higher concentrations of Mg^{2+} are required to saturate activity at pH 6.0. In contrast, above pH 8.5, when IPP is in the 3^- state, coordination of a single Mg^{2+} is insufficient to completely neutralize the negative charge on the pyrophosphate moiety, which may lead to unfavorable electrostatic interactions between the IPP-Mg complex and the anionic reduced FMN resting state of the enzyme, leading to the large observed K_m.

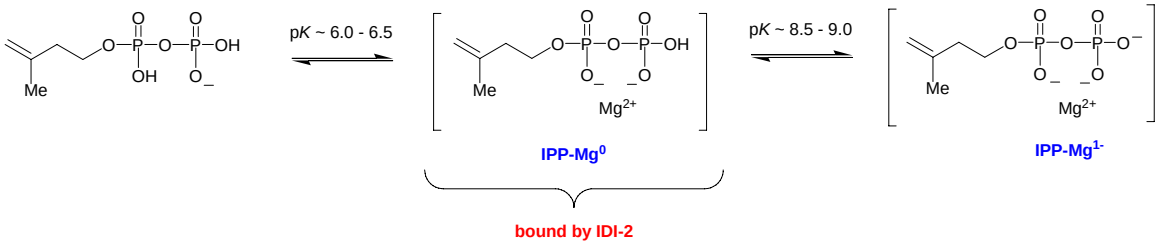

Scheme 3.2: Potential explanation for the increased K_m for IPP at low and high pH.

3.3.3 Rapid-mix chemical quench studies: To gain an understanding of the position of the rate limiting step in the kinetic mechanism relative to the formation of the product (DMAPP), we conducted a pre-steady state rapid-mix chemical quench experiment using a saturating concentration of substrate (IPP). In this experiment, IDI-2 and IPP were

mixed and were allowed to react for variable lengths of time in the pre-steady state, prior to quenching the reaction and analyzing the DMAPP content of the individual time points in a manner very similar to that employed for the steady state kinetic studies. Under saturating IPP concentrations, if a step in the kinetic mechanism following the appearance of DMAPP in the active site (such as product release) limits steady state turnover, then a burst of DMAPP formation should be observed as DMAPP accumulates on the enzyme active site in the pre-steady state. The burst phase should be followed by a slower phase of DMAPP formation that exhibits a linear dependence on time. The rate of this slower phase should correspond to the rate of steady state turnover. In contrast, if a step in the kinetic mechanism prior to DMAPP formation (such as the chemistry step leading from IPP to DMAPP) limits steady state turnover, then no DMAPP will accumulate on the enzyme (because it is released from the enzyme faster than it is formed) and, consequently, no burst will be observed. In this scenario, the appearance of DMAPP over time should be linear, with a rate that is equivalent to the rate of steady state turnover under saturating substrate concentrations (~ k_{cat}). Thus, this method provides a readily interpretable diagnostic for determining the position of the rate limiting step in the kinetic mechanism of the enzyme relative to the appearance of product. When this experiment was performed with IDI-2 at saturating IPP concentrations (Figure 3.3), no burst in DMAPP formation was observed, and the appearance of DMAPP was linear with respect to time. This observation suggests that the rate limiting step in the kinetic mechanism for IDI-2 occurs before the formation of DMAPP on the IDI-2 active site, and could potentially involve the chemistry step(s). The rate of DMAPP formation in the pre-

steady state was 1.5 s^{-1}, which compares favorably to k_{cat} (1.3 s^{-1}) measured for the *S. aureus* enzyme under similar conditions at 37 °C (*55*).

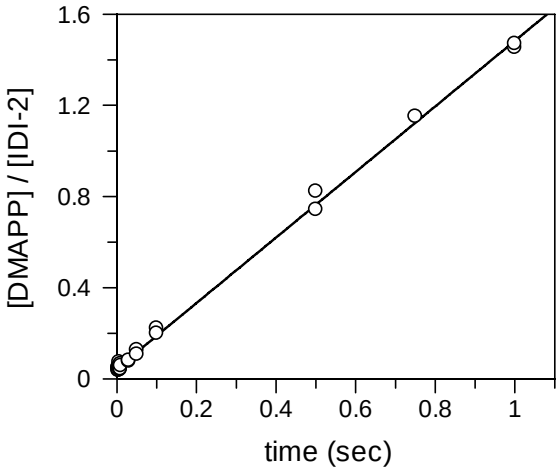

Figure 3.3: Rapid-mix chemical quench experiment to test for the presence of a pre-steady state burst in DMAPP formation. The IDI-2 concentration was 20 μM

3.3.4 Substrate kinetic isotope effects: Emboldened by the lack of burst kinetics in the pre-steady state rapid quench studies, we next tested whether deprotonation at C2 of IPP limits steady state turnover. Previous studies had indicated that the *pro R* C2 proton of IPP is stereospecifically removed by IDI-2 during turnover (*58*). We reasoned that if IPP deprotonation limits IDI-2 turnover, then it may be possible to measure a substrate deuterium kinetic isotope effect using an IPP substrate that is stereospecifically deuterated at C2. Thus, Wei-chen Chang (a graduate student in our lab), chemically synthesized (*R*)-[2-^{2}H]-IPP according to reported protocols (*114*). Because this compound does not contain the ^{14}C label that is detected using the standard steady state kinetic assay, we relied on an ^{1}H-NMR assay for measuring the rate of DMAPP

formation from the protiated and deuterated IPP substrates (*7, 90*). Here, the formation of the (*Z*)-methyl resonance of DMAPP is followed over time and its integrated peak area is compared to an acetate internal standard to calculate the concentration of DMAPP at each time point. Linear regression over the time course is then used to calculate the initial velocity for each substrate (k_H and k_D) in order to calculate the corresponding isotope effect by direct comparison of the initial velocities ($^Dk_{cat} = k_H/k_D$). The time-dependent formation of DMAPP from IPP and (*R*)-[2-^{2}H]-IPP (normalized by the enzyme concentration used in the assay) is shown in Figure 3.4, and comparison of the initial velocities gave a substrate deuterium kinetic isotope, $^Dk_{cat} = 2.2$. The magnitude of the isotope effect is large enough to suggest that cleavage of the C2-H/D bond of IPP is at least partially rate limiting in the isomerization reaction catalyzed by IDI-2, an observation that is consistent with the lack of a pre-steady state burst of DMAPP formation.

3.3.5 Solvent kinetic isotope effects: To assess the involvement of solvent exchangeable protons in the step(s) that limit steady state turnover in IDI-2 catalysis, we performed a variety of steady state kinetic experiments in buffers containing D_2O. First, in order to select an appropriate pL for investigation of the solvent KIEs, we screened for the activity of IDI-2 under pseudo-first order substrate concentrations in the pL range 7.0 - 8.5 using buffers prepared in either 100% H_2O or 100% D_2O (Figure 3.5). These data indicated that a solvent KIE on k_{cat} ($^{D_2O}k_{cat} \sim 1.5$) is present and its magnitude is relatively independent of pL from 7.5 – 8.5 (*90*). Next, to determine the solvent KIEs on k_{cat} and

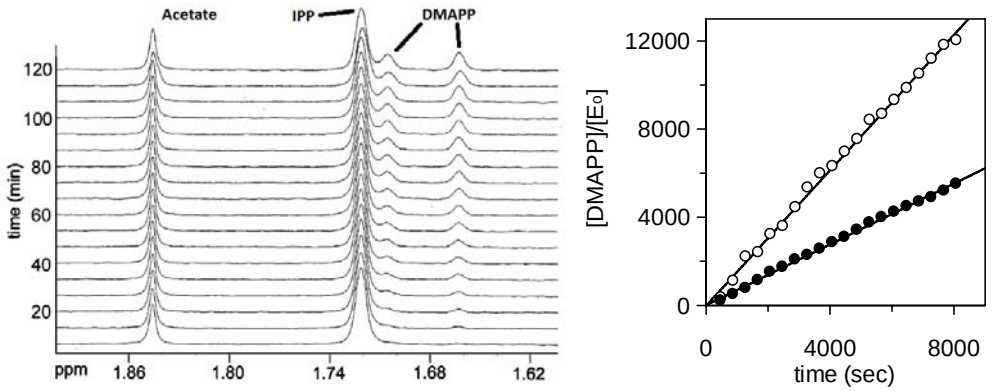

Figure 3.4: ^{1}H-NMR assay used for determination of the kinetic isotope effect on k_{cat} using the stereospecifically deuterated IPP, (*R*)-[2-^{2}H]-IPP. The left panel shows the ^{1}H-NMR resonances of the acetate internal standard, the Me group of IPP, and the (*E*)- and (*Z*)-methyl groups of DMAPP, and how these signals change over time in the presence of IDI-2. The right panel shows the time-dependent formation of the (*Z*)-methyl group of DMAPP (1.66 ppm) from IPP (open circles) and (*R*)-[2-^{2}H]-IPP (filled circles). The DMAPP concentrations at each time point in this figure were calculated by normalization to the acetate signal, and have been normalized by the enzyme concentration used in the assay to facilitate comparison between the two time courses.

k_{cat}/K_m ($^{D_2O}k_{cat}$ and $^{D_2O}k_{cat}/K_m$), we performed steady state kinetic assays on the wild type IDI-2 catalyzed reaction at pL 8.0 in buffer prepared with either 100% H_2O or 100% D_2O using the standard assay conditions. This analysis gave normal solvent KIEs of 1.4 and 3.8 on k_{cat} and k_{cat}/K_m, respectively (Figure 3.5). At a first approximation, the magnitude of the normal solvent KIEs on k_{cat} and k_{cat}/K_m suggest that bonds to solvent exchangeable protons are breaking in the step(s) that limit steady state turnover, and are consistent with chemical mechanisms for IDI-2 involving proton transfer to IPP from a general acid in the active site.

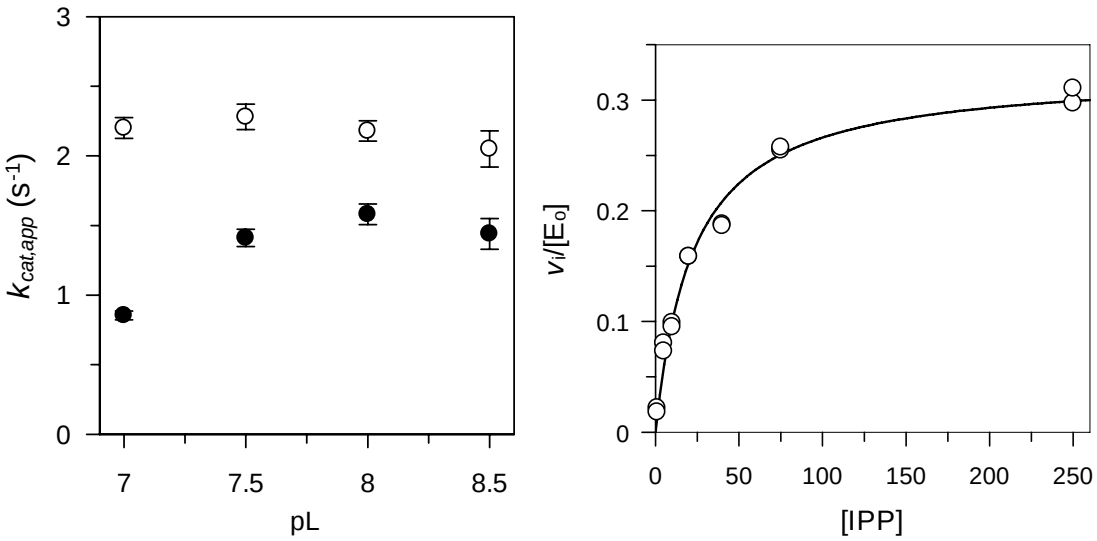

Figure 3.5: Solvent kinetic isotope effects on the wt IDI-2 reaction. The left panel shows the pL-dependence of the initial velocity under pseudo-first order conditions in buffers prepared in H_2O (open circles) and buffers prepared in D_2O (filled circles). The right panel shows the dependence of the initial velocity on IPP concentrations at pL 8.0 in buffers containing nearly 100% D_2O. Other than the substitution of H_2O for D_2O, the reaction conditions used for collecting the data in the right panel are identical to those in Figure 3.1.

In order to better understand the potential origins for the different magnitudes of the solvent KIEs measured on k_{cat} and k_{cat}/K_m for wild the type IDI-2, it is useful to first consider the origins of primary kinetic isotope effects. Analyzed within the context of transition state theory, kinetic isotope effects arise from differences in zero point bond vibrational energies of the bonds to the two isotopes under consideration (in this case, H and D) upon moving from the ground state to the transition state (Figure 3.6). The zero point energy (ZPE) of these bonds is inversely proportional to the reduced mass of the bond and, thus the ZPE for a bond to D is less than the ZPE for an otherwise identical bond to H. In general, normal primary deuterium kinetic isotope effects indicate a

substantial degree of bond cleavage to H/D in the transition state. In this scenario, the

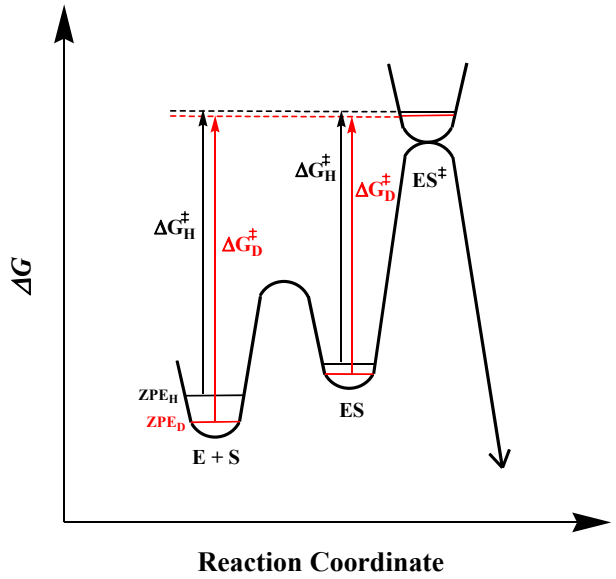

Figure 3.6: Illustration of the origin of primary kinetic isotope effects and a potential explanation for the larger solvent KIE measured on k_{cat}/K_m for the wt IDI-2 reaction. In this figure, E + S and ES represent effective ground states for an enzyme-catalyzed reaction under k_{cat}/K_m and k_{cat} conditions, respectively, and $ES^{\ddagger}$ represents a single rate limiting transition state. The zero point energies (ZPE) of bonds to solvent exchangeable H and D at a particular exchangeable site in the enzyme are denoted in black and red, respectively, in each enzyme form.

energies of the bonds to H and D in the transition state are closer to one another, because the bonds are only partially formed. Upon moving from the reactant state to the transition state, this leads to a free energy change for cleavage of the bond to D ($\Delta G^{\ddagger}_{D}$) that is larger than the free energy change for cleavage of the bond to H ($\Delta G^{\ddagger}_{H}$). This, in

turn specifies that $k_H > k_D$ for passage through this transition state, which leads to a normal kinetic isotope effect ($k_H/k_D > 1$).

Keeping this in mind, and assuming that the solvent KIE is expressed on a single transition state in the IDI-2 catalyzed reaction, the differences in magnitude between the solvent KIEs measured on k_{cat} and k_{cat}/K_m (1.4 and 3.8, respectively) may be attributable to the different effective ground states for these two steady state kinetic parameters (Figure 3.6). Under k_{cat} conditions, the effective ground state is the Michaelis complex between the enzyme and substrate (ES), because the substrate concentration under these pseudo-first order conditions is sufficiently high to saturate the rate of the substrate binding step in the kinetic mechanism. However, the kinetic parameter k_{cat}/K_m is an estimation of the 2nd order rate constant at infinitely low substrate concentrations, where the energetic barrier for the substrate binding step is kinetically significant. It follows logically that under k_{cat}/K_m conditions, the effective ground state is the free enzyme + free substrate (E + S). Therefore, if the degree of bonding to the solvent exchangeable H/D that is responsible for the normal solvent KIE in the IDI-2 catalyzed reaction is larger in the free enzyme form than it is in the Michaelis complex, then a larger solvent KIE will be measured on k_{cat}/K_m than on k_{cat}. A potential explanation for this type of behavior is that the bond to the kinetically significant H/D is fully formed in the free enzyme resting state, but is partially broken in the Michaelis complex, such that $\Delta\Delta G^{\ddagger}$ for passage of the two isotopically substituted bonds through the transition state is smaller when starting from the Michaelis complex as the effective ground state. This explanation assumes that a single solvent exchangeable site is responsible for the entire solvent KIE. However,

there could be additional components to the solvent KIE under k_{cat} conditions that serve to lower the observed isotope effect on this parameter. This possibility will be examined more thoroughly with the proton inventory studies described below.

One potential source of error in interpreting solvent KIEs on enzyme catalyzed reactions can arise if the kinetics of the reaction under study are sensitive to pH and the kinetic data were not acquired at equivalent pL values in the H_2O and D_2O solvents (*115, 124*). This is because the acid dissociation constants of most organic bases (including the commonly encountered ionizable amino acid side chains used in enzymes) differ slightly in H_2O and D_2O (oftentimes by a factor of $\Delta pK_a \sim 0.5$). Thus, if the data are not collected at an equivalent pL, and the kinetics are pH-dependent, then the fraction of the active enzyme form may not be equivalent in the two different solvents, and the measured values for the steady state kinetic parameters could be slightly skewed, leading to erroneous measurements of solvent KIEs. We did not measure the pD-dependence of the IDI-2 catalyzed reaction, so we cannot say for certain that the solvent KIE measurements were taken at an equivalent pL. However, the steady state kinetic parameters in H_2O appear to be relatively constant from pH ~ 7.5 – 8.5 (Figure 3.2). Assuming that there are no drastic alterations of this pattern in D_2O, pL 8.0 should be within the region of equivalency for the IDI-2 catalyzed reaction and, thus, the measured $^{D_2O}k_{cat}/K_m$ should be fairly reliable. The $^{D_2O}k_{cat}$ value is known with greater reliability because our control experiments (Figure 3.5) demonstrated the pL independence of this parameter at pL 8.0.

3.3.6 Proton inventory studies: To more closely investigate the origin of the solvent KIE on k_{cat} for wild type IDI-2, we performed a proton inventory study under pseudo-first order conditions at pL 8.0. Operationally, to conduct a proton inventory, one measures the rate (or equilibrium) constant of interest (k_{cat}) as a function of the mole fraction of D_2O present in the reaction mixture and analyzes the data according to the Gross-Butler equation (Eqtn 3.3), where k_o and k_n are the rate constants in 100% H_2O and buffer of deuterium atom fraction, n, respectively, and Φ_R and Φ_T are fractionation factors for exchangeable sites in the reactant and transition states. When analyzing the effects of n on rate constants, the terms in the numerator of this equation arise from exchangeable transition state sites, while the terms in the denominator reflect exchangeable sites in the reactant state. As can be quickly seen, any exchangeable site with a fraction factor of unity will not contribute to the observed solvent KIE. Using Eqtn 3.3, the number of exchangeable sites in the reactant (v_{Rj}) and transition state (v_{Ti}) that contribute to a solvent kinetic isotope effect can be "inventoried" by including the appropriate number of terms in the numerator and denominator. In favorable circumstances, a proton inventory analysis can provide insight into the number of solvent exchangeable sites that contribute to an observed solvent KIE, whether these sites are in the effective reactant state or the transition state, and the magnitude of the fractionation factor associated with each site (*115, 124*).

Eqtn 3.3

$$k_n/k_o = \prod_i^{\nu_T} (1\text{-}n+n\phi_{Ti}) \Big/ \prod_j^{\nu_R} (1\text{-}n+n\phi_{Rj})$$

Full derivations of the Gross-Butler equation can be found in several excellent review articles by Richard Schowen (*115, 124*). The following discussion highlights some of the salient points and key assumptions of these equations, in order to better illustrate the meaning of the fraction factors and how this parameter is related to solvent kinetic isotope effects measured in isotopic water mixtures. For our purposes, it is useful to consider the hydrogenic exchange equilibrium between an exchangeable solute species and bulk water (Eqtn 3.4), where A is an exchangeable site (e.g., an active site amino acid residue), HOL and DOL are water molecules (L = H or D), and X are the fractional concentrations of the various species (*124*).

Eqtn 3.4:

$$AH + DOL = AD + HOL;\ K_{exch} = (X_{AD}X_{HOL})/(X_{AH}X_{DOL})$$

This equation can be rearranged into Eqtn 3.5 to define the fractionation factor for site A:

Eqtn 3.5:

$$K_{exch} = \Phi_A = (X_{AD}/X_{AH})/(X_{DOL}/X_{HOL})$$

When expressed in this manner, the fractionation factor for site A (Φ_A) relates the energetic preference for binding deuterium at site A to the preference for binding deuterium at a bulk water site. In general, "deuterium prefers the stronger bond," so if site A binds the hydrogen isotope more strongly than a bulk water site, the numerator in Eqtn 3.5 will be larger than the denominator and Φ_A will be > 1. Conversely, if the hydrogen isotope binds site A more loosely than it binds a bulk water site, $\Phi_A < 1$. The strength of binding is usually thought of in terms of the extent of covalent bond formation to the hydrogen isotope. Thus, if a hydrogen isotope at a particular exchangeable site is "moving" in the transition state of a reaction, the fractionation factor for that site will be lower in the transition state than in the ground state (because the bonds to the hydrogen isotope are only partially formed in the transtition state).

If it is assumed that water mixtures containing variable amounts of D_2O will adopt a composition where all H and D atoms are statistically distributed between D_2O, HOD and H_2O species, then the denominator of Eqtn 3.5 can be expressed in terms of the atom fraction of deuterium (n) to give Eqtn 3.6.

Eqtn 3.6:

$$\Phi_A = (X_{AD}/X_{AH})/(n/[1-n])$$

Equations 3.4 – 3.6 assume the rule of the geometric mean, which states that isotopic substitution at the exchangeable protein and solvent sites effect free energy changes that are independent of each other (*124*). This, in turn, allows us to assume that the

equilibrium constant for the exchange reaction (K_{exch} in Eqtn 3.4) is independent of whether L = H or D, that the exchange equilibria at specific sites (both in the solvent and the protein) are independent of each other, and that mixtures of D_2O and H_2O will produce statistically scrambled mixtures of solvent species (e.g., in a 50:50 mixture of D_2O:H_2O, 25% of the solvent species will be H_2O, 50% will be HOD, and 25% will be D_2O).

To illustrate the relationship between fraction factors and kinetic isotope effects, consider the reaction shown in Eqtn 3.7, where a reactant species (RL) with an exchangeable hydrogenic site (L = H or D) is converted to a transition state (TL) with the rate constant, k_L.

Eqtn 3.7:

$$RL \underset{}{\overset{k_L}{\rightleftharpoons}} TL \qquad k_L = X_{TL}/X_{RL}$$

The kinetic isotope effect (^Dk) for this reaction can be defined in the normal way assuming "ultrasimple" transition state theory, where the ground state and transition state are assumed to be in a quasi-equilibrium with each other (Eqtn 3.8):

Eqtn 3.8:

$$^Dk = k_H/k_D = (X_{TH}/X_{RH})/(X_{TD}/X_{RD})$$

Eqtn 3.8 can be rearranged to Eqtn 3.9 and the fractional concentrations (X) of the TL and RL species can be defined (as in Eqtn 3.6) in terms of the free energy of exchange of their hydrogenic sites (L) with bulk solvent to give Eqtn 3.10:

Eqtn 3.9:

$$k_H/k_D = (X_{RD}/X_{RH})/(X_{TD}/X_{TH})$$

Eqtn 3.10:

$$k_H/k_D = [(X_{RD}/X_{RH})/(n[1\text{-}n])\ ] / [(X_{TD}/X_{TH})/(n[1\text{-}n])] = \Phi_{RL}/\Phi_{TL}$$

Thus, the solvent kinetic isotope effect for exchangeable site L upon moving from reactant state R to transition state T is equivalent to the ratio of the fractionation factors for site L in the reactant and transition states.

In mixtures of D_2O and H_2O with deuterium atom fraction n, the rate constant (k_n) for conversion of reactant state R to transition state T can be written as in Eqtn 3.11, where k_H and k_D represent the rate constants for formation of the transition state when the exchangeable site is protiated or deuterated, respectively, and X_{RH} and X_{RD} represent the fractional concentrations of the reactant state with the exchangeable site in the protiated and deuterated forms:

Eqtn 3.11:

$$k_n = k_H X_{RH} + k_D X_{RD} = k_H[X_{RH} + (k_D/k_H)X_{RD}]$$

Remembering that X_{RH} and X_{RD} represent fractional concentrations (i.e., $X_{RH} + X_{RD} = 1$), Eqtn 3.6 can now be rewritten in terms of X_{RH} and X_{RD} to give Eqtns 3.12 and 3.13, respectively (*115, 124*):

Eqtn 3.12:

$$X_{RH} = (1 - n)/(1 - n + n\Phi_{RL})$$

Eqtn 3.13:

$$X_{RD} = n\Phi_{RL}/(1 - n - n\Phi_{RL})$$

Substitution of 3.12 and 3.13 into Eqtn 3.11, remembering from Eqtn 3.10 that $k_D/k_H = \Phi_{TL}/\Phi_{RL}$, and defining $k_H = k_o$ as the rate constant in 100% H_2O yields equation 3.14:

Eqtn 3.14:

$$k_n = k_o\,[(1 - n + \Phi_{TL})/(1 - n + n\,\Phi_{RL})]$$

This equation can be generalized over *v* exchangeable reactant and transition state sites to give the familiar form of the Gross-Butler (Eqtn 3.3).

The proton inventory data for the IDI-2 catalyzed reaction under pseudo-first order conditions is shown in Figure 3.7, along with non-linear fits to several different forms of the Gross-Butler equation and the corresponding residual plots. The algebraic definition for each model is tabulated in Table 3.3 along with the fitted parameter values, their associated standard errors, the mean square residuals of the fit (MSR), and the

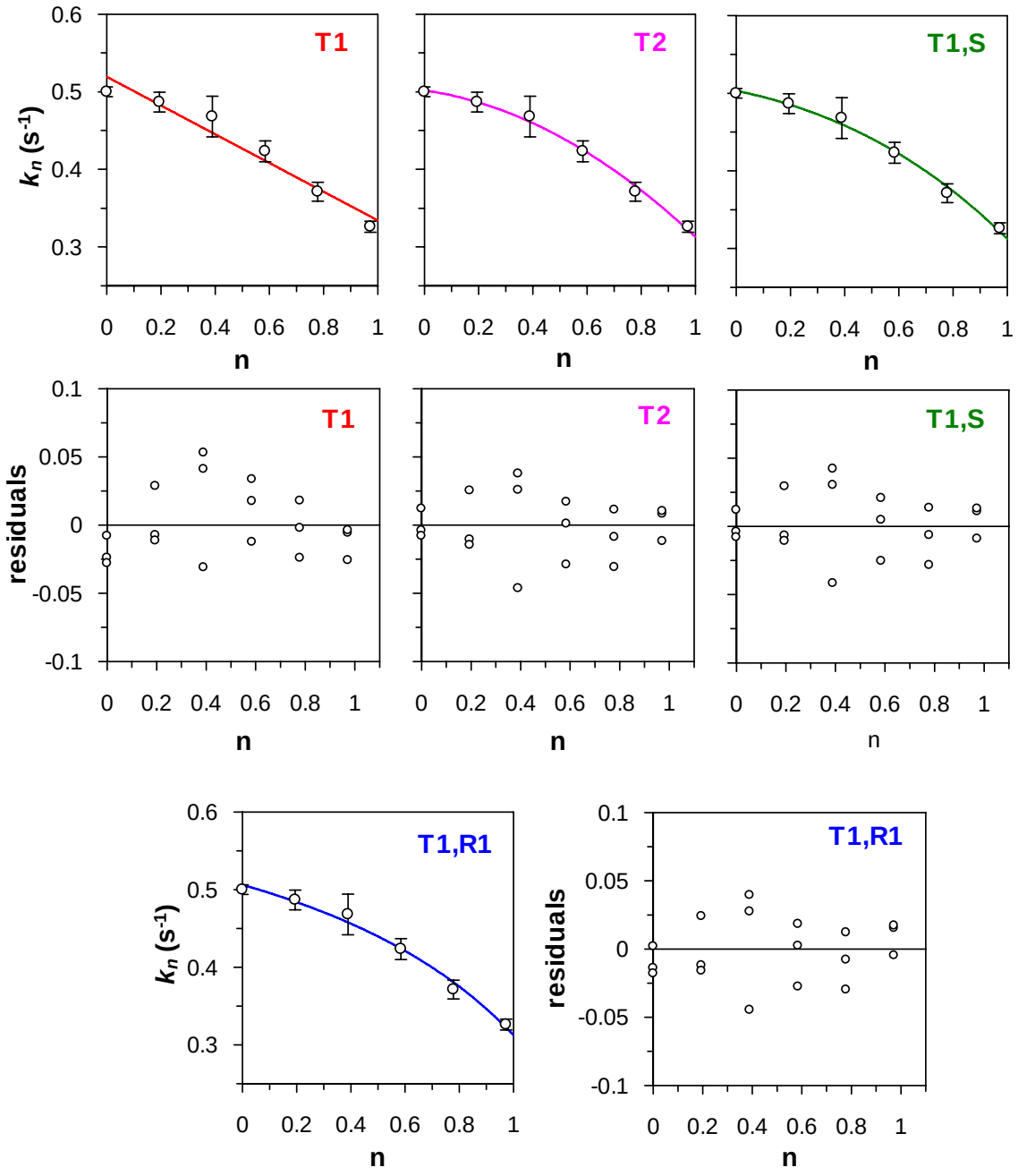

Figure 3.7: Proton inventory for the wt IDI-2 showing non-linear fits to several different forms of the Gross-Butler equation. The fitted parameter values for each model are shown in Table 3.3.

Model	k_n/k_o =	k_o	Φ_{T1}	Φ_{T2}	Φ_S	Φ_{R1}	MSR	$^{D_2O}k_{cat}$
T_1	$(1 - n + \Phi_{T1})$	0.52(1)	0.64(3)	-	-	-	0.000693	1.56(7)
T_2	$(1 - n + \Phi_{T1})^* (1 - n + \Phi_{T2})$	0.50(1)	0.42(5)	1.5(2)	-	-	0.000531	1.6(3)
T_1S	$(1 - n + \Phi_{T1})^*\Phi_S^n$	0.50(1)	0.39(7)	-	1.6(2)	-	0.0005	1.6(2)
T_1R_1	$(1 - n + \Phi_{T1})/(1 - n + \Phi_{R1})$	0.51(1)	0.3(1)	-	-	0.5(2)	0.0006	1.6(7)

Table 3.3: Comparison of fits of proton inventory data to different forms of the Gross-Butler equation.

calculated solvent KIE at n = 1 using the fitted parameter values. In the T_1 model, it is assumed that a single transition state site has a non-unity fractionation factor (Φ_{T1}) and is, thus, solely responsible for $^{D_2O}k_{cat}$ ($^{D_2O}k_{cat} = 1/\Phi_{T1}$). In the T_2 model, two transition state sites are assumed to have non-unity fractionation factors (Φ_{T1} and Φ_{T2}; $^{D_2O}k_{cat} = 1/[\Phi_{T1}\Phi_{T2}]$). In the T_1S model, one transition state site combines with a medium effect to generate the solvent KIE ($^{D_2O}k_{cat} = 1/[\Phi_{T1}\Phi_S]$). The fractionation factor for the medium effect (Φ_S) is assumed to be composed of many small solvent KIEs at numerous exchangeable sites that cumulatively produce a significant overall effect. In the final model considered in our analysis, T_1R_1, two exchangeable sites are assumed to have non-unity fractionation factors, one in the reactant state (Φ_{R1}) and one in the transition state (Φ_{T1}) with $^{D_2O}k_{cat} = \Phi_{R1}/\Phi_{T1}$.

The proton inventory data appear to be composed of two components - an inverse component that is over-ridden by a stronger normal component which produces a slightly "dome-shaped" proton inventory for k_{cat}. Based on comparison of the MSR values for the different fits and visual inspection of the residual plots in Figure 3.7, it appears that

the simple, single transition state proton model (model T_1) does not adequately describe the experimental data. Most notably, there appears to be clear structure in the residual plot, where the T_1 model over estimates k_n at low and high values for n. In contrast, the measured values of k_n appear to be more or less randomly distributed around the fitted curve described by models T_2, T_1S, and T_1R_1. To provide a more rigorous statistical test to determine whether inclusion of the extra parameter in the fits to models T_2, T_1S, and T_1R_1 is justified, we performed a significance of regression analysis using an *F* test-statistic (calculated from the data in Table 3.4) as described in (*125*). The *F* values calculated by individual comparison of the T_2, T_1S, and T_1R_1 models with the T_1 model were found to be significant (or nearly significant) at the 5% level, indicating that we are justified in including the extra parameter in the fits to the T_2, T_1S, and T_1R_1 models, and that we should look with suspicion upon the T_1 model.

Each of the more likely models for the proton inventory data (T_2, T_1S, and T_1R_1) has a component (Φ_{T1}) that predicts a normal comtribution to the solvent kinetic isotope ranging from ~ 2.4 – 3.3 (where $^{D_2O}KIE = 1/\Phi_{T1}$). These values are within the range expected for a primary solvent deuterium kinetic isotope effect, where a solvent exchangeable proton is being transferred from a proton donor to an acceptor, and are perhaps consistent with transfer of a solvent exchangeable proton to the double bond of IPP by an active site acid in the transition state for isomerization. The relatively large inverse contribution to $^{D_2O}k_{cat}$ (ranging from ~ 0.5 – 0.67) is more difficult to explain.

Model	N_d	N_p	d_X	$d_{X\Delta}$	SSR_X	MSR_X	$SS_{X\Delta}$	$M_{X\Delta}$	$F_{1,15}$
T_1	18	2	16	0	0.0111	0.000693	-	-	-
T_2	18	3	15	1	0.00801	0.000534	0.00309	0.00309	5.79
T_1S	18	3	15	1	0.00818	0.000545	0.00292	0.00292	5.36
T_1R_1	18	3	15	1	0.00855	0.00057	0.00255	0.00255	4.47

Table 3.4: Calculation of the *F* test-statistic for the significance of regression analysis of the proton inventory data. N_d and N_p indicate the number of raw data points and number of parameters in the fit, respectively, d_X are the degrees of freedom ($d_X = N_d - N_p$) for model "x", $d_{X\Delta} = d_{T1} - d_X$, SSR_X and MSR_X indicate the sum square residual and mean square residual of the fit to model x (where $MSR_X = SSR_X/d_X$), $SS_{X\Delta} = SSR_{T1} - SSR_X$, $M_{X\Delta} = SS_{X\Delta}/d_{X\Delta}$, and $F_{1,15} = M_{X\Delta}/MSR_X$, where the subscript "1,15" denotes the degrees of freedom in the $M_{X\Delta}$ and MSR_X terms of the *F* statistic, respectively. The critical *F* value with these degrees of freedom is $F_c = 4.54$ at the 5% significance level (*125*).

Within the context of the models tested, this inverse contribution to the solvent KIE is derived either from a second transition state site with a fractionation factor greater than unity ($\Phi_{T2} = 1.5$ in the T_2 model), a reactant state site with a fractionation factor less than unity ($\Phi_{R1} = 0.5$ in the T_1R_1 model), or to an aggregate effect of multiple exchangeable sites whose net fractionation factors become larger upon moving from the reactant state the transition state ($\Phi_S = 1.6$ in the T_1S model).

Concerning the T_2 model, we are unaware of any instances where a single transition state site has been shown to have a fractionation factor as large as $\Phi_{T2} = 1.5$. Qualitatively, this model implies that a bond to a kinetically significant proton is strengthening in the transition state. This could occur if a hydrogen bond is forming in the transition state, though it is still unclear whether this single hydrogen bond could have

a fractionation factor as large as 1.5. Alternatively, in the T_1S model, a number of relatively weak hydrogen bonds could be forming in the transition state, collectively generating a substantial inverse solvent KIE.

The T_1R_1 model predicts the presence of two sites, one in the reactant state and one in the transition state, both of which have low fractionation factors. An interesting possible explanantion for the low reactant state fractionation factor is the formation of a low-barrier hydrogen bond (LBHB) in the Michaelis complex. NMR and solvent kinetic isotope effect studies of several enzymes have demonstrated that low barrier hydrogen bonds typically have fractionation factors ranging from ~ 0.4 – 0.6 (*126-130*), with a lower limit of ~ 0.3 estimated from model studies (*131*). These types of hydrogen bonds are characterized by proton bridges that are roughly equidistant between two heteroatoms that have closely matched pK_a values and which are separated by short internuclear distances of < 2.6 Å (*131-134*). If a strong hydrogen bond present in the Michaelis complex reactant state is lost upon forming the transition state (as in the T_1R_1 model), then a large inverse solvent KIE could be observed for this site. At present though, it is not exactly clear whether these types of hydrogen bonds play a role in IDI-2 catalysis, as no putative LBHBs in the active site can be seen in the reduced IDI-2:FMN:IPP co-crystal structure (*89*), which is assumed to represent the reactant state under pseudo-first order conditions.

It is also tempting to speculate that a low reactant state fractionation factor (Φ_{R1} = 0.5) in the Michaelis complex could be in part responsible for the decrease in magnitude of $^{D_2O}k_{cat}$ relative to $^{D_2O}k_{cat}/K_m$ (vide supra). Namely, this exchangeable site may have a

fractionation factor near unity in the free enzyme form, where the active site is open and is readily accessible to solvent (*60, 61*). Upon IPP binding, the active site becomes closed off to solvent molecules (which are known to disfavor formation of LBHBs), allowing the reactant state site to form a strong hydrogen bond in the Michaelis complex. In this scenario, the reactant state site would not contribute to $^{D_2O}k_{cat}/K_m$ because its fractionation factor is near unity in the free enzyme form. However, this site could contribute to $^{D_2O}k_{cat}$ because in the Michaelis complex, its fractionation factor is ~ 0.5. It is also interesting to note that the transition state fractionation factor determined by the T_1R_1 model ($\Phi_{T1} = 0.3$) predicts a normal isotope effect on $^{D_2O}k_{cat}$ of 3.3, which is very similar to the normal effect measured value on $^{D_2O}k_{cat}/K_m$ of 3.8. This result is expected if a single transition state site dominates the normal KIE and if the same transition state is rate limiting under both k_{cat} and k_{cat}/K_m conditions. In contrast, the T_2 and T_1S models predict both normal and inverse contributions to the KIE arising from transition state sites. If the transition states under k_{cat} and k_{cat}/K_m conditions are the same, these inverse effects should also have been expressed on $^{D_2O}k_{cat}/K_m$, which would be expected to lower $^{D_2O}k_{cat}/K_m$ to a value similar to $^{D_2O}k_{cat}$.

***3.3.7 Viscosity effects*:** When performing solvent kinetic isotope effect studies, it is also important to conduct viscosity variation experiments. This is because the relative viscosity of 100% D_2O solutions ($\eta_{rel} = 1.23$) is higher than the relative viscosity of 100% H_2O solutions, defined to be $\eta_{rel} = 1.00$ (*135*). Thus, it is possible that any apparent solvent KIEs are actually due to the variation in solvent viscosity that occurs when H_2O

is replaced with D_2O. Increasing the solvent viscosity lowers the diffusion coefficient of solutes which, in turn, slows the rates of bimolecular association and dissociation processes. In the case of enzyme catalysis, viscosity effects are often manifested on steps in the kinetic mechanism involving substrate/product binding or release, or when large-scale unimolecular enzyme conformational changes occur (*118, 136-141*). To assess the dependence of the IDI-2 catalyzed reaction on solvent viscosity, we analyzed the effects of glycerol concentration on the rate of the reaction under pseudo-first order conditions (Figure 3.8). These results clearly demonstrate that k_{cat} is not limited by product dissociation or large-scale enzyme conformational changes, and are consistent with the results of the rapid-quench experiment, which suggested that product dissociation steps do not limit the rate of DMAPP formation under pseudo-first order conditions. In addition, these results indicate that the $^{D_2O}k_{cat}$ measured in the previous section is a legitimate solvent KIE, and is not the result of increasing the relative viscosity of the solvent.

3.3.8 Multi-wavelength stopped flow studies: In Chapter 2, we demonstrated that a reduced flavin intermediate characterized by absorption maxima at 325 and 435 nm accumulates upon IPP or DMAPP binding. Subsequent biochemical, spectroscopic, and computational studies suggested that this species is likely an anionic reduced flavin. In

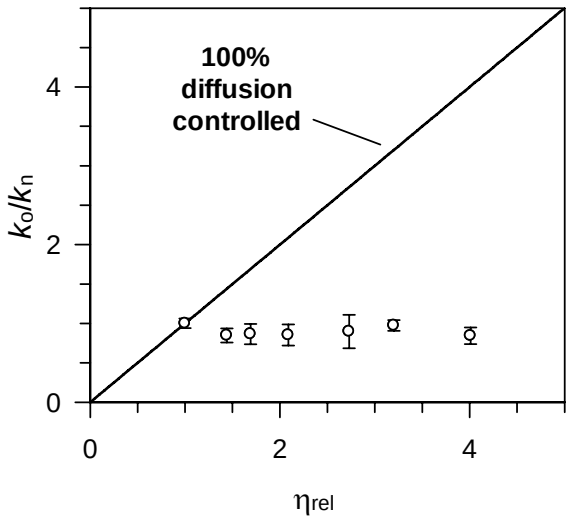

Figure 3.8: Viscosity effects on wt IDI-2 reaction under pseudo-first order conditions. The parameters in this figure are defined by Eqtn 3.1 in the Methods section. The rate of the IDI-2 catalyzed reaction under pseudo-first order conditions appears to be independent of the relative viscosity of the solution. The line depicts the expected dependence of k_o/k_η on η_{rel} for a reaction that is completely diffusion controlled.

order to determine whether this species is relevant to catalysis by IDI-2, we performed single turnover stopped flow studies and followed the time-dependent changes in the flavin absorption spectrum. If the putative FMNH- intermediate species is on the catalytic pathway, then it must form and decay at kinetically competent rates (i.e., at rates $\geq k_{cat}$) under single turnover conditions. In addition to validating the kinetic competence of the intermediate observed in steady state reaction mixtures, the multi-wavelength stopped flow studies could also reveal the presence of transient intermediates that may accumulate in the pre-steady state, but which are not present in significant quantities in the steady state.

As shown in Figure 3.9, the pre-steady state changes in the absorption spectrum of the IDI-2 bound reduced FMN in the forward direction (with IPP as the substrate) and in the reverse direction (with DMAPP as the substrate) are qualitatively similar. Namely, a species consistent with the flavin intermediate observed in the steady state accumulates rapidly in the pre-steady state with both IPP and DMAPP at observed rates of $k_{obs,1}$ = 17 s^{-1} and 33 s^{-1}, respectively. The concentration of this intermediate then approaches an equilibrium level in a slower phase ($k_{obs,2}$ = 1.9 s^{-1} and 2.9 s^{-1} for IPP and DMAPP, respectively) that is kinetically competent in both reaction directions (see Table 3.1). No additional flavin species were observed in these single turnover studies. While it would have been ideal to conduct these single turnover experiments using photoreduced enzyme (in order to assess any transient absorbance changes in the 300 – 400 nm range), we had difficulty preventing O_2 contamination under photoreduced conditions. Nevertheless, these studies demonstrate that a similar kinetically competent flavin intermediate forms in both reaction directions, which suggests that this intermediate is likely important for the interconversion of IPP and DMAPP catalyzed by IDI-2.

The main difference in the pre-steady state time courses of the forward and reverse reactions is that in the forward reaction direction with IPP as the substrate, the flavin intermediate reaches a maximum concentration in the pre-steady state and then decays to an equilibrium level in the slow phase (Figure 3.9C and D). In contrast, in the reverse direction with DMAPP as the substrate, the flavin intermediate still forms rapidly but it does not accumulate to the levels seen in the forward reaction. Following the fast phase, a flavin intermediate with similar absorption properties continues to accumulate in

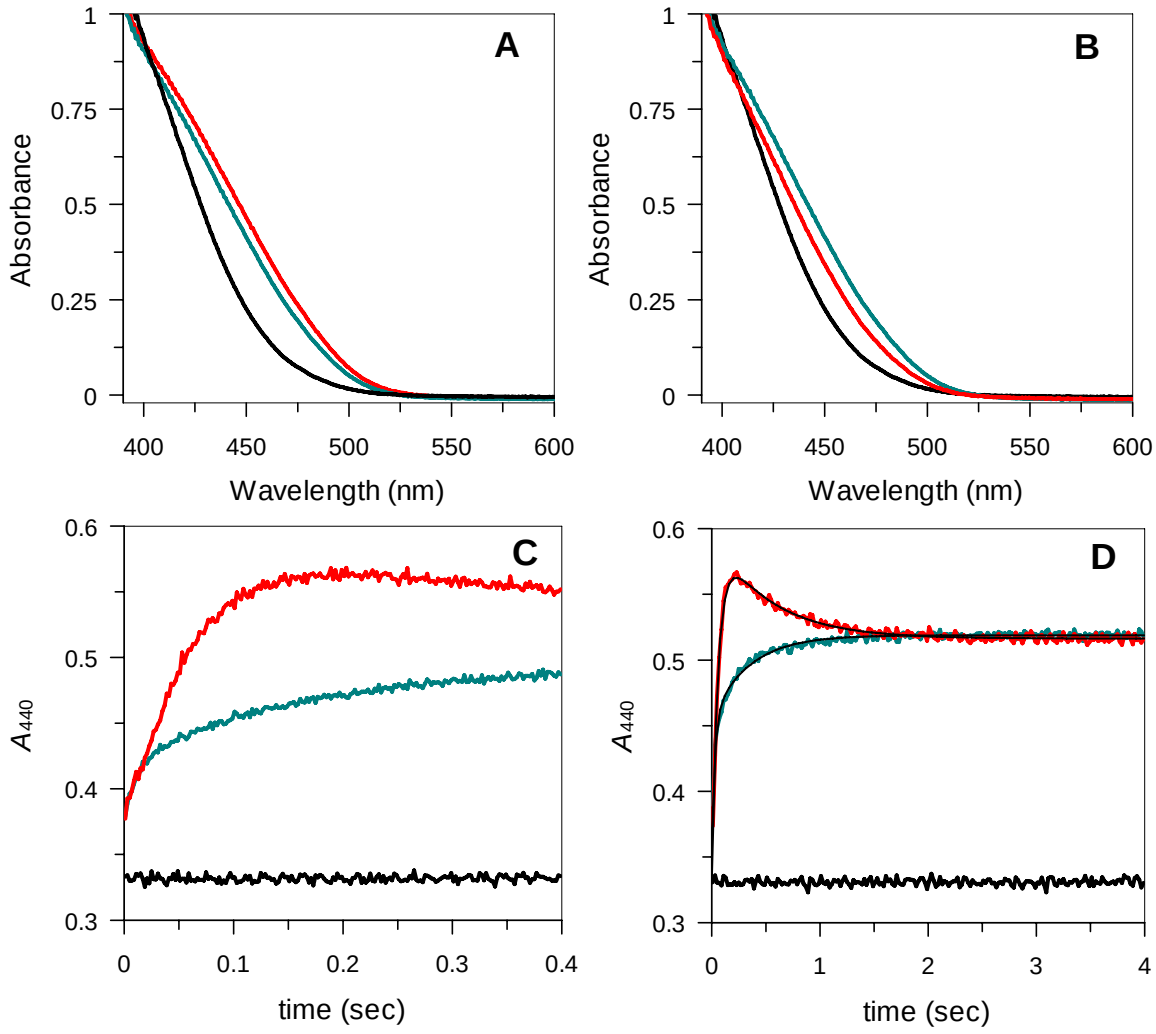

Figure 3.9: Multi-wavelength stopped-flow studies of the forward (A) and reverse (B) reactions under single turnover conditions and time-dependent changes in the absorbance at 440 nm (C and D). In A, the red and teal curves are spectra taken at 0.23 and 4.0 sec, respectively. In B, the red and teal curves are spectra taken at 0.05 and 4.0 sec, respectively. In C and D, the red and teal curves are from reactions with IPP and DMAPP, respectively. In all panels, the black curves are from reactions with no substrate.

the slow phase until equilibrium is reached. A possible explanation for these observations is that two separate enzyme forms with similar absoption properties are

contributing to the spectra. These two enzyme forms could represent ternary complexes between the enzyme, the flavin intermediate, and either IPP or DMAPP. A potential explanation for the differing extents of flavin intermediate accumulation in the forward and reverse directions could be that the relative rates of intermediate formation and decay are different in the forward and reverse reactions. Alternatively, the extinction coefficients of putative IDI-2:$FMN_{intermediate}$:IPP and IDI-2:$FMN_{intermediate}$:DMAPP complexes could be different.

3.3.9 Single-wavelength stopped flow studies: In order to gain more insight into the kinetic mechanism for IDI-2 and to provide initial estimates for rate constants to be used in the global simulations (vide infra), we analyzed the effects of IPP and DMAPP concentration on the rates and amplitudes of the fast and slow pre-steady state kinetic phases. For these studies, we followed the absorbance changes in the flavin chromophore at 440 nm – a wavelength where the flavin intermediate absorbs strongly. The pattern of pre-steady state absorbance changes for the forward and reverse directions are shown over several time scales in Figure 3.10. The equilibrium absorbance levels achieved with identical concentrations of IPP and DMAPP were very similar, suggesting that the concentration of the IPP and DMAPP stock solutions used for the experiment are fairly accurate.

The time courses for the absorbance changes in the forward and reverse reaction directions were fitted with exponential equations in an attempt to extract estimates for the rates and amplitudes of the pre-steady state kinetic phases. The parameter estimates from

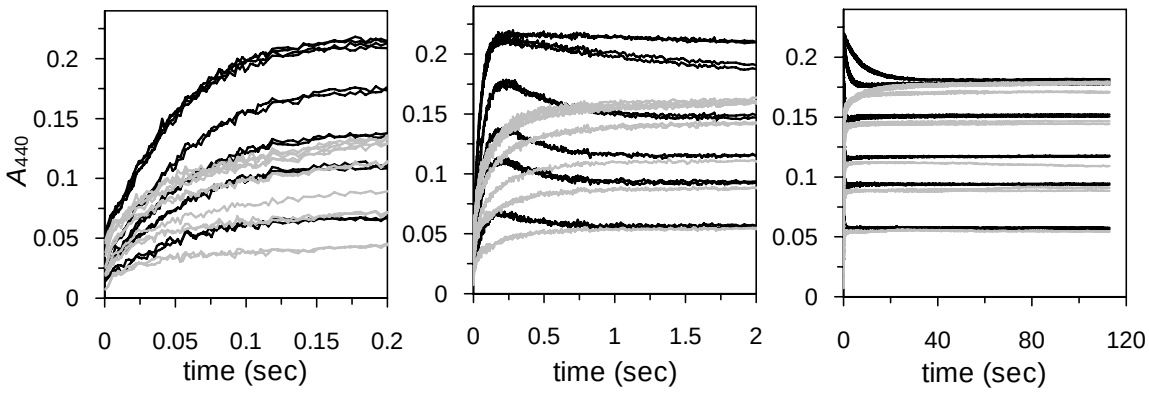

Figure 3.10: Pre-steady state absorbance changes at 440 nm in the presence of variable concentrations of IPP (black curves) or DMAPP (gray curves). The same data are replotted over several different time scales. The enzyme concentration is 75 μM and the concentrations of IPP and DMAPP in each panel are (from bottom to top): 20, 40, 60, 100, 500, and 2000 μM. All other conditions are given in the Methods section. The background absorbance at 440 nm has been subtracted. Note the non-zero absorbance offsets at time = 0 (left panel), the differences in the extent of intermediate accumulation in the forward and reverse directions (middle panel), and the similarity in the equilibrium absorbance values when identical concentrations of IPP or DMAPP are used as the substrate (right panel).

the exponential fits are summarized in Table 3.5 and are graphically illustrated as a function of IPP or DMAPP concentration in Figures 3.12 and 3.14, respectively. The IPP time courses were fit with a double exponential equation (Eqtn 3.15), and the quality of the double exponential fits are illustrated over several time scales for the lowest (20 μM) and highest (2000 μM) concentrations of IPP used in the experiment (Figure 3.11).

Eqtn 3.15:

$$\Delta A_{440} = A_1(1 - e^{-k_{obs,1}t}) + A_2(1 - e^{-k_{obs,2}t}) + C$$

Forward Reaction

[IPP] (μM)	A_1	$k_{obs,1}$ (s^{-1})	A_2	$k_{obs,2}$ (s^{-1})	C
20	.074(1)	15.2(2)	.032(1)	4.7(1)	.0153(3)
40	.143(2)	13.4(2)	.070(2)	4.9(1)	.0199(3)
60	.21(1)	12.4(2)	.11(1)	5.4(1)	.0221(3)
100	.213(3)	13.4(2)	.089(3)	4.0(1)	.026(1)
500	.177(1)	19.9(1)	.0420(2)	.65(1)	.042(1)
2000	.173(1)	20.6(1)	.0380(1)	.135(1)	.046(1)

Reverse Reaction

[DMAPP] (μM)	A_1	$k_{obs,1}$ (s^{-1})	A_2	$k_{obs,2}$ (s^{-1})	A_3	$k_{obs,3}$ (s^{-1})	C
20	.0212(4)	75(3)	.0246(2)	4.6(1)	.0013(1)	.13(2)	.0079(4)
40	.033(1)	59(2)	.0362(3)	4.3(1)	.0019(1)	.15(2)	.019(1)
60	.033(1)	55(3)	.044(2)	6.1(.4)	.012(3)	1.8(2)	.023(1)
100	.043(1)	56(2)	.061(1)	5.1(1)	.011(1)	.63(4)	.029(1)
500	.037(1)	56(2)	.0719(4)	6.1(1)	.0216(2)	.310(4)	.0402(4)
2000	.038(1)	41(2)	.070(1)	5.4(1)	.0211(1)	.108(2)	.049(1)

Table 3.5: Pre-steady state kinetic parameters determined from fits of the absorbance change at 440 nm to either Eqtn 3.15 (for the forward reaction) or Eqtn 3.18 (for the reverse reaction). Standard errors on the parameter estimates are shown in parenthesis.

While lack of fit *F*-tests (*142*) indicated that there is no reason to assume that the double exponential model is incorrect at the 95% confidence interval, clear structure can be seen in the residual plot of the 2 mM IPP time course, suggesting that an additional

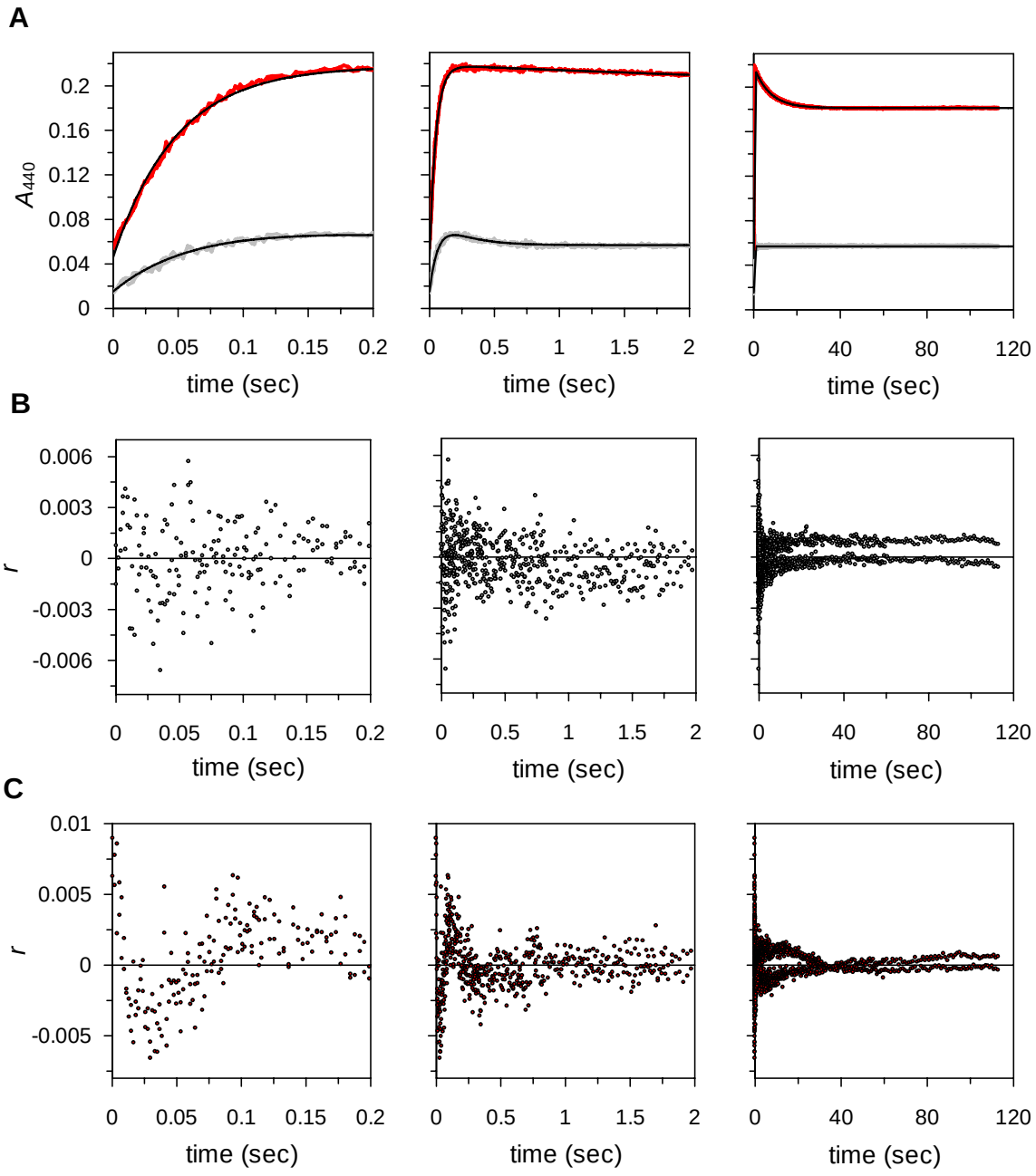

Figure 3.11: Double exponential fits (black lines) of the absorbance changes at 440 nm for the reactions containing 20 (gray) and 2000 μM (red) IPP are shown in A. Residual plots for the 20 and 2000 μM reactions are shown over the same time scales in B and C, respectively.

exponential phase may be required for fitting the time courses for reactions with higher IPP concentrations. However, for the sake of comparison between individual runs, we fit all of the IPP time courses with a double exponential equation. As shown in Figure 3.12, the rate of the fast phase was relatively constant under single turnover conditions ($k_{obs,1}$ ~ 13 s^{-1}) and appeared to saturate at a value of ~ 21 s^{-1} at 2 mM IPP. The fast phase was followed by a slower phase ($k_{obs,2}$ ~ 5 s^{-1}) that is kinetically competent under single turnover conditions (k_{cat} under similar conditions is 0.47 s^{-1}) but which decreases at higher concentrations of IPP to a value of ~ 0.1 s^{-1}. The amplitude changes for the fast and slow phases determined by the exponential fits (A_1 and A_2, respectively) exhibited a complex dependence on IPP concentration where the fitted parameter values for A_1 and A_2 exhibit a biphasic dependence on IPP concentration. However, visual inspection of the time courses in Figure 3.10 clearly suggests that the amplitudes of both the fast and slow phase increase in magnitude and saturate with increasing IPP concentration. This discrepancy in the amplitudes is likely attributable to the non-linear fitting process, and may be due to the similarity in the observed rates of the two kinetic phases and/or to the similar amplitudes of the two kinetic phases. Finally, there was also a significant offset (C in Eqtn 3.15) in the extrapolated A_{440} at t = 0 that saturated as a function of IPP concentration. This phenomenon may represent the rapid formation of a Michaelis complex between IDI-2 and IPP which exhibits only slightly different absorbance properties from the free enzyme form. The dependence of C (in ΔA_{440} units) on IPP concentration was fitted with a quadratic equation (Eqtn 3.16), where K_d is the binding constant for IPP ($K_{d,IPP}$), E_o is the total concentration of IDI-2, A_i and A_f are the offset and

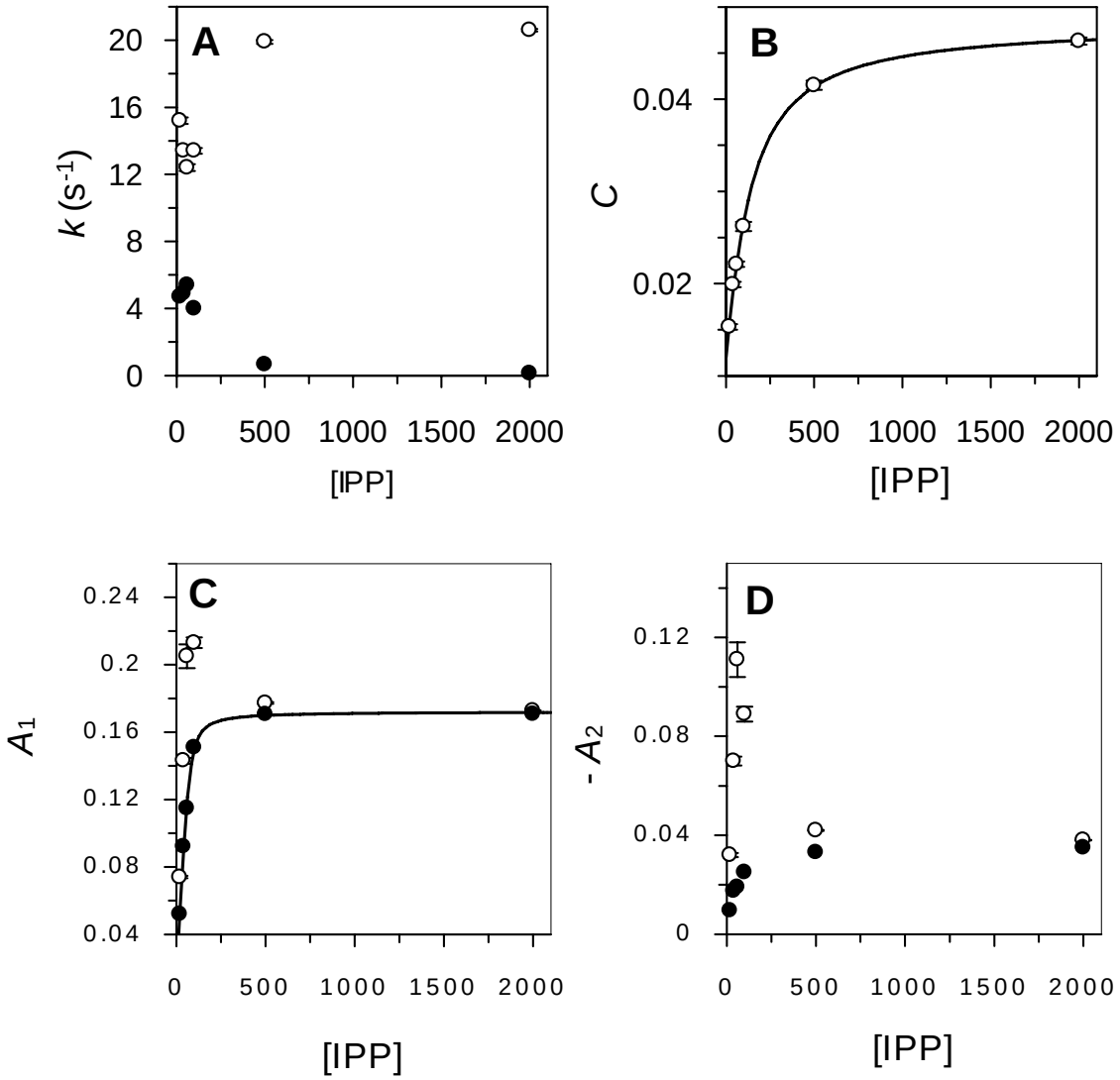

Figure 3.12: Dependence of the fitted parameter estimates on IPP concentration. All IPP concentrations are in μM and amplitudes represent changes in A_{440}. A) Observed rates for the fast ($k_{obs,1}$, open circles) and slow ($k_{obs,2}$, closed circles) phases. B) Dependence of offset, C, on [IPP], fitted to Eqtn 3.16. C and D) The amplitudes for the fast and slow phases (A_1 and A_2, respectively) are plotted as values determined from the non-linear fits (open circles) and as values estimated from visual inspection of the time courses (filled circles). The visually estimated values for A_1 were fit with Eqtn 3.16.

the final absorbance changes at 440 nm, respectively, and S is the IPP concentration. From this fit, we obtained values for the IPP binding constant ($K_{d,IPP}$ = 102 ± 14 μM) and the maximum absorbance change for this phase ($A_i + A_f$ = 0.048 A.U.), the latter of which allowed an estimation of the change in extinction coefficient for the Michaelis complex relative to the free enzyme form ($\Delta\varepsilon_{440}$ = 630 $M^{-1}cm^{-1}$). The enzyme concentration had to be held contant in order to get fits to Eqtn 16 that converged. However, as suggested below by the fits of the fast phase amplitude (A_1) to Eqtn 3.16, the nominal value of E_o in our experiments (75 μM) seems to be fairly accurate.

Eqtn 3.16:

$$\Delta A_{440} = A_i + A_f \left[\frac{(E_o + S + K_d) - \left[(E_o + S + K_d)^2 - 4E_oS \right]^{1/2}}{2E_o} \right]$$

Because the concentration of the flavin intermediate appeared to reach a saturation level in the fast phase of the reaction with IPP, we decided to use this amplitude data to estimate an extinction coefficient for the flavin intermediate. The amplitude of the fast phase (A_1) was estimated from visual inspection of the time courses (plotted as the filled circles in Figure 3.12) and was fit versus IPP concentration to Eqtn 3.16. The A_1 values used in the fit were corrected by subtracting the absorbance offsets (C) obtained from the double exponential fits of the time courses. The $K_{d,app,IPP}$ for formation of the flavin intermediate determined by this fit (7 ± 2 μM) is within error of the $K_{m,IPP}$ value measured in the steady state kinetic analysis (9 ± 1 μM), and the total

enzyme concentration estimated by the fit (71 ± 9 μM) is within error of the IDI-2 concentration determined by the Bradford assay (75 μM). The change in extinction coefficient at 440 nm upon flavin intermediate formation was calculated from A_f (0.16 ± 0.009) to be $\Delta\varepsilon_{440}$ = 2100 $M^{-1}cm^{-1}$. It should be noted that this extinction coefficient is within the range expected for a reduced flavin species (*94*). The accuracy of this number depends on what fraction of the enzyme accumulates the flavin intermediate in the pre-steady state with IPP, and is assumed to be 100% at 2 mM IPP.

From the $K_{d,IPP}$ determined by fitting of the offset data to the quadratic ($K_{d,IPP}$ ~ 100 μM) and the $K_{d,app,IPP}$ determined by fitting the A_1 data with the quadratic ($K_{d,app,IPP}$ ~ 7 μM), estimates can be obtained for the equilibrium constants for the putative two-step binding mechanism that leads to formation of the flavin intermediate (Scheme 3.3). In this scheme, E represents the free enzyme, S represents IPP, ES represents the Michaelis complex that forms in the dead time of the stopped flow ($\Delta\varepsilon_{440}$ ~ 630 $M^{-1}cm^{-1}$), FS represents the flavin intermediate that accumulates in the fast phase of the forward reaction ($\Delta\varepsilon_{440}$ ~ 2100 $M^{-1}cm^{-1}$), and K_1 and K_2 are the associated equilibrium constants for this binding process. Assuming that $K_1 = 1/K_{d,IPP}$, $K_{d,app,IPP}$ can be used to calculate K_2 ~ 13 by Eqtn 3.17:

Eqtn 3.17:

$$K_{d,app,IPP} = 1/[K_1(1+K_2)]$$

These estimates indicate that, while binding of IPP to IDI-2 to form the Michaelis complex (ES) may have a relatively unfavorable equilibrium constant ($K_1 \sim 0.01\ \mu M^{-1}$), a favorable forward equilibrium constant ($K_2 \sim 13$) may be helping to pull the ES complex to the FS complex, lowering the net K_d from ~ 100 μM to ~ 7 μM.

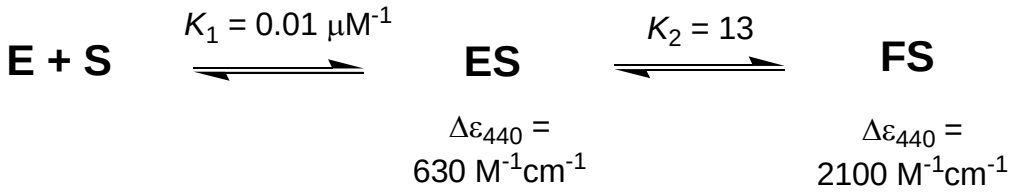

Scheme 3.3: A putative two-step binding model for IPP.

Fits of the time courses for reactions containing 20 μM and 2 mM DMAPP to a triple exponential equation (Eqtn 3.18) are shown over several time scales in Figure 3.13. The DMAPP time courses were fit to a model with an additional exponential term because lack of fit *F*-tests performed on fits to Eqtn 3.15 yielded significant *F*-values at the 95% confidence interval, indicating that the double exponential model is inadequate (data not shown).

Eqtn 3.18:

$$\Delta A_{440} = A_1(1 - e^{-k_{obs,1}t}) + A_2(1 - e^{-k_{obs,2}t}) + A_3(1 - e^{-k_{obs,3}t}) + C$$

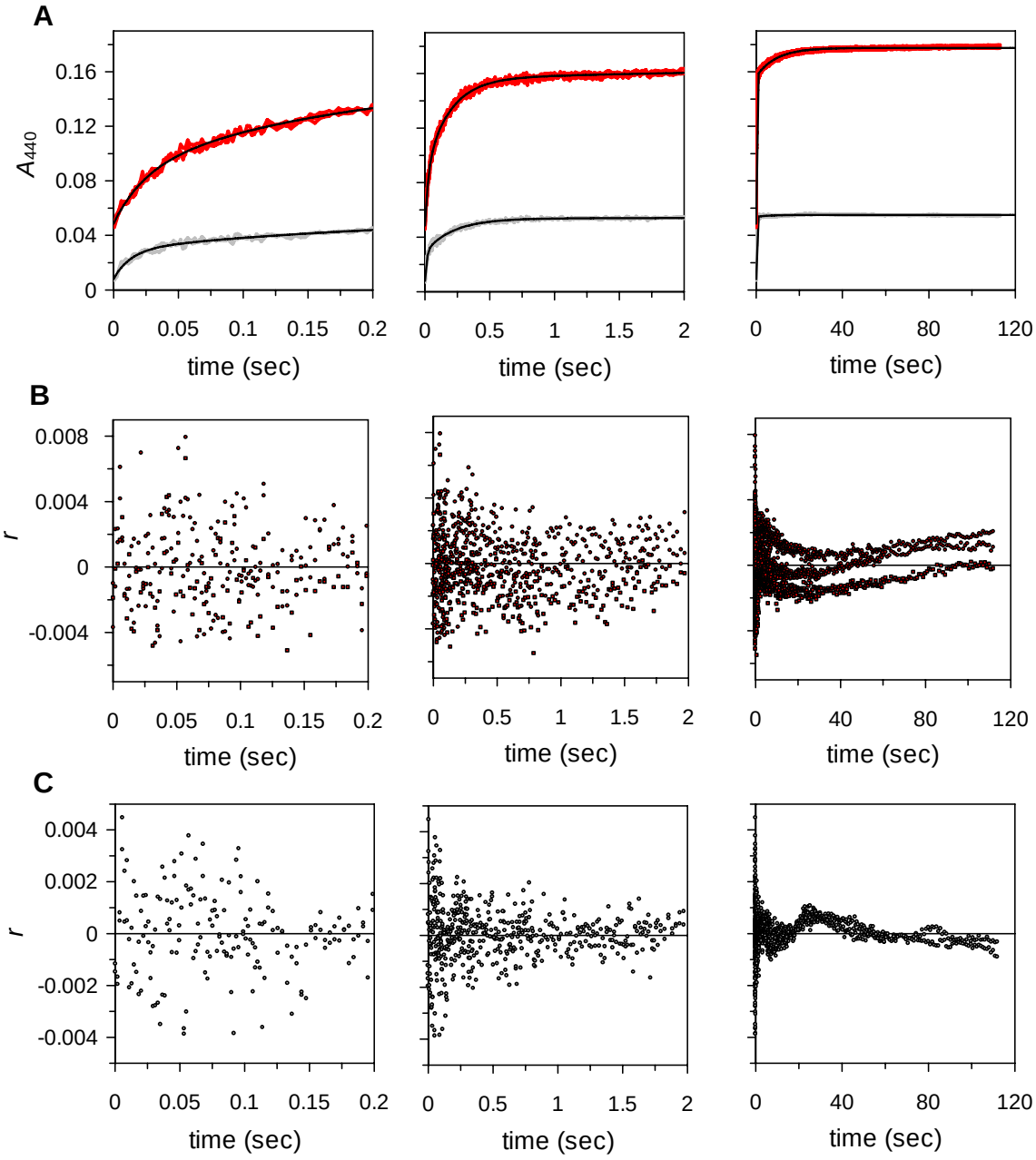

Figure 3.13: Triple exponential fits (black lines) of the absorbance changes at 440 nm for the reactions containing 20 (gray) and 2000 μM (red) DMAPP are shown in A. Residual plots for the 20 and 2000 μM reactions are shown over the same time scales in B and C, respectively.

The dependence of the fitted parameter values on DMAPP concentration is shown in Table 3.5 and in Figure 3.14. These data suggest that both $k_{obs,1}$ (~ 60 s^{-1}) and $k_{obs,2}$ (~ 5 s^{-1}) are relatively independent of DMAPP concentration and are both > k_{cat} in the reverse direction (~ 0.19 s^{-1}), while $k_{obs,3}$ exhibits a biphasic dependence on DMAPP concentration. Because $k_{obs,3}$ is not kinetically competent under all of the single turnover conditions tested, it is not clear whetheher this phase is relevant to catalysis. It is also possible that the small amplitude changes associated with A_3 at low DMAPP concentrations prevent accurate determinations of $k_{obs,3}$ by non-linear regression. The fitted amplitude change for each phase appears to saturate as a function of DMAPP concentration. As was observed in the forward reaction with IPP, there was a significant non-zero absorbance offset at t = 0 in the reverse direction that appeared to saturate as a function of DMAPP concentration. Thus, DMAPP may also rapidly form a Michealis complex with IDI-2 in which the bound FMN exhibits similar but slightly different absorbance properties than the free enzyme form. This data could not be fit with the quadratic equation without obtaining unreasonable standard error estimates on the fitted parameters, but fitting to a hyperbola yielded estimates for an apparent DMAPP binding constant (74 ± 9 μM) and the maximum absorbance change (0.049 ± 0.002 A.U.). This latter parameter allowed the extinction coefficient for the putative Michaelis complex between IDI-2 and DMAPP to be estimated ($\Delta\varepsilon_{440}$ = 650 $M^{-1}cm^{-1}$), assuming that the Michaelis complex is fully saturated at 2 mM DMAPP.

Finally, the changes in the pre-steady state absorbance of the flavin intermediate were also investigated under single turnover conditions in the presence of (*R*)-[2-^{2}H]-IPP

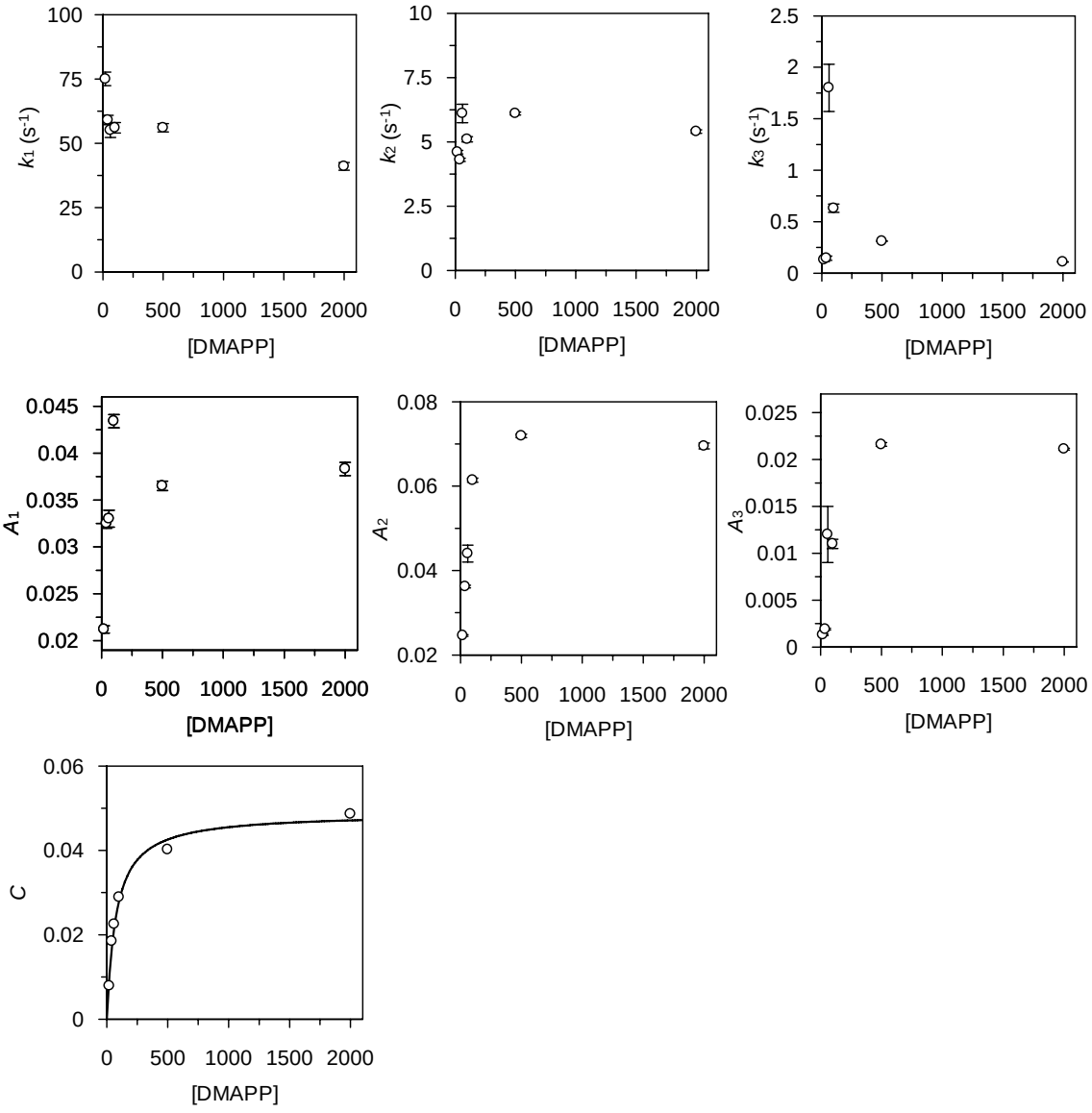

Figure 3.14: Dependence of fitted parameter estimates on DMAPP concentration. The offset (*C*) data were fitted to a hyperbola.

(Figure 3.15). When compared with the time course obtained in the reaction with IPP (under otherwise identical reaction conditions), it is clear that the amplitude of the fast phase gets larger and the rate of the slow phase decreases with (*R*)-[2-^{2}H]-IPP as the

substrate. The reactions with the two different substrates reach similar equilibrium absorbance levels, once again suggesting that the nominal concentrations of our substrate stock solutions appear to be accurate. Fitting of the (*R*)-[2-^{2}H]-IPP time courses to a double exponential equation (Eqtn 3.15) yielded values for $k_{obs,1}$ and $k_{obs,2}$ of 13.2 ± 0.1 and 0.95 ± 0.01, respectively. Under these single turnover conditions, $k_{obs,2}$ is greater than k_{cat} (0.69 s^{-1}, calculated from the data in Figure 3.4), suggesting that the flavin intermediate that forms in the (*R*)-[2-^{2}H]-IPP is also kinetically competent. These data allowed the calculation of apparent KIEs on the fast and slow rates to be $^{D}k_{obs,1}$ = 0.94 and $^{D}k_{obs,2}$ = 5.7, respectively (using the $k_{obs,1}$ and $k_{obs,2}$ parameters from the reaction with 60 μM IPP reported in Table 3.5).

The KIE of near unity on the fast phase rate suggests that formation of the flavin intermediate in the pre-steady state does not involve cleavage of the C2-H/D bond of IPP. This observation is consistent with a fast phase governed by IPP binding steps and/or enzyme conformational changes, rather than steps involving isomerization chemistry. In contrast, the decay of the flavin intermediate that accumulates in the fast phase to its equilibrium level seems to involve a step where the C2-H/D bond is cleaved, as the magnitude of the KIE on the slow phase (5.7) is clearly indicative of a primary substrate deuterium KIE on at least one of the microscopic rate constants that governs flavin intermediate decay under single turnover conditions. The increased magnitude of the KIE measured on $k_{obs,2}$ (5.7) relative to the KIE measured on k_{cat} in the forward reaction (2.2) suggests that other steps in the kinetic mechanism (that are not sensitive to the

presence of D at C2 of IPP) may be involved in lowering the observed KIE under steady state turnover conditions.

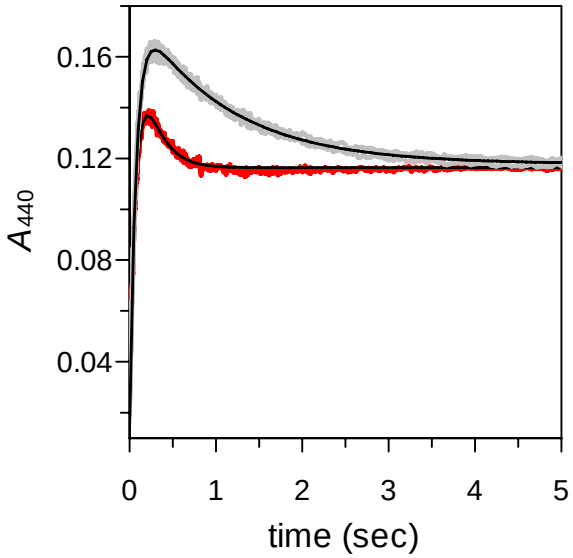

Figure 3.15: Comparison of the single turnover time courses for reactions with IPP (red) and (R)-[2-^{2}H]-IPP (gray). Reactions contained 75 μM IDI-2 and 60 μM substrate. All other reaction conditions are reported in the Methods section and were identical to those used for the data in Figures 3.10, 3.11, and 3.13.

3.4 Conclusions and Mechanistic Implications

3.4.1 Summary of kinetic data: The steady and pre-steady state kinetic studies described in this chapter have provided several key insights into the nature of the IDI-2 catalyzed reaction, and have helped to better define the intermediates involved in the reaction pathway, the sequence of events leading to turnover, and the factors that govern catalysis. The rapid-mix chemical quench studies indicate that a step in the forward reaction direction (IPP → DMAPP) prior to the formation of DMAPP in the active site limits

steady state turnover, because no pre-steady state burst in DMAPP formation was observed. Second, substrate kinetic isotope effect studies suggest that the rate-limiting step involves cleavage of the C2-H/D bond of IPP. Combined with the rapid quench data, this result indicates that the step (or steps) involving the isomerization of the IPP double bond are at least partially rate limiting under steady state conditions. Furthermore, solvent deuterium exerted significant isotope effects on the steady state kinetic parameters, suggesting that the transfer of solvent exchangeable protons also plays an important role in the rate-limiting step(s). Viscosity variation experiments show that the observed solvent KIE is not due to the increase in the relative viscosity of buffer containing D_2O, and provide further evidence that DMAPP dissociation from the enzyme does not limit steady state turnover in the forward direction. The normal solvent and substrate kinetic isotope effects measured in our studies suggest that acid/base chemistry involving proton transfers to and from IPP may be rate-limiting. However, we were unable to detect any significant effects on k_{cat} for the IDI-2 reaction when the pH was varied from 6.0 – 10.0. Because of this, we were unable to provide definitive kinetic evidence for general acid/base catalysis in the IDI-2 catalyzed reaction. The pH-independence of k_{cat} does not rule out an acid/base chemical mechanism, but instead suggests that there are no ionizations in the catalytically competent Michaelis complex over the pH range assayed that are detrimental to catalysis. Nevertheless, these studies still provide strong evidence that isomerization chemistry is at least partially rate-limiting to IDI-2 catalysis.

Site-directed mutagenesis studies have provided insight into the putative roles of several active site amino acids and, when analyzed in terms of the available X-ray crystal structures, indirectly suggest that the reduced FMN plays a direct role in catalysis. Our steady state kinetic studies of these mutant enzymes indicate that His149 and Lys186 play important roles in IPP binding, but are relatively expendable in terms of their effects on k_{cat}. This result is consistent with the available structural information, which shows that H149 and K186 likely function to bind the Mg^{2+} ion complexed to the pyrophosphate moiety of IPP and the N_1 atom of FMNH-, respectively, but neither H149 nor K186 appears to be within reach of the the carbon atoms of the substrate where proton transfers occur. In contrast, the T67A and Q154N mutations led to significant reductions in k_{cat}, but to only modest alterations in $K_{m,IPP}$, suggesting that these residues are somehow important for stabilizing the rate-limiting transition state(s) of the IDI-2 catalyzed reaction. The crystal structure shows that Gln154 and Thr67 are located on opposite sides of the bound substrate molecule, with Gln154 positioned close to the C4 carbon of IPP/DMAPP, where it could function in the delivery or removal of protons during turnover. This putative catalytic function is underscored by preliminary studies with the Q154A mutant, whose activity is severely reduced. While the hydroxyl side chain of Thr67 is not in direct contact with IPP, it is positioned adjacent to the Met66 rediue (within a conserved MTGG motif) that appears to hydrogen bond with the N5 atom of the FMN. The N5 atom is, in turn, only ~ 3 Å away from the C2 atom of IPP/DMAPP, and is positioned appropriately for abstraction of the *pro R* C2-H of IPP. Our hypothesis is that mutation of T67 leads to a structural distortion of the MTGG motif that alters the

interactions between Met66 and the N5 atom of the flavin, and that the altered electronic environment of the N5 atom is somehow detrimental to catalysis. Importantly, other than the flavin and the amide side chain of Gln154, there do not appear to be any other groups in the direct vicinity of the substrate that would be capable of transferring protons to and from IPP/DMAPP during catalysis.

Additional insights into the mechanism of the IDI-2 catalyzed reaction are provided by pre-steady state stopped-flow studies. The time-dependent changes in the absorption spectrum of IDI-2 under single turnover conditions revealed that a single flavin species (or a mixture of enzyme forms bound to flavin species with similar absorption properties) accumulates and approaches an equilibrium level at observed rates that are kinetically competent. This result suggests that the flavin intermediate could be on the reaction pathway leading to IPP/DMAPP isomerization. Our biochemical, spectroscopic, and computational studies performed in Chapter 2 suggest that this flavin intermediate is likely an anionic, reduced FMN (FMNH-), whose isoalloxazing ring structure becomes shielded from solvent and structurally distorted from its planar resting state conformation upon IPP/DMAPP binding.

The dependence of the formation and decay kinetics of the flavin intermediate on IPP and DMAPP concentration were also studied with single wavelength stopped flow studies. These data indicated that both the forward and reverse directions are at least biphasic (and possibly triphasic) and are characterized by a rapid increase in the levels of the flavin intermediate, followed by a slower approach to an equilibrium level. Fitting of the time courses to exponential equations suggested that there was a significant non-zero

absorbance offset at time = 0 in both reaction directions that saturated as a function of IPP/DMAPP concentration. This absorbance change is attributed to the rapid formation of Michaelis complexes between IDI-2:FMNH- and both IPP and DMAPP within the mixing dead time of the stopped flow and prior to the accumulation of the flavin intermediate. These putative Michaelis complexes appear to share very similar absorbance properties with the IDI-2:FMNH- resting state. Single-turnover studies with the (*R*)-[2-^{2}H]-IPP analogue show that the rate of the fast phase of flavin intermediate accumulation is unaffected by the isotopic substitution at C2 of IPP, whereas the rate of the slow phase was significantly reduced. These observations, in combination with the rapid quench and steady state substrate kinetic isotope effect studies, suggest that in the forward direction, the flavin intermediate accumulates prior to a partially rate determining chemistry step that involves IPP C2-H/D bond cleavage. In conjunction with the kinetic competence of the flavin intermediate (with both IPP and (R)-[2-^{2}H]-IPP), these data imply that the flavin intermediate may play a direct and important role in the 1,3-allylic isomerization of the IPP double bond.

3.4.2 A minimal kinetic mechanism for IDI-2: With this data in hand, a minimal kinetic mechanism can be proposed for IDI-2 catalysis (Scheme 3.4). In the resting state, the free enzyme form (E) has FMNH- bound in the active site. As suggested by our DFT calculations in Chapter 2, the FMNH- bound to the reduced IDI-2:FMN complex may have a relatively planar conformation, and could be exposed to solvent. Upon IPP (S) binding, a Michaelis complex (ES) forms. As suggested by the slight increase in ε_{440} in

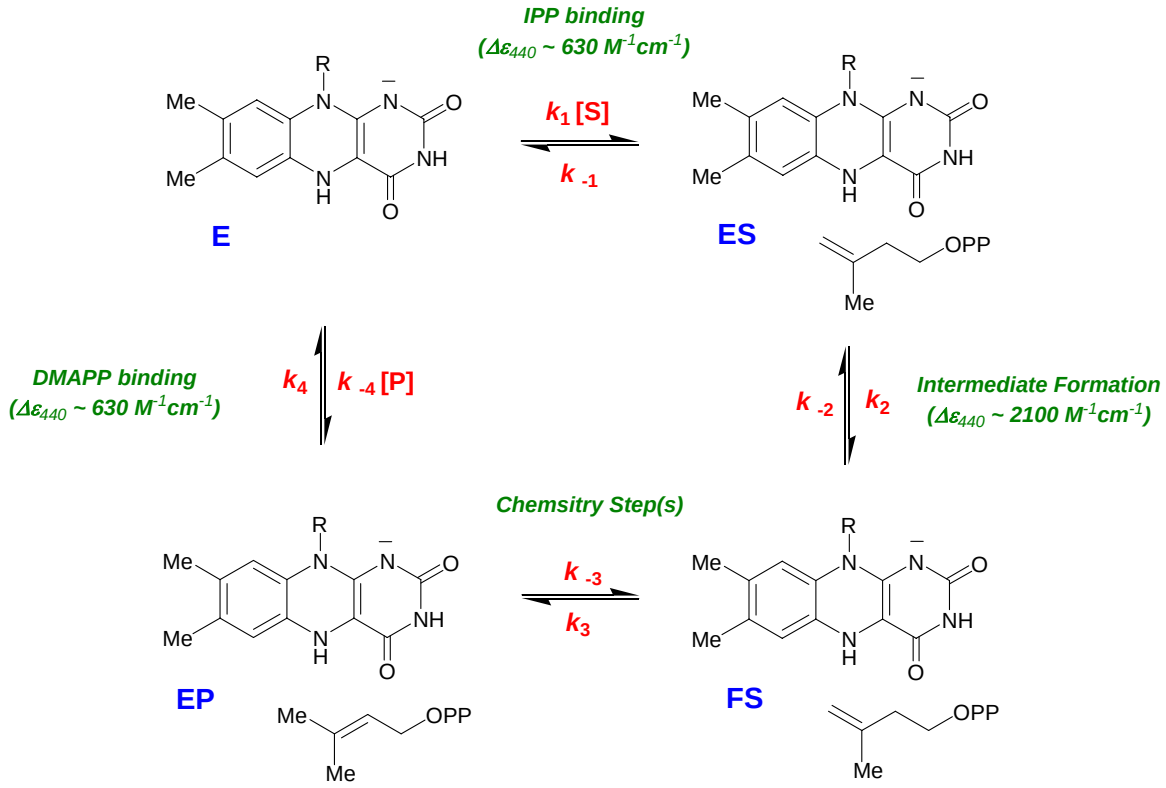

Scheme 3.4: Proposed minimal kinetic mechanism for the IDI-2 catalyzed conversion between IPP and DMAPP.

the single wavelength stopped-flow studies and the lack of any detectable shifts in the λ_{max} of the flavin in the multi-wavelength stopped-flow studies, the flavin bound to the ES complex seems to have similar absorbance properties as the free enzyme and, thus, may also be a planar, solvent-exposed FMNH- species. Following IPP binding, the ES complex is converted to the FS complex. During this step, the absorbance of the reduced flavin is altered as described in Chapter 2, leading to large changes in ε_{440} that may be the result of active site desolvation, bending of the FMNH- molecule, and/or π-stacking between IPP and the flavin. This step is tentatively assigned as a conformational change,

where the *N*-terminal region of IDI-2 folds into the closed conformation observed in the crystal structure. A chemistry step involving isomerization of the IPP double bond then converts the FS complex to the EP complex. In this minimal model, the EP complex represents the Michaelis complex between IDI-2 and DMAPP. The flavin in the EP complex is assumed to exhibit similar absorption properties as the ES complex. DMAPP dissociation from the EP complex then completes the catalytic cycle and regenerates the resting form of the enzyme (E).

To assess the feasibility of this minimal kinetic model, we globally simulated the pre-steady state absorbance changes in the forward and reverse reaction directions (i.e., the data in Figure 3.10) using KinTek Global Kinetic Explorer. The concentrations of IPP, DMAPP, and IDI-2 used in the global fits were unaltered from the nominal values reported in the context of the stopped-flow studies. The output function used to simulate the changes in absorbance at 440 nm is shown in Eqtn 3.19:

Eqtn 3.19:

$$\Delta A_{440} = f_1(ES + EP) + f_2(FS)$$

Here, ES, EP, and FS represent the concentrations of the enzyme forms shown in Scheme 3.4, and f_1 and f_2 represent the $\Delta\varepsilon_{440}$ values for these complexes that were estimated from the pre-steady state stopped-flow data. For starting parameter estimates, the equilibrium contants for the IPP and DMAPP binding steps (K_1 and $1/K_4$, respectively) were set to a value of 0.01, and the magnitude of the microscopic rate constants (k_1, k_{-1}, k_4, and k_{-4})

were increased until the absorbance change associated with this phase was complete within 1.5 msec. The other rate constants in the pathway were adjusted to produce progress curves that were similar in appearance to the raw data. During this process, we were careful to keep the overall equilibrium constant ($K_{eq} = K_1K_2K_3K_4$) similar to its experimentally-determined value (1.2). The initial estimates for the extinction coefficients in the output function (f_1 and f_2) were set to values of 0.0021 $\mu M^{-1}cm^{-1}$ and 0.0006 $\mu M^{-1}cm^{-1}$, respectively, in accordance with the values estimated from the pre-steady state kinetic data. During the initial global fitting process, all of the rate constants and the two extinction coefficients were allowed to vary. Following the initial fit, K_1 and K_4 were held in the fixed ratios suggested by the initial fit and the data were re-fit with all other parameters being allowed to vary.

The best fit values of the variable parameters for the minial mechanism are shown in Scheme 3.4 and in Table 3.6, along with the standard error estimates on the best fit value, the upper and lower bounds of each parameter, and the overall statistics of the global fit. The simulated curves are shown along with the experimental data in Figure 3.16. As can be seen, the simulated curves seem to reproduce most of the salient features of the stopped-flow data. However, among the variable parameters, the K_1 ratio was unbounded on its upper end, and all of the other variable parameters were free to adopt a fairly significant range of values (see the upper and lower bounds in Table 3.6), suggesting that the model is not very well constrained by the data that was simulated. The relatively large error boundaries calculated for the rate constants may be due to the

close similarity between the magnitudes of the individual rate constants in the

Parameter	Best Fit Value	s_e	Lower Bound	Upper Bound
k_1 ($\mu M^{-1}s^{-1}$)‡	2.5	0.5	0.45	*
k_{-1} (s^{-1})‡	39	7	-	-
k_2 (s^{-1})	9.6	0.6	3.32	15.8
k_{-2} (s^{-1})	3.2	0.4	0.923	10.7
k_3 (s^{-1})	3.8	0.2	2.62	6.37
k_{-3} (s^{-1})	2.8	0.1	1.62	3.25
k_4 (s^{-1})‡	14	0.2	6.68	29.5
k_{-4} ($\mu M^{-1}s^{-1}$)‡	2.6	0.4	-	-
f_1 ($M^{-1}cm^{-1}$)	820	30	670	911
f_2 ($M^{-1}cm^{-1}$)	4800	200	3970	12200

Table 3.6: Parameter estimates from global simulations of the pre-steady state absorbance changes at 440 nm to the model shown in Scheme 3.4. Statistics of the fit: N = 3602, d_f = 3592, χ^2 = 0.209, χ^2/d_f = 5.82 x 10^{-5}, σ = 0.0076, where N is the number of data points, d_f are the degrees of freedom, χ^2/d_f is the mean square residual of the fit, and σ is the standard deviation of the fit. ‡ The ratios (k_1/k_{-1} and k_4/k_{-4}) were held fixed during the fit. * The K_1 ratio was unbounded on its upper limit.

mechanism, a case in which none of the rate constants would dominate the appearance of the progress curves. At the present time, the parameters shown in Scheme 3.4 and Table 3.6 should only be considered estimates, and additional model refinement will be needed before a more definitive statement on the validiy of our model can be made. It should also be noted that we could obtain global fits of the stopped flow data to more

complicated models. In these cases however, most of the variable parameters were unbounded, so these fits are not presented.

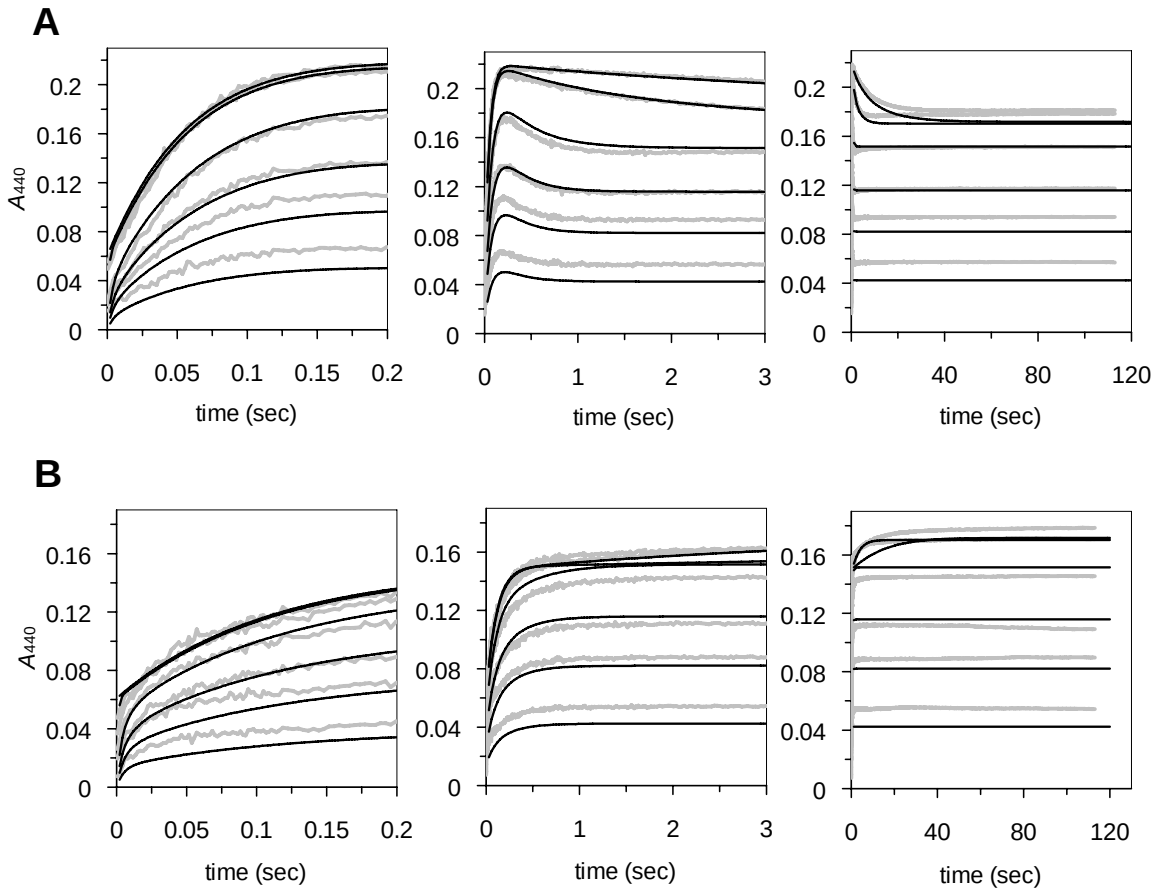

Figure 3.16: Comparison of simulated absorbance changes at 440 nm to the experimental progress curves in the forward direction (panel A) and the reverse direction (panel B). The quality of the simulations are shown over several different time scales.

Nevertheless, the fitted parameter values of the minimal model seem to be consistent with several of our experimental measurements. First, the K_{eq} calculated from the simulated rate constants (1.4) is very similar to the experimentally determined K_{eq} (1.2). Second, the step (k_3) involving the conversion of IPP to DMAPP is the slowest

step in the forward direction, which is consistent with the lack of a pre-steady state burst and the expression of a kinetic isotope effect on k_{cat}. Also, for the mechanism shown in Scheme 3.4, the expressions for k_{cat} and k_{cat}/K_m can be derived (Eqtn 3.20 and 3.21, respectively). When the simulated kinetic constants are substituted into these equations, the calculated steady state kinetic parameters (k_{cat} = 1.7 s^{-1}, K_m = 6 μM, and k_{cat}/K_m = 2.7 x 10^5 $M^{-1}s^{-1}$) are in reasonable agreement with the experimentally-determined parameters (k_{cat} = 0.47 s^{-1}, K_m = 9 μM, and k_{cat}/K_m = 5.4 x 10^4 $M^{-1}s^{-1}$).

Eqtn 3.20:

$$k_{cat} = (k_2k_3k_4)/(k_{-2}k_4 + k_{-2}k_{-3} + k_3k_4 + k_2k_4 + k_2k_{-3} + k_2k_3)$$

Eqtn 3.21:

$$k_{cat}/K_m = (k_1k_2k_3k_4)/(k_{-1}k_{-2}k_4 + k_{-1}k_{-2}k_{-3} + k_{-1}k_3k_4 + k_2k_3k_4)$$

Finally, using the parameter estimates from the simulated minimal mechanism, we used the single turnover stopped flow data obtained from the (*R*)-[2-^{2}H]-IPP experiment to estimate the intrinsic kinetic isotope effect on C2-H/D abstraction, which is assumed to be step k_3 in our minimal mechanism (Scheme 3.4). For this estimation, we assumed that there was no equilibrium isotope effect on step 3 (i.e., $K_3 = k_3^H/k_{-3}^H = k_3^D/k_{-3}^D$), and that none of the other steps in the kinetic mechanism were affected by isotopic substitution at C2 of the substrate. Under these assumptions, we varied the magnitude of k_3 (holding the k_3/k_{-3} ratio constant) until the simulated time course approximated the experimental time

course (Figure 3.17). Based on this rough estimation, the intrinsic deuterium KIE on k_3 was calculated to be ${}^{D}k_3 = 3.8/0.93 = 4.1$ and ${}^{D}k_{cat}$ was calculated to be 2.9 using Eqtn 3.20. This latter parameter is similar to the experimentally measured ${}^{D}k_{cat} = 2.2$ and, as expected, the magnitude of ${}^{D}k_{cat}$ is lower than the intrinsic isotope effect on the C2-H/D bond cleavage step (${}^{D}k_3$), indicating that the other steps in the kinetic mechanism (which appear to be similar in magnitude to the isotope-sensitive step – see Table 3.6) alter the expression of the isotope effect on k_{cat}.

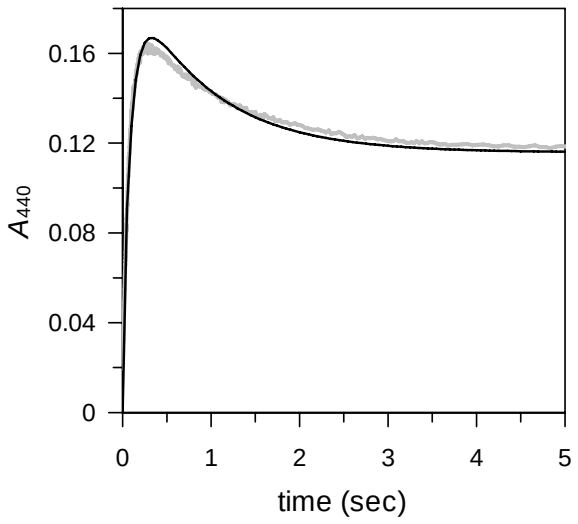

Figure 3.17: Simulation of single turnover stopped flow data for the (*R*)-[2-^{2}H]-IPP reaction. The raw data is shown by the gray curve and the simulated data is shown by the black curve.

3.4.3 Outlook: The data presented in this and the previous chapter have helped to define the nature of the chemical mechanism for IDI-2. These results have helped to identify steps that limit steady state turnover, clarify the order of events leading to the conversion

of IPP and DMAPP, and have provided correlations between spectroscopically observable flavin species and steps in the chemical mechanism. However, on the basis of this data, the exact function of the flavin in the chemical mechanism is still unclear. In the following chapter, a series of flavin analogues will be synthesized and these compounds will be used to perturb the kinetics of the IDI-2 catalyzed reaction. These studies will help to illuminate the relationship between the electronic properties of the flavin and the rates of the steps that limit IDI-2 catalysis, and will enable an evaluation of putative roles for the flavin in the 1,3-allylic isomerization of IPP and DMAPP (see Scheme 1.15).

Chapter 4: Probing the Function of the FMN Coenzyme in IDI-2 Catalysis using Flavin Analogues

4.1 Introduction

The spectroscopic and kinetic studies presented in the previous two chapters have helped to define key elements of the IDI-2 catalyzed reaction. Most notably, they have helped to identify a kinetically competent flavin intermediate (most likely an anionic, reduced FMNH- species) that forms upon IPP or DMAPP binding and have demonstrated that steps in the kinetic mechanism involving isomerization of the IPP double bond likely contribute to the steady state rate limitation. In addition, solvent kinetic isotope effect studies suggest that IPP protonation/deptronation events could be occurring in the rate-limiting steps. However, these experiments have not yet addressed one of the most interesting questions regarding IDI-2 catalysis. Namely, what role does the reduced flavin coenzyme play in the isomerization step(s) and does the flavin participate directly in acid/base catalysis? To address these questions, we reasoned that if isomerization chemistry limits turnover by IDI-2 and if the flavin plays a direct role in this process, then the steady (and pre-steady) state kinetic parameters of the IDI-2 catalyzed reaction should be sensitive to the electronic properties of the flavin. Thus, in this chapter, a series of flavin analogues with modified electronic properties were synthesized, and their effects on the kinetics of IDI-2 catalysis were evaluated. This data, when analyzed in terms of the mechanistic data presented in Chapters 2 and 3, and the results from

investigations by other research groups, are used to refine our model for IDI-2 catalysis and to exclude several of the putative chemical mechanisms presented in Chapter 1.

4.2 Methods

4.2.1 Chemoenzymatic synthesis of flavin analogues: The FMN analogues employed in this study were chemoenzymatically synthesized according to Scheme 4.1. The riboflavin versions of each analogue (compound **1**) were chemically synthesized by Wei-chen Chang (a graduate student in our lab) starting from D-ribose and commercially available compound **2**. The riboflavin analogues were then converted to their corresponding FAD forms (**3**) by FAD synthetase from *Corynebacterium ammoniagenes* as described previously with slight modifications (*56, 84*). A typical 500 mL reaction contained ~ 15 mg of riboflavin analogue, 500 mg ATP, 960 mg $MgCl_2$, and 18.1 mg of FAD synthetase in 30 mM potassium phosphate buffer, pH 7.5. The reaction was incubated overnight at 37 ˚C with shaking. The 500 mL reaction was filtered using a YM-10 membrane (Millipore Corp., Bedford, MA.) to remove the FAD synthetase and was concentrated and lyophilized. The FAD analogues were purified by P2 size exclusion chromatography using water as the eluent, followed by reverse-phase high performance liquid chromatography (RP-HPLC) using an Econosil C18 10u semiprep column (Alltech, Deerfield, IL.) and a gradient elution. Following injection, the column was washed for 5 min with 95% buffer A (5 mM NH_4HCO_3, pH 7.0) and 5% buffer B (MeOH). The concentration of MeOH was then increased to 100% over 20 min. The

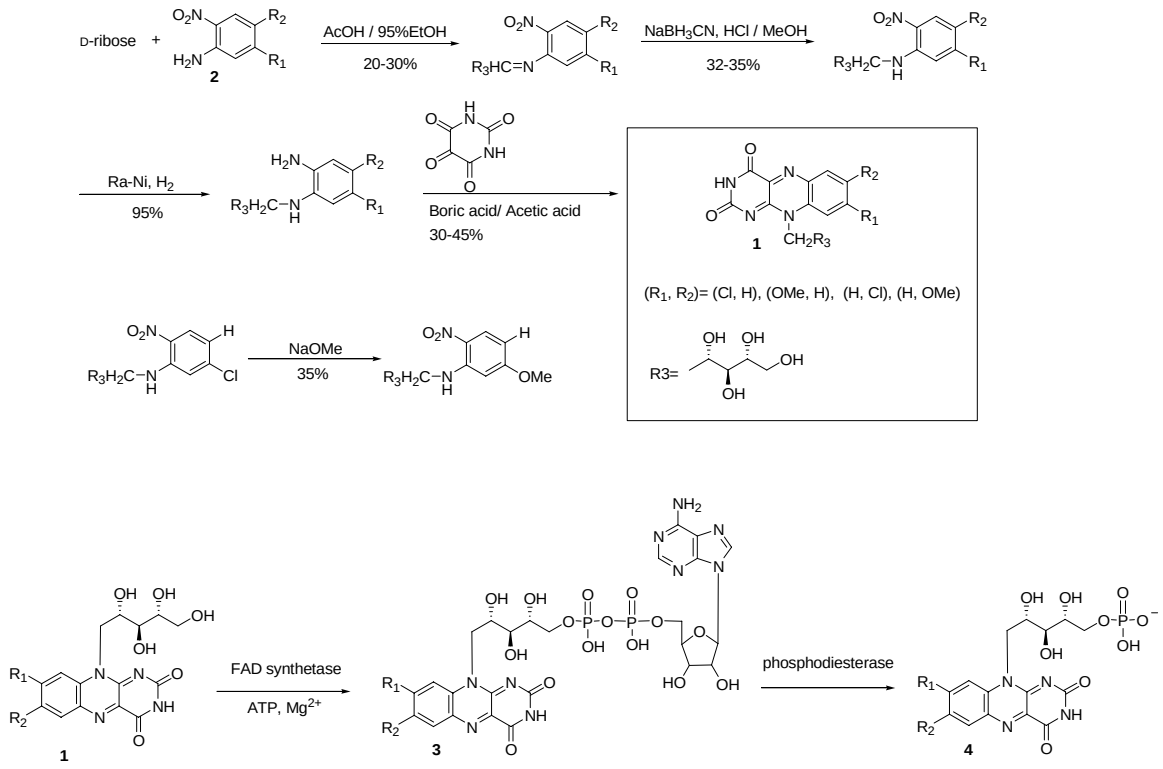

Scheme 4.1: Chemoenzymatic synthesis of FMN analogues.

colored fractions (containing FAD) were pooled and lyophilized. The FAD analogues purified by HPLC were dissolved in 150 mL of 20 mM potassium phosphate buffer (pH 7.6) along with 6 mg of Naja naja snake venom phosphodiesterase (Sigma, St. Louis, MO.) to generate the corresponding FMN analogues (**4**). The reactions were incubated for 2 hours at room temperature with stirring. The phosphodiesterase was removed by YM-10 filtration and the remainder of the reaction was lyophilized, re-dissolved in 1-2 mL of H_2O, and purified by RP-HPLC as described above. The identity of each compound was verified by ^{1}H- and ^{31}P-NMR as well as by low and high resolution ESI-

MS. **7-OMe-FMN**. ^{1}H NMR (600 MHz, D_2O) δ 3.92 (m, 7 H), 4.36 (dt, *J* =9.8, 3.5 Hz, 1 H), 4.88 (d, *J* =14.2 Hz, 1 H), 5.06 (m, , 1 H), 7.50 (d, *J* =2.9 Hz, 1 H), 7.64 (dd, *J* =2.9, 9.6 Hz, 1 H), 8.01 (d, *J* =9.6 Hz, 1 H); ^{31}P NMR (500 MHz, D_2O) δ 4.2. High resolution ESI-MS calc. for $C_{16}H_{18}N_4O_{10}P$ $(M)^{-1}$ 457.0766, found 457.0763. **7-Cl-FMN**. ^{1}H NMR (600 MHz, D_2O) δ 3.96 (m, 4 H), 4.35 (m, 1 H), 4.85 (d, *J* =11.5 Hz, 1 H), 5.01 (m, 1 H), 7.94 (dd, *J* =2.0, 8.0 Hz, 1 H), 8.02 (d, *J* =8.0 Hz, 1 H), 8.13 (d, *J* =2.0 Hz, 1 H); ^{31}P NMR (500 MHz, D_2O) δ 1.9. High resolution ESI-MS calc. for $C_{15}H_{15}N_4O_9PCl$ $(M)^{-1}$ 461.0270, found 461.0271. **8-Cl-FMN**. ^{1}H NMR (500 MHz, D_2O) δ 3.91 (m, 5 H), 4.36 (dt, *J* =10.0, 3.0 Hz, 1 H), 4.79 (d, *J* =14.5 Hz, 1 H), 7.67 (dd, *J* =2.0, 9.0 Hz, 1 H), 8.05 (d, *J* =9.0 Hz, 1 H), 8.13 (d, *J* =2.0 Hz, 1 H); ^{31}P NMR (500 MHz, D_2O) δ 3.8. High resolution ESI-MS calc. for $C_{15}H_{15}N_4O_9PCl$ $(M)^{-1}$ 461.0270, found 461.0266. **8-OMe-FMN**. ^{1}H NMR (600 MHz, D_2O) δ 3.90 (m, 4 H), 3.98 (s, 3 H), 4.43 (m, 1 H), 4.74 (d, *J* =13.5 Hz, 1 H), 5.19 (m, 1 H), 7.33 (dd, *J* =2.4, 9.2 Hz, 1 H), 7.40 (d, *J* =2.4 Hz, 1 H), 8.01 (d, *J* =9.2 Hz, 1 H); ^{31}P NMR (600 MHz, D_2O) δ 2.7. High resolution ESIMS calc. for $C_{15}H_{15}N_4O_9PCl$ $(M)^{-1}$ 457.0766, found 457.0760. NMR and mass spectra can be seen in the Appendix to this chapter.

4.2.2 UV-visible absorption spectroscopy: In order to obtain UV-visible absorption spectra of the IDI-2 bound FMN analogues in the oxidized, reduced, and IPP-bound states, anaerobic incubations containing 100 μM apo-IDI-2, 50 μM flavin, 2 mM IPP, 5 mM $MgCl_2$, and 1 mM DTT in 100 mM potassium phosphate buffer (pH 8.0) were

prepared in the glove box. Apo-IDI-2 was prepared by dialysis of the as-purified enzyme against 6 L of buffer containing 2 M KBr, 10% glycerol, 50 mM potassium phosphate (pH 7.5), followed by dialysis against 6 L of storage buffer (50 mM potassium phosphate, 10% glycerol, pH 7.5). Enzyme concentrations were determined by the Bradford assay using bovine serum albumin as the standard. Extinction coefficients for the flavin analogues were taken from the literature and were used to calculate the concentration of flavin stock solutions (*143*). All solutions were allowed to degas in the glove box prior to use. Larger volumes (10 mL) of H_2O and concentrated buffer were allowed to degas in the glove box for several days with stirring, whereas smaller volumes (20-100 μL) of concentrated flavin, IPP, $MgCl_2$, DTT, and enzyme stock solutions were allowed to degas in the glove box for several hours the day of use. After the reaction components were mixed, a spectrum of the oxidized, IDI-2 bound FMN was recorded. The reaction mixture was then photoreduced directly in the cuvette for 1.5 min using a Kodak slide projector. Following photoreduction, the spectrum of the reduced, IDI-2 bound flavin was recorded. Spectra were recorded periodically over a 5 min period to ensure that the flavin was not reoxidizing. IPP was then added to each reaction and the spectrum of the IDI-2:flavin:IPP complex was recorded at 0, 1, 2, and 5 min to ensure that the absorbance changes had reached an equilibrium level.

4.2.3 Comparison of IDI-2 bound flavin analogue intermediate absorbance at pH 8.0 to free flavin analogue absorbacne at pH 4.0: All incubations contained 50 μM flavin, 20 mM $Na_2S_2O_4$, and 5 mM $MgCl_2$ in 100 mM potassium phosphate buffer. For the

spectra of the free, reduced flavins, the pH of the phosphate buffer was adjusted to pH 4.0 to record the spectrum of the neutral reduced flavin or to pH 8.0 to record the spectrum of the anionic reduced flavin. For the spectra of the IDI-2 bound reduced flavin analogues, an IDI-2 concentration of 120 μM was used. Under these conditions, the majority of the 50 μM reduced flavin should be enzyme bound in the presence and absence of IPP. The pH of the phosphate buffer was adjusted to 8.0 and spectra were recorded in the absence and presence of 2 mM IPP (a saturating IPP concentration at pH 8.0). All absorbance spectra were recorded at 25 °C in quartz cuvettes.

4.2.4 Steady state kinetics: The steady state kinetic parameters for the IDI-2 catalyzed conversion of IPP to DMAPP were determined with each different flavin analogue according to the acid lability assay described in section ***3.2.2***. Prior to determining the k_{cat} and k_{cat}/K_m for IPP, the concentration of each FMN analogue was varied at a constant, saturating IPP concentration to ensure that the concentration of each FMN analogue was at a saturating level. These reactions contained 50 nM apo IDI-2 and variable flavin concentrations (from 0 – 20 μM). The other reaction conditions, derivitiaztion, workup, and data analysis procedures were identical to those described in section ***3.2.2*** for the standard steady state kinetic assay. These results indicated that a 20 μM concentration of each FMN analogue was sufficient for maximal activity. Next, the FMN concentration was held fixed at 20 μM, and the IPP concentration was varied from 1 to 150 μM to determine the steady state kinetic parameters for IPP turnover. The reaction conditions and workup were identical to the standard assay conditions except that 500 nM apo IDI-2

was used in the 7-Cl-FMN, 8-Cl-FMN, and 7-*O*-Me-FMN catalyzed reactions. For each reaction, the initial velocities (v_i) of DMAPP formation were plotted against the [IPP] and GraFit 5 (Erithacus Software, Surrey, U.K.) was used to fit the data to the Michaelis-Menten equation using non-linear regression. The values for k_{cat} and k_{cat}/K_m were normalized by the total [IDI-2]. The dependence of the steady state kinetic parameters on the electronic properties of the flavin were then analyzed using linear free energy relationships (LFERs) as described in the Results and Discussion.

4.2.5 Pre-steady state kinetics: To monitor the kinetics of flavin intermediate formation and decay in the pre-steady state, the changes in IDI-2 bound flavin absorbance at 440 nm were monitored upon mixing with 60 μM IPP or (*R*)-[2-^{2}H]-IPP in the stopped flow under the conditions described in section ***3.2.10***. For studies with the 8-Cl-FMN analogue, the concentrations of IDI-2, 8-Cl-FMN, and IPP (or (*R*)-[2-^{2}H]-IPP) were scaled up to 200 μM, 500 μM, and 160 μM, respectively, to account for the smaller $\Delta\varepsilon_{440}$ associated with this coenzyme upon IPP binding. The ratio of the IDI-2:flavin and substrate concentrations for the 8-Cl-FMN reaction was identical to the ratio used for the other flavin analogues. Stopped-flow studies were not performed with the 8-OMe-FMN analogue due to the extremely small $\Delta\varepsilon_{440}$ observed for this coenzyme upon IPP binding. Injections were performed in triplicate at 25 ˚C over various time scales, depending on the relative rates of the observed kinetic phases with each flavin analogue. Upon mixing, absorbance changes at 440 nm were followed using a log time scale to collect as many data points as possible in each kinetic phase of the reaction. After subtraction of the

background absorbance, the time-courses were fitted with exponential equations using GraFit 5 to determine the rates and amplitudes of the observed fast and slow kinetic phases.

4.2.6 Kinetic isotope effect studies and assay for $k_{cat,rev}$: The effects of the flavin analogues on $^{D}k_{cat}$ in the forward direction were assessed using the ^{1}H-NMR assay described in section ***3.2.6***. Reactions (660 μL) contained varying concentrations of apo-IDI-2, 20 μM flavin, 20 mM sodium dithionite, 10 mM IPP (or (*R*)-[2-^{2}H]-IPP), 10 mM $MgCl_2$, 1 mM DTT, 2 mM sodium acetate, and 60 μL D_2O in 100 mM potassium phosphate (pH 8.0) at 27 °C. Enzyme concentrations for each reaction were scaled such that < 10% of the reaction occurred over the 120 min period of data collection (K_{eq} = 1.2, section ***3.2.3***). The pair of reactions (one containing IPP and one containing (*R*)-[2-^{2}H]-IPP) for each analogue was conducted on the same day using the same stock enzyme solution. Initial velocities for DMAPP formation were determined as described in section ***3.2.6***. The assays for the reverse reaction (DMAPP → IPP) were conducted under similar conditions, except that 20 mM DMAPP was used, and the time-dependent formation of the C2-methylene signal of IPP was followed to calculate the initial velocity of IPP formation.

4.3 Results and Discussion

***4.3.1 UV-visible absorption properties of the IDI-2 bound flavin analogues*:** Apo-IDI-2 was reconstituted with each of the FMN analogues under anaerobic conditions in order to obtain absorbance spectra for the IDI-2:flavin complexes in the oxidized, reduced, and IPP-bound states. As can be seen in Figure 4.1, the overall pattern of absorbance changes in the different states is very similar between the different coenzyme analogues. Namely, upon photoreduction, the extinction coefficients of the flavins decrease markedly in the 400-500 nm region. When a saturating concentration of IPP was added to the photoreduced IDI-2:flavin complexes, a slight red shift and intensity increase in the major absorption band was observed. Thus, it appears that IPP binding induces similar perturbations in the absorption spectra of each coenzyme, suggesting that variation of the flavin coenzyme structure does not drastically alter the binding of IPP in the active site, and that a similar flavin intermediate is forming in each case.

As in section ***2.3.3***, we next determined whether IPP binding to reduced IDI-2:flavin at pH 8.0 induced similar changes in the flavin absorption spectrum as changing the pH of free reduced flavin analogue solutions from 8.0 to 4.0 (Figure 4.2). As was observed with FMN in Chapter 2, the difference spectra for these experiments show that the absorbance changes associated with IPP binding to reduced IDI-2:flavin are red-shifted and are more intense than the absorbance change associated with free reduced flavin when the solution pH is lowered from 8.0 to 4.0 (see Table 4.1). Our tentative interpretation of these results is that similar changes are occurring in the active site upon IPP binding to IDI-2 reconstituted with each flavin analogue. As discussed in Chapter 2, the change in the flavin absorbance is likely due either to protonation of the anionic

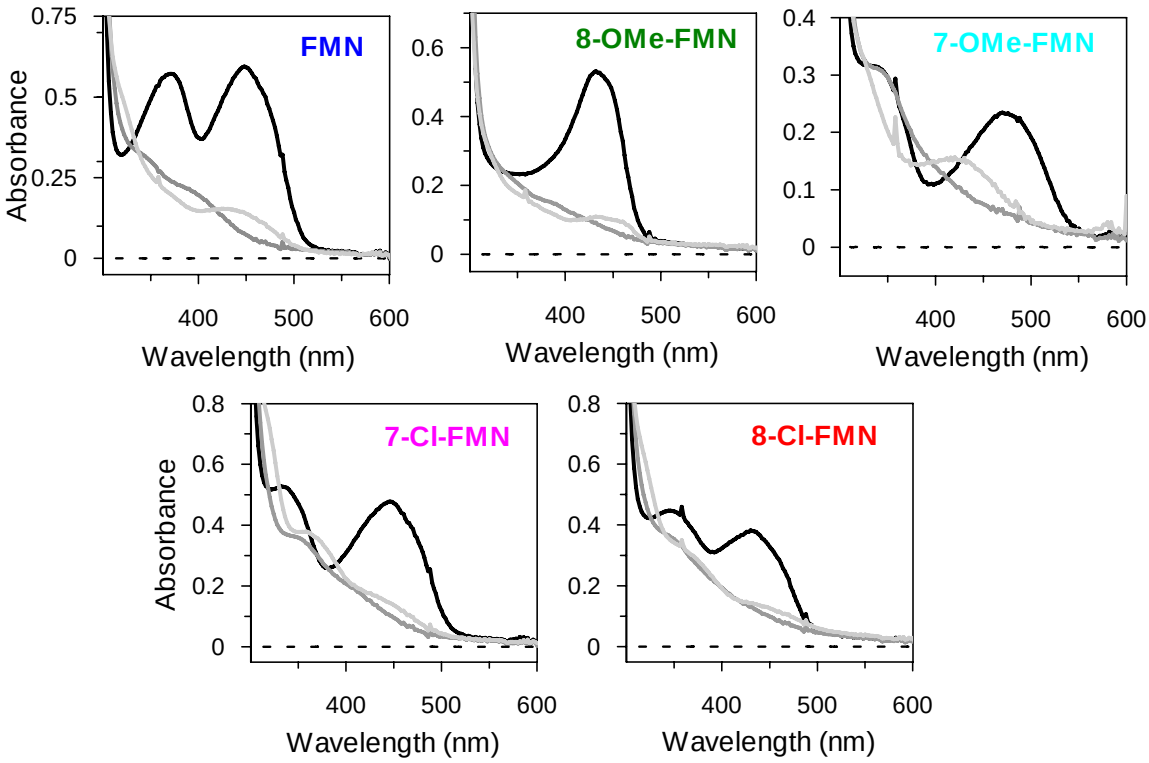

Figure 4.1: UV-visible absorbance properties of IDI-2 bound FMN analogues in the presence and absence of IPP. The FMN analogue used for each set of experiments is indicated in each panel. Spectra were recored with the flavin in the oxidized (black) and photoreduced states in the absence (dark gray) and presence (light gray) of IPP.

reduced flavin (to form an $FMNH_2$ species) or to a structural distortion in the isoalloxazine moiety of anionic reduced flavin, perhaps combined with a stacking interaction between the substrate and the coenzyme analogues and/or desolvation of the active site.

4.3.2 Effects of the flavin analogues on the steady-state kinetic parameters: Next, the activity of IDI-2 reconstituted with each flavin analogue was assessed using the standard

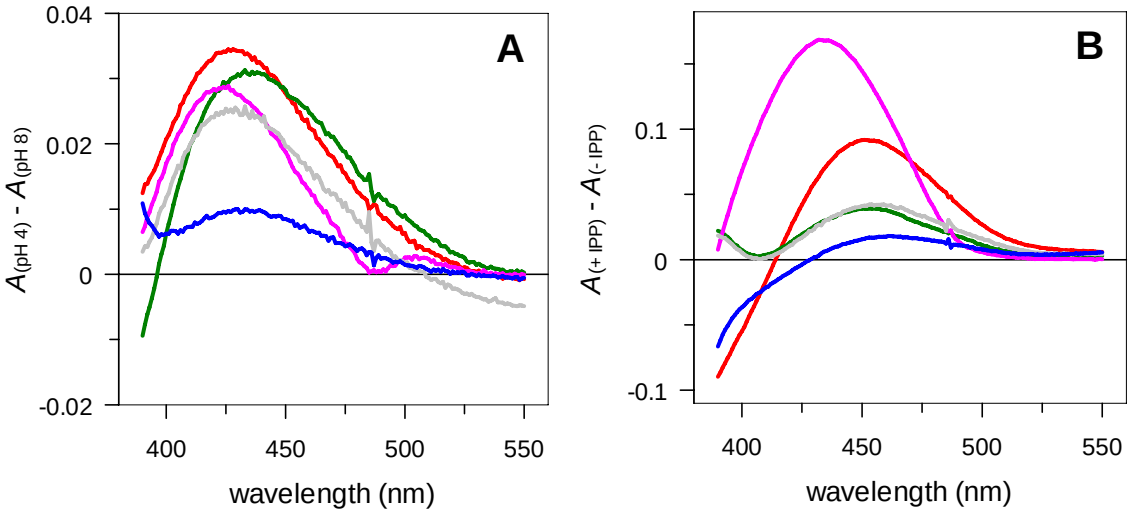

Figure 4.2: Comparison of absorbance changes for FMN (red), 7-Cl-FMN (green), 7-OMe-FMN (fuschia), 8-Cl-FMN (gray), and 8-OMe-FMN (blue) as a function of pH (panel A) and the presence of IPP (panel B). In panel A, the spectrum of each free flavin analogue in solution was recorded at pH 8.0 and pH 4.0. The difference spectra plotted show the increase in absorbance in the 400 – 500 nm region as the pH is lowered from 8.0 to 4.0. In panel B, the spectrum of each IDI-2 bound flavin analogue was recorded in the presence and absence of IPP at pH 8.0. The spectra recorded in the absence of IPP were then subtracted from the spectra recorded in the presence of IPP to illustrate the absorbance increase between 400 – 500 nm that accompanies IPP binding at pH 8.0.

assay conditions to determine whether the altered flavin substituents induced systematic changes in the steady state kinetic parameters. Control experiments were first performed at saturating IPP concentrations in order to determine the appropriate (saturating) concentration of flavin analogue to use for the steady state kinetic studies (Figure 4.3). These data suggested that the binding properties of the flavin analogues appeared to be similar and that a 20 μM concentration of each flavin analogue was sufficient to saturate that initial velcoity under the reaction conditions used. The steady state kinetic

parameters for the forward reaction were then determined for IDI-2 reconstituted with

	pH 8.0 → pH 4.0		- IPP → + IPP	
Flavin	λ_{max}	**Intensity**	λ_{max}	**Intensity**
FMN	427	0.0346	453	0.093
8-OMe-FMN	432	0.0101	461	0.0207
8-Cl-FMN	428	0.0252	456	0.0437
7-OMe-FMN	423	0.0287	435	0.169
7-Cl-FMN	436	.031	453	.0402

Table 4.1: Comparison of the λ_{max} and intensity of the absorbance changes associated with each FMN analogue for the experiments in Figure 4.2.

each flavin analogue and using IPP as the variable substrate (Figure 4.4 and Table 4.2). In addition, the ^{1}H-NMR assay was used to estimate k_{cat} in the reverse direction with each analogue (Figure 4.5 and Table 4.2).

4.3.3 Linear free energy relationships (LFERs) on the steady state kinetic parameters: Interestingly, when the steady state kinetic data for the forward and reverse IDI-2 catalyzed reaction reported in Table 4.2 were plotted versus either the sum of the Hammett inductive substituent constants (for the 7- and 8-substituents of the flavin isoalloxazine) or the estimated pK_a of the N5 atom of the flavin (Figure 4.6), linear relationships were observed between the kinetic constants and the electronic properties of the flavin analogues (*122*). The data were fitted with linear regression to either the Hammett equation (Eqtn 4.1) or the Brønsted equation (Eqtn 4.2) to assess the sensitivity

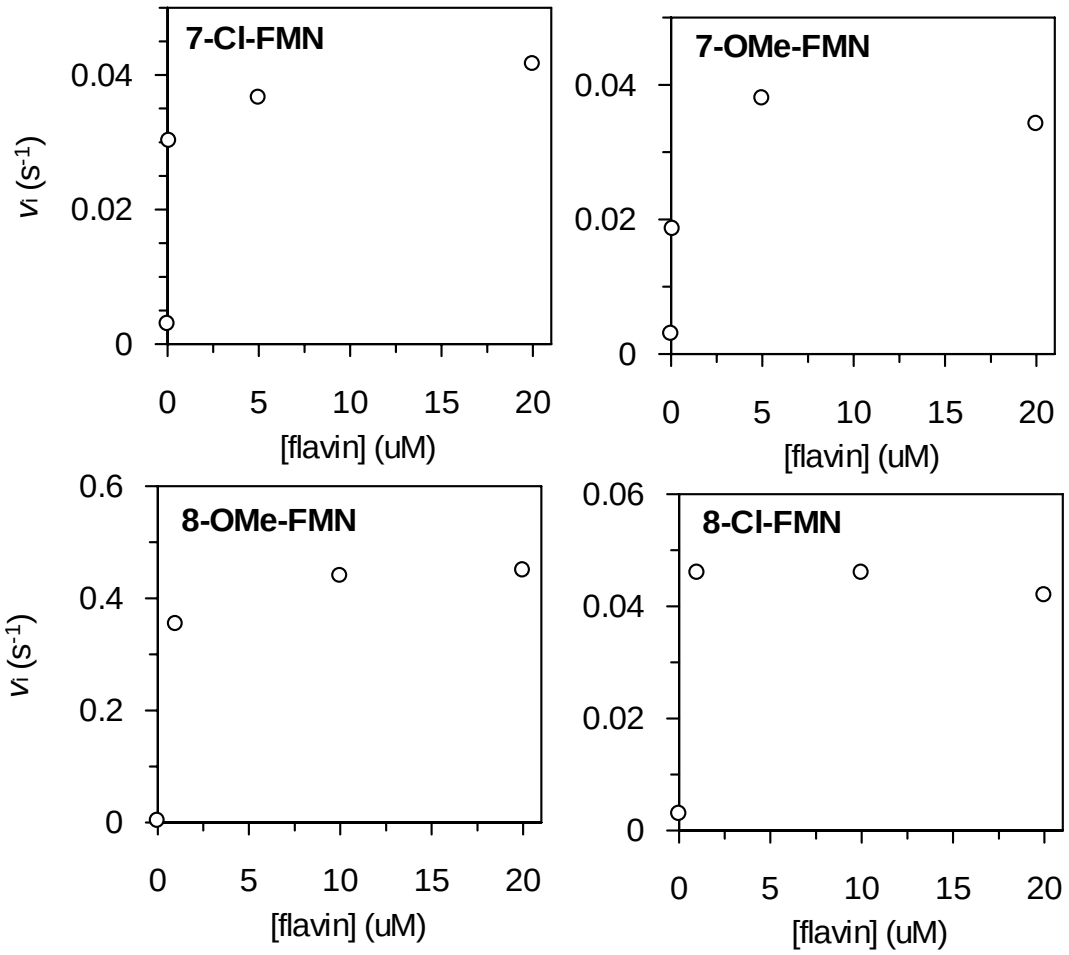

Figure 4.3: Dependence of initial reaction velocity in the forward direction on the concentration of each FMN analogue at a saturating concentration of IPP (*122*). Reaction velocities have been normalized by the concentration of IDI-2 used in each assay.

of the IDI-2 catalyzed reaction to the inductive properties of the substituents or to the estimated pK_a of the flavin, respectively. Before discussing the meaning of the sensitivity constants (ρ and β) in these equations and what information they supply regarding IDI-2 catalysis, we will first explore the origins of linear free energy relationships (*144*).

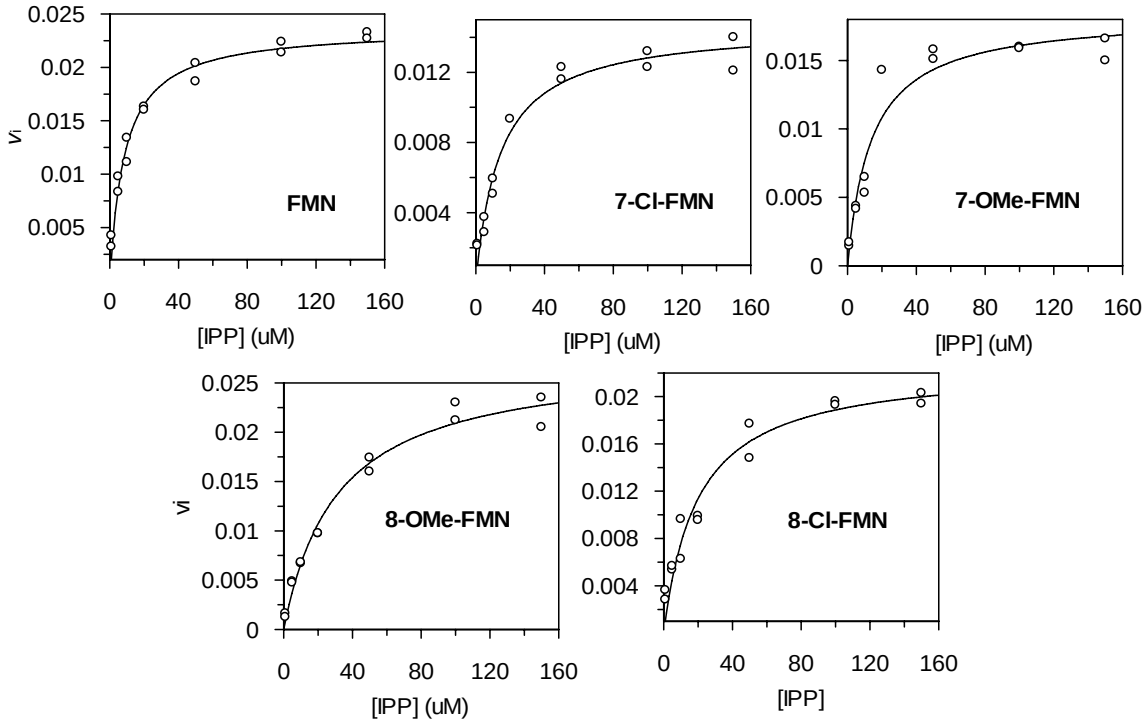

Figure 4.4: Effects of flavin analogues on the steady state kinetic parameters (*122*). Kinetic data were collected using the standard steady state kinetic assay conditions (section ***3.2.2***). Initial velocities are plotted in units of μM DMAPP/sec. A total enzyme concentration of 50 nM IDI-2 was used for the FMN and 8-OMe-FMN reactions, and 500 nM IDI-2 was used for the other flavin analogues. The data were fitted with the Michaelis-Menten equation to determine the steady state kinetic paramters, which are shown in Table 4.2.

Eqtn. 4.1:

$$\log (k_x) = \rho \cdot \sigma_x + \log (k_r)$$

Eqtn. 4.2:

$$\log (k_x) = \beta \cdot pK_x + \log (k_r)$$

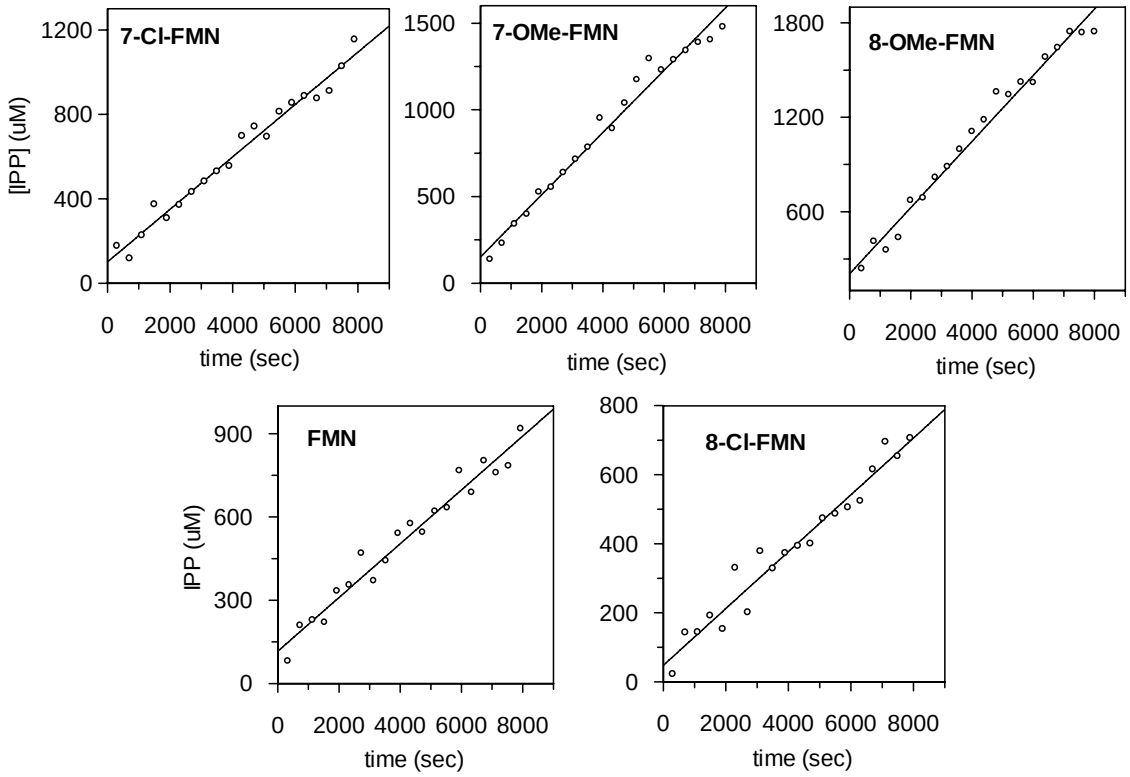

Figure 4.5: Effects of flavin analogues on the initial velocity of the reverse reaction. The time-dependent formation of the C2 methylene proton resonance of IPP was followed by ^{1}H-NMR under pseudo-first order DMAPP concentrations. The [IDI-2] used in the assays was 500 nM (FMN), 1 μM (8-OMe-FMN), 2.5 μM (7-OMe-FMN), 10 μM (8-Cl-FMN), and 20 μM (7-Cl-FMN). The raw data were fitted with a line to determine the initial velocities of the reaction, which are shown in Table 4.2.

The free energy change associated with a given reference reaction is shown in Eqtn 4.3, where the subscript o denotes a reference substituent. This equation is written for an equilibrium process, but the derivation for a kinetic process (assuming the validity of transition state theory) is identical, except that reaction free energy term (ΔG) becomes an activation energy term ($\Delta G^{\ddagger}$) and the equilibrium constant (K) becomes a rate constant

(*k*). When the *same reaction* is repeated with a reactant containing a *different substituent*

flavin	σ_x	pK_x	$k_{cat,for}$	$K_{m,IPP}$	$(k_{cat}/K_m)_{for}$	$k_{cat,rev}$	$K_{m,DMAPP}$
8-*O*-Me-FMN	-0.27	5.32	0.56(2)	31(4)	18000(2000)	0.21	14
FMN	-0.24	5.17	0.48(1)	9(0.9)	53000(5000)	0.19	4
7-*O*-Me-FMN	0.12	4.22	0.037(2)	14(3)	2600(500)	0.63	291
8-Cl-FMN	0.23	4.03	0.045(2)	20(4)	2300(500)	0.0081	4
7-Cl-FMN	0.37	3.42	0.029(1)	14(2)	2100(300)	0.21	120

Table 4.2: Summary of flavin substituent effects on the steady state kinetic parameters (*122*). The $K_{m,DMAPP}$ was calculated from $(k_{cat},K_m)_{for}$, $k_{cat,rev}$, and K_{eq} using the Haldane relationship.

(x), the free energy difference between the two reactions can be formulated as in Eqtn 4.4, which illustrates that the free energy difference for the *same reaction* with two *different substituents* is directly proportional to the logarithm of the ratio of the equilibrium (or rate) constants.

Eqtn 4.3:

$$\Delta G_o = -2.302RT \log(K_o)$$

Eqtn 4.4:

$$\Delta\Delta G = \Delta G_o - \Delta G_x = 2.302RT \log(K_x/K_o)$$

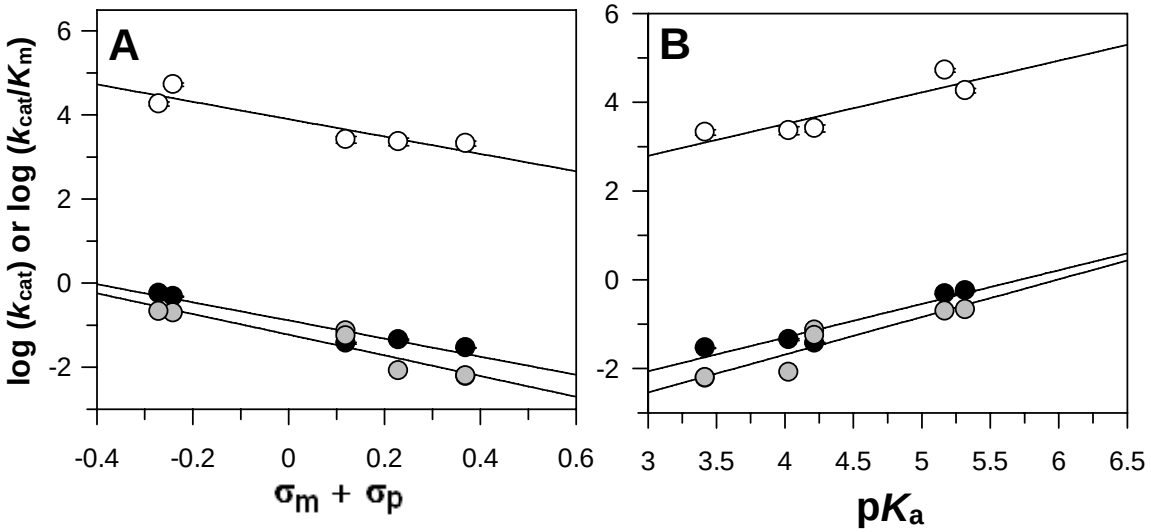

Figure 4.6: Linear free energy relationships between the steady state kinetic parameters for the wt IDI-2 catalyzed reaction and the electronic properties of the flavin (*122*). Data is taken from Table 4.2. Hammett plots for k_{cat}/K_m (white circles), $k_{cat,for}$ (black circles), and $k_{cat,rev}$ (gray circles) are shown in panel A and the Bronsted plots are shown in panel B. The ρ values determined for k_{cat}/K_m, $k_{cat,for}$, and $k_{cat,rev}$ in panel A were -2.1 ± 0.5, -2.2 ± 0.3, and -2.5 ± 0.4, respectively. The β values determined for the same kinetic parameters in panel B were 0.7 ± 0.2, 0.8 ± 0.1, and 0.8 ± 0.2, respectively.

The effects of the *same substituents* on the free energy changes associated with a *different reaction of interest* can be written in an analogous manner (Eqtn 4.5).

Eqtn 4.5:

$$\Delta\Delta G' = \Delta G_o' - \Delta G_x' = 2.302RT \log(K_x'/K_o')$$

The relative effects of the *same substituents* on the two *different reactions* is then defined by the ratio of Eqtn 4.5 to Eqtn 4.4 to give Eqtn 4.6:

Eqtn 4.6:

$$\Delta\Delta G'/\Delta\Delta G = \log(K_x'/K_o') / \log(K_x/K_o)$$

The relationship in Eqtn 4.6 makes no assumptions on the nature of the reference reaction or the reaction of interest, or on the structures of the reactant, products, or transition states involved; it simply relates the relative effects of two specific substituents (o and x) to the free energy changes associated with two specific reactions. Eqtn 4.6 can be rearranged and new parameters (Q and C_x) can be defined to give the familiar form (Eqtn 4.7) of linear free energy relationships (e.g. see the Hammett and Bronsted equations above).

Eqtn 4.7

$$\log(K_x'/K_o') = QC_x$$

Here, Q is the ratio of the free energy changes for the reaction of interest and the reference reaction when the substituents o and x are used ($Q = \Delta\Delta G'/\Delta\Delta G$) and is termed the sensitivity constant for the reaction. The parameter C_x ($= \log(K_x/K_o)$) is termed the substituent constant for substituent x and is defined by the reference reaction (as in Eqtn 4.4).

Quick inspection of Eqtn 4.7 predicts that a linear relationship should exist between the equilibrium (or rate) constants of two different reactions as long as Q is a constant function of the substituents used to compare the properties of the two reactions. Inspection of the definition of the sensitivity constant ($Q = \Delta\Delta G'/\Delta\Delta G$) in terms enthalpy and entropy (Eqtn 4.8) provides insight into how this seemingly unlikely scenario usually holds true, regardless of the substituents used to perturb the two reactions under study.

Eqtn 4.8

$$\Delta\Delta H' - T\Delta\Delta S' = Q(\Delta\Delta H - T\,\Delta\Delta S)$$

This equation shows that as long as the enthalpy and entropy changes associated with each reaction scale proportionately, then Q will be constant. Namely, changes in $\Delta\Delta H'$ and $\Delta\Delta S'$ in the reaction of interest must scale linearly with the changes in $\Delta\Delta H$ and $\Delta\Delta S$ in the reference reaction across a range of substituents. In practice, it is often found that the enthalpy and entropy for reactions that exhibit LFERs do scale linearly (*144*). For example, increases in activation enthalpy ($\Delta H^{\ddagger}$) for a kinetic process (indicating weaker bonding in the transition state) are usually associated with corresponding increases in the entropy of activation (indicating that the transition state is less organized). Thus, as long as a set of substituents influence the enthalpy and entropy terms of the two reactions under comparison in a consistent manner, LFERs should exist between the equilibrium or kinetic constants of the two reactions.

Having explored the origins of LFERs, we will return to the two LFERs used to correlate the IDI-2 kinetic data: the Hammett equation (Eqtn 4.1) and the Brønsted equation (Eqtn 4.2). In both Eqtn 4.1 and 4.2, k_x is defined as the kinetic constant of interest (either k_{cat}, k_{cat}/K_m, or $k_{cat,rev}$) determined for the IDI-2 catalyzed reaction using the flavin analogue with substituents, x, and log (k_r) is the y-intercept of the plot, which has no physical meaning. In the Hammett equation, the substituent constant is σ_x and the sensitivity constant is ρ. (Recall that these two parameters are equivalent to the C_x and Q

parameters, respectively, discussed above). The reference reaction used to define the σ_x values (Eqtn 4.9) is the ionization of the benzoic acid, where K_H and K_X are the ionization constants of benzoic acid and benzoic acid with substituent x, respectively.

Eqtn 4.9

$$\sigma_x = \log (K_X/K_H)$$

The negative charge that develops as benzoic acid is ionized cannot be delocalized by resonance into the benzene moiety, thus any electronic effects of altered benzene ring substituents on the ionization constant of benzoic acid should be largely attributable to inductive effects (through σ-bonds) rather than to resonance effects (through π-bonds). From Eqtn 4.9, it can be seen that substituents that inductively stabilize the negative charge on the benzoate anion lead to $K_X > K_H$, resulting in $\sigma_x > 0$. Conversely, substituents that destabilize the negative charge that forms upon benzoic acid ionization lead to $K_X < K_H$ and, hence, to $\sigma_x < 0$.

The Hammett equation (Eqtn 4.1) relates the kinetic (or equilibrium) constants of the reaction of interest (in our case, the steady state kinetic constants for the IDI-2 catalyzed reaction) to the reference reaction (benzoic acid ionization) via the sensitivity constant, ρ. If the reaction under study exhibits the same sensitivity to the inductive effects of the substituents as the reference reaction, then $\rho = 1$, and Eqtn 4.1 reduces to Eqtn 4.10:

Eqtn 4.10:

$$\log (k_x/k_r) = \sigma_x = \log (K_X/K_H)$$

Because the inductive effects of the same set of substituents on charge accumulation should be similar in the two reactions (if indeed only inductive electronic effects are important), this result would suggest that the reaction under study and the reference reaction accumulate similar amounts of negative charge (or, equivalently, the reaction of interest could be losing an identical amount of positive charge). In contrast, ρ = - 1 indicates that the reaction under study and the reference reaction have the opposite sensitivity to the substituents, implying either that negative charge is being lost or that positive charge is being gained in the reaction under study. If the magnitude of ρ is less than 1, then either the formal charge is not fully formed in the transition state or product of the reaction under study, or the charge is forming at a position in the substituted molecule that is more remote from the altered substituents, in which case the developing charge would not "feel" the inductive effects of the substituents as strongly as the developing charge in the reference reaction. In contrast, if the magnitude of ρ is greater than 1, then either multiple formal charges of the same sign are forming in the reaction under study, the charge is forming at a position in the substituted molecule that is closer to the altered substituents, or the surrounding medium somehow serves to magnify the inductive effects of the substituents relative to the reference reaction (which was carried out in water). Thus, the magnitude and sign of ρ determined from a Hammett plot

provides information on the extent, location, and the type of charge accumulation in the products (if an equilibrium process is being studied) or in the transition state (if a kinetic process is being studied).

For our Hammett analysis of the IDI-2 kinetic data, we defined the 7- and 8-substituents of the isoalloxazine moiety of the flavin to be *meta* and *para*, respectively, to the N5 atom of the flavin (Scheme 4.2). Under this assumption, the σ_x substituent constant used to correlate the data can be expressed as the sum of the σ_m and σ_p constants for the 7- and 8-substituents, respectively (*i.e.*, $\sigma_x = \sigma_m + \sigma_p$). Previous structure activity relationship studies (*145*) have deomonstarted linear correlations between the electronic properties of 7- and 8-substitued flavins with the sum ($\sigma_m + \sigma_p$). The σ_m and σ_p inductive substituent constants used to calculate σ_x were taken from Hansch et.al. (*146*).

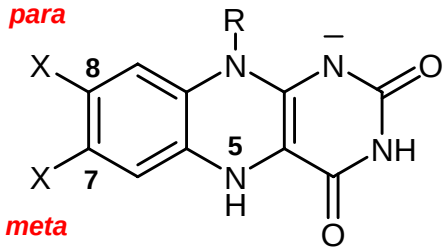

Scheme 4.2: The orientation of the 7- and 8-substituents of the flavin analogues relative to the N5 atom was taken to be *meta* and *para*, respectively for the Hammett analysis.

Fits of the IDI-2 steady state kinetic data to the Hammett equation yielded sensitivity constants, ρ, equal to -2.2, -2.1, and -2.5 for k_{cat}, k_{cat}/K_m, and $k_{cat,rev}$, respectively (Figure 4.6). According to the discussion above, this observation indicates that the IDI-2 catalyzed reaction is more sensitive to the inductive properties of the 7- and

8-isoalloxazing ring substituents than the ionization of benzoic acid is to *meta* and *para* substituents on the benzene ring. The negative sign of ρ indicates either that negative charge is being lost or that positive charge is being gained *on the flavin in the step(s) that limit steady state turnover*. Furthermore, the magnitude of ρ is > 1, suggesting that charge accumulation/diminution on the flavin may be occurring closer to the altered substituents than the position of charge accumulation in the reference reaction (the oxygen atoms of the benzoate anion carboxyl group), such that the developing charge on the IDI-2 bound flavin "feels" the inductive effects of the substituents more strongly. Another possibile explanation for the magnitude of ρ for the IDI-2 catalyzed reaction is that the closed, hydrophobic IDI-2 active site may be magnifying the effects of the substituents on charge accumulation in the transition state. The similar magnitudes of the ρ values on k_{cat} and k_{cat}/K_m imply that the same transition state(s) in the kinetic mechanism is/are rate determining under both limiting and saturating IPP concentrations. In addition, the similarity of the ρ values measured on k_{cat} and $k_{cat,rev}$ (-2.2 ± 0.3 and -2.5 ± 0.4, respectively), suggest that the same transition state is likely rate-limiting in both reaction directions. Finally, the fact that the relationship between the kinetic parameters of the IDI-2 catalyzed reaction and the reference reaction appears to be linear suggests that similar amounts of charge are accumulating in the transition state for the IDI-2 catalyzed reaction with each flavin analogue. This, in turn, implies that the mechanism is not being altered when the substituents are changed.

The logic behind the derivation of the Brønsted equation (Eqtn. 4.2) is very similar, except that the Hammett inductive substituent constants (σ_x) are replaced with

acid dissociation constants (pK_x), and the sensitivity constant is called β. Because pK_a values are defined by a reaction in which the covalent bond between a base and a proton is completely formed, the β sensitivity constant is usually interpreted as the extent of bond formation between a proton and the basic atom, with β = 1.0 indicating complete proton transfer to the basic atom. Thus, for a reaction where a proton is completetly transfered to the basic atom in the transition state, a one unit increase in pK_a of the basic atom should lead to a 10-fold increase in the rate constant for passage through that transition state.

In the Brønsted plots of the IDI-2 kinetic parameters (Figure 4.6B), the pK_x values we used to correlate the data are the estimated pK_a values of the N5 atom of the reduced flavin analogue with substituents, x, which were assumed to be equivalent to the pK_a values for the first ionization constant of similarly substituted aniline derivatives (Scheme 4.3). The pK_x values for the substituted aniline compounds measured at 25 °C were taken from Perrin (*147*), and previous studies have suggested that the aniline portion of the reduced flavin isoalloxazine moiety indeed behaves very similarly to aniline. Most notably, Macheroux and co-workers demonstrated that the ionization constant of both the N5-H group of reduced flavin and the -NH_2 group of aniline have similar pK_a values of ~ 20 (*87*). Also, the pK_a for formation of the zwitterionic reduced flavin (the 5,5-dihydro-$FMNH_2$ tautomer species in Scheme 4.3) has been estimated to be > 4 (*87, 148*), in good agreement with the pK_a of the $–NH_3^+$ group of aniline (pK_a = 5.2). In reduced flavins, the pK_a of the protonated N5-H group (a secondary amine) is expected to be slightly higher than the pK_a of the $–NH_3^+$ group (a primary amine) in the corresponding aniline

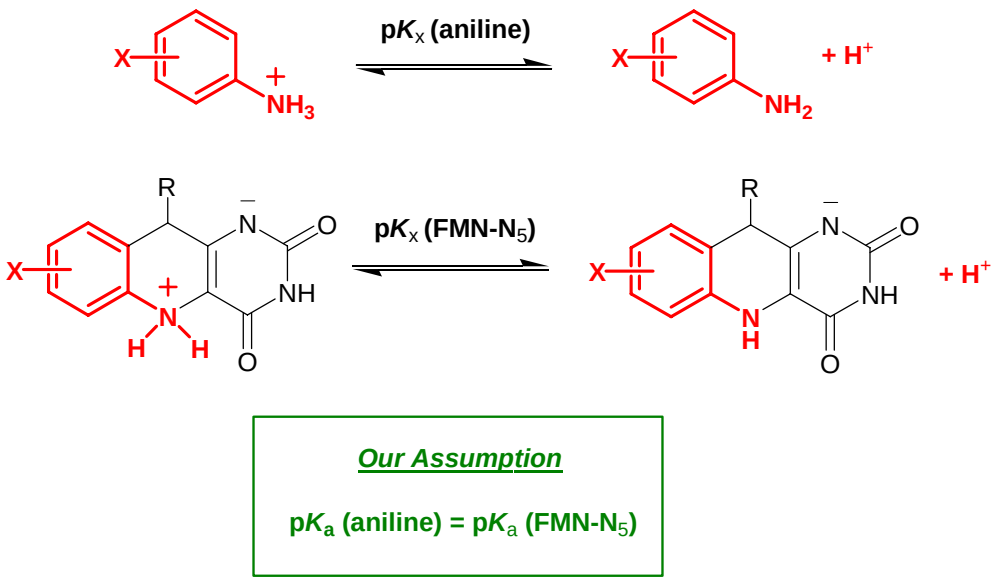

Scheme 4.3: The pK_a of the N5 position of reduced flavin was assumed to be equivalent to the pK_a of aniline.

compound, because inductive donation of electron density to the N5 atom by the ring system of the reduced flavin should help to slightly stabilize the protonated form.

The β values measured in the Brønsted plots for k_{cat}, k_{cat}/K_m and $k_{cat,rev}$ for the IDI-2 catalyzed reaction were 0.8, 0.7, and 0.8, respectively, suggesting a substantial amount of proton transfer to the N5 atom of the flavin in the rate limiting transition state(s). Qualitatively, these results are also consistent with the farily large, negative ρ values measured in the Hammett plots, which are suggestive of the accumulation of positive charge in the direct vicinity of the 7- and 8-substituents of isoalloxazine. Together, the LFERs in Figure 4.6 are consistent with a transition state for the IDI-2 catalyzed reaction involving proton transfer to the N5 atom of the reduced FMN, which leads to a

concommittant accumulation of positive or partial positive charge on N5. When considered in light of the rapid quench and kinetic isotope effect studies presented in Chapter 3 and the X-ray crystallographic evidence showing the close juxtaposition of N5 and the C2 atom of IPP, these data strongly suggest that the reduced flavin of IDI-2 plays a direct role in isomerizing the IPP double bond, perhaps by deprotonation of the *pro R* C2-H of IPP.

***4.3.4 Linear free energy relationships on the pre-steady state kinetic parameters*:** The similarity in the pattern of absorbance changes observed when IPP binds to IDI-2 reconstituted with each reduced flavin analogue (Figures 4.1 and 4.2) and the linearity of the LFER plots (Figure 4.6) suggests that the IDI-2 mechanism is not changing as the flavin substituents are altered. To provide additional evidence for this assertion and to characterize the effects of the modified flavins on the pre-steady state kinetics, we performed single-turnover stopped-flow experiments with IDI-2 reconstituted with each flavin analogue, using either IPP or (*R*)-[2-^{2}H]-IPP as the substrate. The background-corrected data are shown in Figure 4.7 along with non-linear fits to exponential equations. The fitted kinetic parameters are summarized in Table 4.3.

The data reveal several interesting patterns. First, as was observed with FMN in section ***3.3.9***, the time-dependent changes in the absorbance of each IDI-2 bound flavin analogue upon mixing with IPP were very similar and were characterized by a rapid increase in absorbance followed by a slower, but kinetically competent approach to an equilibrium absorbance level (Figure 4.7). This suggests that there are no gross

alterations in the kinetic mechanism when different flavin analogues are used as coenzymes. Interestingly, the observed rates of both kinetic phases (for both IPP and (*R*)-[2-^{2}H]-IPP substrates) were sensitive to the altered 7- and 8-substituents of the flavin analogues, and Hammett plots of the pre-steady state kinetic paramters yielded ρ values of ~ -1.5 and ~ -3 for $k_{obs,1}$ and $k_{obs,2}$, respectively, for both substrates (Figure 4.8). The different ρ values measured for $k_{obs,1}$ and $k_{obs,2}$ suggest that multiple steps in the IDI-2 catalyzed reaction may be sensitive to the electronic properties of the flavin and, if this is the case, these steps appear to be effected to different extents by the inductive properties of the substituents.

Based on the results from Chapters 2 and 3, we concluded that the flavin intermediate that forms in the fast phase of the forward reaction and which persists in significant quantities at equilibrium is an anionic, reduced flavin (FMNH-) with altered absorption properties relative to the resting enzyme form. However, the significant ρ value measured on the observed rate of formation of the intermediate seems to suggest that a substantial degree of negative charge is being lost on the flavin during the fast reaction phase. One potential explanation for this is that the FMNH- in the resting state is indeed being protonated at N1 to form an $FMNH_2$ intermediate. At present though, it is not clear whether protonation at N1 could lead to a ρ value with a magnitude as large as ~ 1.5, as the charge being lost at N1 would be farther away from the altered substituents than the charge-bearing atoms in the reference reaction. It is possible (as suggested by the preliminary global kinetic simulations in Chapter 3) that the rate of

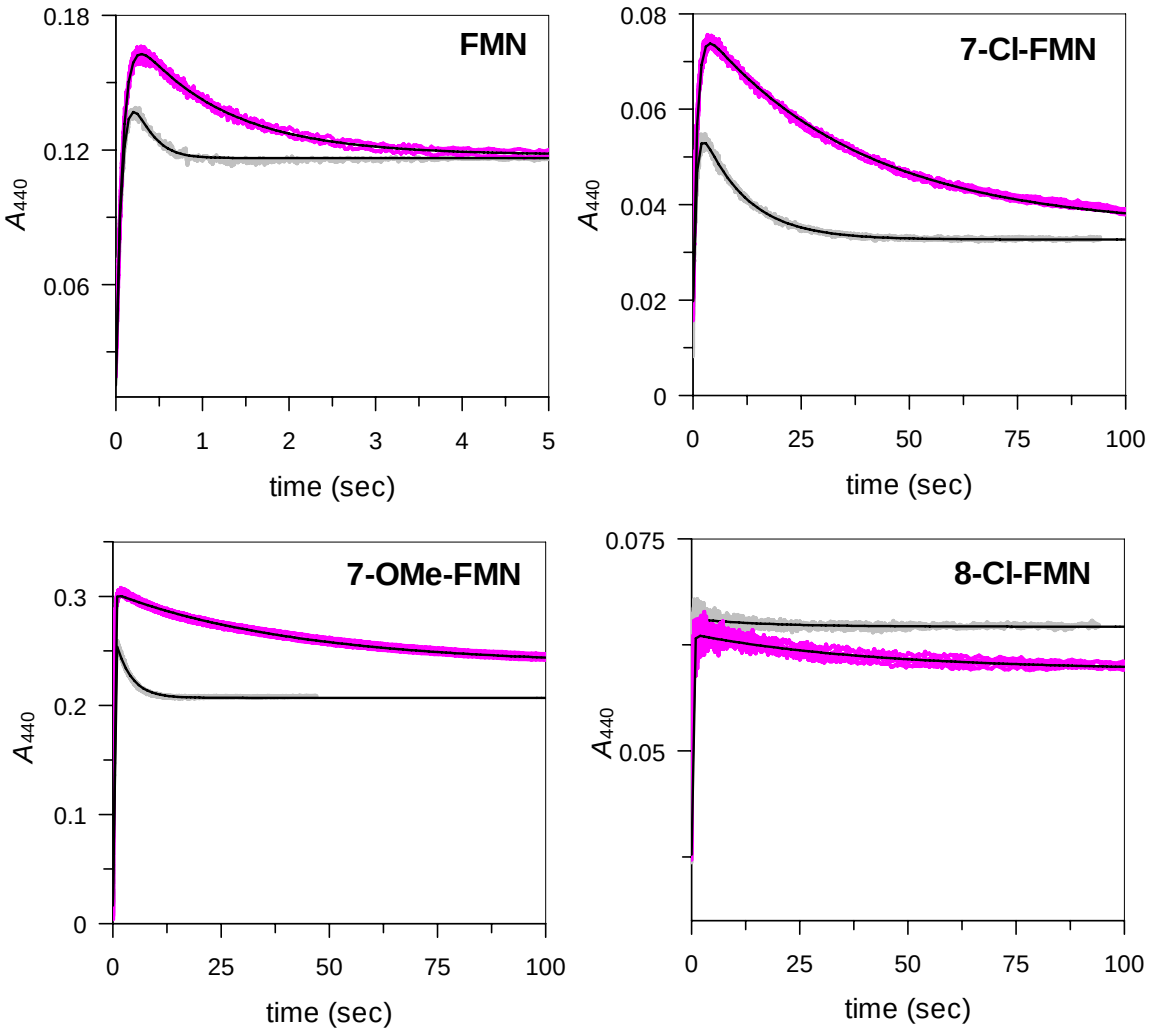

Figure 4.7: Single-turnover stopped flow studies with either IPP or (*R*)-[2-^{2}H]-IPP as the substrate using IDI-2 reconstituted with the FMN analogues. The flavin used for each set of reactions is indicated in each individual panel. The raw data were corrected by subtracting the background absorbance and the data are plotted as a change in absorbance at 440 nm. The time courses with IPP as the substrate are shown in gray and the time courses with (*R*)-[2-^{2}H]-IPP as the substrate are shown in fuschia. The data were fitted with exponential equations (fits are shown with black lines). The parameter estimates derived from the fits are shown in Table 4.3.

flavin intermediate accumulation is similar to its rate of decay, in which case substituent effects on the rate of decay of the intermediate could also contribute significantly to the

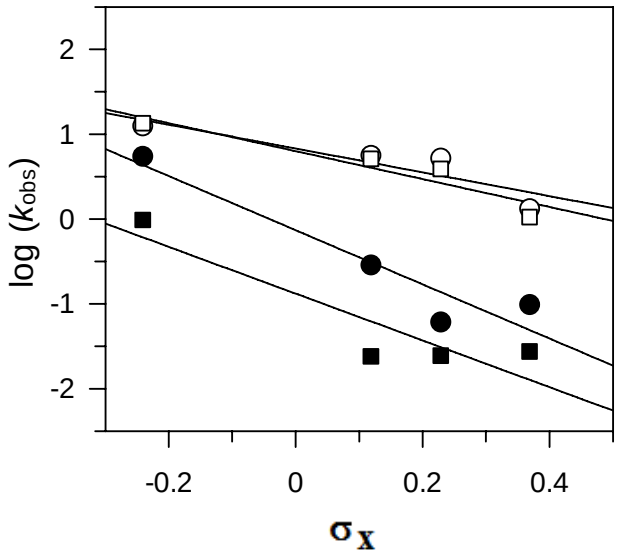

Figure 4.8: Hammett plots of the pre-steady state kinetic rate constants, $k_{obs,1}$ (white symbols) and $k_{obs,2}$ (black symbols), for the reaction with IPP (circles) and (*R*)-[2-^{2}H]-IPP (squares). The ρ values for $k_{obs,1}$ and $k_{obs,2}$ for the IPP reaction were -1.4 ± 0.5 and -3.2 ± 0.7, respectively. The ρ values for $k_{obs,1}$ and $k_{obs,2}$ for the (*R*)-[2-^{2}H]-IPP reaction were -1.6 ± 0.4 and -3 ± 1, respectively.

apparent LFER on the fast phase rate. Alternatively, the putative enzyme conformational change, structural distortion of the FMNH- molecule, and stacking interaction between the bound substrate and FMNH- could somehow serve to redistribute the electron density of the flavin in the fast reaction phase, leading to a net loss of electron density near the benzene portion of the isoalloxazine moiety. In this scenario, the negative charge on FMNH- may become localized primarily on the N1 atom, where it could be electrostatically stabilized by the side chain of Lys186.

The observed rate of the slow phase ($k_{obs,2}$) seems to be more sensitive to the flavin substituents than the fast phase, giving ρ values of ~ -3 in the Hammett plots for IPP and (*R*)-[2-^{2}H]-IPP. This observation suggests that the microscopic rate constants

that most strongly govern $k_{obs,2}$ are affected more strongly by the inductive properties of the subsitituents than the microscopic rate constants that most strongly govern the fast phase rate. The significant kinetic isotope effects measured on $k_{obs,2}$ with (*R*)-[2-^{2}H]-IPP as the substrate (Table 4.3) suggest that this phase involves IPP C2-H/D bond cleavage. Interestingly, as was observed with FMN as the coenzyme in Chapter 3, the substrate kinetic isotope effect does not appear to be strongly expressed on $k_{obs,1}$, as the calculated $^{D}k_{obs,1}$ values were all near unity (ranging from ~ 0.9 – 1.3). Because of these observations, our tentative interpretation of the pre-setady state kinetic data is that the LFERs on $k_{obs,1}$ and $k_{obs,2}$ arise from substituent effects on different steps of the IDI-2 catalyzed reaction, with the stronger effect (ρ ~ -3) being somehow correlated with IPP deprotonation in the slow reaction phase. If the reduced LFER on $k_{obs,1}$ (ρ ~ -1.5) was the result of a partial expression of a stronger substituent effect (ρ ~ -3) on a slower step following flavin intermediate formation (which could happen if the LFER is only expressed on the microscopic rate constant leading to flavin intermediate decay and if the relative rates of intermediate formation and decay are similar), then we would have likewise expected a partial expression of the substrate kinetic isotope effect on $k_{obs,1}$ that is proportional to the expression of the LFER on $k_{obs,1}$.

4.3.5 Linear free energy relationships on $^{D}k_{cat}$: The single turnover stopped-flow results presented in the previous section suggested that multiple steps in the IDI-2 catalyzed reaction may be sensitive to the altered electronic properties of the flaivn analogues,

which could lead to the different sensitivity constants determined in Hammett plots of the

flavin	substrate	A_o	k_o	A_1	$k_{obs,1}$	$^{D}k_{obs,1}$	$-A_2$	$k_{obs,2}$	$^{D}k_{obs,2}$	C
FMN	H-IPP	-	-	.21(1)	12.4(2)	0.94	.11(1)	5.4(1)	5.7	.0221
	D-IPP	-	-	.167(1)	13.2(1)		.064(1)	.95(1)		.0151
7-OMe	H-IPP	-	-	.248(1)	5.5(1)	1.1	.063(1)	.281(4)	12	.0218(1)
	D-IPP	-	-	.287(1)	5.0(1)		.066(1)	.0231(2)		.017(1)
8-Cl	H-IPP	.0088(2)	99(6)	.0150(1)	5.1(1)	1.3	.0010(1)	.06(1)	2.5	.0418(3)
	D-IPP	.0080(4)	49(5)	.0180(2)	3.8(1)		.0042(1)	.024(1)		.0378(4)
7-Cl	H-IPP	-	-	.041(1)	1.30(1)	1.3	.0281(2)	.096(1)	3.6	.0197(1)
	D-IPP	-	-	.059(1)	1.03(1)		.0440(1)	.0269(1)		.0199(1)

Table 4.3: Summary of pre-steady state kinetic constants determined by fitting the single-turnover reactions shown in Figure 4.7 to a double exponential equation. The reaction with 8-Cl-FMN required an additional fast exponential phase for fitting.

fast and slow pre-setady state kinetic rates. To determine whether these other steps in the kinetic mechanism are more sensitive to flavin substituents than the step involving IPP C2-H/D bond cleavage, we performed a combined KIE/LFER study to quantify the effects of the flavin substituents on the initial velocity of DMAPP formation from either IPP or (*R*)-[2-^{2}H]-IPP under pseudo-first order conditions (*122*). The results (Figure 4.9 and Table 4.4) show that primary substrate kinetic isotope effects of similar magnitude are measured on k_{cat} for each FMN analogue, suggesting that IPP C2-H/D bond cleavage is at least partially rate limiting with each flavin as the coenzyme. Hammett plots of the reactions with IPP and (*R*)-[2-^{2}H]-IPP (*122*) suggest that the sensitivities of the two reactions (ρ = -2.5 ± 0.4 and -2.7 ± 0.5, respectively) to the inductive properties of the

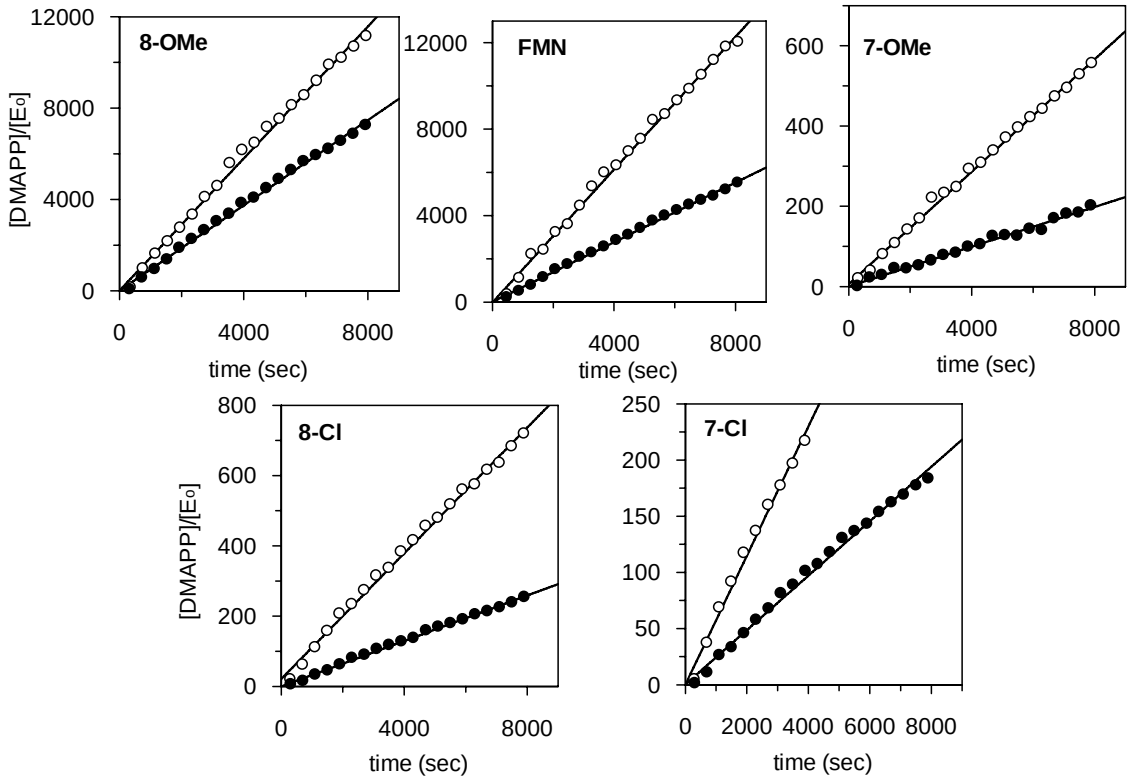

Figure 4.9: Flavin substituent effects on the initial velocity of DMAPP formation from IPP (open circles) and (*R*)-[2-^{2}H]-IPP (closed circles) substrates as determined by ^{1}H-NMR. The flavin analogue used for each set of experiments is indicated in each panel. To facilitate comparison, the DMAPP concentrations have been normalized by the total enzyme concentration used in the assay (listed in Table 4.4).

flavin substituents are within error of each other. Thus, the extent of charge accumulation on the flavin in the rate-limiting transition state(s) appears to be similar for both substrates, and the relative extents of C2-H and C2-D bond cleavge in the transition state seem to be similar as the flavin substituents are altered. This is the result expected if proton transfer is occurring from IPP to the N5 atom of the flavin in the transition state and if the mechanism is not changing as the flavin substituents are altered (i.e., the

position of the transition state along the reaction coordinates for charge accumulation and proton transfer is not moving). If multiple steps in the kinetic mechanism are sensitive to the inductive effects of the flavin substituents, then the heights of the energetic barriers to these steps may be altered to similar extents, such that the expression of the kinetic isotope effect on k_{cat} is relatively unaltered.

flavin	substrate	[E] (μM)	k_{cat} (s^{-1})	R^2	log (k_{cat})	$^{D}k_{cat}$
8-OMe-FMN	IPP	0.1	1.45(2)	0.998	0.16(1)	1.6
	(*R*)-[2-^{2}H]-IPP	0.2	0.93(1)	0.999	-0.032(5)	
FMN	IPP	0.1	1.54(2)	0.998	0.19(1)	2.2
	(*R*)-[2-^{2}H]-IPP	0.3	0.691(7)	0.999	-0.161(4)	
7-OMe-FMN	IPP	1	0.0700(9)	0.999	-1.15(1)	2.8
	(*R*)-[2-^{2}H]-IPP	2	0.0247(6)	0.995	-1.61(1)	
8-Cl-FMN	IPP	1.5	0.089(1)	0.998	-1.05(1)	2.7
	(*R*)-[2-^{2}H]-IPP	3	0.0324(4)	0.999	-1.49(1)	
7-Cl-FMN	IPP	5	.057(2)	0.995	-1.24(2)	2.4
	(*R*)-[2-^{2}H]-IPP	5	.0242(4)	0.997	-1.62(1)	

Table 4.4. Summary of combined KIE/LFER kinetic data.

4.4 Mechanistic Implications

In Chapter 1, we proposed several potential chemical mechanisms for the 1,3-allylic isomerization of IPP to DMAPP catalyzed by IDI-2 (Scheme 1.15) based on studies performed on other flavoenzymes that catalyze reactions involving no net redox

change. In these proposed mechanisms for IDI-2, a variety of putative catalytic roles were considered for the reduced FMN coenzyme. These included cryptic $1e^-$ or $2e^-$ redox cycles, electrostatic catalysis, nucleophilic catalysis, and acid/base chemistry. We will now revisit several of these putative chemical mechanisms in light of the spectroscopic and mechanistic studies performed in Chapters 2-4. Our results most strongly support a role for the reduced FMN coenzyme as an acid/base catalyst.

4.4.1 A flavin intermediate accumulates upon IPP or DMAPP binding: Early mechanistic studies of IDI-2 indicated that the FMN coenzyme needs to be reduced for catalysis and that only catalytic quantities of reductant are required for multiple turnovers of IPP to DMAPP (*55, 56, 82*). Consistent with the lack of a net redox change in the substrate/product, these studies indicated that each IDI-2 catalytic cycle begins and ends with a reduced flavin. The UV-visible absorption properties of the IDI-2 bound reduced flavin reported in Chapter 2 and in other studies (*56, 90, 92*) are consistent with an anionic reduced flavin species (FMNH-) bound to the IDI-2 active site in the resting form of the enzyme. This assignment seems to make sense because the pK_a for the N1 atom of reduced FMN in solution is 6.7 (*94, 95*), suggesting that the majority of the reduced flavin within cells should be ionized at physiological pH values. In addition, X-ray crystallographic (*60, 61, 88, 89*) and bioinformatic studies (*7*) have shown that an absolutely conserved lysine residue (Lys186 in *S. aureus* IDI-2) is within hydrogen bonding distance of N1. If this Lys residue is protonated at physiological pH, then it could engage in electrostatic interactions with the reduced flavin to facilitate binding of

$FMNH^-$ to apo-IDI-2. A role for Lys186 in $FMNH^-$ binding is also supported by our control experiments for the kinetic studies of the K186A mutant in Chapter 3, which showed that increased levels of reduced FMN were required to saturate the rate of steady state turnover for this mutant.

Binding of IPP or DMAPP to the IDI-2:$FMNH^-$ resting state is coupled to a change in the absorbance of the $FMNH^-$ chromophore, suggesting the accumulation of a flavin intermediate during catalysis (*90, 92*). The pre-steady state single turnover stopped flow studies presented in Chapter 3 demonstrate that this flavin intermediate forms quickly and then approaches an equilibrium level at observed rates that are kinetically competent in both the forward and reverse reaction directions (*90*), strongly suggesting that the flavin intermediate is important for the interconversion of IPP and DMAPP. The identity of the flavin intermediate is still not known. Based on comparison to the pH-dependent absorbance properties of other flavoenzymes and flavin analogues, the intermediate was proposed initially to be a neutral reduced FMN species ($FMNH_2$), where the N1 atom of $FMNH^-$ becomes protonated upon IPP/DMAPP binding (*90, 92*).

However, the results presented in Chapter 2 argue that the intermediate could be an anionic FMNH- species, whose ring conformation or active site environment differs from that of the resting enzyme form. Several lines of evidence support this hypothesis. First, the UV-visible absorbance spectrum of the flavin intermediate is relatively insensitive to changes in solution pH from the 7.0 - 10.0. Thus, if the N1 atom is being protonated upon IPP binding, then the pK_a of N1 is being elevated in the IDI-2:$FMNH_2$:IPP complex to a value > 10.0 (at least 3 pK_a units higher that the pK_a of N1 in

solution). Second, the absorbance of the IDI-2 bound flavin intermediate is red-shifted and is more intense than the absorbance of free $FMNH_2$ in solution. Third, when the most likely amino acid candidates for protonation of N1 (Lys186 and His149) are mutated, there is very little effect on the absorbance properties of the flavin intermediate. Finally, time-dependent DFT calculations, guided by the co-crystal structure of IDI-2 in complex with reduced FMN and IPP (*89*), suggested that a combination of active site desolvation, conformational distortion of the isoalloxazine moiety, and π-stacking between the flavin and IPP can potentially lead to absorbance changes similar to those observed experimentally, without having to protonate the N1 atom of $FMNH^-$.

Our currently favored hypothesis is that IPP binding to the IDI-2:$FMNH^-$ resting state induces an enzyme conformational change involving the closure of the *N*-terminal portion of IDI-2. This region of IDI-2 is disorderd in the crystal structures solved in the absence of IPP or pyrophosphate (*60, 61*), but folds in to make several intramolecular and intermolecular (with IPP) hydrogen bonding and electrostatic contacts in the presence of either IPP or pyrophosphate (*88, 89*). This putative conformational change would be consistent with the increase in binding affinity of FMN to the IDI-2:FMN:IPP ternary complex relative to the IDI-2:FMN binary complex (*56*). We propose that this putative conformational change results in the desolvation of the IDI-2 active site and in the structural distortion of the flavin isoalloxazine moiety, which together serve to alter the absorption properties of the FMNH- coenzyme. It is still unclear whether a similar $FMNH^-$ intermediate species forms rapidly upon DMAPP binding in the reverse direction. While the pre-steday state changes in the UV-visible absorption spectrum of

the reduced flavin associated with DMAPP binding are very similar to the changes seen in the forward direction, our data did not seem to require the inclusion of an IDI-2:$FMNH^-_{intermediate}$:DMAPP species for global simulation of the kinetic data.

As will be highlighted below, the protonation state of the N1 atom of the reduced falvin in the IDI-2:FMN_{red}:IPP complex is critical for assessing the role of the flavin in IDI-2 catalysis. At present, while our data points towards and FMNH- species as the intermediate, we cannot exclude the possible existence of an $FMNH_2$ species in the IDI-2:FMN_{red}:IPP complex. We are currently working on experiments using uniformly enriched ^{15}N-FMN and NMR spectroscopy to study the protonation state of N1 in the IDI-2:FMN_{red}:IPP complex more closely. In the following sections where the putative chemical mechanisms for the 1,3-allylic isomerization of IPP to DMAPP are discussed, we will operate under the assumption that the flavin intermediate is an $FMNH^-$ species unless otherwise stated.

4.4.2 Considering an isomerization mechanism involving nucleophilic catalysis: One mechanistic possibility proposed for the reduced FMN of IDI-2 in Chapter 1 is that the N5 atom facilitates the isomerization reaction by forming an N5-alkyl adduct with the substrate, concommitant with protonation of the double bond (Scheme 4.4) in a reaction reminiscent of the mechanism proposed for the isomerization reaction catalyzed by the reduced FAD coenzyme of UDP-galactopyranse mutase (*68*). The formation of such an adduct could help to lower the energy of the transition state for protonation of the double bond by delocalizing the incipient cation from the substrate moiety onto the flavin

isoalloxazine ring system. It is unclear how much the pK_a of the substrate C2 position would be lowered upon formation of the N5-alkylated zwitterionic species (**5**), but the protonated flavin moiety should serve as a good leaving group for the subsequent C2 deprotonation to give DMAPP and the reduced FMNH$^-$ form of the coenzyme with the assistance of an active site base.

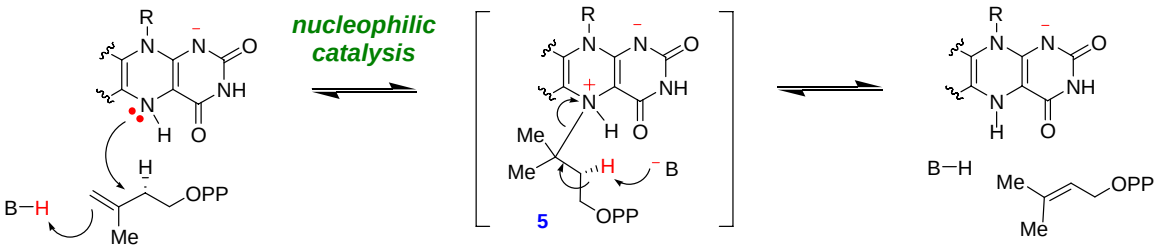

Scheme 4.4: A putative nucleophilic mode of IDI-2 catalysis

While this mechanistic proposal would be consistent with the biochemical, spectroscopic, and LFER studies reported in this dissertation, it is at odds with the inhibition studies performed by the Eguchi and Poulter groups (*86, 111, 149*). Namely, these researchers found that a variety of electrophilically activated IPP and DMAPP analogues (**6-9**, Scheme 4.5) irreversibly inactivated IDI-2 by formaing covalent N5-alkyl adducts with the flavin. The mechanism for inactivation in these studies was proposed to involve protonation of the electrophilic moiety or leaving group, followed by

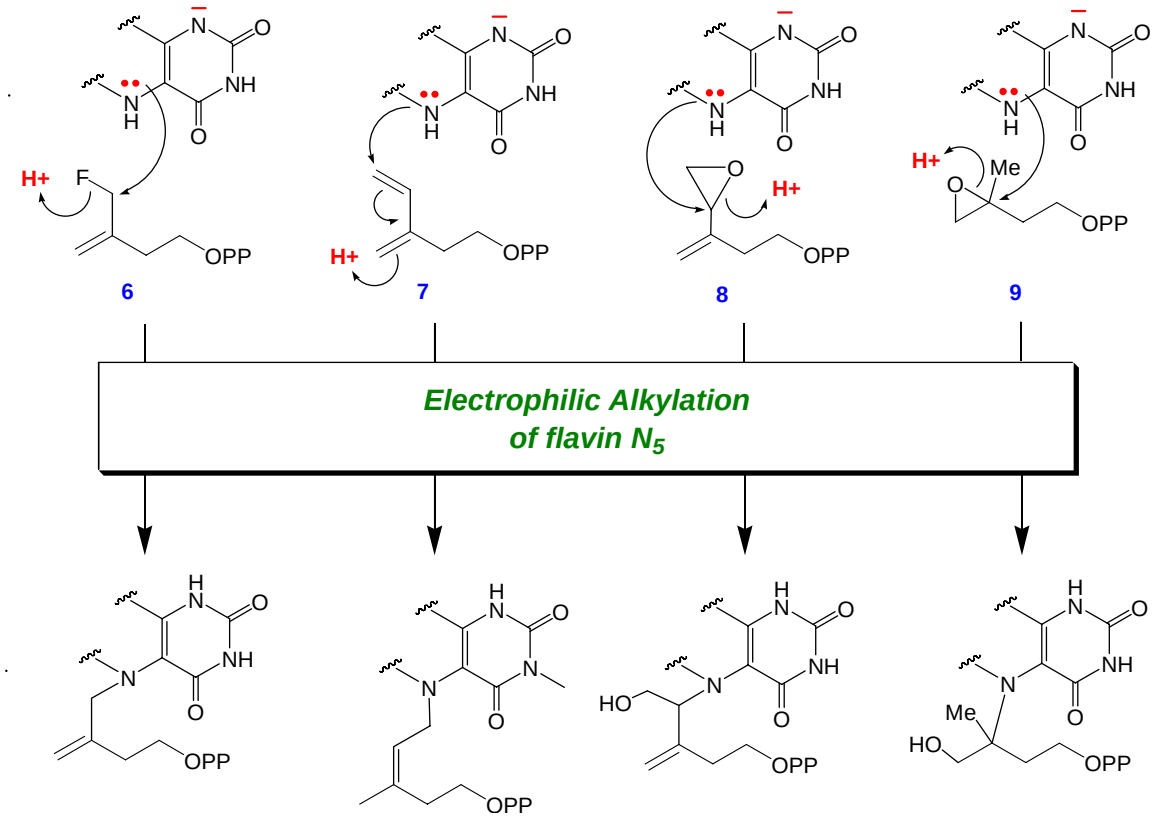

Scheme 4.5: Inhibition of IDI-2 with electrophilic IPP analogues. The flavin N5-alkyl adduct structures were proposed as shown based on the UV-visible absorbance properties and mass spectra of the adducts (*111*).

or concomitant with nucleophilic addition of the N5 atom of the flavin onto the electron-deficient inhibitor (*111*). Interestingly, the epoxide compound (**9**) was also found to be an irreversible inhibitor of IDI-1, where it forms a covalent adduct with the active site cysteine residue that is belived to serve as the base in the isomerization of IPP to DMAPP (*50*). Apparently, the adducts that form between the reduced flavin and these inhibitors in the active site of IDI-2 cannot be deprotonated to form isomerized products. This suggests either that the pK_a of the inhibitor moiety is not acidic enough to be

deprotonated by the active site base, or that adduct formation may somehow orient the inhibitor moiety away from the active site base, or that similar to IDI-1, the active site base of IDI-2 (the N5 atom of the flavin) is unavailable to deprotonate the substrate because is has been used to form an adduct with the inhibitor. Regardless of the explanation for the irreversible inhibition, the observation that these N5-alkyl adducts cannot be further processed into isomerized products strongly suggests that an IDI-2 mechanism involving nucleophilic catalysis by the reduced flavin is unlikely.

Despite this conclusion, these experiments provided several important insights into the active site environment and into the electronic properties of the flavin in the reduced IDI-2:FMN:inhibitor complexes that may be pertinent to the chemical mechanism of the wild type IDI-2 reaction. First, the formation of the N5-alkyl adducts suggests that the N5 atom of reduced FMN is positioned close to the inhibitor in the active site (which subsequent crystallographic studies have confirmed (*89*)) and that the N5 atom accumulates sufficient electron density to serve as a nucleophile with the various inhibitors. While the inhibitors are likely artificially activated (relative to IPP) towards nucleophilic addition of the flavin, these observations nevertheless suggest that the electron density on the N5 atom of the flavin may not be strongly delocalized into other portions of the isoalloxazine. This electron density in the vicinity of N5 could therefore be available to facilitate isomerization of the IPP/DMAPP double bond by other means – such as by serving as a base to catalyze proton transfers to and from the substrate. The inhibition data also imply that a separate active site group may be required to protonate the inhibitor prior to (or concomitant with) nucleophilic attack, suggesting

that a general acid may be present somewhere in the active site. The detailed structures of the inhibition adducts are not known (only mass spectrometry data was reported), so it is still unclear whether the inhibition mechanism is stepwise or concerted. If each of the inhibition reactions led to a single FMN N5-alkyl product, this would suggest a concerted protonation/nucleophilic addition mechanism, which would in turn support the presence of a general acid moiety that is distinct from the N5 atom of the reduced flavin. Due to the potential resonance structures available upon protonation of some of the inhibitors (**6-8**), multiple alkylated flavin products could possibly be obtained if the inhibition occurs in a stepwise fashion through cationic intermediates.

4.4.3 Considering an electrostatic mode of FMN catalysis: Due to the extended π-electron system of the isoalloxazine moiety of flavins, another possible mechanistic role for the reduced FMN of IDI-2 is the electrostatic stabilization of a substrate-derived carbocation intermediate or transition state (Scheme 4.6). In this mechanism, active site amino acid residues are required to catalyze the 1,3-proton addition-elimination reaction. The electron-rich reduced flavin could help to stabilize the cationic intermediate/transition state associated with this reaction. A similar role in the electrostatic stabilization of the cationinc substrate intermediate/transition state has been proposed for a conserved tryptophan residue within the active site of IDI-1 (*50, 51*).

Even though an electrostatic mode of FMN-dependent catalysis is an appealing mechanistic proposal for IDI-2, it is at odds with several different experimental observations. First, IDI-2 is inactive when the flavin is fully oxidized (*55*). While the

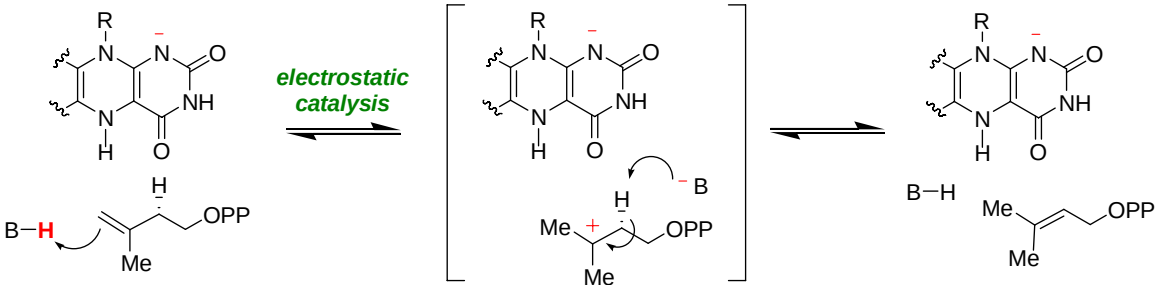

Scheme 4.6: Electrostatic mode of IDI-2 catalysis

distribution of π-electrons in the fully oxidized coenzyme is undoubtedly different from the distribution in the fully reduced coenzyme, the fully oxidized flavin is still an electron-rich molecule that would be expected to support at least a basal level of IDI-2 activity if the primary role of the flavin is to electrostatically stabilize a substrate-derived cation. Similarly, the $2e^-$ -reduced 5-deaza-FMN coenzyme does not support IDI-2 catalysis, which seems unlikely for an electrostatic mode of catalysis unless the stabilization is strongly dependent upon the N5 position of the isoalloxazine (*56, 82*). Finally, and perhaps most importantly, the crystal structure of the fully complexed enzyme in the reduced state reveals the absence of the two putative catalytic amino acid-derived acid/base functional groups required for this mechanism (*89*).

Very recently, a bacterial lycopene cyclase (CrtY) was shown to require a reduced FAD coenzyme to catalyze a non-redox reaction that is very similar to the IDI-2 catalyzed reaction (*150*). CrtY cyclizes both ends of lycopene (a tetraterpenoid) to form *β*-carotene (Scheme 4.7). The cyclization reaction catalyzed by CrtY is typical of isoprenoid biosynthetic enzymes in that it involves protonation of the terminal double

bond of lycopene to form a 3° carbocationic intermediate, followed by C-C bond migration (electrophilic alkylation of the cation) and deprotonation of the resulting carbocation to generate the cyclized products. The CrtY catalyzed reaction is also similar to the IDI-2 catalyzed reaction in that chemistry is mediated by acid/base catalysis through electron deficient intermediates/transition states and requires a reduced $FADH^-$ coenzyme for activity. In this study, the authors synthesized a variety of 8-substituted FAD analogues and demonstrated a linear correlation between the rate of the CrtY-catalyzed reaction and the $2e^-$ redox potential of the flavin analogues. Their results show that as the flavin becomes more electron rich (i.e., as the redox potential decreases), the rate of lycopene cyclization increases. However, in contrast to IDI-2, reduced 5-deaza-flavin was the most active analogue tested, suggesting that the electronic properties of the N5 postion are not very critical for catalysis by CrtY. The reduced 1-deaza-FAD analogue also led to similar levels of activity as the native reduced FAD coenzyme. Thus, the nitrogen atoms at positions 1 and 5 of the isoalloxazine do not seem to be necessary for lycopene cyclization. In addition, mutation of a conserved glutamate residue (proposed to be involved in acid/base catalysis) resulted in the complete loss of lycopene cyclase activity. Because of these observations, the authors proposed that the reduced flavin does not participate directly in the proton addition/abstraction steps required for lycopene cyclization, but rather, serves to electrostatically stabilize cationic intermediate(s) that form during the cyclization process.

Interestingly, if the kinetic data for the flavin analogues reported in this study are potted versus the Hammett σ_x vlaues of the 7- and 8-substituents of the flavin rather than

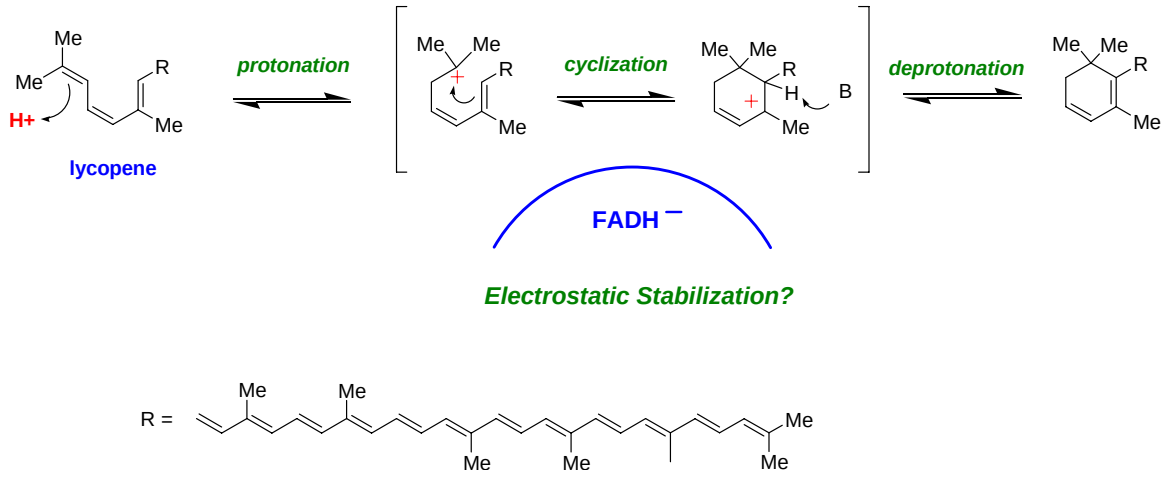

Scheme 4.7: Putative electrostatic catalysis by FADH- in CrtY – a lycopene cyclase (*150*).

the redox potential of the flavin, a ρ value of ~ -0.7 is obtained. When compared to the ρ value of ~ -2.0 determined for the steady state kinetic rate constants for IDI-2, the electrostatic stabilization role proposed for the reduced FAD coenzyme of CrtY appears to result in a smaller degree of positive charge accumulation (or negative charge loss) on the flavin. This result might be expected if the flavin in IDI-2 is acting as a base and if proton transfer to the N5 atom is nearly complete in the transition state, such that a larger amount of positive charge is accumulating on the flaivn in the IDI-2 reaction relative to the CrtY-catalyzed reaction.

4.4.4 Considering acid/base modes of flavin catalysis: If the flavin is not helping to catalyze the isomerization of IPP to DMAPP by electron transfer, nucleophilic, or electrophilic catalysis, then perhaps it functions directly in the protonation/deprotonation

steps as an acid/base catalyst (Schemes 4.8 and 4.9). This hypothesis seems to be in line with the close juxtaposition of the C2 and C4 atoms of IPP with the N5 and N1 atoms of the reduced FMN, respectively, and the lack of any obvious amino acid-derived acid/base functional groups in the vicinity of C2 (*89*). In addition, the rapid quench, KIE and LFER studies reported in Chapters 3 and 4 suggest that the partially rate limiting proton transfer events leading to the 1,3-allylic isomerization are coupled with changes in the electron density of the flavin, most notably the apparaent accumulation of positive charge near the N5 atom. Our data are most consistent with one of two possible modes of flavin catalyzed acid-base chemistry, which differ primarily in the protonation state of the reduced flavin in the effective ground state.

The first possibility is that the flavin provides one of the catalytic acid/base groups, while an active site amino acid provides the other (Scheme 4.8). In this scenario, the structural evidence indicates that the N5 atom likely catalyzes proton transfer at the C2 position of IPP/DMAPP, and that Gln154 is somehow involved in proton transfer to the C4 atom of IPP/DMAPP. The N5 atom of the flavin and the amide side chain of Gln154 are located on opposite faces of the IPP molecule in the active site and appear to be positioned appropriately for an *anti*-1,3-proton addition-elimination. The involvement of Gln154 in catalysis is supported by the absolute conservation of Gln154 in IDI-2 proteins (*7*) and the observation that the Q154N and Q154A mutant enzymes result in ~ 170x and ~860x reductions in k_{cat} in the forward direction, which indicate that the chemical properties of the amide side chain of Gln154 are important for lowering the energy of the rate limiting transition state(s).

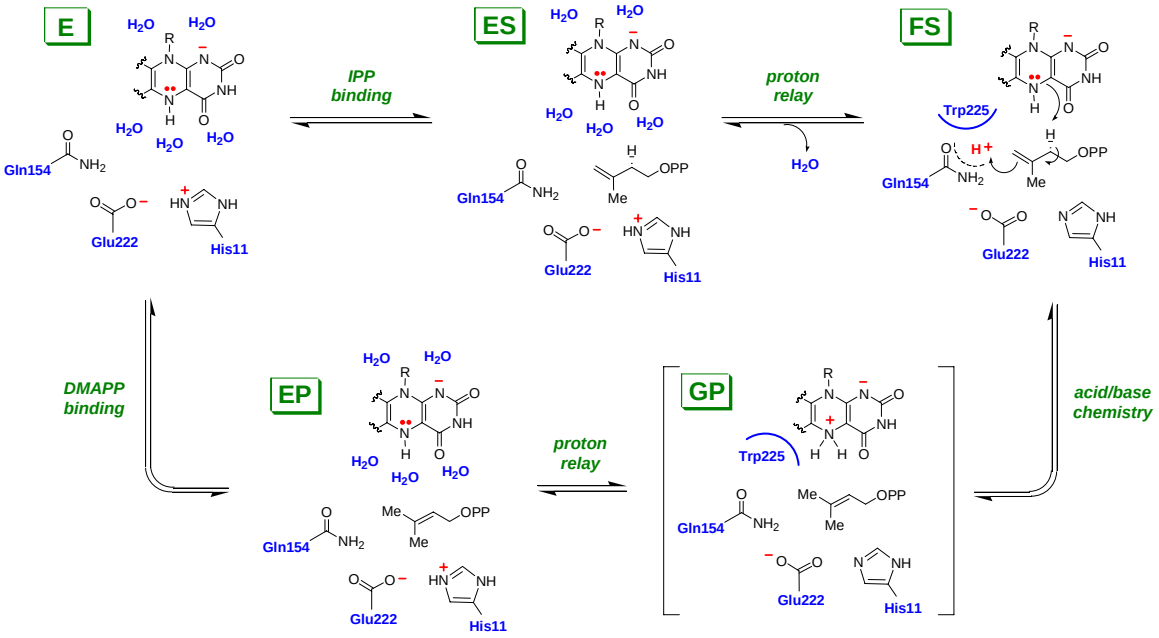

Scheme 4.8: Acid/base chemical mechanism for IDI-2 involving the N5 atom of FMN and the active site Gln154 residue

The pK_a value for protonation of the N5 atom of FMNH$^-$ to form a zwitterionic species is unknown, but has been estimated to lie within the physiological pH range (*87*). The pK_a of N5 could be modulated by the bending of the isoalloxazine ring observed in the crystal structure, which appears to increase the sp^3 character of N5. In this regard, the ^{15}N-NMR studies proposed above should be informative. In addition, a hydrogen bond appears to form between the proton on N5 of FMNH$^-$ and the backbone carbonyl moiety of Met66. This may also enhance the basicity of the N5 postion, and the importance of this interaction for IDI-2 catalysis is underscored by the reduction in k_{cat} observed for the T67A mutant, which is proposed to perturb this hydrogen bonding interaction. The pK_a values for the carbonyl and amine moieties of the amide side chain of Gln154 (pK_a ~ 0 and ~ 16, respectively) suggest that interactions with other active site residues and/or the

electrostatic environment of the active site are likely required to facilitate an acid/base function for Gln154 (*151*). Interestingly, Gln154 appears to be closely associated with two other conserved amino acid residues, His11 and Glu222, which may function together to set up a proton relay from His11 to the C4 position of the bound substrate. Comparing the X-ray crystal structures of IDI-2 from *Sulfolobus shibatae* (*89*) in the presence and absence of IPP reveals slight, but perhaps significant, differences in the orientation of these putative proton relay components upon IPP binding (Figure 4.10). Most notably, these structures show that, upon IPP binding, the distances between both the imidazole side chain of His11 and the carboxylate side chain of Glu222 and the amide group of Gln154 shorten by 0.5 and 0.7 Å, respectively. Based on these observations, it is tempting to speculate that the ultimate proton source could be His11, and that the acidic proton is somehow localized in the direct vicinity of the substrate C4 atom by a combination of hydrogen bonding interactions with Gln154 and electrostatic stabilization by the anionic $FMNH^-$, the alkene moiety of the substrate, and the conserved aromatic side chain of position 225 (which is a Trp residue in the case of *S. aureus* IDI-2).

In this scenario, the ground state for the forward and reverse reactions under pseudo-first order conditions would be the FS and EP complexes (using the same nomenclature that was used to describe the minimal kinetic mechanism in Chapter 3). From our discussion above and in Chapters 2 and 3, we propose that the reduced flavin is in the $FMNH^-$ form in all of the kinetically detectable complexes, with the FS form exhibiting different absorbance properties from E, ES, and EP due to a combination of active site desolvation, bending of the flavin molecule, and/or π-stacking with IPP. From

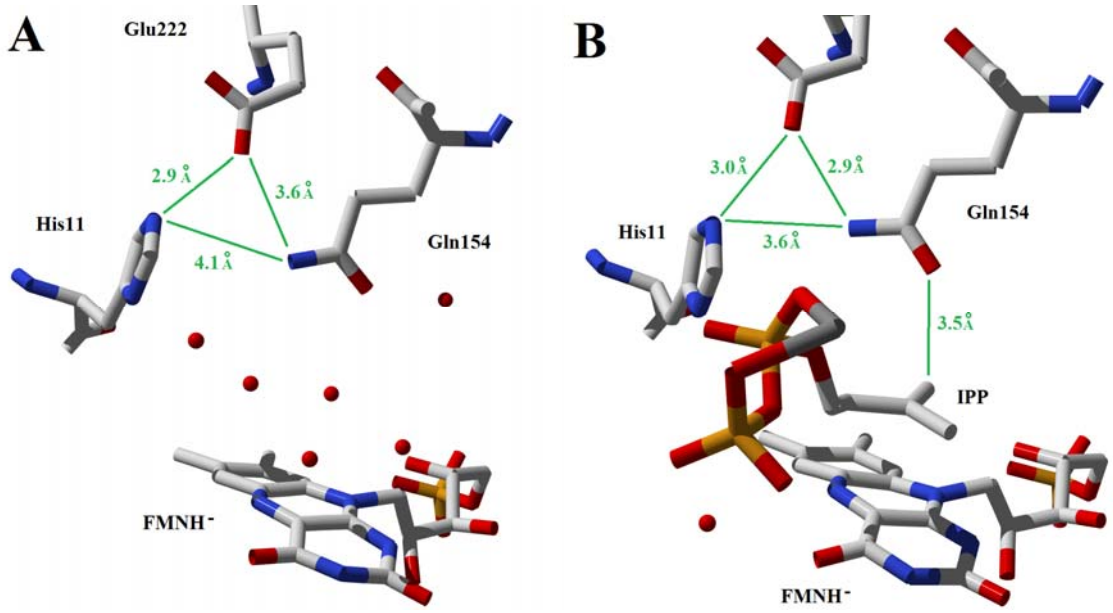

Figure 4.10: Active site of IDI-2 from *Sulfolobus shibatae* in the absence (A) and presence (B) of IPP (*89*). The conserved amino acid residues involved in the putative proton relay are indicated and water molecules are shown as red spheres.

the FS form of the enzyme, Gln154 would help to deliver a proton (perhaps derived ultimately from His11) to C4 of IPP in the forward direction, while the N5 atom of $FMNH^-$ would abstract the *pro R* C2 proton from IPP. In the reverse direction, the EP form of the enzyme may be converted to an unstable reverse-protonated state (GP in Scheme 4.8), where the N5 atom of the zwitterionic $FMNH_2$ could then serve as the acid to protonate C2 of DMAPP, while Gln154 assists in the deprotonation of the DMAPP (*E*)-methyl group. The similarity in the Hammett ρ values for the forward and reverse reactions under pseudo-first order conditions suggests that the net type and amount of charge accumulation on the flavin in the transition state is similar in both reaction directions. This implies that a single transition state may be rate-limiting, and that the

amount of electron density on N5 in the respective ground states for the forward and reverse reactions (FS and EP) is similar.

We have included the extra species (GP) in Scheme 4.8 in order to uphold the principle of microscopic reversibility. At present, however, we do not have any spectroscopic evidence for the existence of the zwitterionic $FMNH_2$ species, and our pre-seady state kinetic data were not conditioned well enough to include an additional species in the global simulations. It should be mentioned that we could achieve convergent global fits of the pre-steady state kinetic data using a kinetic mechanism with 5 steps, but while the standard errors on the variable parameters in these fits were reasonable, most of the variable parameters were unbounded on their upper ends. Thus, if the GP species exists, its free energy is likely substantially higher than any of the other enzyme forms, such that GP does not accumulate to detectable levels in the pre-steady state or at equilibrium. The GP species is also expected to be a kinetically unstable species that either rapidly protonates DMAPP in the reverse direction, or that rapidly isomerizes to the resting protonation state (as in EP) in the forward direction. It is also tempting to speculate that an unstable intermediate (such as GP) could contribute to the heterogeneous appearance of the pre-steady state time courses of flavin intermediate accumulation in the forward and reverse directions (Chapter 3).

The second possibility is that the reduced flavin coenzyme of IDI-2 catalyzes proton transfer at both the C2 and C4 positions of IPP/DMAPP, with the N5 and N1 atoms catalyzing acid/base chemistry at C2 and C4, respectively (Scheme 4.9). In contrast to the acid/base chemical mechanism proposed above, where the N5 atom acts in

concert with Gln154 to catalyze an *anti*-1,3-proton addition-elimination, if the flavin catalyzes both proton transfers, the stereochemical course of the reaction should be a *syn*-1,3-proton addition-elimiation. A postdoctoral research associate in our lab (Dr. Jordi Calveras) is currently trying to address the stereochemistry of solvent deuterium incorporation into the (*E*)-methyl group of DMAPP using stereospecifically tritiated IPP compounds and a chiral methyl analysis approach. If successful, these studies would help us to distinguish whether the general acid in the forward direction protonates IPP from the *re* face (implicating Gln154 as the acid) or the *si* face (implicating the N1 atom of FMN as the acid). Thus, this experiment could provide direct evidence in favor of one of the two acid/base chemical mechanism involving the flavin.

If this mechanism in Scheme 4.9 is operative, the canonical 1,5-dihydro-$FMNH_2$ tautomer could be accumulating in the FS form of the enzyme. If this is the case, the pH-dependence of the UV-visible absorbance of the FS species (reported in Chapter 2), suggests that the pK_a of the N1 position in the FS complex is > 10.0. The chemical mechanism for the *syn*-1,3-proton addition-elimination in this scenario would be initiated by transfer of the proton from N1 to the IPP double bond and by abstraction of the C2 proton of IPP by N5 to make the zwitterionic $FMNH_2$ complex with DMAPP (GP). Gln154 may assist catalysis by holding the isoprene substrate in a proper orientation relative to the flavin, helping to ensure optimal proton transfer rates. The GP complex would then be deprotonated at N5 to generate the EP complex. Consistent with the LFER studies, the N5 atom of the flavin would be accumulating positive charge in the transition

state in both reaction directions. As discussed above, the GP complex may not be a true intermediate in the reaction.

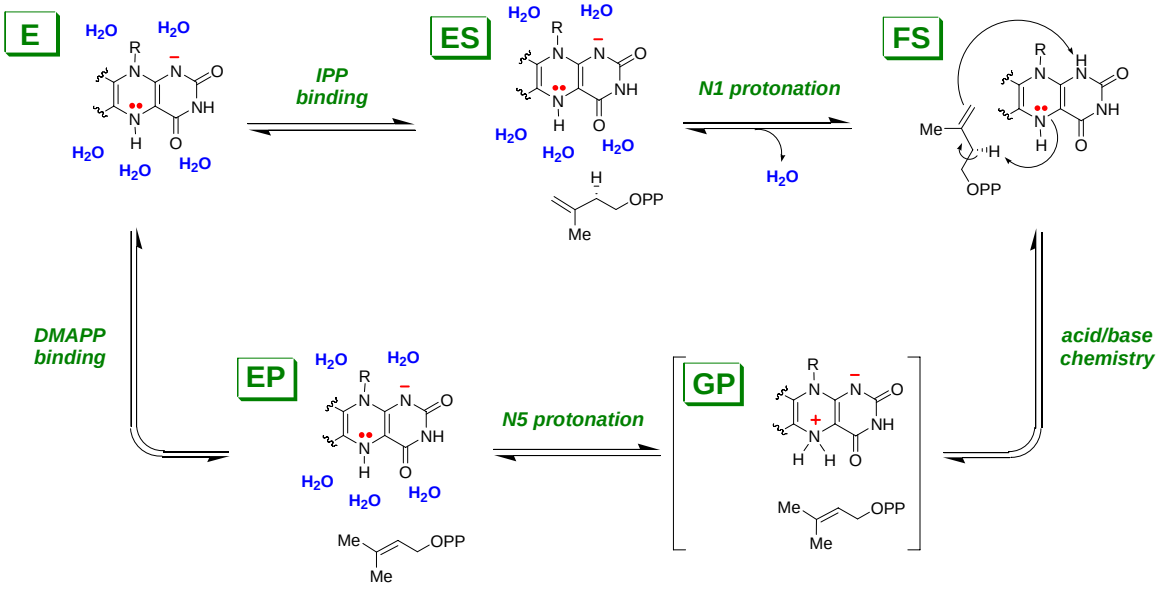

Scheme 4.9: Acid/base chemical mechanism for IDI-2 involving both the N1 and N5 atoms of reduced FMN

As proposed, the acid/base chemical mechanisms in Schemes 4.8 and 4.9 are characterized by transition states where bonds to both solvent exchangeable protons and to the IPP-C2 proton are moving. Thus, these mechanisms could account for the primary, normal kinetic isotope effects measured on k_{cat} and k_{cat}/K_m. In addition, the putative transition states in both mechanisms involve the accumulation of positive charge on the flavin at N5, consistent with the ρ values measured in the LFER studies. The ^{15}N-NMR studies of the flavin intermediate discussed above should help to identify the protonation state of the N1 and N5 atoms of the flaivn in the FS complex, and the chiral methyl

analysis should help to determine the stereochemistry of proton delivery to IPP. Together, these ongoing studies may help us to distinguish among the two proposed mechanisms for flavin-catalyzed acid/base chemistry in the IDI-2 catalyzed reaction.

4.4.5 Considering stepwise and concerted chemical mechanisms for IDI-2 catalysis: At present, we do not have any definitive evidence to distinguish between a stepwise isomerization mechanism involving a tertiary carbocation intermediate and a concerted mechanism involving simultaneous protonation/deprotonation at the C2 and C4 atoms of IPP/DMAPP. The proposed mechanisms in Scheme 4.8 and 4.9 are drawn showing a concerted 1,3-proton addition-elimination, but in both cases, a stepwise transformation can be envisioned where protonation precedes deprotonation in both reaction directions. This order of events is likely enforced by the high pK_a of the allylic proton and the electrostatic repulsion that would exist between a cabanionic substrate intermediate and the reduced flavin if deprotonation were to precede protonation. The only stipulation on a stepwise mechanism that can be made on the basis of our data is that the activation energies of the transition states for double bond protonation and tertiary carbocation deprotonation need to be similar in magnitude, such that the deprotonation step is partially rate limiting – enabling the expression of a primary substrate deuterium KIE on k_{cat} in the forward direction. In a stepwise transformation, the tertiary carbocation intermediate would accumulate simultaneously with the anionic $FMNH^-$ in both of our proposed mechanisms and, thus, the energy of the intermediate could be lowered somewhat by electrostatic interactions with the flavin. The preponderance of hydride

shifts, methyl shifts, and C-C bond rearrangements observed in the reactions catalyzed by many isoprenoid biosynthetic enzymes (*32, 52*) suggest that tertiary carbocation intermediates are commonly encountered by isoprenoid biosynthetic enzymes, and the IDI-2 catalyzed reaction may be no exception to this general phenomenon.

At present, the strongest evidence against a stepwise isomerization mechanism for IDI-2 is the observation by Poulter and co-workers that the cationic NIPP analogue (shown in Scheme 1.6) is only a weak competitive inhibitor of IDI-2, with a K_i value in the low μM range – very similar to the K_m value for IPP (*92*). Recall from our discussion in Chapter 1 that the quaternary ammonium center in NIPP is believed to mimic a tertiary carbocation and that this same inhibitor exhibits a K_i value in the pM range for IDI-1 – a full 4-5 orders of magnitude tighter than it binds to IDI-2. Thus, the transition state for the IDI-1 catalyzed reaction appears to involve a substantially higher degree of cationic character on the substrate isoprene moiety than the transition state for the IDI-2 catalyzed reaction – an observation that is consistent with a mechanism that is more stepwise in the case of IDI-1 and more concerted in the case of IDI-2. This conclusion may also be supported by the different solvent deuterium incorporation patterns into IPP and DMAPP catalyzed by IDI-1 and IDI-2 (*43, 59*). In IDI-1, all of the protons (except those at C1) are exchanged with solvent deuterium, perhaps indicating the presence of a reactive carbocation intermediate that can be deprotonated by multiple (weak) bases present in the IDI-1 active site. In contrast, IDI-2 only catalyzes the exchange of the *pro R* proton at C2 of IPP and the (*E*)-methyl protons of DMAPP. This strict regio- and stereochemistry would be expected for a concerted reaction, where no formal substrate carbocation is ever

formed. A concerted mechanism does not necessarily imply that the isoprene moiety in the transition state for isomerization in the IDI-2 catalyzed reaction is devoid of cationic character. Indeed, using (*Z*)-monofluoromethyl- and (*Z*)-difluoromethyl-DMAPP analogues, Poulter and co-workers have estimated that each fluorine atom that is added to the (*Z*)-methyl group of DMAPP reduces the rate of the IDI-2 catalyzed reverse reaction by 30-100x (*111*), a result that is consistent with an electron deficient transition state. Interestingly, the rate reductions observed for these fluoromethyl DMAPP analogues in the IDI-2 catalyzed reaction is somewhat attenuated from the rate reductions observed in the solvolysis of similar fluorinated dimethylallyl methanesulfonate derivatives – a reaction that proceeds via an allylic cation intermediate (*34, 152*). This seems to suggest that a smaller amount of positive charge is accumulating on the substrate in the IDI-2 catalyzed reaction relative to the solvolysis model reaction, perhaps providing indirect evidence for a concerted 1,3-proton addition-elimination in the IDI-2 catalyzed reaction.

4.5 Closing Remarks

The cumulative mechanistic and structural data on IDI-2 provided by us and others suggests that the reduced FMN coenzyme of IDI-2 plays an important role in catalyzing the reversible isomerization of IPP and DMAPP (*7, 55-61, 82, 86, 88-90, 92, 111, 149*). The data point towards a chemical mechanism involving proton addition-elimination chemistry that is either partially or entirely mediated by the reduced flavin. In particular, the involvement of the N5 atom of the $2e^-$ reduced FMNH- in mediating proton transfers in some flavoenzymes has recently gained notoriety (*87, 90, 92, 153-*

156). Key to this acid/base catalytic ability of reduced flavins is the capacity of flavoenzyme active sites to stabilize the zwitterionic form of $FMNH_2$ – a chemical species that has not yet been conclusively demonstrated to exist within an enzyme active site. The participation of flavin coenzymes in reactions that do not involve changes in the redox state of the substrate/product has been recognized recently to be fairly common (*63*), and altogether, many of these flavoenzymes help to illustrate the catalytic diversity of this common coenzyme (*62*).

Chapter 5: Mechanistic Stuides of 1-Aminocyclopropane-1-carboxylate Deaminase (ACCD) from *Pseudomonas* sp. ACP

5.1 Introduction

5.1.1 Background: 1-Aminocyclopropane-1-carboxylic acid (ACC, **1**) was first isolated from the juices of apples, pears, and several other plants in the *Rosaceae* family in 1957 (*157*). It was subsequently discovered that ACC is the immediate biosynthetic precursor to ethylene (*158*), an important plant hormone that regulates fruit ripening, seed germination, leaf scenescence, and responses to environmental stress (*159*). The pathway to ethylene biosynthesis involves two enzymatic steps (Scheme 5.1): conversion of *S*-adenosyl-L-methionine (SAM) to ACC by the PLP-dependent enzyme ACC synthase, followed by the conversion of ACC to ethylene by the non-heme iron enzyme ACC oxidase (*159*). In 1978, Honma and co-workers discovered that two soil-dwelling

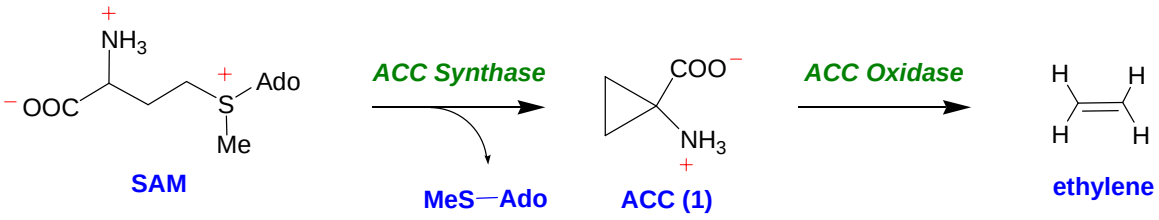

Scheme 5.1: ACC (1) is an intermediate in ethylene biosynthesis in plants.

organisms, the bacterium *Pseudomonas* sp. ACP and the fungus *Hansenula saturnus*, could survive in media containing ACC as the sole nitrogen source (*160*), and have the

ability to convert ACC to α-ketobutyrate (α-KB, **2**) and ammonia (Scheme 5.2). They subsequently purified the enzyme responsible for this activity from both organisms, showed that it contained a tightly bound pyridoxal-5′-phosphate (PLP) coenzyme, and dubbed the enzyme ACC deaminase (ACCD). The physiological function of ACCD in these soil organisms may be to salvage useful sources of carbon and nitrogen for other metabolic needs. However, bacterial ACCDs have been widely used in transgenic plants to regulate ethylene biosynthesis. In fact, ACCD expression in plant tissues can lead to significant delays in fruit ripening, helping to increase the shelf life of fruits and vegetables (*161*).

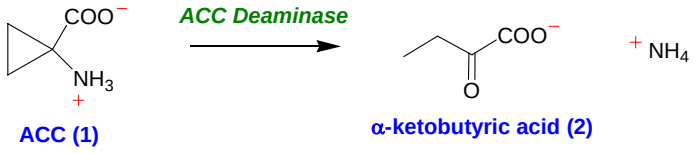

Scheme 5.2: The reaction catalyzed by 1-aminocyclopropane-1-carboxylate deaminase (ACCD) in certain soil bacteria and fungi.

5.1.2 ACCD is unusual among PLP-dependent enzymes: PLP-dependent enzymes catalyze a diverse array of chemical transformations including transamination, decarboxylation, deamination, racemization, β-elimination, and others (*162*). Despite these numerous enzymatic activities, most PLP-dependent enzymes share several common features early in their catalytic cycles (Scheme 5.3). In the resting state of most PLP-dependent enzymes, the PLP coenzyme is covalently linked to an active site lysine residue via an imine linkage (also known as an internal Schiff base or an internal

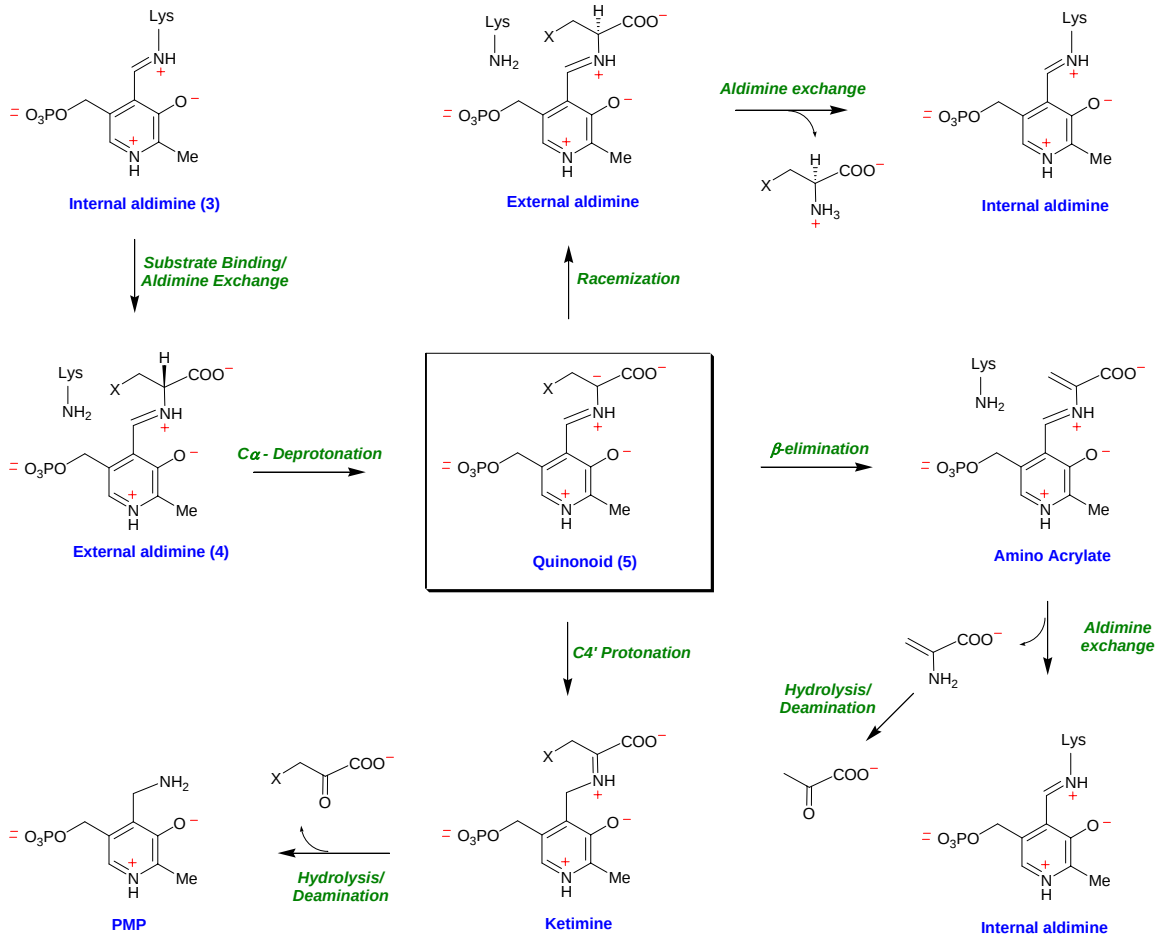

Scheme 5.3: Typical modes of pyridoxal-5′-phosphate (PLP)-dependent catalysis. The catalytic cycles of most PLP-dependent enzymes begin with an aldimine exchange reaction to generate an external aldimine (**4**), from which the PLP-α-anion equivalent (or quinonoid, **5**) is formed.

aldimine, **3**). Upon binding of a substrate containing a primary amine functional group, an aldimine exchange reaction occurs, generating a Schiff base between the coenzyme and the substrate (an external aldimine, **4**) and liberating the active site Lys residue. The formation of the external aldimine links the substrate to the electrophilic pyridinium moiety of PLP via the protonated iminium of the Schiff base. This is a key step in the

chemical mechanism of nearly all PLP-dependent enzymes. The next step in most PLP-dependent enzymes involves generation of a C_α-anion (or quinonoid, **5**), a central intermediate which is stabilized by the electrophilic iminium and pyridinium moieties of PLP. Typically, the quinonoid is generated by C_α deprotonation or decarboxylation. The choice for deprotonation or decarboxylation is governed by which bond (C_α-H or C_α-COO^-) is held perpendicular to the plane of the PLP ring, allowing for maximum orbital overlap between the scissile σ-bond of the substrate and the π-electron system of the coenzyme (*163*). From the quinonoid intermediate, a variety of subsequent chemical transformations can occur. These transformations (some of which are illustrated in Scheme 5.3) are governed by the specific active site architecture of the enzyme in question (*162, 164*).

The reaction catalyzed by ACCD is unusual among PLP-dependent enzymes because the amino acid substrate, ACC, contains no C_α proton and the carboxyl group is retained in the α-KB product. Thus, there is no obvious route to the quinonoid intermediate typically employed in PLP-dependent enzymes. The α-anion equivalent (if it indeed forms) is likely generated by cleavage of one of the two C_α-C_β bonds of ACC. The breaking of a C_α-C_β bond by PLP-enzymes is an extremely rare event, and has been observed in only one other enzyme, serine hydroxymethyltransferase (SHMTase) (*165, 166*). SHMTase transfers a methylene equivalent from serine to tetrahydrofolate, generating glycine and 5,10-CH_2-THF as the reaction products (Scheme 5.4). Following external aldimine formation with serine, two mechanisms have been proposed for the C_α-C_β bond cleavage event: retro-aldol cleavage to generate a formadehyde equivalent (route

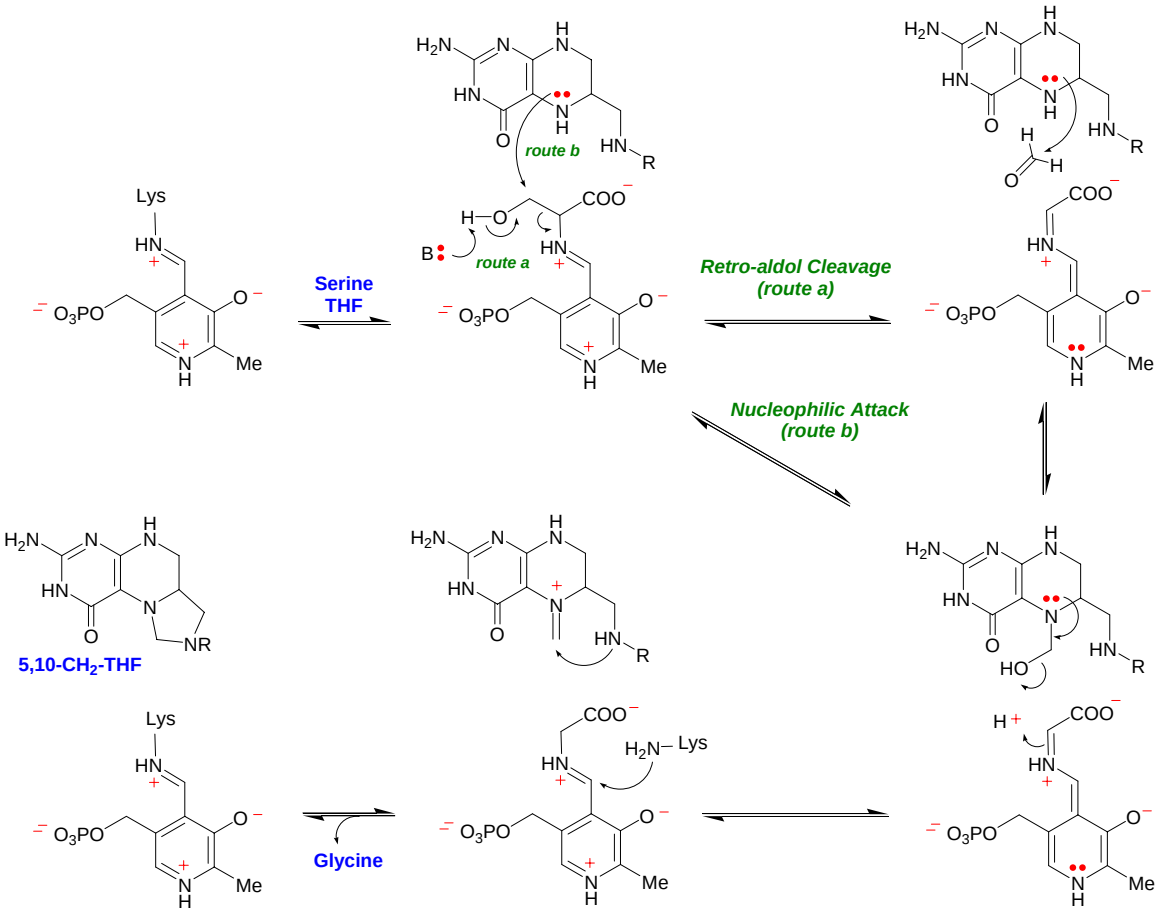

Scheme 5.4: Putative chemical mechanisms for serine hydroxymethyl transferase.

a) or direct nucleophilic attack by the N5 atom of THF on C_β of the Ser-PLP external aldimine (route b). The current data favors the direct nucelophilic addition pathway (route b), because the formaldehyde equivalent has never been detected and because the N5 atom of the bound THF co-substrate appears to be positioned appropriately for nucleophilic attack on C_β with elimination of the quinonoid species.

As shown in Scheme 5.5, several possible mechanisms can be envisioned for the C_α-C_β bond cleavage event catalyzed by ACCD (*167*). Following conversion of the internal Schiff base (**6**) to the ACC-PLP-external aldimine (**7**), an active site nucleophile could break open the cyclopropane ring to yield the quinonoid intermediate (**8**). Cyclopropane rings are known to be susceptible toward nucleophilic addition reactions (*168-171*), and the cyclopropane ring of ACC is expected to be even further activated by the electron withdrawing carboxylate and PLP-Schiff base substituents at C_α. Deprotonation at C3 of the quinonoid (**8**) could eliminate the nucleophile to generate the vinylglycyl-PLP quinonoid intermediate (**9**). C4 protonation to give the PLP-amino acrylate species (**10**), followed by aldimine exchange and hydrolysis of (**11**) could yield the reaction products, α-KB (**2**) and ammonia. A key piece of evidence in support of this mechanism was provided by mechanistic studies with D-vinylglycine (**12**) (*167*), which was found to be converted into the same products generated by the reaction with ACC (α-KB and ammonia) without exhibiting any suicide inhibition. These findings suggest that **12** likely forms an external Schiff base with PLP and is then deprotonated by an active site base to generate the vinylglycyl-PLP quinonoid intermediate (**9**) that is proposed to be a key intermediate for ACC turnover in Scheme 5.5. A second potential mechanism that has been proposed for the ACC ring scission step involves deprotonation of one of the two C_β-methylene carbons of the ACC-PLP-external aldimine (*172*) to generate the extended quinonoid intermediate (**9**) directly. However, the pK_a of ~ 46 for the ring hydrogens of cyclopropane (*173*) seems prohibitively high for this mechanism to be feasible. Interestingly, the proposed nucleophilic cleavage mechanism for ACCD is

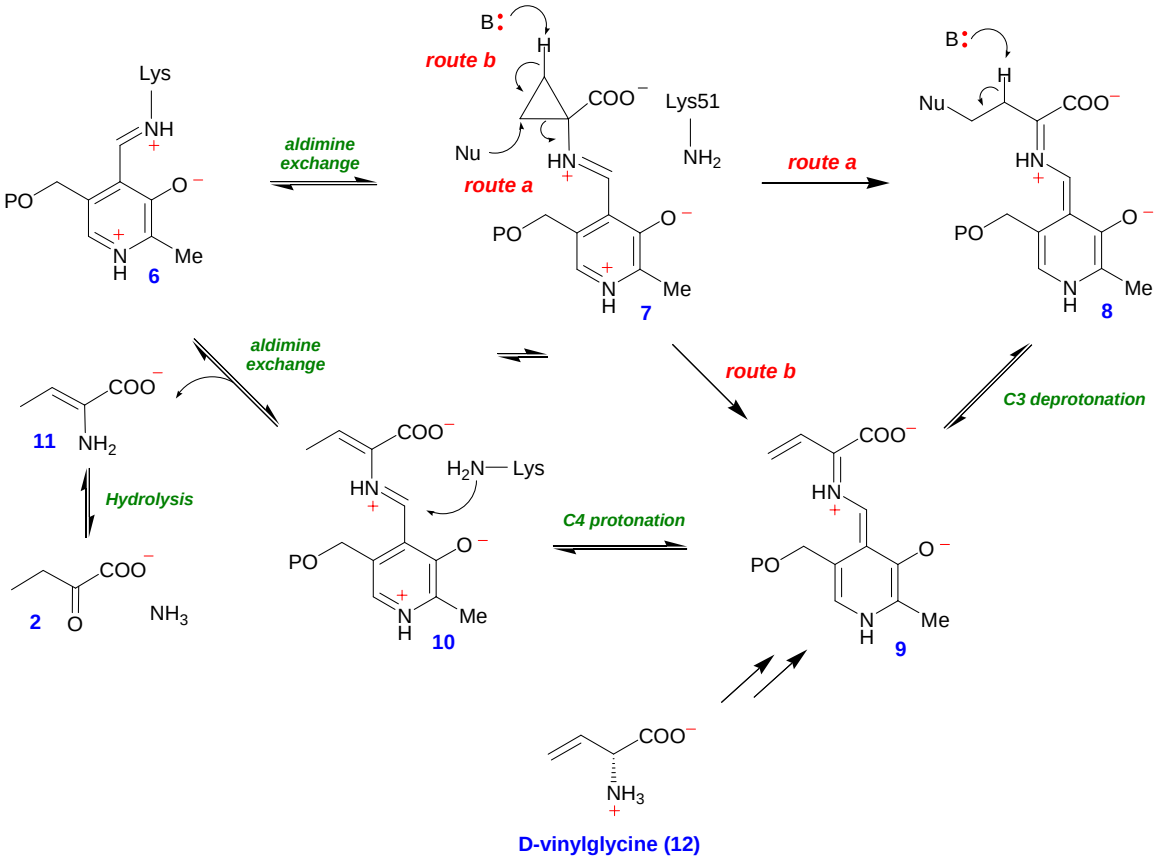

Scheme 5.5: Putative mechanisms for ACCD involving nucleophile and base-catalyzed cyclopropane ring scission (routes a and b, respectively).

essentially the reverse of the reaction catalyzed by ACC synthase during ethylene biosynthesis (Scheme 5.6). Following formation of the SAM-PLP external aldimine (**13**), the proposed mechanism for ACC synthase involves C_α deprotonation to generate the quinonoid (**14**), followed by an intramolecular attack of the C_α anion on C_γ to form the cyclopropane ring and eliminate the thiomethyl adenosine leaving group (*158, 174*). Together, ACCD and ACC synthase are the only two known PLP-dependent enzymes that process cyclopropane ring-containing substrates.

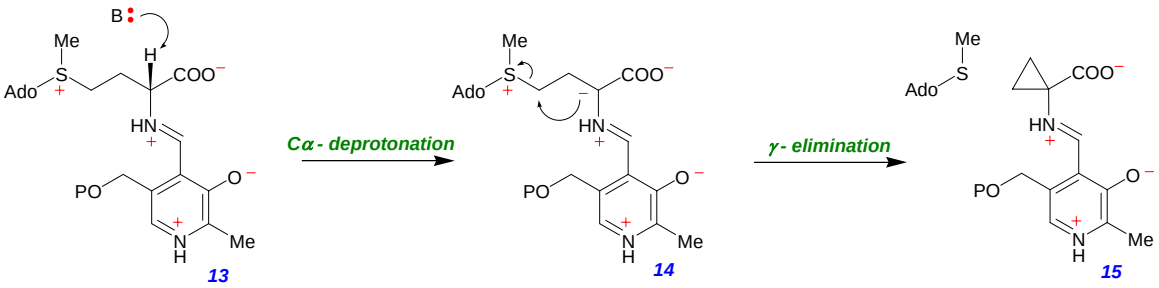

Scheme 5.6: Putative chemical mechanism for ACC synthase.

5.1.3 Stereochemical course of the ACCD-catalyzed reaction: Early attempts to characterize the chemical mechanism of ACCD focused on determining the stereochemistries of C-C bond cleavage and proton addition/removal. The dideuterated ACC substrates (**16** and **17**, Scheme 5.7A) were converted by ACCD into α-KB products (**18** and **19**, respectively) containing deuterium only at C4 and C3 (*175*). This finding demonstrated that ACCD specifically cleaves the *pro-S* C_α–C_β bond of ACC. When reactions containing ACC were carried out in D_2O (*167*), roughly one equivalent of solvent deuterium was incorporated into both C4 and C3 to give (*R*)- and (*S*)-**20**, with C3 incorporation being partially stereospecific (Scheme 5.7B). Close inspection of the NMR spectra of these reaction mixtures showed a reproducible stoichiometry of 1.0 eq. of deuterium incorporated at C4 and 0.85 eq. at C3, suggesting that the proton that is removed from C3 of ACC can be returned to C3 of the α-KB product ~ 15% of the time (*176*). This finding indicates that a single base in the ACCD active site is likely responsible for both C3 deprotonation and C3 protonation, and suggests that exchange of

the C3-derived proton with bulk solvent is slow enough to allow a small percentage of internal hydrogen return.

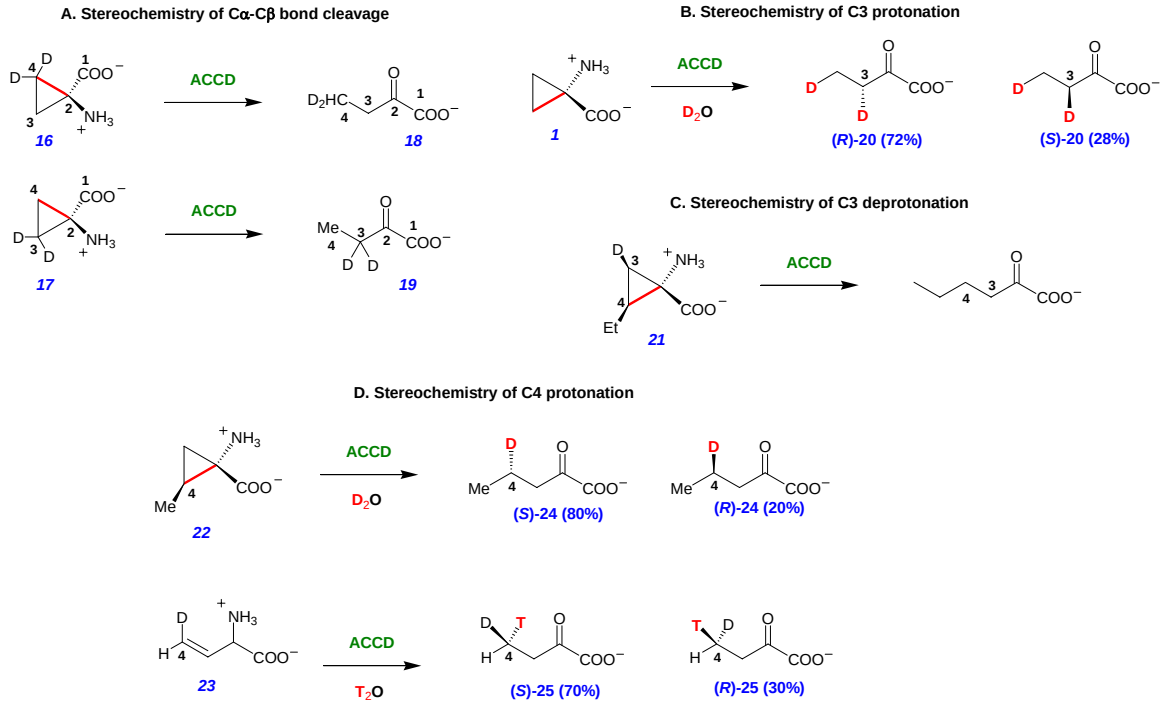

Scheme 5.7: Stereochemical studies of the ACCD-catalyzed reaction. The scissile *pro-S* C_β-C_α bond that is cleaved during ACCD turnover is highlighted in red.

To assess the stereochemistry of proton removal at the *pro-R* methylene of ACC (the C3 carbon of α-KB), 2-ethyl-[3-$^2H_1$]-ACC (**21**, Scheme 5.7C) was synthesized and the deuterium was found to be removed during turnover, suggesting that C3-deprotonation is *pro-R* stereospecific (*176*). To study the stereochemistry of C4 protonation, (*S*)-2-methyl-ACC (**22**) and (*Z*)-[4-$^2H_1$]-D-vinylglycine (**23**) were synthesized (*176*). When (*S*)-2-methyl-ACC was incubated with ACCD in D_2O (Scheme

5.7D), solvent deuterium was incorporated into C4 of the product (**24**) with an 80:20 mixture of the *S*:*R* enantiomers. Similarly, when (*Z*)-[4-$^2H_1$]-D-vinylglycine was incubated with ACCD in ^3H_2O, the stereochemistry of tritium incorporation at C4 of the product (**25**) was 70:30 (*S*:*R*). Thus, in contrast to the strict stereochemistry observed for C_α-C_β bond cleavage and for C3 deprotonation, both the C3 and C4 protonation events Scheme 7B and D, respectively) appear to have relaxed stereospecificity.

A revised chemical mechanism for ACC deaminase that accounts for the stereochemical studies discussed above is illustrated in Scheme 5.8. Following cleavage of the *pro-S* C_α–C_β bond by an active site nucleophile (**7** → **8**), the *pro-R* proton at C3 is removed by an active site base (B_1) to eliminate the nucelophile (**8** → **9a** + **9b**). The vinylglycyl-PLP-quinonoid intermediate (**9**) generated in this step likely exists in both cisoid (**9a**) and transoid (**9b**) conformations (relative to the C_α-N bond), with the cisoid conformation as the dominant form (~ 70%). This conclusion can be rationalized by the similarity in the partial stereospecificities observed for C3 and C4 protonation (Scheme 5.7B and D). Namely, the ratio of *S*:*R* stereochemistry for C4 protonation (~70:30) is very similar to the ratio of *R*:*S* stereochemistry for C3 protonation (72:28). In this model, protonation at C4 of the cisoid conformation of the quinonoid (**9a**) by a separate active site base (B_2) would yield the (*Z*)-aminoacrylate-PLP species (**10a**) with (*S*) stereochemistry at C4. Following aldimine exchange, the (*Z*)-aminoacrylate (**11a**) would be protonated with (*R*) stereochemistry at C3 by the same base (B_1) that removed C3 (to account for the partial internal hydrogen return noted above). By analogy, and assuming that the same active site residues are serving as the catalytic acid/base groups, the trans-

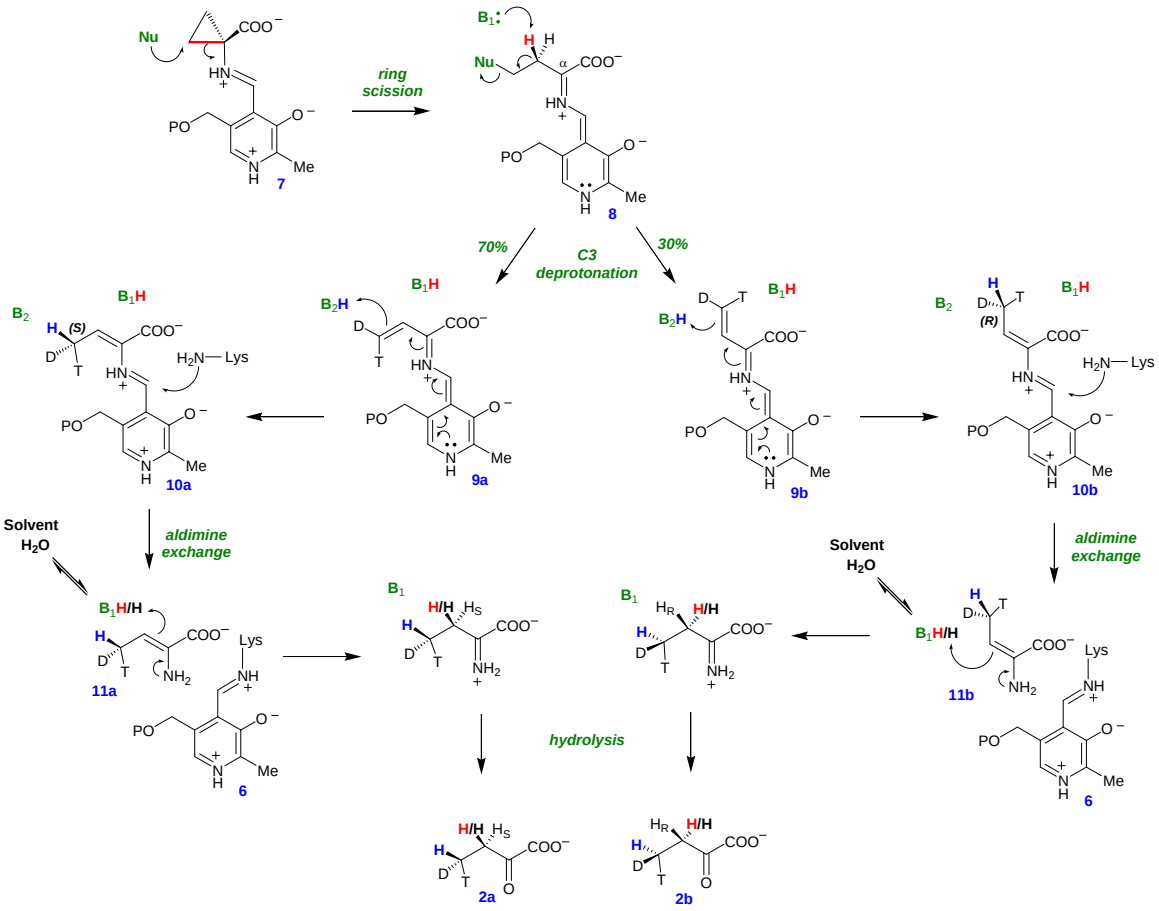

Scheme 5.8: Revised mechanism for ACCD accounting for the stereochemical observations summarized in Scheme 5.7. In this model, separate acid/base groups (B_1 and B_2) - both located on the *si* face of the C_α atom of the substrate-PLP adduct (above the plane of the page) - are required for C3-protonation/deprotonation and C4 protonation. The C3 proton removed by B_1 (shown in red) can partially exchange with solvent. The hydrogen isotopes at C4 are distinguished to illustrate how different final stereochemistries can be obtained at C4 of the product (**2a**/**b**) from a mixture of **9a** and **9b**.

vinylglycyl-PLP-quinonoid (**9b**) would eventually lead to product (**2b**) with (*S*) and (*R*) stereochemistry at C3 and C4, respectively. In this model, C3-deprotonation, C3-protonation, and C4-protonation all occur from the same face of the molecule (the *si* face

of the C_α-N bond). This seems to require at least two active site bases – one for C3 protonation/deprotonation (B_1) and one for C4 protonation (B_2).

5.1.4 X-ray crystal structures provide insight into the mechanism of ACCD catalysis: The X-ray crystal structures of ACCD enzymes from both yeast and bacterial sources have been reported (*177-180*), and these studies have provided insight into the putative roles of several active site amino acid residues in the ACCD-catalyzed reaction. The active site of the wild type ACCD from *Pseudomonas* sp. ACP (the ACCD enzyme investigated in this study) in the presence of ACC is shown in Figure 5.1 (*179, 180*). An unusual feature of the ACCD-ACC co-crystal structure is the apparent accumulation of the *gem*-diamine species in the active site, where both the amino groups of ACC and the Schiff-base forming lysine residue (Lys51 in ACCD from *Pseudomonas sp. ACP*) are covalently linked to the C4′ atom of the coenzyme. In most PLP-dependent enzymes, the *gem*-dimaine is a transient species during the aldimine exchange reaction that converts the internal aldimine to the external aldimine. Putative roles for several of the conserved active site amino acid residues in ACCD will be discussed below.

The Schiff-base forming lysine residue (Lys51 in ACCD from *Pseudomonas sp. ACP*) forms the internal aldimine with the PLP coenzyme in the resting state – an observation that is consistent with spectroscopic studies of a yeast K51A mutant enzyme (*181*), which was found to bind the PLP coenzyme in its free aldehyde form rather than as an internal aldimine. Upon binding to ACC, the K51A mutant forms a species whose UV-visible absorption is consistent with an external aldimine intermediate (*181*).

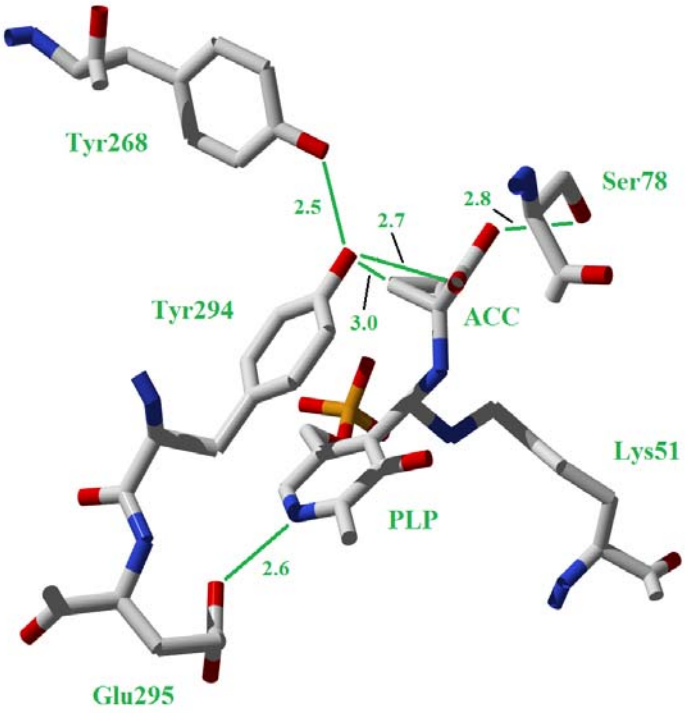

Figure 5.1: Active site of wt ACCD from *Pseudomonas sp. ACP* in complex with ACC. Distances are indicated in Å.

However, this external aldimine forms extremely slowly and the K51A mutant is devoid of catalytic activity, suggesting that the Lys51 residue likely plays a critical role in catalysis. An external aldimine between ACC and PLP was observed in the X-ray crystal structure of the *Hansenula saturnus* K51T enzyme which, like K51A, is also inactive (*178*). Interestingly, in this structure, the side chain of the mutant Thr51 residue is located on *re* face of the C_α-N bond of the external aldimine. Assuming that the side chain of Lys51 would occupy a similar region of the active site upon forming the external aldimine, it does not appear that the Lys51 side chain would be capable of accessing the *pro-S* C_β atom of ACC. Thus, while the catalytic inactivity of the K51A and K51T

enzymes clearly suggests an important function for Lys51 in ACCD catalysis, the available crystal structures and the known stereochemistry of C_α-C_β bond cleavage suggest that Lys51 is most likely not the nucleophile responsible for cleaving the cyclopropane ring of ACC. Following ring scission, Lys51 could potentially serve as one of the two catalytic bases required for mediating proton transfers at C3 and C4 of the substrate (B_1 or B_2 in Scheme 5.8).

In contrast to the amino side chain of Lys51, the phenoxyl side chain of Tyr294 is positioned on the *si* face of the ACC-PLP adduct in the active site, where it is located only 3 Å from the *pro-S* C_β of the ACC cyclopropane ring (Figure 5.1). As such, it appears to be positioned appropriately for a role as a nucleophile to cleave the scissile C_α-C_β bond of the ACC cyclopropane ring (Scheme 5.5). In support of this essential catalytic role, the Y294F mutant is completely inactive and no consumption of ACC was detected by ^{1}H-NMR following a 24 h incubation (*179*). While Tyr268 does not make direct contact with ACC, its phenoxyl side chain appears to hydrogen bond with the phenoxyl group of Tyr294 (2.5 Å). This interaction could serve to lower the pK_a of Tyr294 for a role as a catalytic nucleophile. Consistent with this hypothesis, the catalytic efficiency of the Y268F mutant is lowered 60-fold relative to the wild type enzyme (*179*). In addition to its close juxtaposition to the *pro-S* C_β atom of ACC, the Tyr294 phenoxyl group is also within hydrogen bonding distance of the ACC carboxyl group. The hydroxyl group of the conserved Ser78 residue also appears to hydrogen bond to the carboxyl moiety of ACC (2.8 Å). Together, Tyr294 and Ser78 likely play critical roles in mediating ACC binding.

Like Tyr294, Ser78 is also located close to the ACC-PLP adduct in the active site, where it hydrogen bonds with the carboxyl group of ACC and could help to mediate proton transfers during turnover. The pK_a of Ser78 could potentially be lowered by hydrogen bonding interactions with the backbone amide atoms of Gln80 and Thr81 (3.2 and 3.1 Å away, respectively). In addition, Ser78 is located on the *N*-terminus of an α-helix formed by residues Gln80→Leu91. Thus, it is possible that a helix-diople interaction could help to stabilize an anionic form of Ser78. These interactions could impart unusual activity to Ser78, allowing this residue to function as a base. The involvement of Ser78 in catalysis is consistent with the lowered catalytic efficiency of the S78A mutant (43-fold less than wt ACCD), the labeling of Ser78 by electrophilic ACC analogues, and the abilitiy of Ser78 to deprotonate the C_α-hydrogen of D-amino acid-PLP external aldimine adducts (*182*).

Finally, in the crystal structures, Glu295 appears to form an ion pair interaction with the pyridinium group of PLP. Such interactions are common in PLP enzymes and are generally believed to raise the pK_a of the pyridine ring in order to maximize the electrophilic properties of the coenzyme. Interestingly, the β-family of PLP enzymes (to which ACCD belongs) typically have a Ser or Thr residue H-bonded to the pyridine; thus, ACCD appears to be somewhat unusual with respect to its closest structural homologues. It has been reported that the yeast E295Q ACCD mutant is inactive (*178*), suggesting that the mechanism for ACCD catalysis likely involves delocalization of ACC-derived electrons into the pyridine moiety of the coenzyme, which would be consistent with a nucleophilic mode of cyclcopropane ring scission (Scheme 5.5).

While a mechanism for ACCD catalysis involving nucleophilic cleavage of the cyclopropane ring seems to be most consistent with the available mechanistic and structural data, the observation of the unusual *gem*-diamine species in the wt ACCD-ACC co-crystal structure (Figure 5.1) prompted us to consider an alternative mechanistic possibility for ACCD, in which Tyr294 acts as an active site acid to facilitate the cleavage of the cyclopropane ring directly from the *gem*-diamine (*179*). As depicted in Scheme 5.9, after formation of the *gem*-diamine (**26**) a "push" by the electron pair of the ACC amine and a "pull" by the concomitant protonation at the *pro-S* C_β of ACC by Tyr294, could facilitate the cleavage of the C_α-C_β bond to generate **27**. Stereospecific C3 deprotonation could generate **28**, and the aldimine exchange reaction could release the aminoacrylate (**11**) and regenerate the internal aldimine (**6**). Compound **11** could then be converted to α-KB (**2**) by hydrolysis to eliminate ammonia. In this mechanism, the external aldimine never forms, the PLP remains covalently bound to Lys51 throughout the reaction, and ACC-derived electrons are never formally delocalized into the PLP coenzyme. Although this proposal represents an unprecedented catalytic cycle for a PLP-dependent enzyme, it could provide a rationale for the accumulation of the *gem*-diamine in the wt ACCD-ACC co-crystal structure. Furthermore, the acid-catalyzed electrophilic cleavage of cyclopropanes is a well-documented phenomenon (*183-187*).

5.1.5 Thesis Statement: 1-Aminocyclopropane-1-carboxylic acid (ACC) deaminase is a pyridoxal 5'-phosphate (PLP) dependent enzyme that catalyzes the ring scission of ACC to give α-ketobutyric acid and ammonia. ACCD plays an important role in the regulation

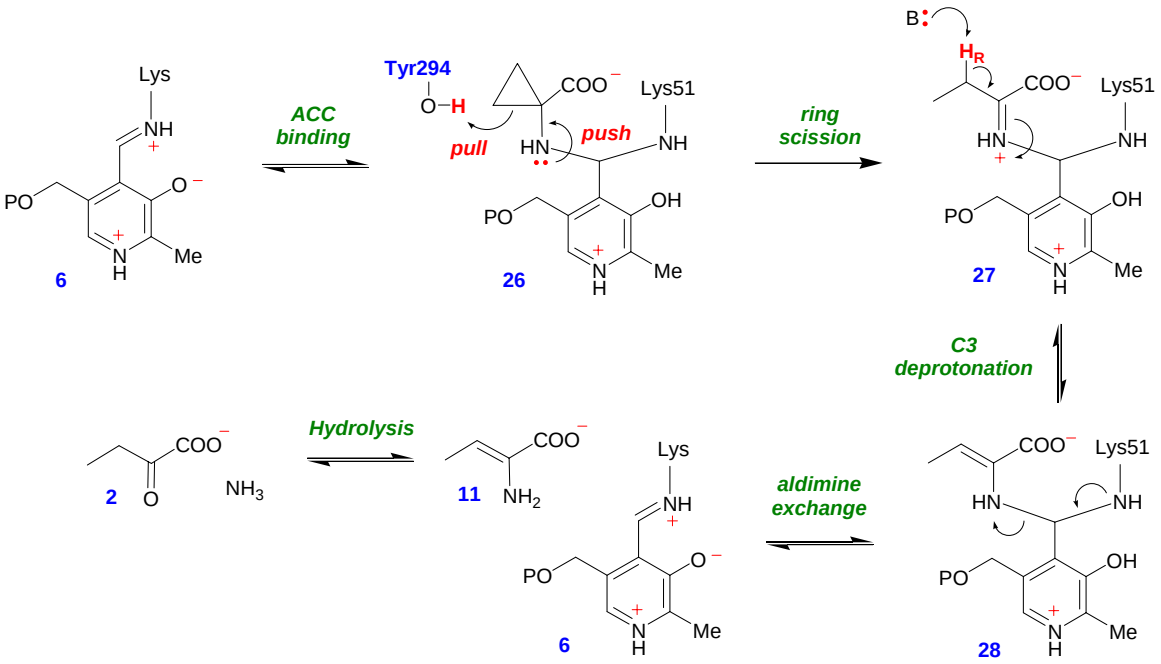

Scheme 5.9: Putative acid-catalyzed ring opening mechanism for ACCD.

of ethylene levels in plants, and has proven to be commercially useful for increasing the shelf life of fruits and vegetables. The overall chemical transformation catalyzed by ACCD involves the cleavage of the C_α-C_β bond of the amino acid substrate, which is a rare event in PLP-dependent enzyme catalysis. Potential mechanisms involving nucleophile- or acid-catalyzed cyclopropane ring opening have been proposed for this unusual transformation, but the mode of cyclopropane ring cleavage remains obscure. Recent X-ray structural studies revealed the presence of an unusual *gem*-diamine intermediate in the active site of the wild-type enzyme in complex with substrate, ACC. These structural studies also suggested that several conserved active site residues likely play key roles in catalysis. In this report, we aim to elucidate the mechanistic features of

ACCD catalysis by investigating the kinetic properties of wt ACCD and several of its mutant enzymes. In addition, we perform solvent kinetic isotope effect (SKIE), proton inventory, and ^{13}C KIE studies of the wt enzyme in an attempt to distinguish among the potential mechanisms for ring cleavage.

5.2 Methods

5.2.1 General: Overexpression and purification protocols for the recombinant wt ACCD isolated from *Pseudomonas* sp. ACP, and its Y268F and Y294F enzymes were described previously (*180*). Briefly, the wt ACCD, Y268F, and Y294F genes were cloned into pET28b(+) (Stratagene, La Jolla, CA), overexpressed in *Escherichia coli* BL21(DE3)pLysS (Novagen, Madison, WI) as *N*-terminal His_6-tagged fusion proteins, and purified by Ni-NTA chromatography to near homogeneity. The wt ACCD gene in the pET28b(+) construct was used as a template to generate the Glu295→Asp295 mutation using the QuickChange site-directed mutagenesis kit (Amersham, Arlington Heights, IL) with the following set of mutagenesis primers (the sequences in bold denote the mutated codon): forward, 5'-GCTGACCGATCCCGTCTAC**GAT**GGCAAA-TCGATGCACGGCA-3'; reverse, 5'-TGCCGTGCATCGATTTGCC**ATC**GTAGACGGGATCGGTCAGC-3'. The mutation was confirmed by DNA sequencing performed by the Institute of Cellular and Molecular Biology Core Labs of the University of Texas at Austin, using T7 primers and terminators (Stratagene). The E295D protein was expressed and purified in a similar

fashion to the other enzymes used in this study. L-Lactic dehydrogenase from rabbit muscle, β-nicotinamine adenine dinucleotide (NADH), ACC, and all buffer components used in this study were purchased from Sigma-Aldrich (St. Louis, Mo). All protein concentrations were determined by the Bradford method (*188*) using bovine serum albumin as the standard. All curve fitting was performed with GraFit 5 (Erithacus Software, Horley, Surrey, UK).

5.2.2 pH-Dependence of the steady state kinetic parameters: All steady state kinetic measurements were performed by monitoring the rate of NADH consumption by the coupled enzyme L-lactate dehydrogenase (LDH), which reduces the α-KB (**2**) produced during ACC (**1**) turnover to 2-hydroxybutanoic acid (*182*). A typical 500 μL reaction contained 100 units of LDH, 200 μM NADH, 1.68 μM wt ACCD, and variable concentrations of ACC (0.1-50 mM) in assay buffer adjusted to the appropriate pH with 10 M HCl or 10 M NaOH. The assay buffer (25 mM MOPS, 25 mM MES, 50 mM 4-hydroxy-*N*-methylpiperidine, HMP) is a three component system which maintains constant ionic strength over the pH range used (*189*). After adjusting the buffer pH, the final ionic strength was raised to 100 mM by the addition of NaCl. Enzyme and LDH stock solutions were diluted 50-fold into the assay buffer and incubated for at least 5 min prior to the addition of NADH and ACC to initiate the reaction. The rate of decrease of NADH absorbance at 340 nm (ε_{340} = 6220 $M^{-1}cm^{-1}$) was monitored at 25 ^{o}C. The pH dependence of the Y268F and E295D mutants, and for the wt ACCD in D_2O were determined in a similar manner except more enzyme was used (15.4 μM, 4.95 μM, and

3.36 μM, respectively) to speed up data collection. For assays performed in D_2O, the assay buffer components were mixed directly in D_2O (99.9 atom %D, Sigma-Aldrich) and were adjusted to the appropriate pD (pD = pH meter reading + 0.4) with 10 M HCl or NaOH. This solution was used to make the NADH, LDH, ACC, and enzyme stock solutions. For all reactions, the final mole fraction of protium (contributed by ionizable protons from buffer components, ACC, HCl or NaOH, and the H_2O from the enzyme stock solution) was < 5%.

The choice of ACC concentrations used depended on the K_m at the particular pH being assayed, but in all cases at least 3-4 different substrate concentrations both above and below the K_m were used. The initial velocity at each substrate concentration was measured in triplicate and the substrate concentration dependence of the initial velocities were fit to the Michaelis-Menten equation for the determination of k_{cat} and K_m. The k_{cat} and k_{cat}/K_m values determined at each pH ($k_{cat,app}$ and $k_{cat}/K_{m,app}$) were normalized by the enzyme concentration and the log of these kinetic constants were plotted versus pH and fit with Equations 1-3. The log ($k_{cat}/K_{m,app}$) data were fit with Equations 5.1 or 5.2, which describe inverse bell-shaped profiles with slopes of +1 and -1 at low and high pH, respectively. In these equations, k_{cat}/K_m is the pH-independent value of k_{cat}/K_m at the optimum pH, pK_1 and pK_2 are the pK_a values of groups that need to be unprotonated and protonated, respectively, for substrate binding, and pK′ (in Eqtn 5.2) is the average of two closely spaced pK_a values. Equation 3 describes a profile that increases to a maximum value (k_{cat}) at high pH with a slope of +1 and the dissociation constant, pK_3.

Eqtn 5.1:

$$\log (k_{cat}/K_{m,app}) = \log [(k_{cat}/K_m)/(1 + 10^{pK_1\text{-}pH} + 10^{pH\text{-}pK_2})]$$

Eqtn 5.2:

$$\log (k_{cat}/K_m)_{app} = \log [(k_{cat}/K_m)/(2 + 10^{pK'\text{-}pH} + 10^{pH\text{-}K'})]$$

Eqtn 5.3:

$$\log (k_{cat,app}) = \log [k_{cat}/(1 + 10^{pK_3\text{-}pH})]$$

5.2.3 Spectrophotometric pH titrations of the internal aldimine: To monitor the pH dependence of the tautomerization between the enolimine and ketoenamine forms of the internal aldimine, enzymes (in storage buffer 50 mM Na_2HPO_4, 10% glycerol, pH 7.5) were diluted to 50 μM in 100 mM buffer and, following a 1 min incubation, the absorbance of each sample was recorded from 200 – 900 nm on a Beckman DU 650 spectrophotometer at 25 ^oC. The buffers used were HEPES (pH 6.8-7.5), EPPS (pH 7.3-8.2), TAPS (pH 8.0-9.0), and CAPSO (pH 9.2-10.2). The spectra were normalized by setting the average absorbance values from 850-900 nm to zero.

5.2.4 Viscosity variation experiments: Viscosity variation experiments were performed under pseudo-first order conditions with wt ACCD using glycerol as the viscogen. The reactions contained 1.19 μM ACCD, 30 mM ACC, and variable concentrations of glycerol (0, 10, 16, 20, 24, 30, and 32 % w/v) in 25 mM MOPS, 25 mM MES, 50 mM HMP, pH 7.5, 25 °C. The coupled LDH reporter assay described in section ***5.2.2*** was

used to detect the α-KB product. Each reaction was performed in triplicate and the dependence of the initial velocity on the relative viscosity of the solution was determined by fitting the data to Eqtn 5.4 as desctribed in Chapter 3, where k_o, k_n, and η_{rel} are the initial velocity in buffer with no added viscogen, the initial velocity in buffer of relative viscosity η, and the relative viscosity of the solution, respectively.

Equation 5.4

$$k_o/k_\eta = S\bullet(\eta_{rel} - 1) + 1$$

5.2.5 Proton inventory study of wt ACCD: To determine the number of solvent exchangeable protons moving in the transition state for the wild type enzyme and the solvent kinetic isotope effect contributed by each proton, we performed a proton inventory study (*115*). To simplify the reaction conditions, a more facile measurement of ACCD activity was employed, in which the production of α-KB was monitored directly by following the increase in absorbance at 329 nm (ε_{329} = 0.0176 $mM^{-1}cm^{-1}$ for α-KB). The reactions were performed at pL = 8.0, where the k_{cat} in both 100% H_2O and 100% D_2O is independent of pL. TAPS buffer (50 mM) was prepared with 0, 20, 40, 50, 60, 70, 80, or 100 % (v/v) D_2O/H_2O. The pL was adjusted to 8.0 using 10 M and 1 M solutions of NaOH, and the ionic strength was adjusted to 100 mM with NaCl. In each separate D_2O/H_2O water mixture, 10 μL of the wt ACCD stock (in H_2O, 1.19 mM) and 30 μL of a 500 mM ACC solution (dissolved in the appropriate D_2O/H_2O mixture) were added to a total reaction volume of 500 μL, giving wt ACCD and ACC in 23.8 μM and 30

mM final concentrations, respectively. The mole fraction of deuterium for each water mixture (moles D/(moles D + moles H)) was corrected to account for the different molar volumes of H_2O and D_2O, and also for solvent exchangeable protons derived from TAPS, NaOH, ACC, and the components of the stock enzyme solution. To ensure full equilibration of exchangeable hydrogenic sites on the enzyme with the solvent, the enzyme was pre-incubated in each water mixture for approximately 30 min prior to the addition of ACC to start the reaction. Following a 4 min incubation, the production of α-KB was monitored over 4 min by the increase in A_{329}. Under these conditions, the formation of α-KB was a linear function of time for all reactions. For each water mixture, 3 replicate measurements were made and the initial velocities (k_n) measured at each mole fraction of deuterium (n), were fitted with several different forms of the Gross-Butler equation (Equation 5.5), where the k_o, Φ_{TS}, and Φ_R parameters are the initial velocities in 100 % H_2O, and fractionation factors for exchangeable hydrogenic sites in the transition and reactant states, respectively, as described in Chapter 3.

Eqtn 5.5:

$$k_n/k_o = \prod_i^{v_i} (1-n+n\phi_{TS})_i \Big/ \prod_j^{v_j} (1-n+n\phi_R)_j$$

5.2.6 ^{13}C-KIE studies of the wt ACCD-catalyzed reaction: To investigate whether cleavage of the C-C bond of ACC contributes to steady state rate limitation, the method

of Singleton was employed to measure the ^{13}C-KIEs on k_{cat}/K_m ($^{13}k_{cat}/K_m$) for the wt ACCD-catalyzed reaction (*190*). As summarized by Singleton: "As any reaction proceeds, the starting materials [ACC] are fractionatively enriched in isotopically slower-reacting components. The proportion of a minor isotopic component in recovered material compared to the original starting material (R/Ro) is related to the fractional conversion of reactants (F) and the KIE (relative rate for the major/minor isotopic components). As a reaction approaches completion ($F \rightarrow 1$), R/Ro approaches ∞, and KIEs become greatly magnified in the observable R/Ro." The equation for calculating the KIE (with parameters as defined by Singleton) is shown in Equation 5.6 (*190-193*), along with equations (5.7 – 5.9) for calculating the uncertainties in the KIE (ΔKIE_F and ΔKIE_R) that result from errors in the measurement of F and R/R_o (ΔF and $\Delta R/R_o$, respectively):

Eqtn 5.6:

$$KIE_{calc} = \ln(1-F)/\ln[(1-F)R/R_o]$$

Eqtn 5.7:

$$\Delta KIE_F = -\ln(R/R_o)\ \Delta F/[(1-F)\ln^2[(1-F)R/R_o]]$$

Eqtn 5.8:

$$\Delta KIE_R = -\ln(1-F)\ \Delta(R/R_o)/[(R/R_o)\ln^2[(1-F)R/R_o]]$$

Eqtn 5.9:

$$\Delta KIE_{calc} = KIE_{calc}[(\Delta KIE_F/KIE_{calc})^2 + (\Delta KIE_R/KIE_{calc})^2]^{1/2}$$

For reactions where the heavy isotopic component is present in trace quantities, the calculated KIE is related to the relative catalytic efficiencies of the enzyme for the substrate molecules containing the light and heavy isotopes at the scissile bond (which leads to the enrichment of the heavy isotope if there is a KIE) and, thus, the Singleton method is a competition experiment that measures heavy atom isotope effects on k_{cat}/K_m for an enzymatic reaction (*191-193*). For the ACCD reaction, if there is a $^{13}k_{cat}/K_m$, then the starting ACC material (with ^{13}C present at natural abundance) should become enriched in ^{13}C at the carbon atoms bearing the scissile C-C bond (C_α and the *pro-S* C_β) as the reaction proceeds. This enrichment can be measured by ^{13}C NMR to provide the ratio (R/R_o) that is needed for calculation of the KIE, providing that the reaction is scaled up such that a sufficient quantity of ACC can be recovered from the reaction to allow accurate ^{13}C NMR integrations.

Large scale reactions were performed by dissolving ~ 950 mg of ACC to a final concentration of 50 mM in 100 mM potassium phosphate (pH 7.5). To initiate the reaction, wt ACCD enzyme was added and the reaction was slowly stirred at room temperature. The reaction was performed in duplicate. The progress of the reaction was periodically assessed using the coupled LDH assay to determine the concentration of reaction product, α-KB (see below). The enzyme activity was slowly lost over ~ 24 h, so additional aliquots of enzyme were periodically added to drive the reaction towards completion. As the reaction neared completion, a 0.5 mL aliquot was removed for determining the fraction of reaction (*F*, described below) and the remainder of the reaction was cooled to 4 °C and filtered using a YM-10 membrane to remove the enzyme.

The filtered sample was loaded onto Dowex-50 cation exchange resin (100 mL) to recover the unreacted ACC starting material. Prior to loading the large scale reaction onto the column, the resin was charged with 250 mL of 2 M HCl and washed with H_2O (~ 300 mL) until the pH of the column eluate was neutral. After loading the reaction onto the column, the resin was washed with an additional 500 mL of H_2O to elute the reaction product (α-KB) and buffer. ACC was then eluted with 300 mL of 6% NH_4OH in H_2O (pH 11.5) and the solvent was removed by rotary evaporation and lyophilization. The column eluate was repeatedly dissolved in ~250 mL H_2O and lyophilized to remove the majority of the NH_3. For each large scale reaction, a separate commercial batch of ACC was used. Prior to conducting each reaction, a 50 mg sample of ACC was saved from each commercial batch for determination of the ^{13}C content of unreacted starting material (the R_o parameter in Eqtn 5.6). This 50 mg of ACC was dissolved in ~ 200 mL of 100 mM potassium phosphate (pH 7.5) and was purified by cation exchange chromatography in a manner identical to that described for the recovery of unreacted ACC from the large scale reactions.

To determine the fraction of reaction (F) needed for the calculation of the KIE by Eqtn 5.6, the concentration of the α-KB product in the large scale reactions were determined by coupling its reduction to NADH oxidation using lactate dehydrogenase (LDH). A 1 mL solution containing 150 μM NADH, 4 units of LDH, and 100 mM sodium phosphate buffer (pH 7.0) was transferred to a cuvette and the absorbance at 340 nm was recorded over several minutes. A 1 μL aliquot of the large scale reaction was then added and the change in absorbance at 340 nm was allowed to reach its equilibrium

level. The change in absorbance at 340 nm was then used to calculate the concentration of α-KB (C_{rxn}, Eqtn 5.10) at the end of the large scale reaction using the ε_{340} of NADH (6220 $M^{-1}cm^{-1}$). A total of 10 replicate measurements of the α-KB concentration were made to determine the average C_{rxn} and the standard error associated with this measurement. To determine the fraction of reaction, a 20 μL sample of the large scale reaction was mixed with an equal volume of concentrated ACCD sample to drive the reaction to 100% completion. The α-KB concentration of the completed reaction (C_{100}) was then measured by the coupled LDH assay as described above. The fraction of reaction was then calculated using Eqtn 5.10 and the propagated standard error was calculated to give ΔF (for use in Eqtn 5.7).

Eqtn 5.10:

$$F = C_{rxn}/C_{100}$$

As a measurement of the R/R_o parameter that is needed to calculate the KIE by Eqtn 5.6, NMR spectroscopy was used to determine the enrichment in ^{13}C at each carbon atom of the ACC substrate recovered from the large scale reaction relative to the ^{13}C content of unreacted ACC samples. Following purification, the ACC samples were dissolved in 660 μL of an H_2O:D_2O mixture (90:10 v/v). For each sample, the relaxation times of each of the ^{13}C nuclei in ACC were determined prior to the collection of the NMR spectra, and the delay time between successive pulses was adjusted to be 10x the longest relaxation time. This ensures that each C nucleus has sufficient time to

completely relax to its ground state between subsequent rounds of excitation, and is required for accurate integrations of the ^{13}C NMR signals. A total delay time between pulses of 80 sec was found to be sufficient for all of the ACC samples that were analyzed. NMR spectra were collected on a Varian Unity 500 MHz NMR spectrometer at the NMR core facility at the University of Texas, Austin. For each sample, 256 scans were used to generate a single ^{13}C-NMR spectrum, and a total of 10 spectra were recorded for each sample. For signal integration of the first spectrum of each set, a zeroth order baseline correction was made in the vicinity of each peak and the peak areas of each carbon signal were determined by integrating a 10 Hz window centered around the chemical shift of each peak. These integration parameters were then applied to the other 9 spectra in the set. The ^{13}C content of the carboxyl carbon (at 175 ppm) was used as an internal standard to normalize the ^{13}C content of C_α and C_β, measured at 35 and 12 ppm, respectively. This relative measurement of the ^{13}C content of C_α and C_β is hereafter referred to as R for ACC samples recovered from large scale wt ACCD reactions, or as R_o for unreacted ACC samples. In this analysis, we assume that the ^{13}C-KIEs on the carboxyl carbon and the *pro-R* C_β are unity. For each sample, average values for R or R_o were determined from the 10 replicate spectra, and the ratio R/R_o and its associated standard error $\Delta(R/R_o)$ was determined. It should be emphasized that *for each large-scale reaction, the R and R_o measurements are derived from the same commercial batch of substrate*; thus, batch-to-batch variation in the ^{13}C content of ACC does not need to be taken into account when calculating the KIEs and when comparing replicate KIE measurements. From the F and

R/R_o parameters (and their associated standard errors, ΔF and $\Delta(R/R_o)$), KIE_{calc} and ΔKIE_{calc} for C_α ad C_β were then calculated for each reaction using Eqtns 5.6-9.

5.2.7 Stopped-flow absorbance measurements: All pre-steady state absorbance changes in the PLP chromophore were measured with a HI-TECH Scientific SF-61 Double Mixing Stopped-Flow System equipped with a diode array detector for monitoring time dependent changes in the PLP spectrum. The pH of all stock solutions was adjusted to the appropriate value immediately prior to conducting the experiments at 25 °C. The ionic strength of the final reaction mixtures were 150 mM. All concentrations given below correspond to those after mixing in the stopped flow. For wt ACCD, the reactions contained 100 μM enzyme and 50 mM ACC in 100 mM EPPS (pH 7.5). For Y268F, the reactions contained 96.5 μM enzyme and 50 mM ACC in 100 mM TAPS (pH 8.8). For E295D, reactions contained 60 μM enzyme and 50 mM ACC and were performed in 100 mM MOPS (pH 7.5). For Y294F, reactions contained 50 μM enzyme, 50 mM ACC, and were performed in 100 mM MOPS (pH 7.5). The pre-steady state kinetic data were fit with exponential equations (Eqtn 5.11 or 5.12) as described in Chapter 3 to estimate the amplitudes and rates associated with each observable kinetic phase.

Eqtn 5.11:

$$A_t = A_1(1-e^{kobs,1 \cdot t}) + A_2(1-e^{kobs,2 \cdot t}) + C$$

Eqtn 5.12:

$$A_t = A_1(1-e^{kobs,1 \cdot t}) + A_2(1-e^{kobs,2 \cdot t}) + A_3(1-e^{kobs,3 \cdot t}) + C$$

5.3 Results and Discussion

5.3.1 Steady State Kinetic Studies: To assess the involvement of acid-base catalysis in the reaction catalyzed by ACCD, the pH-dependence of the steady state kinetic parameters (k_{cat} and k_{cat}/K_m) were studied for wt ACCD, E295D, and Y268F over the pH range of 6.5-9.8 (Figure 5.2). The fitted kinetic parameter values are summarized in Table 5.1 along with the mean square residuals (MSR) of the non-linear fits to Eqtns 5.1-3. The k_{cat}/K_m profiles for each enzyme were fit with both Equation 5.1 and 5.2, and the fit that gave the lowest MSR is reported. For E295D and for wt ACCD in H_2O, the fits give similar values for pK_1 (6.9-7.3) and pK_2 (8.7-9.3) as well as similar pH optima (pH 8.0 and 8.1 for wt ACCD and E295D, respectively). For the wt ACCD reaction in D_2O, the apparent pK_1 and pK_2 values in the k_{cat}/K_m profile are both shifted to more basic pL. This is an expected result in D_2O because bonds between heteroatoms and deuterium are more stable than bonds with protium, and this serves to raise the pK_a of these groups (*115*). For Y268F, the best fits were obtained with Equation 5.2, which contains only a single dissociation constant, pK' = 8.7. This pK' parameter is the arithmetic average of two closely-spaced pK_a values. The relatively large errors associated with the k_{cat}/K_m parameter in each of the fits are likely derived from the close separation of the pK_a values governing the shape of the profiles.

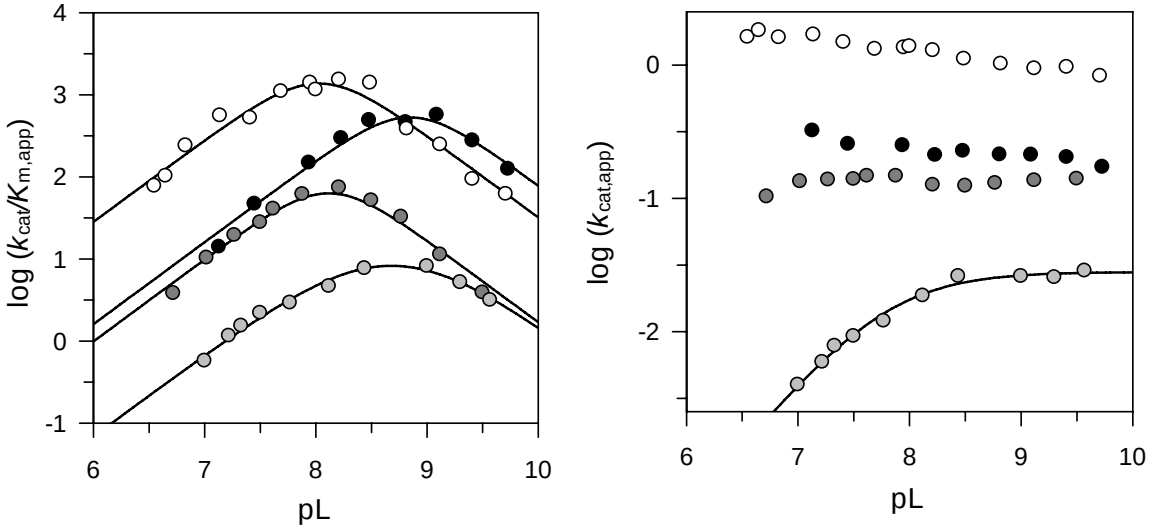

Figure 5.2: pH-Dependence of the steady state kinetic parameters for wt ACCD in H_2O (white circles), wt ACCD in D_2O (black circles), E295D in H_2O (dark gray circles), and Y268F in H_2O (light gray circles).

Enzyme	**Equation**	k_{cat}/K_m **($M^{-1}s^{-1}$)**	pK_1	pK_2	pK'	k_{cat} **(s^{-1})**	pK_3	**MSR**
wt (H_2O)	5.1	1.5(0.7) x 10^4	7.3(2)	8.7(2)	-	1.32(8)†	-	0.0134
wt (D_2O)	5.1	9(5) x 10^3	7.9(3)	9.8(3)	-	0.22(2)†	-	0.0112
E295D	5.1	2(1) x 10^3	6.9.2)	9.3(2)	-	0.132(4)†	-	0.0076
Y268F	5.2	3.3(2) x 10^1	-	-	8.7(3)		7.79(3)	.0029
	5.3					0.028(1)	7.8(0.03)	.0011

Table 5.1: Summary of pH-dependence of the steady state kinetic parameters for wt ACCD and its E295D and Y268F mutants. See Methods for the definitions of Eqtns 5.1-3. †Determined by averaging the k_{cat} values at each pH.

Inspection of the k_{cat}–pH profiles reveals that this parameter is independent of pH in the wt and E295D enzymes across the pH range tested. This indicates that any putative catalytic acid-base groups must be in certain, specific protonation states for catalysis. Unfortunately, as with IDI-2 discussed in Chapter 3, this observation does not

allow any definitive conclusions to be drawn on the involvement of general acid-base catalysis in these enzymes. The k_{cat} parameter for E295D was reduced roughly 10-fold relative to wt ACCD across the pH range studied and this accounted for the majority of the reduction in catalytic efficiency for the E295D mutant. Similar modest reductions in k_{cat} and k_{cat}/K_m have been observed in other PLP-dependent enzymes when conserved Glu and Asp residues that interact with the pyridine N atom of the coenzyme are interchanged (*194-197*). In contrast, replacement of the carboxyl moiety of these residues with other functional groups often results in more drastic reductions in the steady state kinetic parameters (*194, 198-200*). This has been observed with the E295Q mutant of ACCD, which is inactive (*178*). Together, the data are consistent with an important catalytic function for Glu295. In contrast to wt ACCD and E295D, k_{cat} increases at high pH for the Y268F mutant, suggesting that an active site group with a pK_a ~ 7.8 needs to be deprotonated for catalysis. In this mutant, k_{cat} does not appear to level off at lower pH, suggesting that while there may be two forms of the Y268F:ACC Michaelis complex (one protonated and one unprotonated), only the unprotonated enzyme form is active. These results suggest that Tyr268 plays an important role in catalysis, most likely via its hydrogen bonding interaction with Tyr294 (see Figure 5.1).

5.3.2 pH-Dependence of internal aldimine absorption: To help assign the kinetic p*K* values measured in the previous section and to better understand the interactions between Tyr268, Tyr294, and Glu295 with the internal aldimine, the pH-dependence of the electronic absorption of the internal aldimine was studied for the wt ACCD, Y268F,

Y294F, and E295D enzymes. Protonated internal aldimines typically exhibit absorption bands near 330 and 420 nm, which correspond to the enolimine and ketoenamine tautomers of the protonated Schiff base (Scheme 5.10). In contrast, deprotonated Schiff bases typically exhibit an absorption maximum near 380 nm (*189, 201*). Studies with ACC synthase and aspartate aminotransferase (AATase) have illustrated the potential importance of the internal aldimine protonation state in substrate binding. In both of these enzymes, the pK_a of the internal aldimine (9.0 and 7.0 for ACC synthase and AATase, respectively) is adjusted according to the pK_a of the amino groups of their respective substrates (7.8 and 9.9 for SAM and aspartate, respectively). This is believed to help facilitate the aldimine exchange reaction by ensuring that there is not an oberabundance of protons in the active site at physiological pH. As illustrated by these two enzymes, investigating the pH-dependence of the internal aldimine absorbance spectrum of ACCD could provide insight into the ionization state of the PLP coenzyme, which could be helpful for assigning the kinetic pK values.

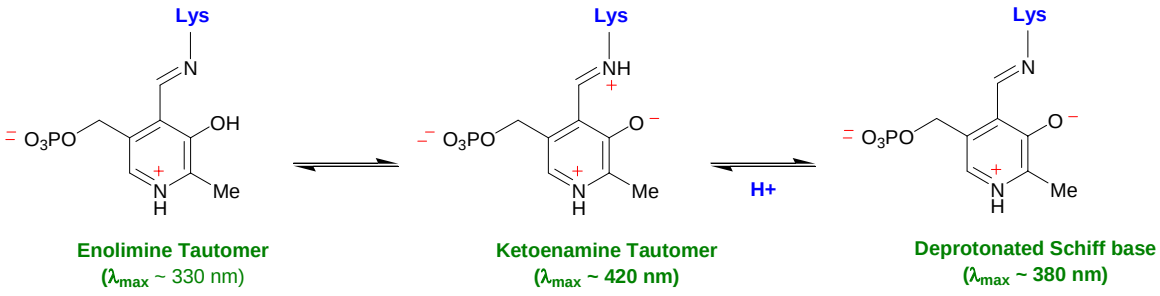

Scheme 5.10: Common protonation states and tautomeric forms of internal Schiff bases.

In the resting state of each enzyme, absorption maxima are observed near 330 and 420 nm, consistent with the presence of both enolimine and ketoenamine forms of the internal aldimine (Figure 5.3), which coexist in many PLP enzymes at physiological pH (*196, 202-207*). As the pH is increased, the ketoenamine tautomer is converted to the enolimine tautomer. Importantly, there is no red shift in the λ_{max} of the enolimine tautomer at high pH in any of the enzymes, suggesting that the internal aldimine is not deprotonated as the pH is increased. Thus, the internal aldimine of ACCD and its mutants is likely protonated in the enzyme form that binds to ACC. Correspondingly, the pK_1, pK_2, and pK_3 values determined from the kinetic-pH profiles likely correspond to other groups – either to active site amino acid side chains or to ionizeable groups on the substrate.

5.3.3 Assignment of groups responsible for kinetic pK_a values: Because the effective resting state under k_{cat}/K_m conditions is the free enzyme + free substrate, the pK values determined from the k_{cat}/K_m profiles report on the ionizations of groups in the free substrate and free enzyme (*171*). The available crystal structures of ACCD are informative in helping to assign the identity of the ionizable groups that govern the pH-dependence of the steady state kinetic parameters (*178, 180*). As noted in section ***5.1.4***, it appears that several active site groups could participate directly in ACC binding (see Figure 5.1). These include the side chains of Tyr294 and Ser78, both of which are within hydrogen bonding distance of the ACC carboxyl group.

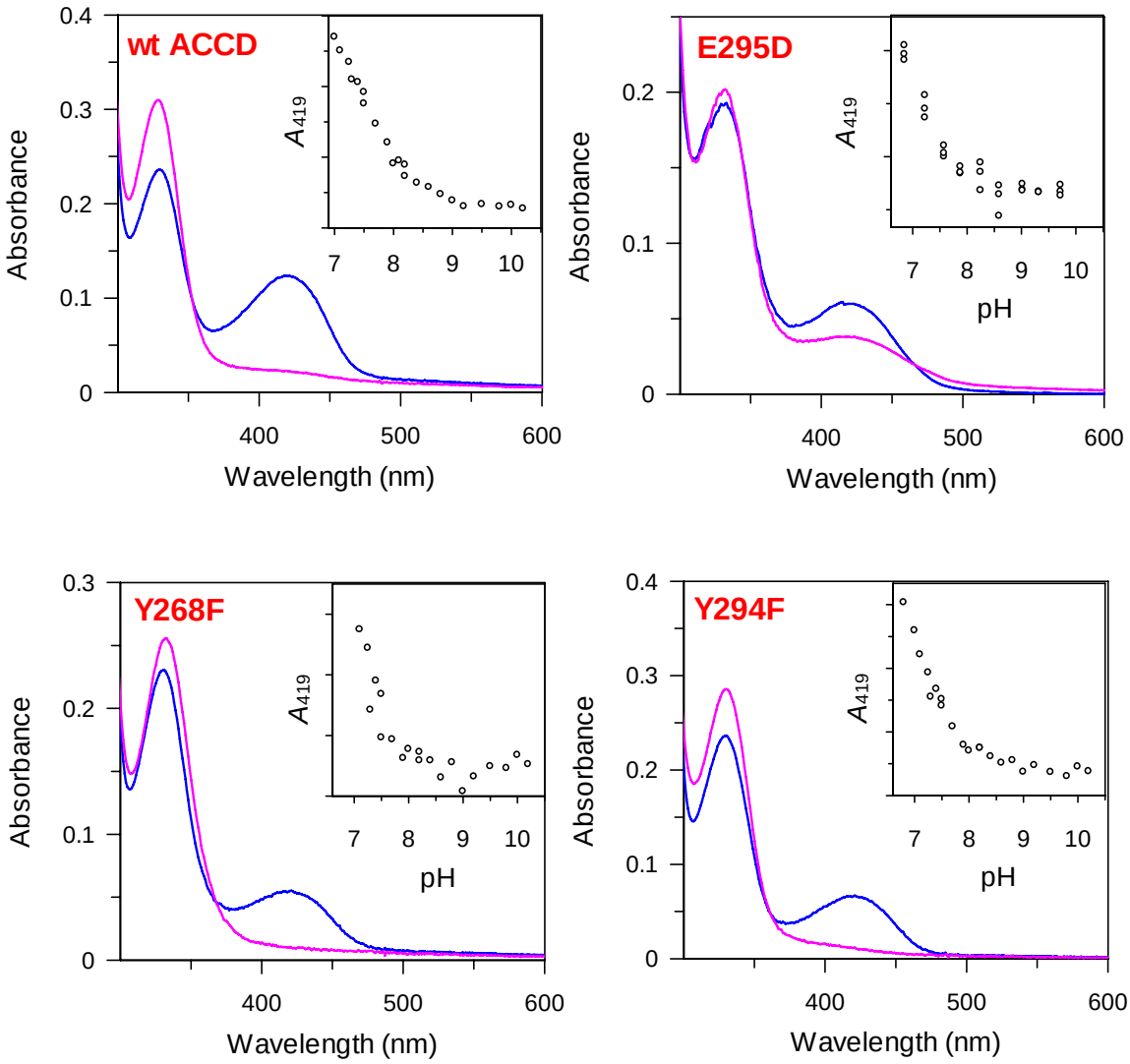

Figure 5.3: UV-visible absorption spectra of the low (blue spectra) and high (fuscia spectra) pH forms of wt ACCD and its mutants. The pH-dependence of the absorbance change at 419 nm is shown in the inset to each panel.

The apparent pK_1 determined from the k_{cat}/K_m–pH profiles for wt ACCD and E295D (6.9-7.3) likely corresponds to the phenoxyl side chain of Tyr294, which could facilitate ACC binding in its unprotonated state by interacting with the positively charged

primary amino group of ACC. The carboxyl side chain of Glu295 likely forms an ion pair with the pyridinium N of PLP, but is not in direct contact with ACC, perhaps explaining the similarity in the pH-dependence of k_{cat}/K_m for this mutant to wt ACCD. While pK_1 ~ 7.3 appears to be low for a tyrosine residue (the pK_a of the tyrosine phenoxyl group is 10.4 in solution), the phenoxyl group of Tyr294 is only 2.5 Å from the phenoxyl group of Tyr268, suggesting that these two residues may form a hydrogen bond in the ACCD active site. This tyrosine pair is conserved in all ACCD homologues, and the hydrogen bonding interaction between these two groups could serve to lower the pK_a of Tyr294 for a role in ACC binding. Consistent with this hypothesis, the kinetic pK_1 value appears to increase in the k_{cat}/K_m-pH profile for the Y268F mutant (Table 5.1 and Figure 5.2). This is consistent with Tyr294 being an important residue for ACC binding, and is also consistent with the idea that Tyr268 serves to depress the pK_a of Tyr294, activating it for a role in ACC binding. The value of pK_1 could not be determined from the non-linear fits of the k_{cat}/K_m data for the Y268F mutant, presumably due to the close separation in the macroscopic pK values. This suggests that pK_1 in this mutant is near 8.7 and thus, that the pK_a of Tyr294 may increase roughly 1.0 – 1.5 units in the Y268F enzyme.

The group that must be protonated for ACC binding may be the same in each enzyme studied, as pK_2 ranges from about 8.7-9.3 in all of the enzymes investigated. This suggests that the pK_a of this group is not very sensitive to the active site mutations that were made. Furthermore, the spectroscopic studies of the internal aldimines discussed in the previous section suggest that the PLP coenzyme is most likely not deprotonated over the pH range assayed. Based on these observations and the available

crystal structures, there are two likely candidates for the group responsible for pK_2. First, the primary amino groups of amino acids typically have pK_a values near 9.0, suggesting that the ACC amine group may need to be protonated for binding to ACCD and its mutants. Alternatively, as discussed in the introduction, Ser78 is located ~ 2.8 Å from the ACC carboxylate group in the enzyme:ACC complex where it appears to hydrogen bond to the ACC carboxyl group in the Michaelis complex, implying that it is likely protonated in the enzyme form that binds to ACC (*180*). Although the pK_2 ~ 9 seems to be a large reduction for the pK_a of a serine residue, we have previously found that Ser78 can be covalently modified by 2-methylene-ACC, an irreversible, electrophilic enzyme inactivator (*182*). Ser78 has also been implicated in the C_α-deprotonation of D-amino acid-external aldimine adducts formed in the ACCD active site (*182*). If Ser78 is responsible for pK_2, the reduction in pK_a for Ser78 could be due (in part) to it is location at the positive end of an α-helix dipole formed by amino acid residues 79-91, where it appears to hydrogen bond to the backbone amide atoms of Gln80 (3.18 Å) and Thr81 (3.09 Å). Similar helix-dipole interactions have been shown to lower the pK_a of Cys residues in model peptides (*208*) and in enzyme active sites (*209, 210*) by nearly two units.

Unlike the other two enzymes investigated in this study, k_{cat} for Y268F is pH-dependent, increasing to a maximum value at high pH. This suggests that in this mutant, an active site group with a pK_a ~ 7.8 is important for catalysis and needs to be deprotonated in the Michaelis complex with ACC for activity. The requirement for a deprotonated catalytic residue in the Y268F mutant is consistent with a mechanism for

ACC ring cleavage involving nucleophilic attack on the cyclopropane ring (Scheme 5.5). The most reasonable candidate for the group with pK_3 ~ 7.8 is Tyr294, because it is in direct contact with Tyr268, because it is positioned 3Å from the *pro-S* C_β of ACC in the crystal structure, and because it is absolutely required for catalysis (*179*). Another possible residue that could be involved in catalysis and which is in the vicinity of ACC in the enzyme:ACC complex is the amino group of Lys51, which is expected to be liberated as ACC forms an external aldimine with PLP in the Y268F mutant. As noted in the introduction, however, there would have to be a substantial rearrangement of the external aldimine that is observed in the X-ray crystal structure of K51T mutant in order for K51 to initiate cyclopropane ring cleavage via nucleophilic attack at the *pro-S* C_β of ACC.

5.3.4 Solvent kinetic isotope and viscosity effects on the wt ACCD reaction: To assess the involvement of solvent exchangeable protons in the reaction catalyzed by wt ACCD, we performed solvent KIE and viscosity variation studies of the wt enzyme. The kinetic-pH profiles for the wt ACCD reaction with ACC in H_2O and D_2O are shown in Figure 5.2 and are summarized in Table 5.1. The k_{cat}/K_m profile in D_2O is shifted to more basic pL relative to the profile in H_2O, an expected result for the substitution of protium for deuterium at ionizable groups involved in enzyme-substrate binding and catalysis (*115*). From these profiles, significant solvent kinetic isotope effects ($^{D_2O}k_{cat}$ = 5.7 and $^{D_2O}k_{cat}/K_m$ = 2.5) were calculated from the data at the pL optimum in each solvent.

This result clearly suggests that solvent exchangeable protons play an important role in ACCD catalysis, and that solvent exchangeable protons are moving in the step(s)

that limit steady state turnover. In addition, the larger magnitude of $^{D_2O}k_{cat}$ relative to $^{D_2O}k_{cat}/K_m$ suggest that there may be solvent kinetic isotope effects on steps following the first irreversible step in the mechanism, which is assumed to be the ACC cyclopropane ring cleavage step. (Microscopic rate constants subsequent to the first irreversible step will not appear in the expression for k_{cat}/K_m and, thus, solvent isotope effects on these steps will not contribute to $^{D_2O}k_{cat}/K_m$.) Inspection of both of the putative mechanisms for ACCD catalysis (Schemes 5.5 and 5.9) show that there are several possible steps following C-C bond cleavge that could potentially exhibit solvent KIEs. Finally, viscosity variation experiments performed under pseudo-first order conditions demonstrate that there is no viscosity effect on k_{cat} (Figure 5.4). As discussed in Chapter 3, this suggests that product dissociation and/or large scale enzyme conformational changes do not contribute to the steady state rate limitation under pseudo-first order conditions and that the solvent KIE measured on k_{cat} is not due to a viscosity effect associated with changing the solvent from 100% H_2O to 100% D_2O.

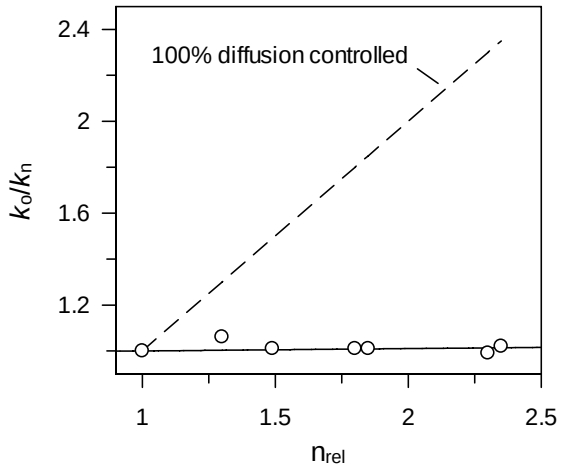

Figure 5.4: Viscosity effects on k_{cat} for wt ACCD.

5.3.5 Proton inventory for the wt ACCD-catalyzed reaction: The proton inventory method was applied to explore the large SKIE measured on k_{cat} for the wt ACCD reaction more closely (*115*). The k_{cat} versus pL profiles for the wt ACCD reaction indicated that k_{cat} was independent of pL over the entire range assayed (Figure 5.2); thus, we chose to perform the proton inventory studies at pL = 8.0 with 30 mM ACC, which is well above the K_m for ACC in both 100% H_2O and 100% D_2O at pL = 8.0. The proton inventory data were fit to several different forms of the Gross-Butler equation (Eqtn 5.5) by a systematic procedure similar to that described in Chapter 3. The non-linear fits of the proton inventory data are shown in Figure 5.5 and the definitions of the various models and summary of the fitted parameters are listed in Table 5.2. The best fits, as evidenced by the lowest mean square residual values (Table 5.2), the residual plots (Figure 5.5), and significance of regression tests (Table 5.3), were obtained with models where multiple transition state protons are moving in the step(s) that limit turnover under pseudo-first order conditions (the T_2 and T_1S models). As discussed in Chapter 3, the significance of regression tests (Table 5.3) suggested that the proton inventory data merit the inclusion of the additional parameter present in the T_2 ad T_1S models, and that the simple linear model (T_1) should be regarded with suspicion (*125*). The slightly bowl-shaped curvature of the proton inventory plots suggests that $^{D_2O}k_{cat}$ is composed of multiple, normal solvent KIEs. In both the T_2 and T_1S models, one exchangeable site (Φ_1) is predicted to be responsible for the majority of the solvent KIE on k_{cat} (Φ_1= 0.3 – 0.33, KIE = 3.0 – 3.3), while a

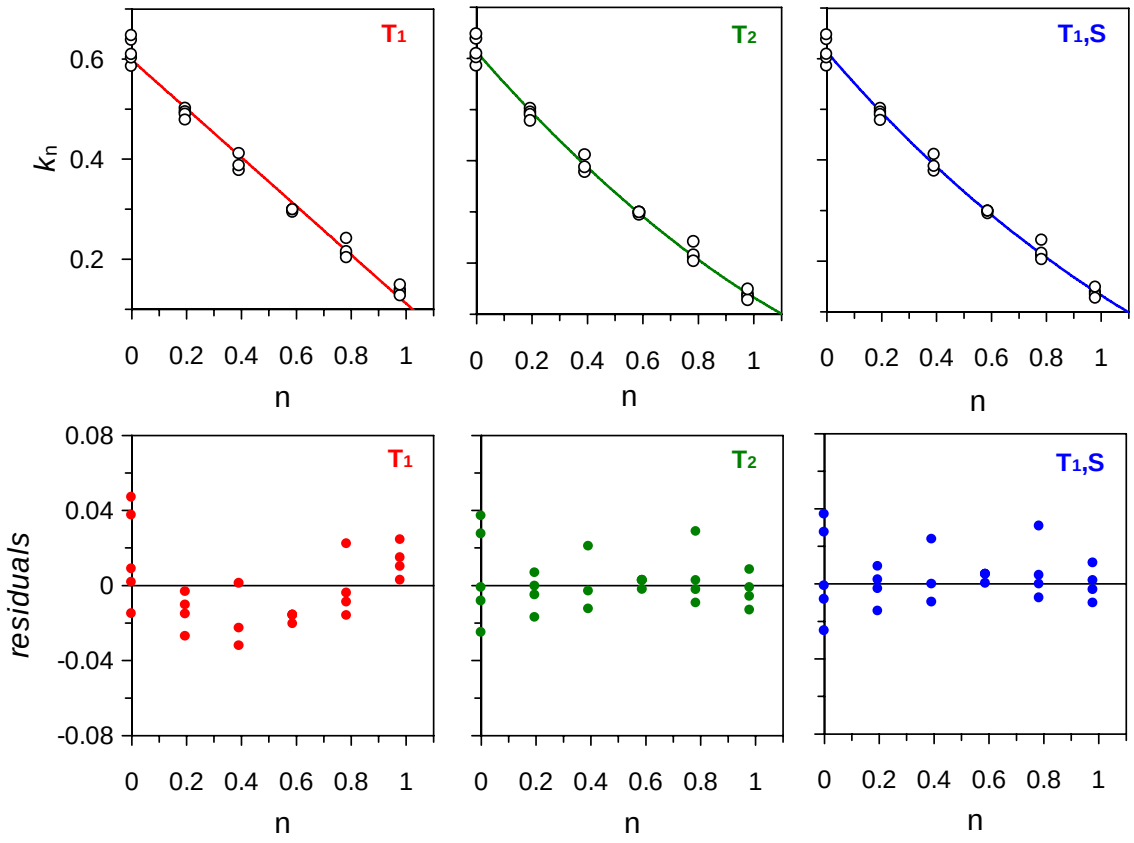

Figure 5.5: Proton inventory data for wt ACCD, showing fits to several different forms of the Gross-Butler equation and residual plots for each fit. See Table 5.2 for the definition of each model and the values for the fitted parameters.

second site (Φ_2) or sites (Φ_S) contributes a smaller normal effect (KIE ~ 1.4 – 1.5). Based on the measured differences in $^{D_2O}k_{cat}$ (5.7) and $^{D_2O}k_{cat}/K_m$ (2.5) discussed above, our hypothesis is that one of the normal solvent KIEs is expressed on a step prior or concomitant with cyclopropane ring cleavage (thus contributing to both $^{D_2O}k_{cat}$ and $^{D_2O}k_{cat}/K_m$), while the other normal solvent KIE is expressed on a step following cyclopropane ring cleavage (and is expressed only on $^{D_2O}k_{cat}$).

Model	Equation (k_n/k_o =)	k_o	Φ_1	Φ_2	Φ_S	MSR
T_1	$(1 - n + n*\Phi_1)$	0.60(1)	0.19(1)	-	-	0.00043
T_2	$(1 - n + n*\Phi_1)(1 - n + n*\Phi_2)$	0.61(1)	0.33(7)	0.7(1)	-	0.00024
T_1S	$(1 - n + n*\Phi_1)\Phi_S^n$	0.61(1)	0.30(4)	-	0.7(1)	0.00023

Table 5.2: Summary of fits of the proton inventory data to the Gross-Butler equation.

Model	N_d	N_p	d_X	$d_{X\Delta}$	SSR_X	MSR_X	$SS_{X\Delta}$	$M_{X\Delta}$	$F_{1,21}$
T_1	24	2	22	0	0.00939	0.000427	-	-	-
T_2	24	3	21	1	0.00494	0.000235	0.00445	0.00445	18.94
T_1S	24	3	21	1	0.00485	0.000231	0.00454	0.00454	19.65

Table 5.3: Analysis of variance and calculation of the *F* test-statistic for the proton inventory data. N_d and N_p indicate the number of raw data points and number of parameters in the fit, respectively, d_X are the degrees of freedom ($d_X = N_d - N_p$) for model "x", $d_{X\Delta} = d_{T1} - d_X$, SSR_X and MSR_X indicate the sum square residual and mean square residual of the fit to model x (where $MSR_X = SSR_X/d_X$), $SS_{X\Delta} = SSR_{T1} - SSR_X$, $M_{X\Delta} = SS_{X\Delta}/d_{X\Delta}$, and $F_{1,21} = M_{X\Delta}/MSR_X$, where the subscript "1,21" denotes the degrees of freedom in the $M_{X\Delta}$ and MSR_X terms of the *F* statistic, respectively. The critical *F* value with these degrees of freedom is $F_c = 4.32$ at the 5% significance level (*125*).

5.3.6 ^{13}C Kinetic isotope effects*: To determine if the ACCD-catalyzed step involving the cleavage of the cyclopropane ring of ACC contributes to steady state rate limitation under k_{cat}/K_m conditions, we conducted a ^{13}C-KIE study of the wt ACCD-catalyzed reaction using the method developed by Singleton (*190*). Using this method, the ^{13}C-KIE at each carbon atom of ACC can be simultaneously determined using NMR to measure the enrichment in ^{13}C at each carbon atom in substrate recovered from large-scale ACCD

reaction mixtures relative to the ^{13}C content of an unreacted ACC sample. As the reaction approaches completion, the residual ACC starting material will become enriched in ^{13}C at the C_α and *pro-S* C_β positions *if there is a ^{13}C-KIE on k_{cat}/K_m for the wt ACCD reaction*, because ACC molecules containing ^{13}C at the scissile C-C will react more slowly than ACC molecules containing ^{12}C at the scissile C-C bond. In order to employ this method, several conditions must be met. First, large quantities of substrate must be readily available, because the reaction must be run to near completion to achieve significant enrichment in ^{13}C and because enough unreacted starting material must be recovered in order to get accurate ^{13}C-NMR integrations. Second, the unreacted substrate must be isolable from the large amount of product that is present in the large-scale reaction mixture. Third, the enzyme-catalyzed reaction must be irreversible, in order to ensure that the reaction mixture is always under kinetic control. Our studies meet all of these requirements because gram quantities of ACC are commercially available, unreacted ACC can be spearted from α-KB on preparative scales using cation exchange chromatography, and because the the ACCD-catalyzed reaction is irreversible. The details for the calculation of the KIEs and the propagation of errors are given in the Methods section and are described by Singleton (*190*).

A typical ^{13}C-NMR spectrum for ACC taken under the conditions used in our study is shown in Figure 5.6. The resonances at ~ 175, 35, and 12 ppm correspond to the carboxyl carbon, the C_α, and the sum of the two C_β atoms of ACC, respectively. Control experiments demonstrated that an 80 sec delay time between successive NMR pulses was sufficient to allow all of the carbon atoms of ACC to relax to their ground

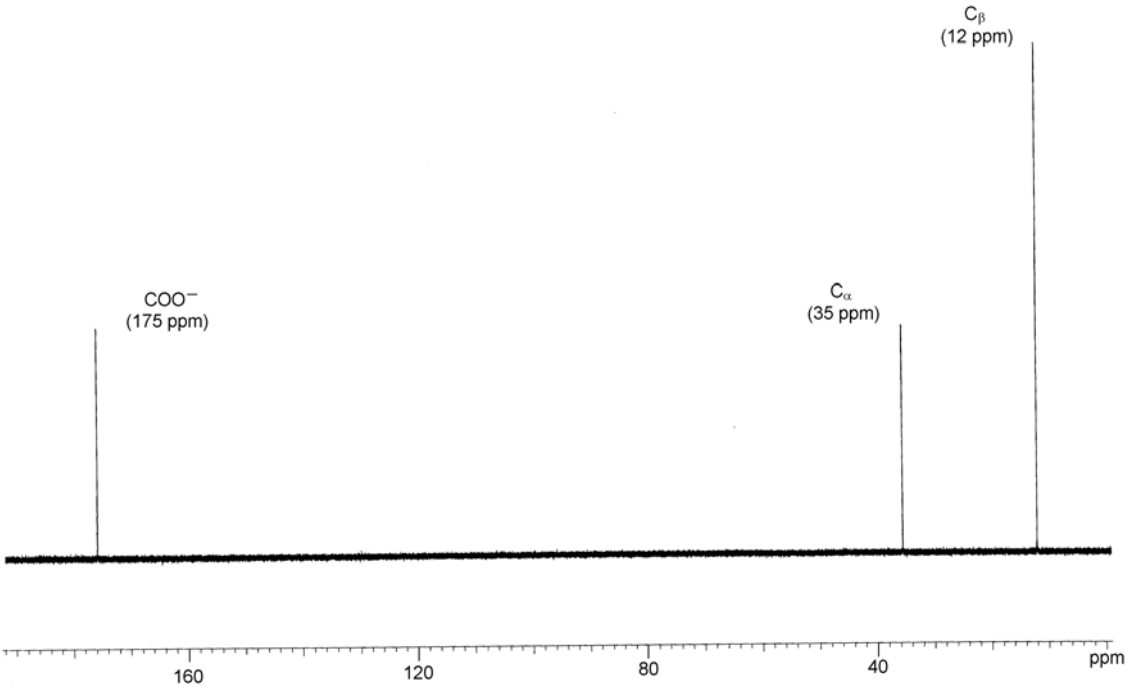

Figure 5.6: ^{13}C-NMR spectrum of ACC.

states (data not shown). A total of ten replicate spectra were recorded for every ACC sample in order to obtain an estimate for the error associated with the NMR measurement. The integrated ^{13}C signal intensities for the ten replicate measurements of each unreacted and recovered ACC sample are shown in Table 5.4. For each spectrum, the ^{13}C content at C_α and $2C_\beta$ was normalized by the ^{13}C content of the carboxyl carbon. The ten replicate measurements were averaged together to give the values for R_o and R (the relative ^{13}C content at C_α and C_β in the unreacted and recovered ACC samples, respectively). R and R_o were then used to calculate the enrichment ratio (R/R_o) for each

carbon atom in each reaction. The R/R_o parameter determined from the NMR data in

Reaction 1

	Unreacted ACC					Recovered ACC				
N	COO-	C_α	C_β	$R_{o(C\alpha)} = C_\alpha/COO-$	$R_{o(C\beta)} = C_\beta/COO-$	COO-	C_α	C_β	$R_{(C\alpha)} = C_\alpha/COO-$	$R_{(C\beta)} = C_\beta/COO-$
1	.75	.746	1.32	.994	1.76	.804	.809	1.4	1.01	1.74
2	.775	.755	1.34	.974	1.73	.808	.824	1.42	1.02	1.76
3	.77	.756	1.31	.982	1.70	.81	.832	1.43	1.03	1.77
4	.772	.749	1.31	.970	1.70	.814	.829	1.43	1.02	1.76
5	.735	.748	1.3	1.02	1.77	.839	.846	1.45	1.01	1.73
6	.755	.733	1.32	.971	1.75	.82	.837	1.45	1.02	1.77
7	.75	.741	1.3	.988	1.73	.823	.829	1.46	1.01	1.77
8	.743	.742	1.33	.999	1.79	.851	.839	1.44	0.986	1.69
9	.749	.737	1.3	.984	1.74	.814	.846	1.45	1.04	1.78
10	.757	.741	1.33	.979	1.76	.825	.848	1.44	1.03	1.75
	Average R_o			0.986(4)	1.74(1)	**Average R**			1.016(5)	1.75(1)

Reaction 2

	Unreacted ACC					Recovered ACC				
N	COO-	C_α	C_β	$R_{o(C\alpha)} = C_\alpha/COO-$	$R_{o(C\beta)} = C_\beta/COO-$	COO-	C_α	C_β	$R_{(C\alpha)} = C_\alpha/COO-$	$R_{(C\beta)} = C_\beta/COO-$
1	.979	.937	1.62	.957	1.655	1.2	1.17	2.03	.975	1.692
2	.977	.908	1.61	.929	1.648	1.21	1.15	2.07	.950	1.717
3	.976	.926	1.62	.949	1.66	1.21	1.19	2.06	.983	1.702
4	.946	.942	1.62	.996	1.712	1.2	1.19	2.07	.992	1.725
5	.97	.906	1.61	.934	1.66	1.21	1.21	2.1	1.00	1.736
6	1.01	.941	1.63	.932	1.614	1.2	1.18	2.07	.983	1.725
7	.99	.954	1.65	.964	1.667	1.23	1.16	2.1	.943	1.707
8	.996	.922	1.61	.926	1.616	1.24	1.19	2.07	.960	1.669
9	.984	.926	1.62	.941	1.646	1.2	1.18	2.06	.983	1.717
10	.999	.948	1.64	.949	1.642	1.22	1.21	2.09	.992	1.713
	Average R_o			.948(7)	1.652(6)	**Average R**			.976(6)	1.710(6)

Table 5.4: Summary of raw ^{13}C-NMR integrations and calculation of average R and R_o values for the C_α and C_β atoms in the two replicate reactions. The values in parentheses on the average R and R_o parameters are standard errors.

Table 5.4, the fraction of reaction measurement (F) determined as described in the Methods section, and the calculated KIE for the C_α and C_β atoms are summarized in Table 5.5. For the calculation of the KIE on the *pro-S* C_β, we assumed that the *pro-R* C_β

exhibited a KIE of unity and that the ^{13}C enrichment at 12 ppm was due solely to enrichment at the *pro-S* C_β atom. Under this assumption, Dr. Mark Ruszczycky (a postdoctoral associate in our lab) derived an expression for the KIE on the *pro-S* C_β:

Eqtn 5.13:

$$KIE_{C\beta} = \ln(1-F)/\ln[(1-F)(2R/R_o-1)]$$

The calculated $^{13}k_{cat}/K_m$ on the C_α and *pro-S* C_β atoms of ACC from the two replicate measurements were then averaged together to give a ^{13}C-KIEs of 1.015 ± 0.005 on C_α and of 1.017 ± 0.017 on *pro-S* C_β, respectively. Unfortunately, while the ^{13}C-KIE on C_α appeared to be significantly larger than unity in both reactions, the averaged ^{13}C-KIE on *pro-S* C_β was within error of unity. Thus, more replicate measurements will be needed before a definitive statement can be made regarding the carbon kinetic isotope effect at the *pro-S* C_β position of the substrate. Nevertheless, these ~ 1 – 2 % isotope effects compare favorably with $^{13}k_{cat}/K_m$ isotope effects measured for enzyme-catalyzed reactions, which typically range from ~ 1 – 4% (*211-216*). The intrinsic ^{13}C-KIE for PLP-catalyzed decarboxylation of amino acids has been estimated to be ~ 1.06 (*215*), suggesting that the C_α-C_β bond cleavage step in ACCD catalysis is likely only partially rate limiting. Overall, these data suggest that the cyclopropane ring cleavage event is at least partially rate-limiting to wt ACCD catalysis under k_{cat}/K_m conditions.

Reaction	$R/R_{o\ (C\alpha)}$	$\Delta R/R_{o(C\alpha)}$	$R/R_{o(C\beta)}$	$\Delta R/R_{o(C\beta)}$	F	ΔF	$KIE_{(C\alpha)}$	$KIE_{(C\beta)}$
1	1.031	0.017	1.000	0.005	0.906	0.006	1.013(7)	1.00*
2	1.030	0.010	1.031	0.006	0.834	0.006	1.017(6)	1.034(3)
							1.015(5)	1.017(17)

Table 5.5: Summary of $^{13}k_{cat}/K_m$ data for the wt ACCD reactions. R/R_o for each reaction was calculated from the NMR data in Table 5.4. The standard errors on the measurements of the R and R_o parameters in Table 5.4 were propagated to determine the error on R/R_o ($\Delta R/R_o$). The fraction of reaction (F) and its uncertainty (ΔF) were determined by the LDH reporter assay as described in the Methods. $KIE_{(C\alpha)}$, $KIE_{(C\beta)}$, and their errors (shown in parentheses) were then calculated using Eqtn 5.6 – 5.9. Finally, the KIEs at each carbon determined from the two replicate measurements were averaged togethers to give the average KIEs and their standard errors. *The R/R_o of unity leads to errors of 0 in Eqtns 5.7 and 5.8.

5.3.7 Multiwavelength stopped-flow studies: In an attempt to identify and characterize the PLP-linked intermediates that form during turnover under saturating ACC concentrations, absorption spectra for wt ACCD and its E295D, Y268F, and Y294F mutants were collected by a stopped-flow apparatus using a diode array detector (Figure 5.7). For wt ACCD, there is a slight increase in absorbance at all wavelengths immediately upon mixing with ACC at pH 7.5, but there are no shifts in the λ_{max} of the internal aldimine peaks (at 329 and 419 nm). This immediate increase in absorbance at all wavelengths upon mixing with ACC was observed in several different buffers at several different pH and ionic strengths (data not shown), and the cause of this phenomenon is currently not clear. In the fast reaction phase for the wt enzyme, the ketoenamine tautomer of the internal aldimine (λ_{max} = 419 nm) is converted into a new species ($k_{obs,1}$ = 260 s^{-1}) that is indistinguishable from the enolimine tautomer of the internal aldimine in the resting enzyme form (λ_{max} = 329 nm). This species is most likely either the enolimine form of an external aldimine or the the *gem*-diamine species that is

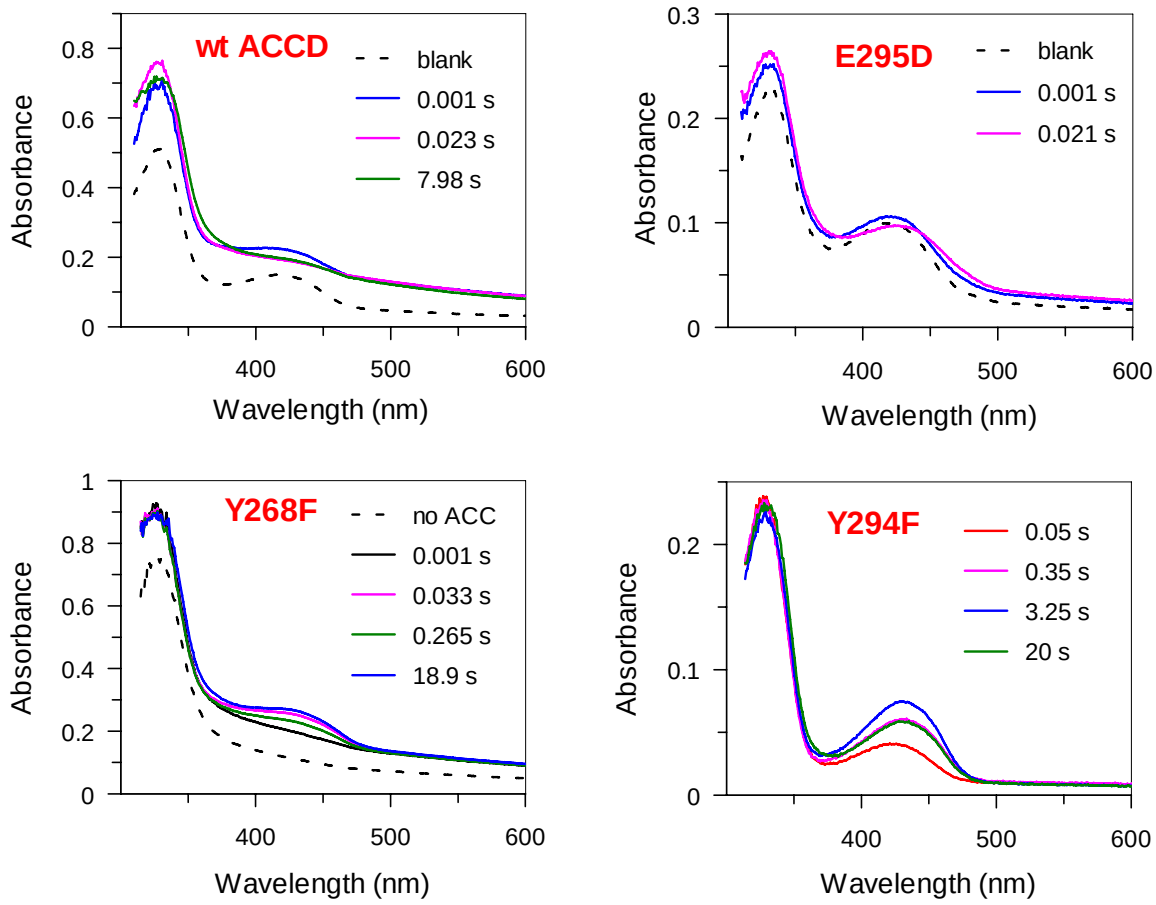

Figure 5.7: Multiwavelength stopped-flow studies of wt ACCD and its mutants. The times in each panel indicate the time after mixing. The "blank" spectra were recorded by mixing enzyme against buffer lacking ACC.

observed in the crystal structure and which also absorbs maximally in the 330 nm region (*180, 217*). After the completion of the fast phase, there is a slower phase occurring at a catalytically competent rate ($k_{obs,2}$ = 2.3 s^{-1}), during which the 329 nm absorption band decreases in intensity and broadens slightly, perhaps indicating the formation of a spectroscopically similar, but distinct PLP-linked intermediate.

Like the wt ACCD reaction, there was an immediate increase in absorbance at all wavelengths upon mixing the E295D mutant with 50 mM ACC at pH 7.5, but there were no shifts in the λ_{max} values of the internal aldimine peaks (λ_{max} = 331 and 421 nm) during this initial phase. In contrast to the wt enzyme, however, the λ_{max} of both of the internal aldimine peaks shift slightly to values of 329 and ~ 428 nm, respectively, at an observed rate of ~ $k_{obs,1}$ = 150 s^{-1}. The spectral shifts are associated with a slight decrease in the absorption intensity in the ~ 420 nm region and a corresponding increase in the ~ 330 nm region. Similar rapid spectral shifts have been observed in other PLP-dependent enzymes, and are usually attributed to the formation of an external aldimine intermediate, whose absorption properties often differ slightly from the internal aldimine (*218*).

In the Y268F mutant, a species with λ_{max} at 431 nm forms upon mixing with ACC at pH 8.8 (the pH optimum for this mutant). As with the E295D mutant, the λ_{max} of this intermediate is red-shifted relative to the λ_{max} of the ketoenamine tautomer of the internal aldimine (419 nm, see Figure 5.3), suggesting that the intermediate that forms in the presence of ACC is distinct from the internal aldimine and is likely an external aldimine. In contrast to the wt ACCD and E295D reactions, the absorbance changes in the ~ 330 nm region are very slight with the Y268F mutant. The absorbance changes at 431 nm are triphasic and, interestingly, the intensity of the 431 nm absorption band increases during the fast phase ($k_{obs,1}$ ~ 70 s^{-1}), then decreases over the next ~ 200 msec ($k_{obs,2}$ ~ 15 s^{-1}), then increases again over the next several seconds in a slow phase ($k_{obs,3}$ ~ 0.5 s^{-1}). All three kinetic phases are fast enough to be kinetically competent (k_{cat} for the Y268F enzyme at pH 8.8 is 0.026 s^{-1}). If all three phases represent reactions that are on the

pathway for conversion of ACC to α-KB, it is not clear why the ketoenamine tautomer of the external aldimine accumulates, decays, and then re-accumulates during the Y268F-catalyzed reaction cycle.

In the catalytically inactive Y294F mutant (*179*), the ketoenamine form of an external aldimine (λ_{max} = 431 nm) also appears to accumulate upon ACC binding at pH 7.5. Support for this assignment has been provided by the X-ray crystal structure of the yeast Y295F enzyme (analogous to the *Pseudomonas* sp. ACP Y294F mutant) solved in the presence of ACC, where an external aldimine species was observed (*178*). Like the Y268F reaction, the absorbance changes in the Y294F mutant at 431 nm upon ACC binding were multi-phasic. However, in this case of Y294F, the 431 nm absorption increased in the fast phase ($k_{obs,1}$ = 6.1 s^{-1}), then continued to increase in an intermediate phase ($k_{obs,2}$ = 0.6 s^{-1}) before decaying in a slow phase ($k_{obs,3}$ = 0.024 s^{-1}).

5.4 Conclusions and Mechanistic Interpretations

The purpose of these studies was to distinguish between mechanisms for ACCD catalysis involving nucleophile or acid-catalyzed cyclopropane ring opening. In principle, these two possibilities can be distinguished with studies on the pH-dependence of the steady state kinetic parameters – if the acid/base chemistry step(s) limit steady state turnover. Thus, we investigated the pH-dependence of the kinetic properties of wt ACCD and several of its mutant enzymes. In the E295D mutant, k_{cat} is reduced roughly 10 fold relative to the wild type enzyme, suggesting that the putative ion pair interaction

between the carboxylate side chain of Glu295 and the protonated pyridinium nitrogen atom of the PLP coenzyme (see Figure 5.1) is somehow important for stabilizing the rate-limiting transition state. Like the wt enzyme, however, k_{cat} for the E295D mutant was not pH-dependent, which prevents us from making any definitive conclusions on the involvement of acid/base catalysis in the rate limiting step(s) of the chemical mechanism. Nevertheless, the most plausible explanation for these findings is that, during ACCD catalysis, electrons from ACC are delocalized into the PLP ring. This is expected to occur if a nucleophile-catalyzed ring cleavage mechanism is operative (Scheme 5.5), but may not be necessary for an acid-catalyzed ring opening (Scheme 5.9). In this mechanism, the increased distance between the carboxylate of Asp295 and the PLP may weaken the ion pair interaction and hinder the ability of the pyridinium moiety to accept ACC-derived electrons. An essential function for the putative ion pair between residue 295 and the PLP is supported by studies of a E295Q mutant, which has been reported to be catalytically inactive (*178*).

Previous studies have shown that the Tyr294 residue is required for catalysis, implicating its phenoxyl group (positioned 3 Å from the *pro-S* C_β of ACC) as either a nucelophile or as an acid in the ACC ring-scission reaction (*178, 179*). Since the Y294F mutant is catalytically inactive (*178, 180*), we speculated that mutation of the adjacent Tyr268 residue (which hydrogen bonds with Tyr294) could alter the kinetic properties of the enzyme if it indeed interacts with Tyr294 and if Tyr294 plays an essential function in catalysis. Consistent with this hypothesis, k_{cat} for the Y268F enzyme was reduced ~ 50 fold relative to the wt enzyme. In addition, the pH-dependence of k_{cat} for Y268F showed

that a residue with a pK_a ~ 7.8 in the Michaelis complex must be deprotonated for maximal catalytic activity. The most likely candidate for the group with pK_a ~ 7.8 is Tyr294, because it is the only amino acid in the ACCD acitive site that is directly adjacent to both the side chain of Tyr268 and the ACC-PLP adduct. These results provide support for a chemical mechanism for ACCD involving nucelophilic attack by Tyr294 on ACC to initiate ring cleavage.

Based on the kinetic characterization of wt ACCD and its mutants, a working hypothesis for the pH-dependence of the steady state kinetic parameters and the protonation states of the important active site residues can be proposed (Scheme 5.11). In this model, pK_1 and pK_2 represent the same groups in the k_{cat}/K_m-pH profiles for wt ACCD, Y268, and E295D. The group responsible for pK_1 is assigned to the phenoxyl group or Tyr294, which must be deprotonated for ACC binding. Support for this conclusion is derived from the similarity of pK_1 in the wt and E295D mutant enzymes, because the mutation of E295 is not expected to severely alter the interaction between Tyr268 and Tyr294. In addition, the shift in pK_1 of ~ 1.5 units in the Y268F enzyme suggests that the loss of the conserved hydrogen bonding interaction between Tyr268 and Tyr294 may serve to raise the pK_a of Tyr294. Tyr294 likely needs to be ionized in order to deprotonate the incoming amino group of ACC and to facilitate the aldimine exchange reaction between ACC and the protonated internal aldimine. A role for Tyr294 as an active site base for deprotonating ACC is also supported by the pre-steady state kinetic studies, which demonstrate that the observed rate of external aldimine formation is significantly reduced in the Y294F mutant enzyme.

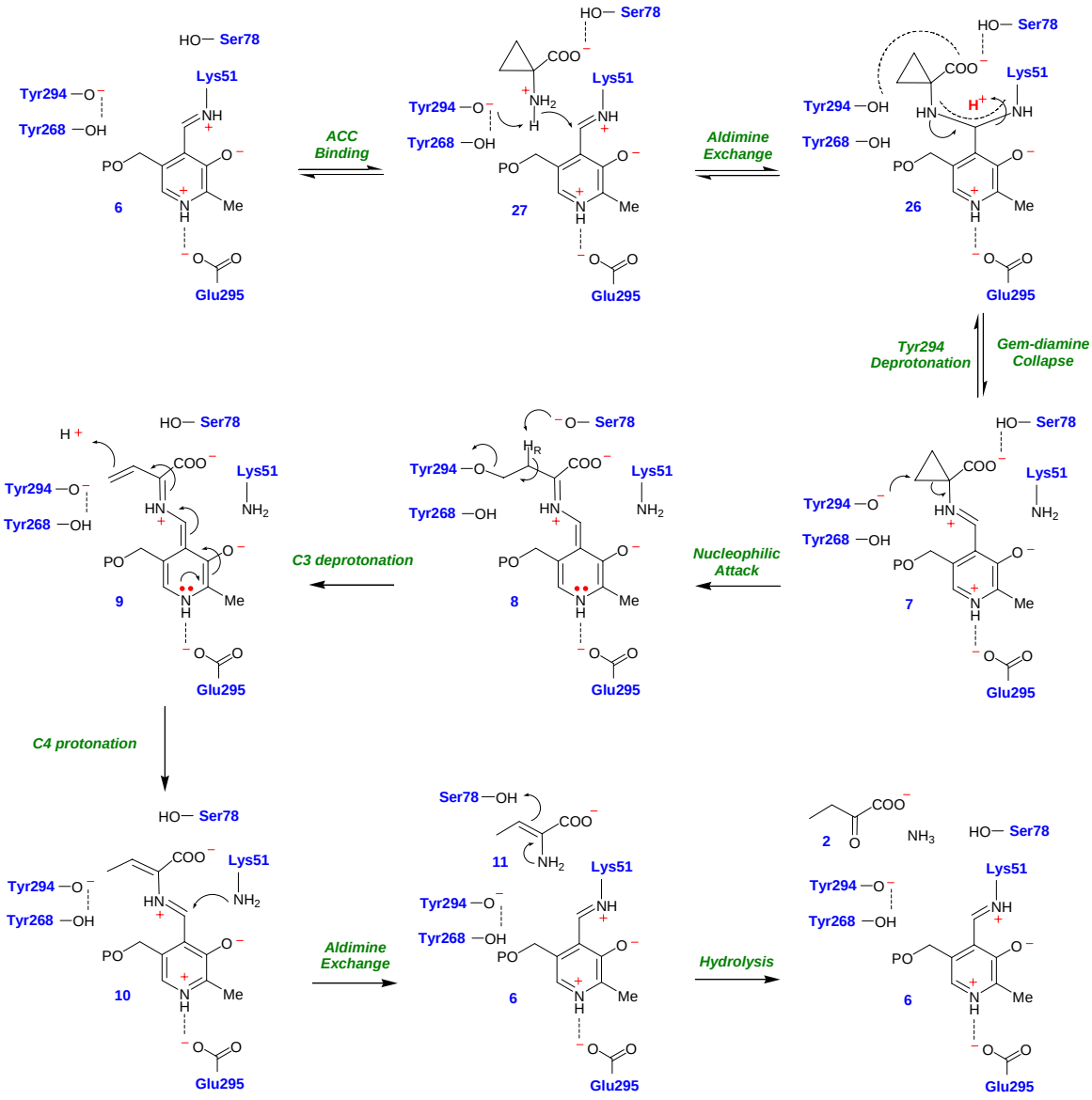

Scheme 5.11: Revised chemical mechanism for ACCD. Putative hydrogen bonds are shown with dashed lines.

The pK_2 values determined from the k_{cat}/K_m-pH profiles are relatively invariant, suggesting that this ionization constant likely corresponds either to the amino group of ACC or the side chain of Ser78. The pK_a of cyclopropylamine is ~ 8.7 in aqueous

solution (*219*), very similar to the kinetic pK_2 values (~ 9) measured in our studies. A protonated, positively-charged ACC amino group could engage in favorable electrostatic interactions with the deprotonated, negatively-charged Tyr294 to facilitate ACC binding. The unprotonated substrate may not bind to ACCD as tightly, leading to the large $K_{m,ACC}$ values observed at higher pH. Alternatively, if Ser78 is responsible for pK_2, Ser78 would need to be protonated to hydrogen bond to the ACC carboxyl (as observed in the crystal structure). The pK_a of the hydroxyl side chain of Ser78 may be lowered by hydrogen bonding interactions with the backbone amide groups of Gln80 and Thr81 and/or through a putative helix-dipole interaction. The lowering of the pK_a of Ser78 could also serve a catalytic function, as this residue has been implicated for a role in acid/base chemistry during turnover, perhaps serving to mediate proton transfers at C3 of the substrate-PLP adduct following cyclopropane ring scission (*182*). Finally, spectroscopic studies of the internal aldimines of wt ACCD, Y268F, and Y294F suggest that the Schiff base remains protonated across the pH range studied, suggesting that the deprotonation of PLP is not responsible for pK_2.

Several important mechanistic conclusions can also be gleaned from the stopped flow data. First, the fast phase of the Y294F reaction with ACC (6.1 s^{-1}) is significantly slower than the fast phases for all of the other mutants (70 – 260 s^{-1}), suggesting that Tyr294 likely plays an important role in ACC binding and in initiating the aldimine exchange reaction between ACC and the internal aldimine (**6** → **27** → **26**, Scheme 5.11). Our hypothesis is that Tyr268 lowers the pK_a of Tyr294, enabling the latter to deprotonate the incoming ACC amine. Second, PLP species consistent with the

ketoenamine tautomer of an external aldimine (**7**) form in the pre-steady state fast phases of the E295D and Y268F-catalyzed reactions. The accumulation of an external aldimine in these catalytically active mutant enzymes, and the requirement for a group with pK_3 ~ 7.8 (most likely the phenoxyl side chain of Tyr294) to be deprotonated for maximal activity in the Y268F mutant, are most consistent with a mechanism involving a nucleophile-induced cyclopropane ring scission, where the protonated iminium group of the ketoenamine form of the external aldimine would help to delocalize the liberated ACC ring electons into the coenzyme.

Interestingly, a clearly definable ketoenamine tautomer of an external aldimine species does not appear to accumulate in the pre-steady state of the wt ACCD reaction. Instead, a species consistent with either an enolimine tautomer of an internal/external aldimine or a *gem*-diamine (**26**) accumulates rapidly within the pre-steady state at an observed rate of ~ 260 s^{-1} under saturating concentrations of ACC. Although the observed species is indistinguishable from the enolimine tautomer of the internal aldimine, the attack of the incoming ACC amine group on the C4′ atom of PLP to initiate the aldimine exchange is expected to be fast, especially when considering that the Y268F and E295D mutant enzymes quickly catalyze the aldimine exchange reaction. The observable species in the stopped-flow studies of the wt enzyme is most likely the *gem*-diamine that is observed in the X-ray crystal structure of the wt ACCD enzyme in the presence of ACC (*179, 180*). A similar *gem*-diamine intermediate forms in incubations of wt ACCD with the slow, tight binding inhibitor, 1-aminocyclopropane-1-phosphonate (*180, 217*). Based on structural studies and our pH profiles, the side chain of Tyr294 is

likely protonated in the *gem*-diamine state of the ACCD-ACC complex, allowing it to hydrogen bond with the ACC carboxyl group (2.7 Å). It is possible that deprotonation of Tyr294 and the collapse of the *gem*-diamine into the external aldimine (**26** → **7**) is partially rate-limiting in the wt ACCD reaction. The resulting external aldimine form of the enzyme would then be poised for nucleophilic attack by Tyr294 on the *pro-S* C_β of ACC. It is interesting to note that the internuclear distance between the oxygen atom of the Tyr294 side chain and the phosphonate oxygen of the 1-aminocycloproane-1-phosphonate (ACP) inhibitor is very short (2.3 Å) in the *gem*-diamine form of the ACP-ACCD complex (*180*). This strong hydrogen bond could help to trap the ACP-ACCD complex in an unreactive *gem*-diamine state. Together, the structural studies of the ACC and ACP complexes with wt ACCD suggest that the deprotonation of Tyr294 may be energetically difficult in the wt ACCD-ACC complex. At present, it is still unclear why the aldimine exchange reaction in wt ACCD is halted in the *gem*-diamine state, while both the Y268F and E295D mutants can apparently move quickly through this intermediate to generate the external aldimine rapidly in the pre-steady state.

The proposed mechanism for ACCD catalysis involving nucleophilic addition into the cyclopropane ring is also consistent with the solvent and ^{13}C kinetic isotope effects determined in this study. Our current hypothesis to explain the kinetic isoptope effects is that the steps leading from *gem*-diamine decay into the external aldimine (**26** → **7**) and from the external aldimine to the quinonoid species (**7** → **8**) are both partially rate limiting to steady state turnover. Here, a solvent KIE could be expressed on the decay of the *gem*-diamine species. In this step, the side chain of Tyr294 needs to be deprotonated

to activate this residue as the nucleophile, and the amino side chain of Lys51 needs to be eliminated from the *gem*-diamine, which requires protonation. Either one of these proton transfers could potentially generate a normal solvent KIE. Following *gem*-diamine decay, a reactive external aldimine intermediate is generated. This species cannot be detected in the pre-steady state of the wt ACCD reaction, perhaps because the subsequent nucleophilic attack step is rapid. Nucleophilic addition into the cyclopropane ring is then expected to irreversibly cleave the C_α-C_β bond, generating the quinonoid species (**8**). In order for the $^{13}k_{cat}/K_m$ isotope effects of ~ 1.5 % on C_α and C_β to be observed, the transition state for the C-C bond cleavage step must be similar in energy to the transition state for the *gem*-diamine decay step if both of these steps are partially rate determining. At this point, it is worthwhile to mention that previous studies using ACC substrate analogues deuterated at the C_β atoms failed to reveal the presence of primary substrate deuterium KIEs on k_{cat} (*176*). Assuming that C-C bond cleavage is at least partially rate limting (as our ^{13}C-KIE studies indicate), these observations argue against a mechanism involving deprotonation of the cyclopropane ring to initiate ring scission, and are most consistent with a nucelophilic mode of catalysis.

Following cleavage of the cyclopropane ring, the tyrosine nucleophile can then be eliminated by the deprotonation of the *pro-R* proton at C-3 of the linearized substrate moiety, yielding the D-vinylglycine quinonoid intermediate (**9**). The catalytic competence of D-vinylglycine and identical patterns of solvent deuterium incorporation into product derived from this substrate provide support for the existence of **9** in the wt ACCD-catalyzed reaction (*167*). Based on stereochemical (*167, 176*), structural (*177*-

180), and biochemical studies (*182*), Ser78 is the most likely candidate for catalyzing this deprotonation, although a role for Lys51 in this process cannot be excluded. Protonation at C4 of the quinonoid species to give the PLP-aminoacrylate species (**10**), followed by aldimine exchange (**10** → **6**), and hydrolysis of the aminoacrylate (**11** → **2**) would complete the catalytic cycle. One or more of these steps is likely responsible for the additional portion of the solvent KIE that is measured only on k_{cat}. The groups responsible for mediating these transformations are not clear, but they likely involve some level of participation by Tyr294, Ser78, Lys51, and the PLP to shift protons around in the active site. The irreversibility of the ACCD-catalyzed reaction and our inability to detect species **7** - **10** in the wt ACCD reaction using stopped-flow spectroscopy has made characterization of the late stages of the reaction mechanism difficult.

The accumulated evidence strongly favors a mechanism for ACCD catalysis involving nucleophilic cleavage of the cyclopropane ring. However, the unexpected stability of the *gem*-diamine intermediate in the wt ACCD-ACC complex prompted us to propose an alternative mechanism (Scheme 5.9) in which Tyr294 acts as a general acid to facilitate the opening of the cyclopropane ring of ACC (*179*). The electrophilic cleavage of the cyclopropane ring by Tyr294 could be facilitated by a "push" of electron density onto the C_α atom by the N atom of the substrate-PLP bond. Precedence for a similar mode of electrophilic cyclopropane ring cleavage has been provided by Jencks and co-workers in their model studies of phenylcyclopropanols (*183*). In this proposed mechanism for ACCD, the decay of the ACC-PLP *gem*-diamine species would be

coupled to C-C bond cleavage in the rate limiting step. Thus, both solvent and ^{13}C-KIEs could be reporting on the same step in the mechanism.

Though this mechanism cannot be rigorously excluded at the moment, it is at odds with several experimental observations. First, the E295D and Y268F enzymes accumulate an external aldimine intermediate (*vide supra*), which is not predicted to form along the putative reaction coordinate for the acid-catalyzed ring opening mechanism. It is possible, however, that the mutant enzymes proceed through different chemical mechanisms than the wt enzyme. Second, stereochemical studies have shown that solvent proton incorporation into C4 of the α-KB product is not totally stereospecific (*176*), which is unexpected if Tyr294 is serving as a general acid to initiate ring cleavage from the *gem*-diamine species observed in the co-crystal structure of the wt enzyme with ACC. Third, the E295Q mutant is inactive (*178*) and the activity of the E295D mutant is significantly decreased (*vide supra*). These observations suggest that electron delocalization into the pyridinium moiety (a hallmark of normal PLP-catalysis that would not be required for turnover in the acid-catalyzed mechanism) is an important feature of wt ACCD catalysis. Finally, wt ACCD catalyzes a variety of C_α-deprotonation and C_β-elimination reactions with numerous other alternative amino acid substrates (*167, 220*). These reactions most likely proceed via quinonoid and amino acrylate-PLP species that are common to many other PLP-dependent enzyme mechanisms. Thus, the wt ACCD enzyme is at least capable of accommodating these typical PLP intermediates, which would not be employed in the acid-catalyzed ring opening mechanism. Altogether, the

cumulative studies on ACCD performed to date are most consistent with a nucleophilic mode of cyclopropane ring cleavage.

Appendix

Electrospray ionization mass spectrometry data for the FMN analogues

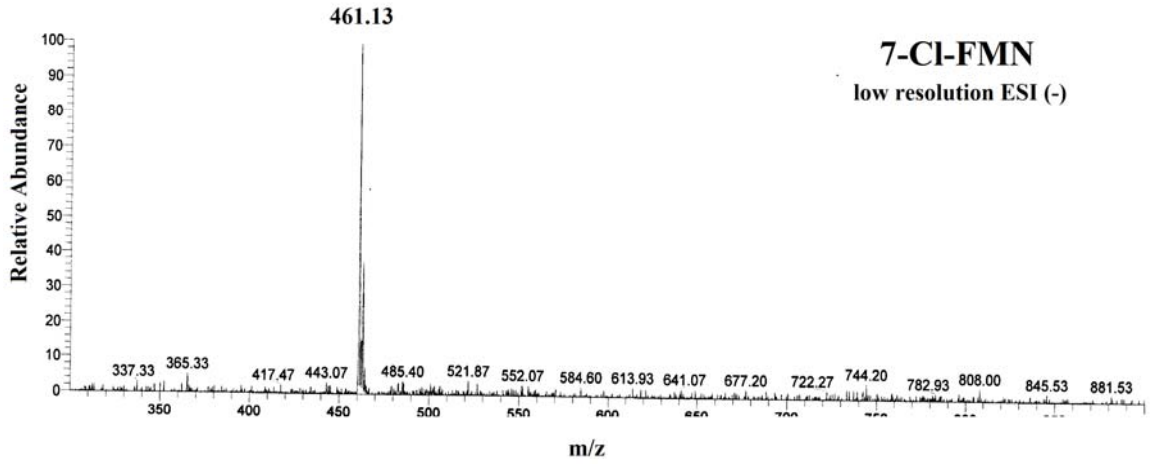

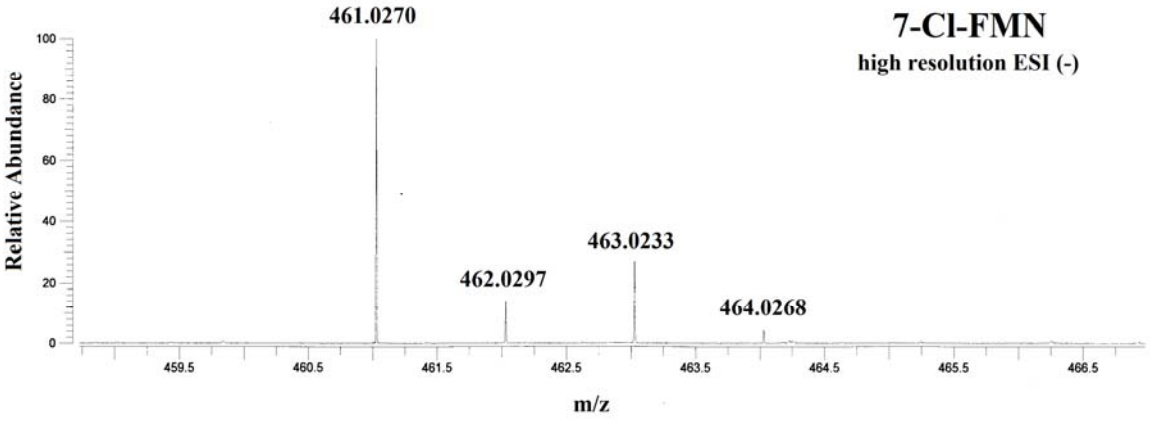

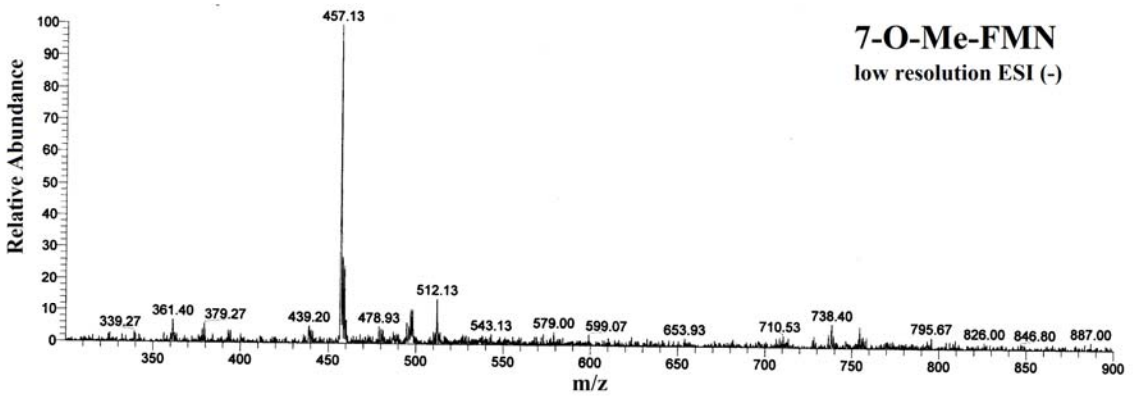
7-O-Me-FMN
low resolution ESI (-)
Relative Abundance
m/z
457.13
512.13
339.27
361.40
379.27
439.20
478.93
543.13
579.00
599.07
653.93
710.53
738.40
795.67
826.00
846.80
887.00

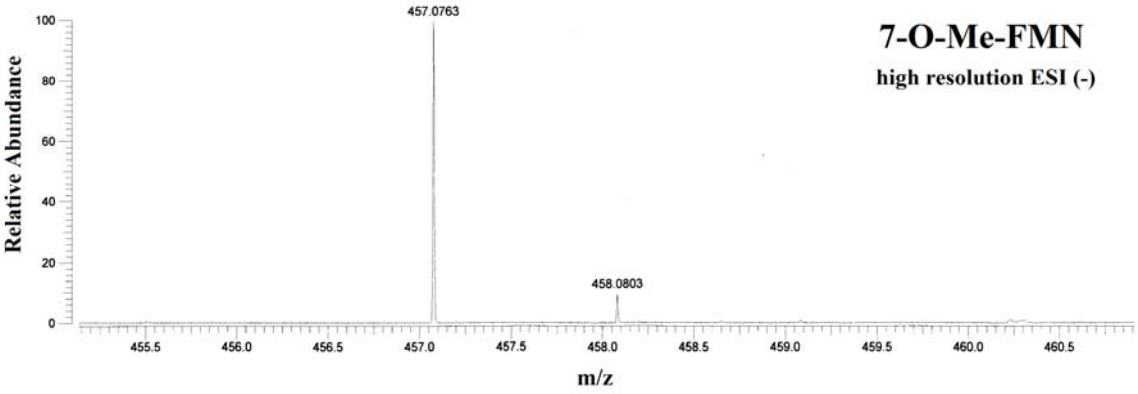
7-O-Me-FMN
high resolution ESI (-)
Relative Abundance
m/z
457.0763
458.0803

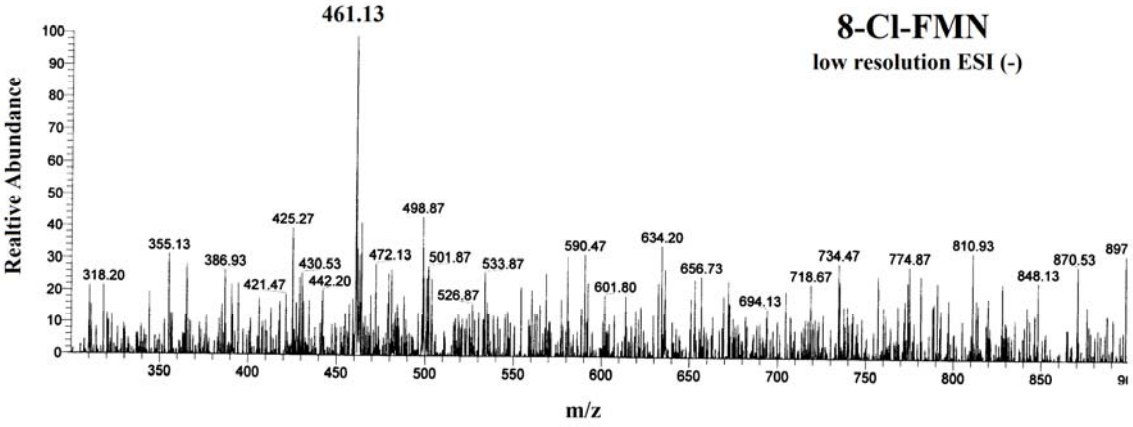
8-Cl-FMN
low resolution ESI (-)
Realtive Abundance
m/z
461.13
318.20
355.13
386.93
421.47
425.27
430.53
442.20
472.13
498.87
501.87
526.87
533.87
590.47
601.80
634.20
656.73
694.13
718.67
734.47
774.87
810.93
848.13
870.53
897

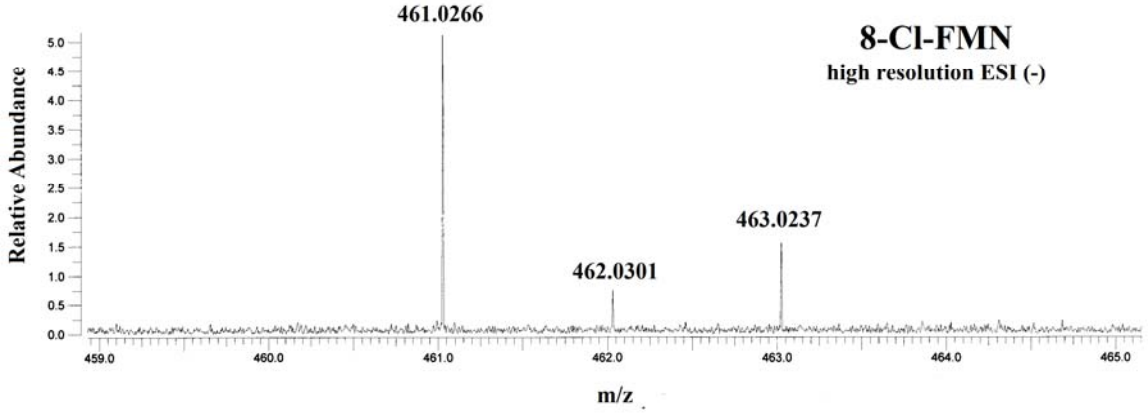
461.0266
8-Cl-FMN
high resolution ESI (-)
463.0237
462.0301
Relative Abundance
m/z

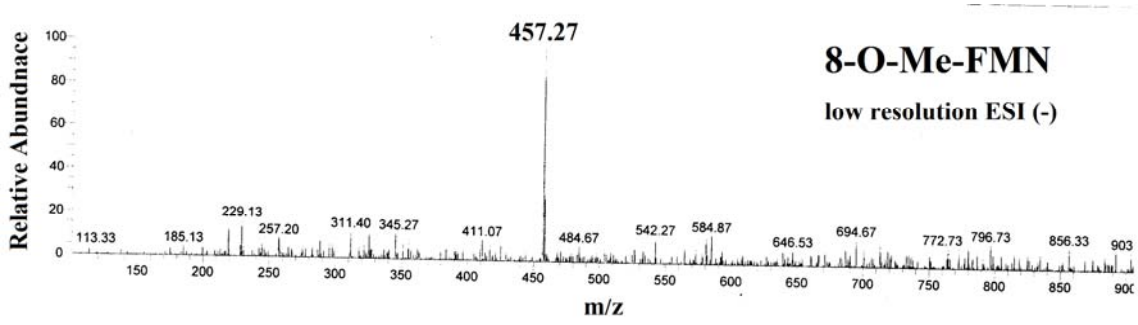
457.27
8-O-Me-FMN
low resolution ESI (-)
Relative Abundnace
m/z

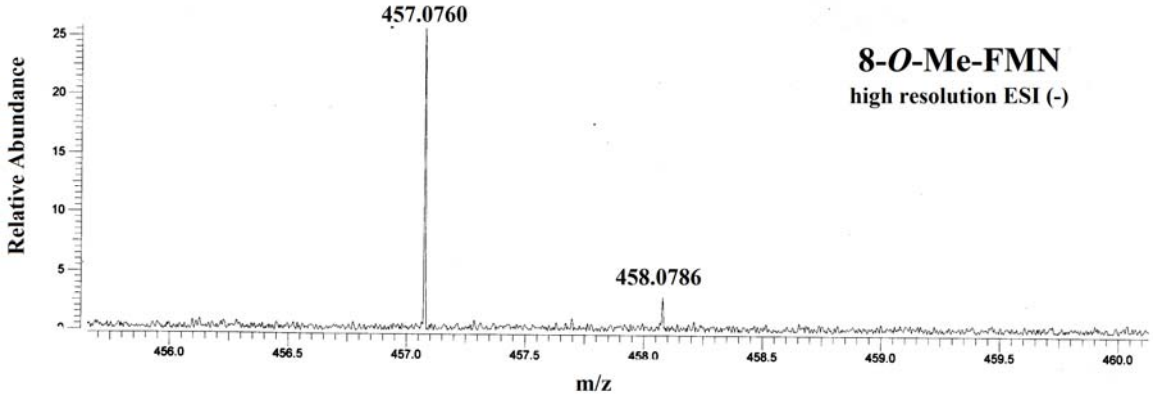
457.0760
8-O-Me-FMN
high resolution ESI (-)
458.0786
Relative Abundance
m/z

^{1}H-NMR spectra for the FMN analogues

7-Cl-FMN

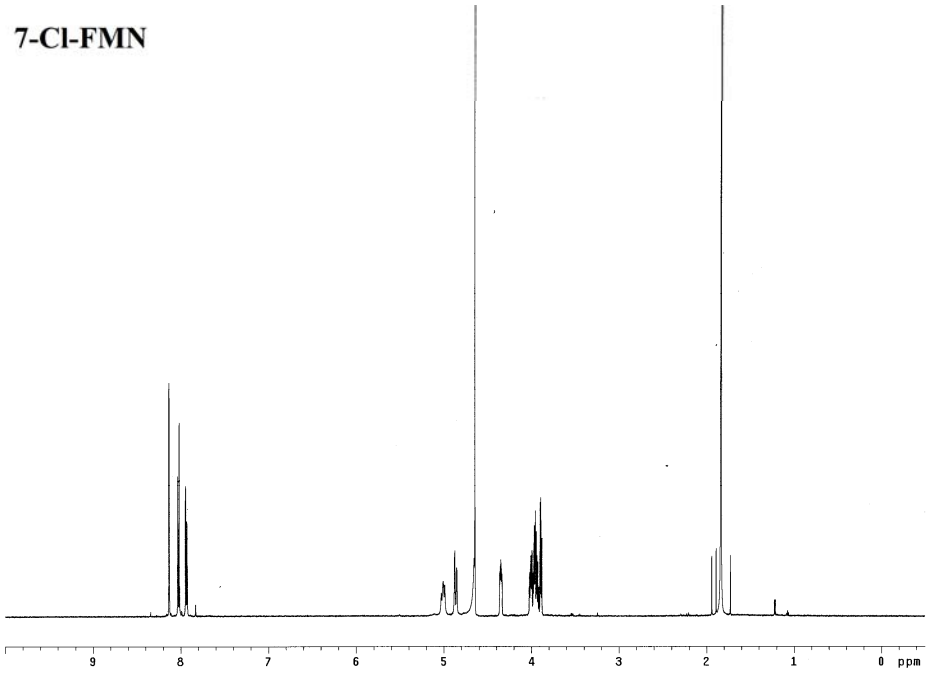

7-Cl-FMN (continued)

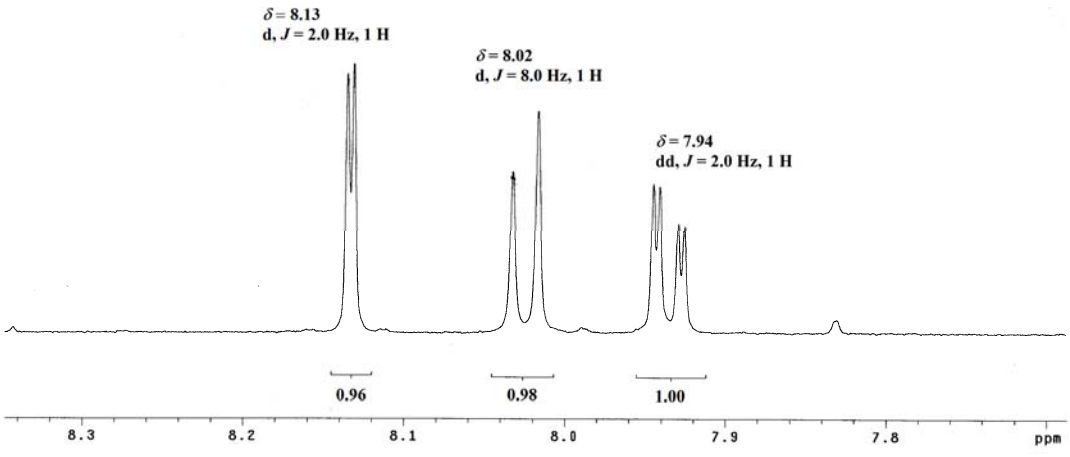

7-Cl-FMN
(continued)

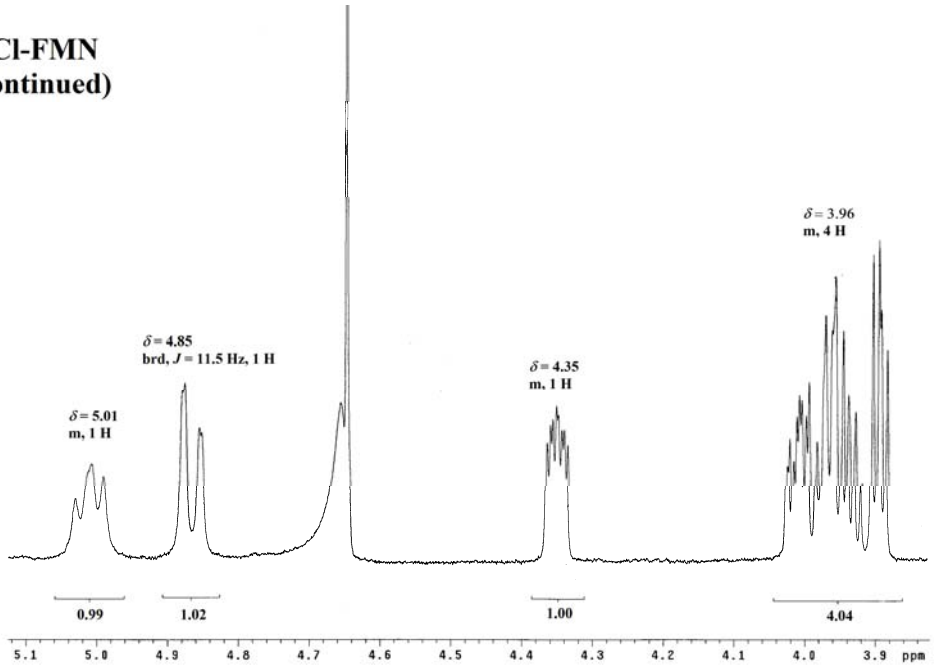

7-*O*-Me-FMN

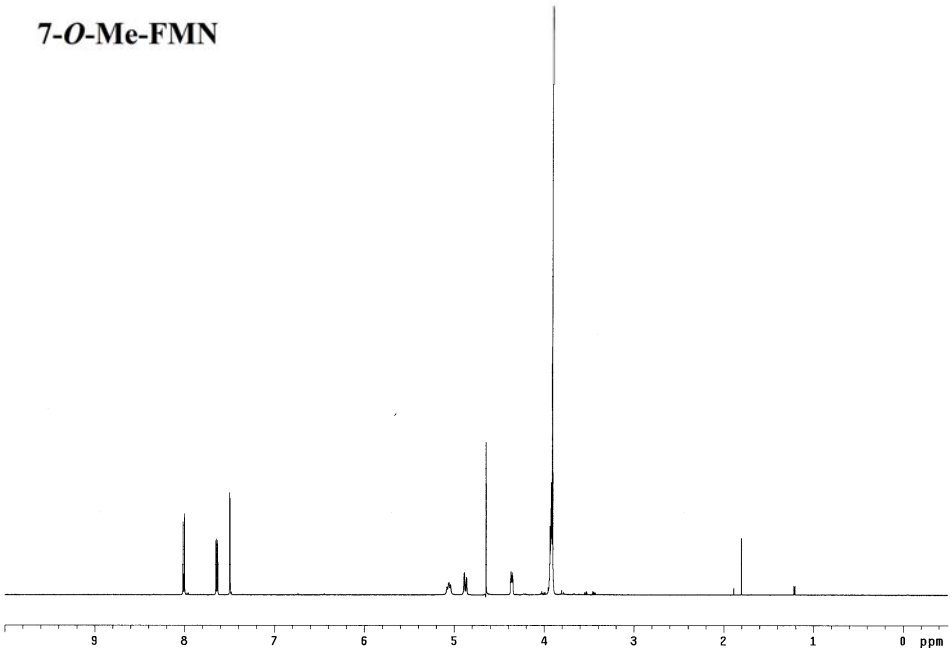

7-O-Me-FMN
(continued)

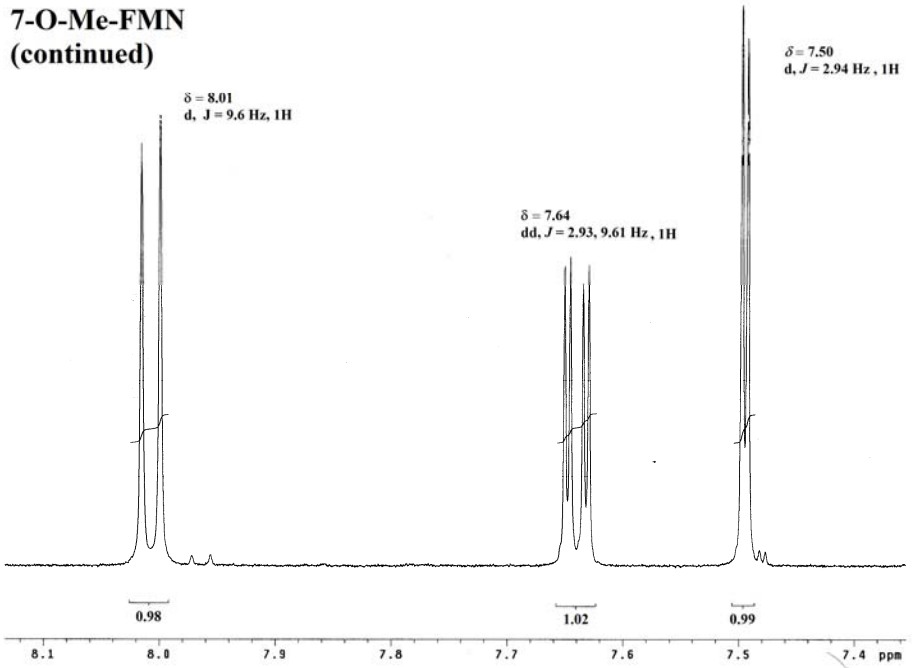

7-*O*-Me-FMN
(continued)

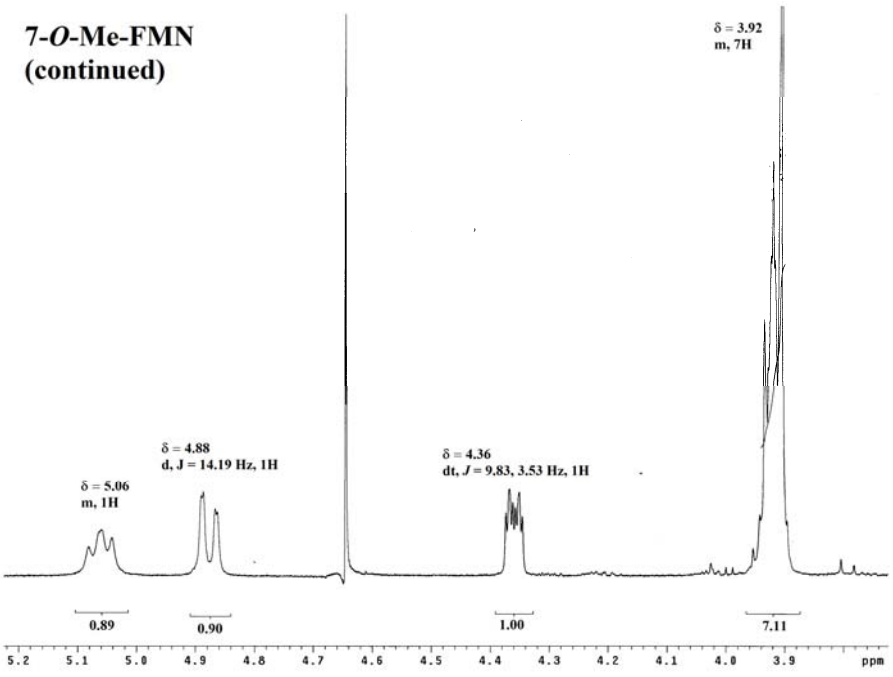

8-Cl-FMN

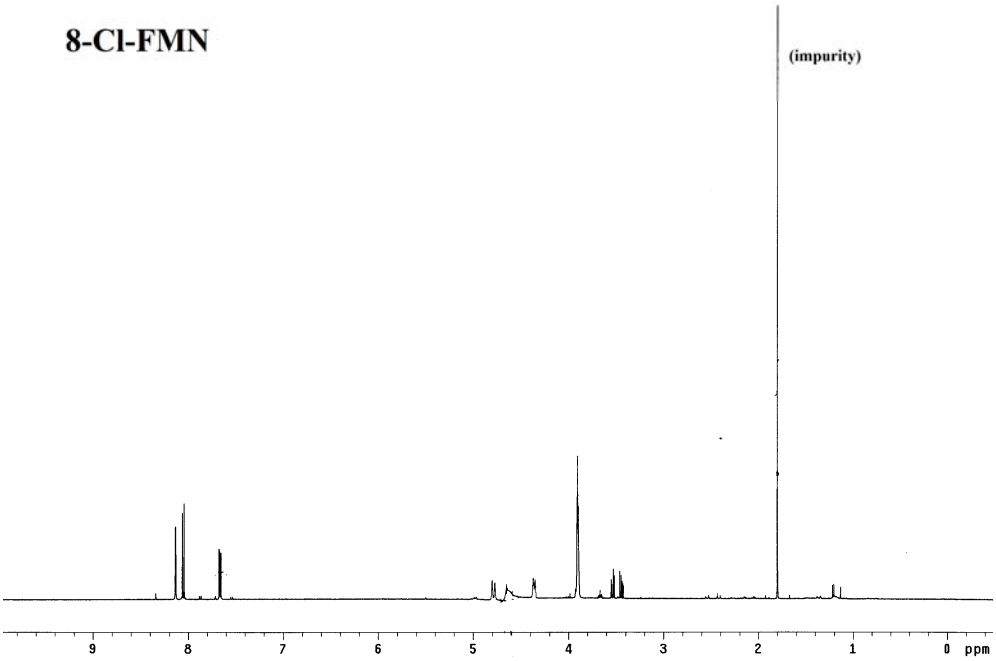

8-Cl-FMN
(continued)

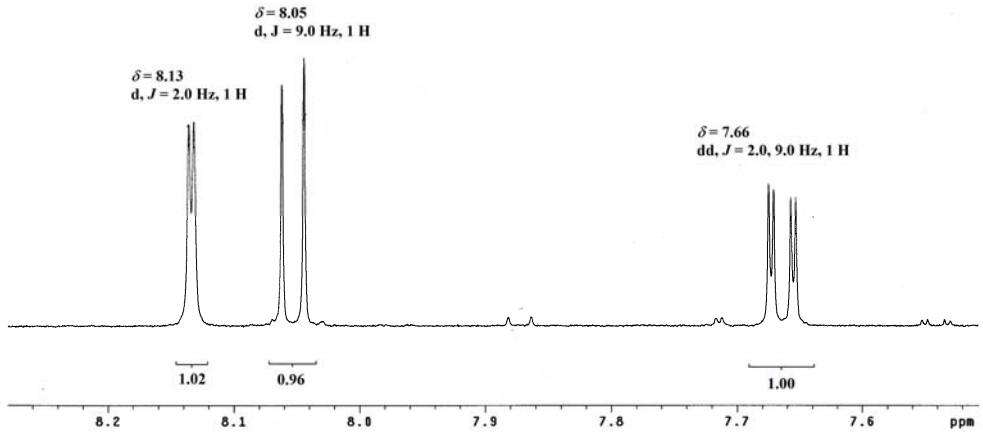

8-Cl-FMN (continued)

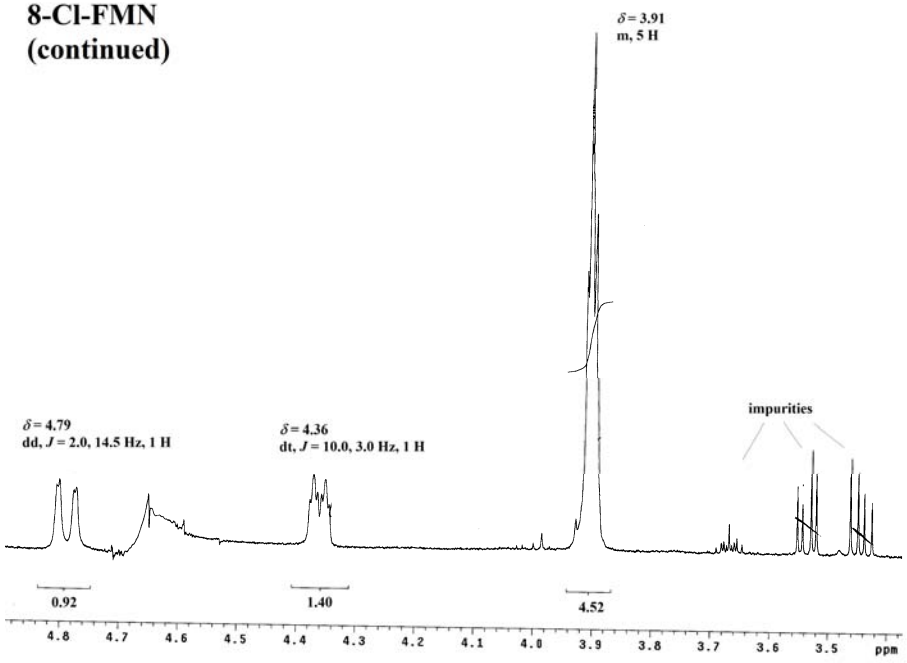

8-*O*-Me-FMN

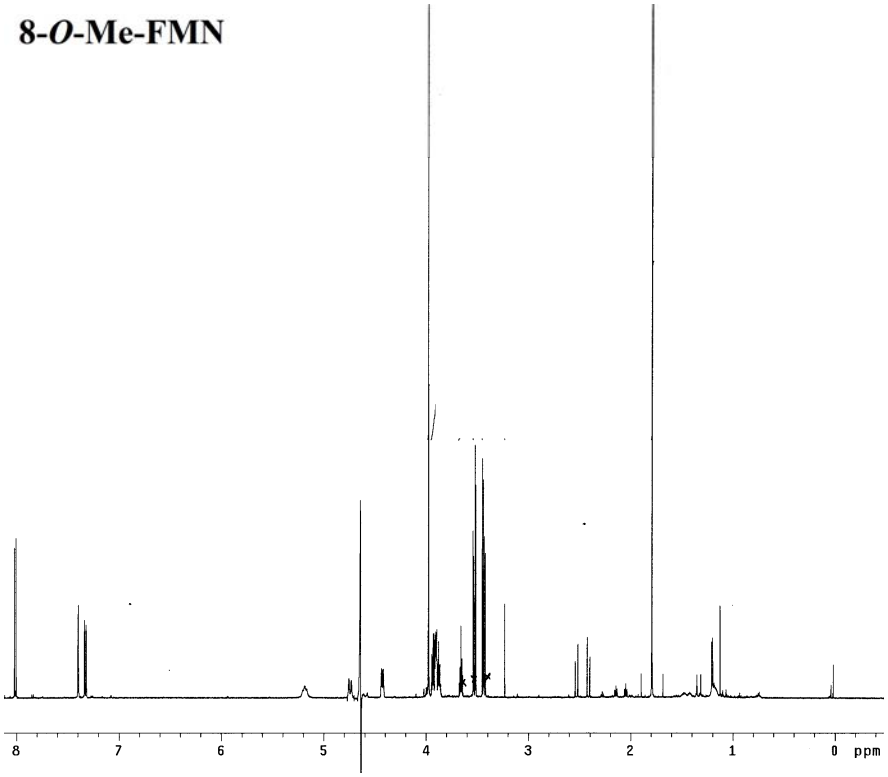

8-*O*-Me-FMN
(continued)

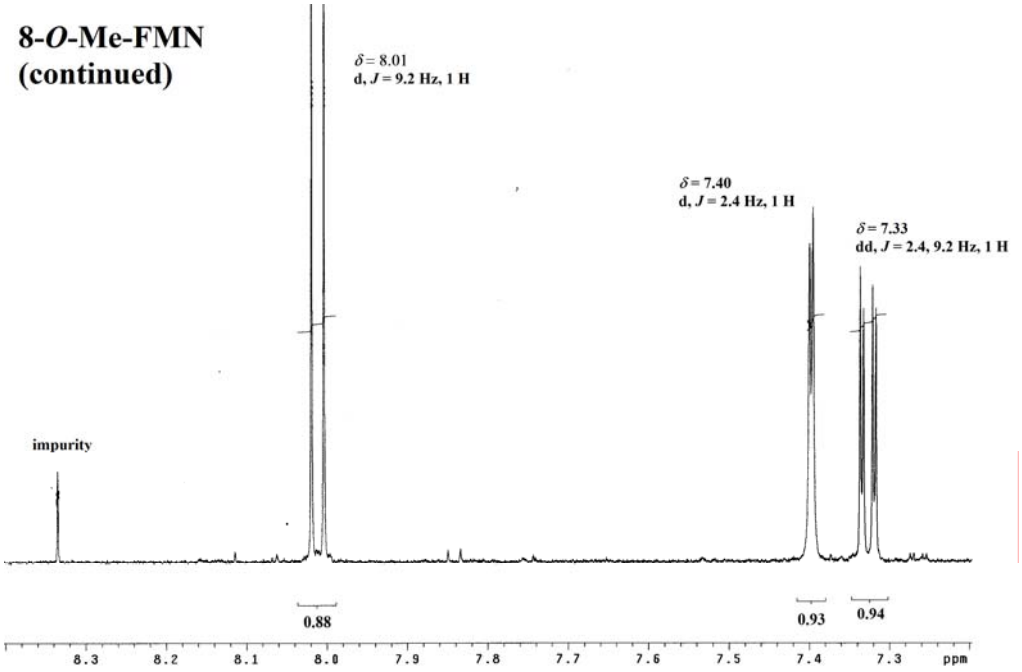

8-*O*-Me-FMN
(continued)

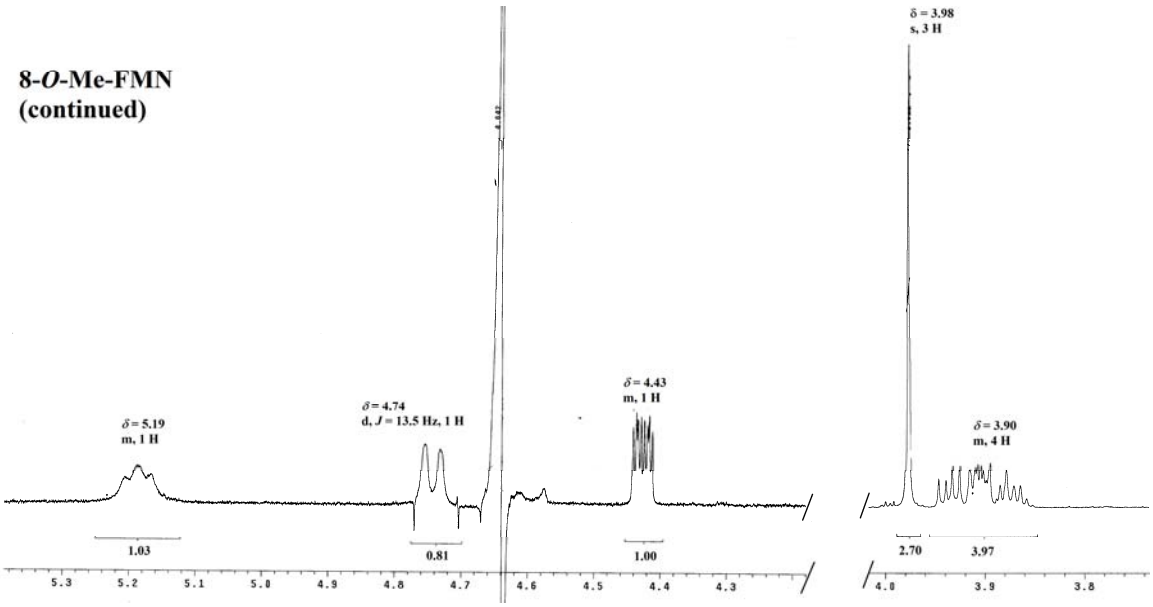

^{31}P-NMR spectra of the FMN analogues

7-Cl-FMN

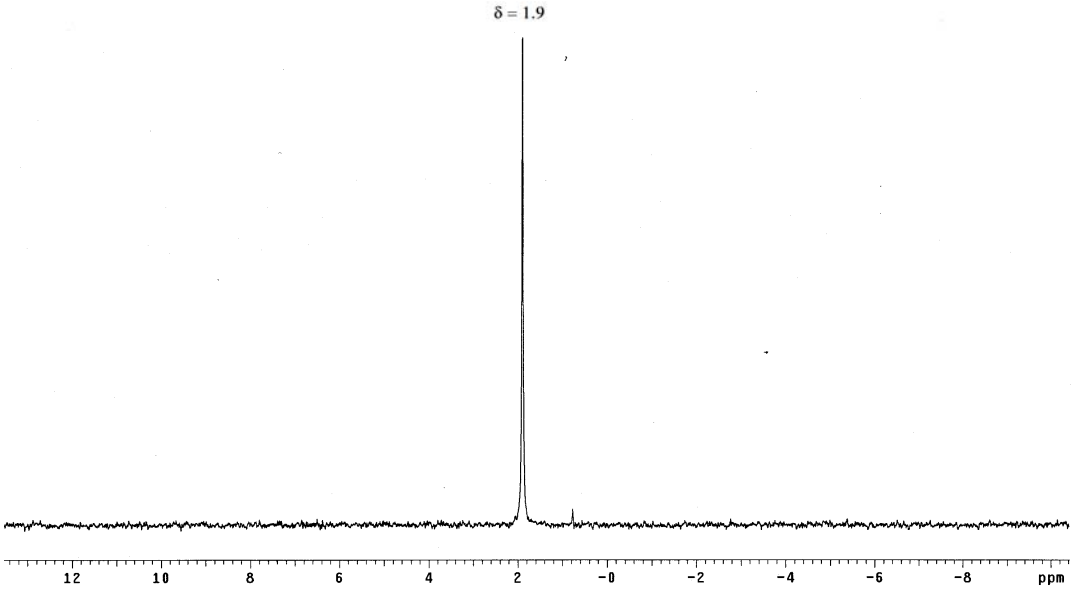

7-*O*-Me-FMN

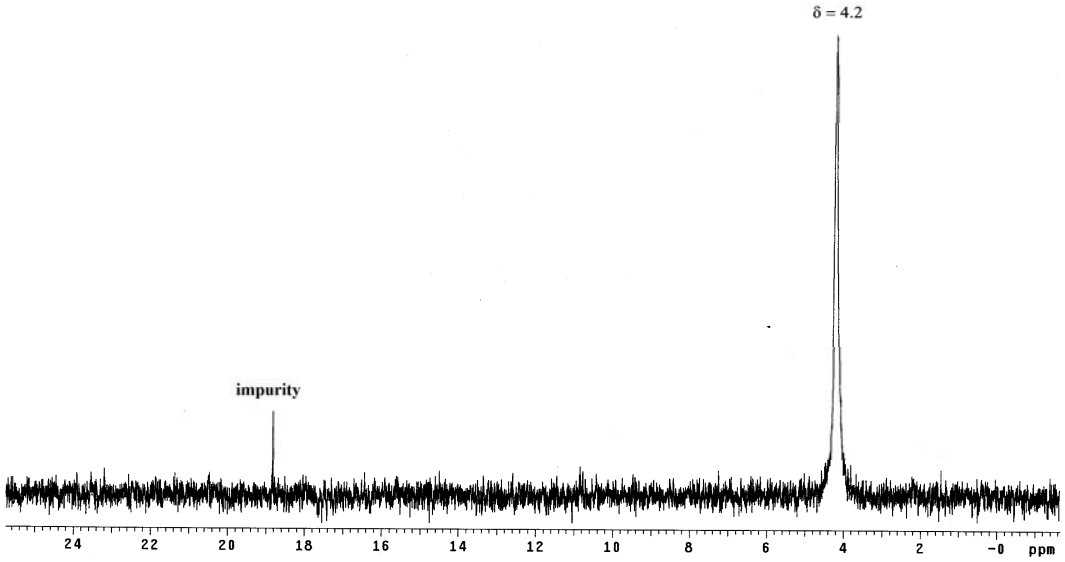

8-Cl-FMN

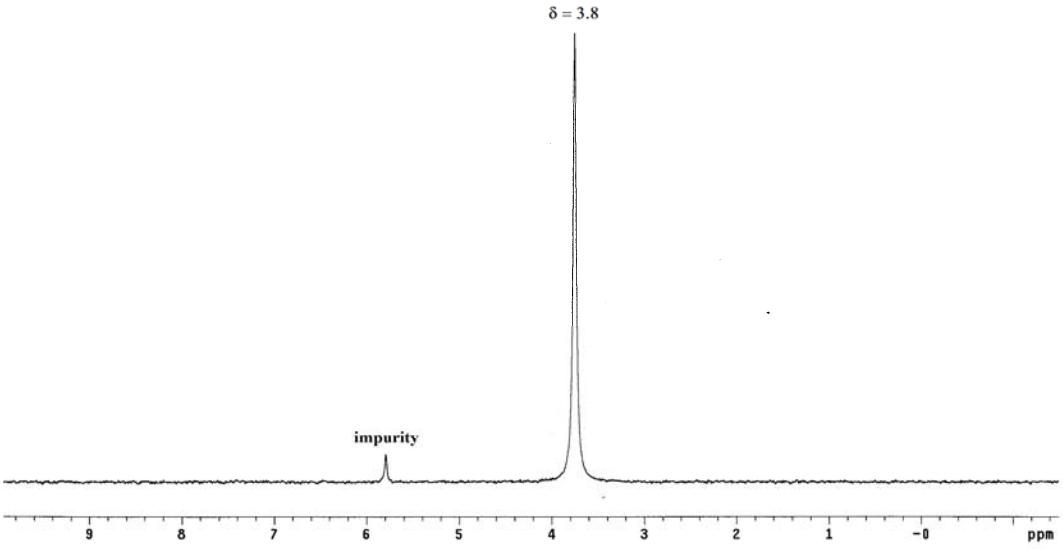

8-*O*-Me-FMN

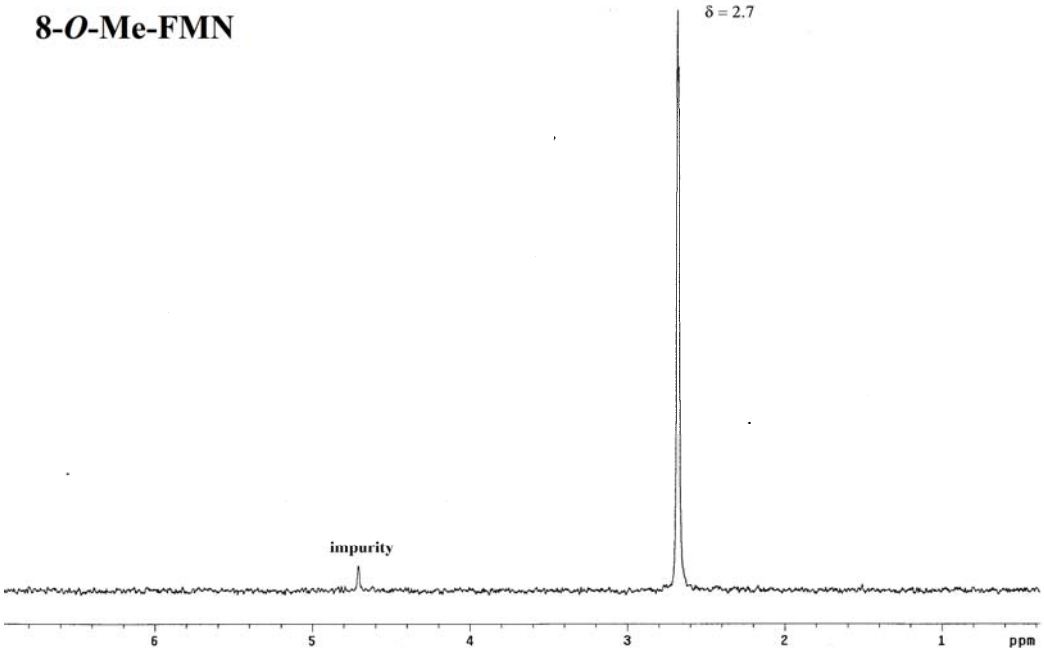

References

(1) Porter, J. W., and Spurgeon, S. L. (**1981**) Conversion of acetyl coenzyme A to isopentenyl pyrophosphate, in *Biosynthesis of isoprenoid compounds* (Porter, J. W., and Spurgeon, S. L., Eds.) pp 1-93, John Wiley and Sons, New York.

(2) Chaykin, S., Law, J., Phillips, A. H., Tchen, T. T., and Bloch, K. (**1958**) Phosphorylated intermediates in the synthesis of squalene. *Proc. Natl. Acad. Sci. USA 44*, 998-1004.

(3) Bloch, K., Chaykin, S., Phillips, A. H., and de Waard, A. (**1959**) Mevalonic acid pyrophosphate and isopentenylpyrophosphate. *J. Biol. Chem. 234*, 2595-2604.

(4) Lynen, F., Eggerer, H., Henning, U., and Kessel, I. (**1958**) *Angew. Chem. 70*, 738-742.

(5) Beytia, E. D., and Porter, J. W. (**1976**) Biochemistry of polyisoprenoid biosynthesis. *Annu. Rev. Biochem. 45*, 113-142.

(6) Rohmer, M. (**1999**) The discovery of a mevalonate-independent pathway for isoprenoid biosynthesis in bacteria, algae, and higher plants. *Nat. Prod. Rep. 16*, 565-574.

(7) Laupitz, R., Hecht, S., Amslinger, S., Zepeck, F., Kaiser, J., Richter, G., Schramek, N., Steinbacher, S., Huber, R., Arigoni, D., Bacher, A., Eisenreich, W., and Rohdich, F. (**2004**) Biochemical characterization of Bacillus subtilis type II isopentenyl diphosphate isomerase, and phylogenetic distribution of isoprenoid biosynthesis pathways. *Eur. J. Biochem. 271*, 2658-2669.

(8) Rodriguez-Concepcion, M. (**2004**) The MEP pathway: A new target for the development of herbicides, antibiotics and antimalarial drugs. *Curr. Pharm. Des. 10*, 2391-2400.

(9) Singh, N., Cheve, G., Avery, M. A., and McCurdy, C. R. (**2007**) Targeting the methyl erythritol phosphate (MEP) pathway for novel antimalarial, antibacterial and herbicidal drug discovery: Inhibition of 1-deoxy-D-xylulose-5-phosphate reductoisomerase (DXR) enzyme. *Curr. Pharm. Des. 13*, 1161-1177.

(10) Gibson, D. M., and Parker, R. A. (**1987**) Hydroxymethylglutaryl-coenzyme A redcutase, in *The Enzymes (3rd ed.)* (Boyer, P. D., and Krebs, E. G., Eds.) pp 179-215, Academic Press.

(11) Istvan, E. S., and Deisenhofer, J. (**2001**) Structural mechanism for statin inhibition of HMG-CoA reductase. *Science 292*, 1160-1164.

(12) Timson, D. J. (**2007**) GHMP kinases - structures, mechanisms, and potential for therapeutically relevant inhibition. *Curr. Enz. Inhib. 3*, 77-94.

(13) Krepkiy, D., and Miziorko, H. M. (**2005**) Investigation of the functional contributions of invariant serine residues in yeast mevalonate diphosphate decarboxylase. *Biochemistry 44*, 2671-2677.

(14) Byres, E., Alphey, M. S., Smith, T. K., and Hunter, W. N. (**2007**) Crystal structures of Trypanosoma brucei and Staphylococcus aureus mevalonate diphosphate decarboxylase inform on the determinanats of specificity and reactivity. *J. Mol. Biol. 371*, 540-553.

(15) Dhe-Paganon, S., Magrath, J., and Abeles, R. H. (**1994**) Mechanism of mevalonate pyrophosphate decarboxylase: evidence for a carbocationic transition state. *Biochemistry 33*, 13355-13362.

(16) Agranoff, B. W., Eggerer, H., Henning, U., and Lynen, F. (**1958**) Isopentenol pyrophosphate isomerase. *J. Am. Chem. Soc. 81*, 1254-1255.

(17) Rohdich, F., Hecht, S., Bacher, A., and Eisenreich, W. (**2003**) Deoxyxylulose phosphate pathway of isoprenoid biosynthesis. Discovery and function of *ispDEFGH* genes and their cognate enzymes. *Pure Appl. Chem. 75*, 393-405.

(18) Kuzuyama, T. (**2002**) Mevalonate and nonmevalonate pathways for the biosynthesis of isoprene units. *Biosci. Biotechnol. Biochem. 66*, 1619-1627.

(19) Rohmer, M. (**2003**) Mevalonate-independent methylerythiyol phosphate pathway for isoprenoid biosynthesis. Elucidation and distribution. *Pure Appl. Chem. 75*, 375-387.

(20) Kuzuyama, T., Takagi, M., Kaneda, K., Dairi, T., and Seto, H. (**2000**) Formation of 4-(cytidine 5'diphospho)-2-C-methyl-D-erythritol from 2-C-methyl-D-erythritol 4-phosphate by 2-C-methyl-D-erythritol 4-phosphate cytidylyltransferase, a new enzyme in the nonmevalonate pathway. *Tetra. Lett. 41*, 703-706.

(21) Rohdich, F., Wungsintaweekul, J., Fellermeier, M., Sagner, S., Herz, S., Kis, K., Eisenreich, W., Bacher, A., and Zenk, M. H. (**1999**) Cytidine 5'-triphosphate-dependent biosynthesis of isoprenoids: YgbP protein of Escherichi coli catalyzes

the formation of 4-diphosphocytidyl-2-C-methylerythritol. *Proc. Natl. Acad. Sci. USA 96*, 11758-11763.

(22) Kuzuyama, T., Takagi, M., Kaneda, K., Dairi, T., and Seto, H. (**2000**) Studies on the nonmevalonate pathway: conversion of 4-(cytidine 5'-diphospho)-2-C-methyl-D-erythritol to its 2-phospho derivative by 4-(cytidine 5'-diphospho)-2-C-methyl-D-erythritol kinase. *Tetra. Lett. 41*, 2925-2928.

(23) Luttgen, H., Rohdich, F., Herz, S., Wungsintaweekul, J., Hecht, S., Schuhr, C. A., Fellermeier, M., Sagner, S., Zenk, M. H., Bacher, A., and Eisenreich, W. (**2000**) Biosynthesis of terpenoids: YchB protein of Escherichia coli phosphorylates the 2-hydroxy group of 4-diphosphocytidyl-2C-methyl-D-erythritol. *Proc. Natl. Acad. Sci. USA 97*, 1062-1067.

(24) Takagi, M., Kuzuyama, T., Kaneda, K., Dairi, T., and Seto, H. (**2000**) Studies on the nonmevalonate pathway: formation of 2-C-methyl-D-erythritol 2,4-cyclodiphosphate from 2-phospho-4-(cytidine 5'-diphospho)-2-C-methyl-D-erythritol. *Tetra. Lett. 41*, 3395-3398.

(25) Herz, S., Wungsintaweekul, J., Schuhr, C. A., Hecht, S., Luttgen, H., Sagner, S., Fellermeier, M., Eisenreich, W., Zenk, M. H., Bacher, A., and Rohdich, F. (**2000**) Biosynthesis of terpenoids: YgbB protein converts 4-diphosphocytidyl-2C-methyl-D-erythritol 2-phosphate to 2C-methyl-D-erythritol 2,4-cyclodiphosphate. *Proc. Natl. Acad. Sci. USA 97*, 2486-2490.

(26) Nyland II, R. L., Xiao, Y., Liu, P. C. L. F., and Meyers. (**2009**) IspG Converts an Epoxide Substrate Analogue to (E)-4-Hydroxy-3-methylbut-2-enyl Diphosphate:

Implications for IspG Catalysis in Isoprenoid Biosynthesis. *J. Am. Chem. Soc. 131*, 17734-17735.

(27) Xiao, Y., Zahariou, G., Sanakis, Y., and Liu, P. (**2009**) IspG Enzyme Activity in the Deoxyxylulose Phosphate Pathway: Roles of the Iron-Sulfur Cluster. *Biochemistry 48*, 10483-10485.

(28) Wang, W., Wang, K., Liu, Y. L., No, J.-H., Li, J., Nilges, M. J., and Oldfield, E. (**2010**) Bioorganometallic mechanism of action, and inhibition, of IspH. *Proc. Natl. Acad. Sci. USA 107*, 4522-4527.

(29) Graewert, T., Span, I., Eisenreich, W., Rohdich, F., Eppinger, J., Bacher, A., and Groll, M. (**2009**) Probing the reaction mechanism of IspH protein by x-ray structure analysis. *Proc. Natl. Acad. Sci. USA, Early Edition 1-5*, 5.

(30) Graewert, T., Rohdich, F., Span, I., Bacher, A., Eisenreich, W., Eppinger, J., and Groll, M. (**2009**) Structure of Active IspH Enzyme from Escherichia coli Provides Mechanistic Insights into Substrate Reduction. *Angew. Chem. Int. Ed. 48*, 5756-5759.

(31) Ogura, K., and Koyama, T. (**1998**) Enzymatic aspects of isoprenoid chain elongation. *Chem. Rev. 98*, 1263-1276.

(32) Kellogg, B. A., and Poulter, C. D. (**1997**) Chain elongation in the isoprenoid biosynthetic pathway. *Curr. Opin. Chem. Biol. 1*, 570-578.

(33) Poulter, C. D., and Rilling, H. C. (**1978**) The prenyl transfer reaction. Enzymic and mechanistic studies of the 1'-4 coupling reaction in the terpene biosynthetic pathway. *Acc. Chem. Res. 11*, 307-313.

(34) Poulter, C. D., and Satterwhite, D. M. (**1977**) Mechanism of the Prenyl-Trasfer Reaction. Studies with (E)- and (2)-3-Trifluoromethyl-2-buten-1-yl Pyrophosphate. *Biochemistry 16*, 5470-5478.

(35) Poulter, C. D., Wiggins, P. L., and Le, A. T. (**1981**) Farnesylpyrophosphate synthetase. A stepwise mechanism for the 1'-4 condensation reaction. *J. Am. Chem. Soc. 103*, 3926-3927.

(36) Poulter, C. D., Argyle, J. C., and Mash, E. A. (**1978**) Farnesyl pyrophosphate synthetase. Mechanistic studies of the 1'-4 coupling reaction with 2-fluorogeranyl pyrophosphate. *J. Biol. Chem. 253*, 7227-7233.

(37) Davisson, V. J., Neal, R. T., and Poulter, C. D. (**1993**) Farnesyl-diphosphate synthase. Catalysis of an intramolecular prenyl transfer with bisubstrate analogs. *J. Am. Chem. Soc. 115*, 1235-1245.

(38) Davisson, V. J., and Poulter, C. D. (**1993**) Farnesyl-diphosphate synthase. Interplay between substrate topology, stereochemistry, and regiochemistry in electrophilic alkylations. *J. Am. Chem. Soc. 115*, 1245-1260.

(39) Agranoff, B. W., Eggerer, H., Henning, U., and Lynen, F. (**1960**) Biosynthesis of terpenes: VII. Isopentenyl pyrophosphate isomerase. *J. Biol. Chem. 235*, 326-332.

(40) Shah, D. H., Cleland, W. W., and Porter, J. W. (**1965**) The partial purification, properties, and mechanism of action of pig liver isopentenyl pyrophosphate isomerase. *J. Biol. Chem. 240*, 1946-1956.

(41) Popjak, G., and Conforth, J. W. (**1966**) Substrate stereochemistry in squalene biosynthesis. *Biochem. J. 101*, 553-568.

(42) Clifford, K., Conforth, J. W., Mallaby, R., and Phillips, G. T. (**1971**) Stereochemistry of isopentenyl pyrophosphate isomerase. *J. Chem. Soc. D*, 1599-1600.

(43) Street, I. P., Christensen, D. J., and Poulter, C. D. (**1990**) Hydrogen exchange during the enzyme-catalyzed isomerization of isopentenyl diphosphate and dimethylallyl diphosphate. *J. Am. Chem. Soc. 112*, 8577-8578.

(44) Reardon, J. E., and Abeles, R. H. (**1986**) Mechanism of action of isopentenyl pyrophosphate isomerase: Evidence for a carbonium ion intermediate. *Biochemistry 25*, 5609-5616.

(45) Muehlbacher, M., and Poulter, C. D. (**1988**) Isopentenyl-diphosphate isomerase: Inactivation of the enzyme with active-site-directed irreversible inhibitors and transition state analogues. *Biochemistry 27*, 7315-7328.

(46) Lee, S., and Poulter, C. D. (**2006**) *Escherichia coli* type I isopentenyl diphosphate isomerase: Structural and catalytic roles for divalent metals. *J. Am. Chem. Soc. 128*, 11545-11550.

(47) Carrigan, C. N., and Poulter, C. D. (**2003**) Zinc Is an Essential Cofactor for Type I Isopentenyl Diphosphate:Dimethylallyl Diphosphate Isomerase. *J. Am. Chem. Soc. 125*, 9008-9009.

(48) Street, I. P., and Poulter, C. D. (**1990**) Isopentenyldiphosphate:dimethylallyldiphosphate isomerase: construction of a high-level heterologous expression system for the gene from Saccharomyces

cerevisiae and identification of an active-site nucleophile. *Biochemistry 29*, 7531-7538.

(49) Street, I. P., Coffman, H. R., Baker, J. A., and Poulter, C. D. (**1994**) Identification of Cys139 and Glu207 As Catalytically Important Groups in the Active Site of Isopentenyl Diph0sphate:Dimethylallyl Diphosphate Isomerase. *Biochemistry 33*, 4212-4217.

(50) Wouters, J., Oudjama, Y., Berkley, S. J., Tricot, C., Stalon, V., Droogmans, L., and Poulter, C. D. (**2003**) Catalytic mechanism of Escherichia coli isopentenyl diphosphate isomerase involves Cys-67, Glu-116, and Tyr-104 as suggested by crystal structures of complexes with transition state analogues and irreversible inhibitors. *J. Biol. Chem. 278*, 11903-11908.

(51) Durbecq, V., Sainz, G., Oudjama, Y., Clantin, B., Bompard-Gilles, C., Tricot, C., Caillet, J., Stalon, V., Droogmans, L., and Villeret, V. (**2001**) Crystal structure of isopentenyl diphosphate:dimethylallyl diphosphate isomerase. *EMBO J. 20*, 1530-1537.

(52) Christianson, D. W. (**2006**) Structural biology and chemistry of the terpernoid cyclases. *Chem. Rev. 106*, 3412-3442.

(53) Toteva, M. M., and Richard, J. P. (**1997**) Mechanistic imperatives for the reaction catalyzed by isopentenyl pyrophosphate isomerase: Free energy profile for stepwise isomerization in water through a tertiary carbocation intermediate. *Bioorg. Chem. 25*, 239-245.

(54) Toteva, M. M., and Richard, J. P. (**1996**) Mechanism for Nucleophilic Substitution and Elimination Reactions at Tertiary Carbon in Largely Aqueous Solutions: Lifetime of a Simple Tertiary Carbocation. *J. Am. Chem. Soc. 118*, 11434-11445.

(55) Kaneda, K., Kuzuyama, T., Takagi, M., Hayakawa, Y., and Seto, H. (**2001**) An unusual isopentenyl diphosphate isomerase in the mevalonate pathway gene cluster from *Streptomyces* sp. strain CL190. *Proc. Natl. Acad. Sci. U.S.A. 98*, 932-937.

(56) Kittleman, W., Thibodeaux, C. J., Zhang, H., Liu, Y.-n., and Liu, H.-w. (**2007**) Characterization and mechanistic studies of type II isopentenyl diphosphate:dimethylallyl diphosphate isomerase from *Staphylococcus aureus*. *Biochemistry 46*, 8401-8413.

(57) Yamashita, S., Hemmi, H., Ikeda, Y., Nakayama, T., and Nishino, T. (**2004**) Type 2 isopentenyl diphosphate isomerase from a thermoacidophilic archaeon *Sulfolobus shibatae*. *Eur. J. Biochem. 271*, 1087-1093.

(58) Kao, C.-l., Kittleman, W., Zhang, H., Seto, H., and Liu, H.-w. (**2005**) Stereochemical analysis of isopentenyl diphosphate isomerase type II from *Staphylococcus aureus* using chemically synthesized (*S*)- and (*R*)-[2-^{2}H]isopentenyl diphosphates. *Org. Lett. 7*, 5677-5680.

(59) Barkley, S. J., Desai, S. B., and Poulter, C. D. (**2004**) Proton exchange in type II isopentenyl diphosphate isomerase. *Org. Lett. 6*, 5019-5021.

(60) Steinbacher, S., Kaiser, J., Gerhardt, S., Eisenreich, W., Huber, R., Bacher, A., and Rohdich, F. (**2003**) Crystal structure of the type II isopentenyl diphosphate:dimethylallyl diphosphate isomerase from *Bacillus subtilis*. *J. Mol. Biol. 329*, 973-982.

(61) de Ruyck, J., Rothman, S., Poulter, C. D., and Wouters, J. (**2005**) Structure of *Thermus thermophilus* type 2 isopentenyl diphospahte isomerase inferred from crystallography and molecular dynamics. *Biochem. Biophys. Res. Commun. 338*, 1515-1518.

(62) Mansoorabadi, S. O., Thibodeaux, C. J., and Liu, H.-w. (**2007**) The diverse roles of flavin coenzymes - Nature's most versatile thespians. *J. Org. Chem. 72*, submitted.

(63) Bornemann, S. (**2002**) Flavoenzymes that catalyse reactions with no net redox change. *Nat. Prod. Rep. 19*, 761-772.

(64) Buckel, W. (**1993**) Unusual dehydrations in anaerobic bacteria. *FEMS Microbiol. Rev. 88*, 211-231.

(65) Eikmanns, U., and Buckel, W. (**1991**) Crystalline green 5-hydroxyvaleryl-CoA dehydratase from *Clostridium aminovalericum*. *Eur. J. Biochem. 197*, 661-668.

(66) Ghisla, S., and Thorpe, C. (**2004**) Acyl-CoA dehydrogenases. *Eur. J. Biochem. 271*, 494-508.

(67) Sancar, A. (**2003**) Structure and Function of DNA Photolyase and Cryptochrome Blue-Light Photoreceptors. *Chem. Rev. 103*, 2203-2237.

(68) Soltero-Higgin, M., Carlson, E. E., Gruber, T. D., and Kiessling, L. L. (**2004**) A unique catalytic mechanism for UDP-galactopyranose mutase. *Nat. Struct. Mol. Biol. 11*, 539-543.

(69) Karunan Partha, S., van Straaten, K. E., and Sanders, D. A. R. (**2009**) Structural Basis of Substrate Binding to UDP-galactopyranose Mutase: Crystal Structures in the Reduced and Oxidized State Complexed with UDP-galactopyranose and UDP. *J. Mol. Biol. 394*, 864-877.

(70) Gruber, T. D., Westler, W. M., Kiessling, L. L., and Forest, K. T. (**2009**) X-ray Crystallography Reveals a Reduced Substrate Complex of UDP Galactopyranose Mutase Poised for Covalent Catalysis by Flavin. *Biochemistry 48*, 9171-9173.

(71) Macheroux, P., Bornemann, S., Ghisla, S., and Thorneley, R. N. F. (**1996**) Studies with flavin analogs provide evidence that a protonated reduced FMN is the substrate-induced transient intermediate in the reaction of *Escherichia coli* chorismate synthase. *J. Biol. Chem. 271*, 25850-25858.

(72) Macheroux, P., Petersen, J., Bornemann, S., Lowe, D. J., and Thorneley, R. N. F. (**1996**) Binding of the oxidized, reduced, and radical flavin species to chorismate synthase. An inverstigation by spectrophotometry, fluorimetry, and electron paramagnetic resonance and electron nuclear double resonance spectroscopy. *Biochemistry 35*, 1643-1652.

(73) Macheroux, P., Schonbrunn, E., Svergun, D. I., Volkov, V. V., Koch, M. H. J., Bornemann, S., and Thorneley, R. N. F. (**1998**) Evidence for a major structural

change in Escherichia coli chorismate synthase induced by flavin and substrate binding. *Biochem. J. 335*, 319-327.

(74) Ramjee, M. N., Coggins, J. R., Hawkes, T. R., Lowe, D. J., and Thorneley, R. N. F. (**1991**) Spectrophotometric detection of a modified flavin mononucleotide (FMN) intermediate formed during the catalytic cycle of chorismate synthase. *J. Am. Chem. Soc. 113*, 8566-8567.

(75) Maclean, J., and Ali, S. (**2003**) The structure of chorismate synthase reveals a novel flavin binding site fundamental to a unique chemical reaction. *Structure 11*, 1499-1511.

(76) Kitzing, K., Auweter, S., Amrhein, N., and Macheroux, P. (**2004**) Mechanism of chorismate synthase. *J. Biol. Chem. 279*, 9451-9461.

(77) Bornemann, S., Lowe, D. J., and Thorneley, R. N. F. (**1996**) The transient kinetics of Escherichia coli chorismate synthase: Substrate consumption, product formation, phosphate dissociation, and characterization of a flavin intermediate. *Biochemistry 35*, 9907-9916.

(78) Balasubramanian, S., Coggins, J. R., and Abell, C. (**1995**) Observation of a secondary tritium isotope effect in the chorismate synthase reaction. *Biochemistry 34*, 341-348.

(79) Bornemann, S., Balasubramanian, S., Coggins, J. R., Abell, C., Lowe, D. J., and Thorneley, R. N. F. (**1995**) *Escherichia coli* chorismate synthase: a deuterium kinetic-isotope effect under single-turnover and steady-state conditions shows that

a flavon intermediate forms before the C-(6*proR*)-H bond is cleaved. *Biochem. J. 305*, 707-710.

(80) Osborne, A., Thorneley, R. N. F., Abell, C., and Bornemann, S. (**2000**) Studies with substrate and cofactor analogues provide evidence for a radical mechanism in the chorismate synthase reaction. *J. Biol. Chem. 275*, 35825-35830.

(81) D., C., Barak, Z., and Schloss, J. V. (**1998**) Biosynthesis of 2-aceto-2-hydroxy acids: acetolactate synthases and acetohydroxyacid synthases. *Biochim. Biophys. Acta 1385*, 401-419.

(82) Hemmi, H., Ikeda, Y., Yamashita, S., Nakayama, T., and Nishino, T. (**2004**) Catalytic mechanism of type 2 isopentenyl diphosphate:dimethylallyl diphosphate isomerase: Verification of a redox role of the flavin cofactor in a reaction with no net redox change. *Biochem. Biophys. Res. Commun. 322*, 905-910.

(83) Spencer, R., Fisher, J., and Walsh, C. (**1977**) One- and two-electron redox chemistry of 1-carba-1-deaza-riboflavin. *Biochemistry 16*, 3586-3594.

(84) Hersh, L. B., and Walsh, C. (**1980**) Preparation, characterization, and coenzymic properties of 5-carba-5-deaza and 1-carba-1-deaza analogues of riboflavin, FMN, and FAD. *Methods Enzymol. 66*, 277-287.

(85) Spencer, R., Fisher, J., and Walsh, C. (**1976**) Preparation, characterization, and chemical properties of the flavin coenzyme analogues 5-deazariboflavin, 5-deazariboflavin 5'-phosphate, and 5-deazariboflavin 5'-diphosphate, 5'-5'-adenosine ester. *Biochemistry 15*, 1043-1053.

(86) Johnston, J. B., Walker, J. R., Rothman, S. C., and Poulter, C. D. (**2007**) Type 2 isopentenyl diphosphate isomerase. Mechanistic studies with cyclopropyl and epoxy analogues. *J. Am. Chem. Soc. 129*, 7740-7741.

(87) Macheroux, P., Ghisla, S., Sanner, C., Rueterjans, H., and Muller, F. (**2005**) Reduced flavin: NMR investigation of N(5)-H exchange mechanism, estimation of ionisation constants and assessment of properties as biological catalyst. *BMC Biochem 6*, 1-11.

(88) de Ruyck, J., Pouyez, J., Rothman, S. C., Poulter, D., and Wouters, J. (**2008**) Crystal structure of type 2 isopentenyl diphosphate isomerase from *Thermus thermophilus* in complex with inorganic pyrophosphate. *Biochemistry 47*, 9051-9053.

(89) Unno, H., Yamashita, S., Ikeda, Y., Sekiguchi, S., Yoshida, N., Yoshimura, T., Kusunoki, M., Nakayama, T., Nishino, T., and Hemmi, H. (**2009**) New Role of Flavin as a General Acid-Base Catalyst with No Redox Function in Type 2 Isopentenyl-diphosphate Isomerase. *J. Biol. Chem. 284*, 9160-9167.

(90) Thibodeaux, C. J., Mansoorabadi, S. O., Kittleman, W., Chang, W.-c., and Liu, H.-w. (**2008**) Evidence for the Involvement of Acid/Base Chemistry in the Reaction Catalyzed by the Type II Isopentenyl Diphosphate/Dimethylallyl Diphosphate Isomerase from *Staphylococcus aureus*. *Biochemistry 47*, 2547-2558.

(91) Frisch, M. J., Trucks, G. W., Schlegel, H. B., Scuseria, G. E., Robb, M. A., Cheeseman, J. R., Zakrzewski, V. G., Montgomery, J. A., Jr., Stratmann, R. E.,

Burant, J. C., Dapprich, S., Millam, J. M., Daniels, A. D., Kudin, K. N., Strain, M. C., Farkas, O., Tomasi, J., Barone, V., Cossi, M., Cammi, R., Mennucci, B., Pomelli, C., Adamo, C., Clifford, S., Ochterski, J., Petersson, G. A., Ayala, P. Y., Cui, Q., Morokuma, K., Malick, D. K., Rabuck, A. D., Raghavachari, K., Foresman, J. B., Cioslowski, J., Ortiz, J. V., Baboul, A. G., Stefanov, B. B., Liu, G., Liashenko, A., Piskorz, P., Komaromi, I., Gomperts, R., Martin, R. L., Fox, D. J., Keith, T. A.-L., M. A., Peng, C. Y., Nanayakkara, A., Gonzalez, C., Challacombe, M., Gill, P. M. W., Johnson, B., Chen, W., Wong, M. W., Andres, J. L., Head-Gordon, M., Replogle, E. S., and Pople, J. A. (**1998**), Gaussian, Inc., Pittsburg, PA.

(92) Rothman, S., Helm, T. R., and Poulter, C. D. (**2007**) Kinetic and spectroscopic characterization of type II isopentenyl diphosphate isomerase from *Thermus thermophilus*: Evidence for formation of substrate-induced flavin species. *Biochemistry 46*, 5437-5445.

(93) Kay, C. M. W., and Weber, S. (**2002**) EPR of radical intermediates in flavoenzymes, in *Electron Paramagnetic Resonance* (Gilbert, B. C., Davies, M. J., and Murphy, D. M., Eds.) pp 222-253, Royal Society of Chemistry, London.

(94) Ghisla, S., Massey, V., Lhoste, J.-M., and Mayhew, S. G. (**1974**) Fluorescence and optical characterisitcs of reduced flavines and flavoproteins. *Biochemistry 13*, 589-597.

(95) Franken, H.-D., Ruterjans, H., and Muller, F. (**1984**) Nuclear magentic resonance investigation of ^{15}N-labeled flavins, free and bound to *Megasphaera elsdenii* apoflavodoxin. *Eur. J. Biochem. 138*, 481-489.

(96) Lowe, H. J., and Clark, W. M. (**1956**) Studies on oxidation-reduction XXIV. Oxidation-reduction potentials of flavin adenine dinucleaotide. *J. Biol. Chem. 221*, 983-992.

(97) Corrado, M. E., Aliverti, A., Zanetti, G., and Meyhew, S. G. (**1996**) Analysis of the oxidation-reduction potentials of recombinant ferredoxin-NADP+ reductase from spinach chloroplasts. *Eur. J. Biochem. 239*, 662-667.

(98) Walsh, C., Fisher, J., Jacobson, F., Spencer, R., Ashton, W., and Brown, R. (**1978**) in *Flavins & Flavoproteins, Proc. Int. Symp., 6th (1980)* (Yagi, K., and Yamano, T., Eds.) pp 13-21, Japan Sci. Soc. Press.

(99) Yalloway, G. N., Mayhew, S. G., Malthouse, J. P. G., Gallagher, M. E., and Curley, G. P. (**1999**) pH-dependent spectroscopic changes associated with the hydroquinone of FMN in flavodoxins. *Biochemistry 38*, 3753-3762.

(100) Moonen, C. T. W., Vervoort, J., and Muller, F. (**1984**) Reinvestigation of the structure of oxidized and reduced flavin: Carbon-13 and Nitrogen-15 nuclear magnetic resonance study. *Biochemistry 23*, 4859-4867.

(101) Vervoort, J., Muller, F., Mayhew, S. G., van den Berg, W. A. M., Moonen, C. T. W., and Bacher, A. (**1986**) A comparative carbon-13, nitrogen-15, and phosphorus-31 nuclear magnetic resonance study on the flavodoxins from

Clostridium MP, *Megasphaera elsdenii*, and *Azobacter vinelandii*. *Biochemistry 25*, 6789-6799.

(102) Ludwig, M. L., Schopfer, L. M., Metzger, A. L., Pattridge, K. A., and Massey, V. (**1990**) Structure and oxidation-reduction behavior of 1-deaza-FMN flavodoxins: Modulation of redox potentials in flavodoxins. *Biochemistry 29*, 10364-10375.

(103) Moonen, C. T. W., van den Berg, W. A. M., Boerjan, M., and Muller, F. (**1984**) Carbon-13 and Nitrogen-15 Nuclear Magnetic Resonance Study on the Interaction between Riboflavin and Riboflavin-Binding Apoprotein. *Biochemistry 23*, 4873-4878.

(104) Binsch, G., Lambert, J. B., Roberts, B. W., and Roberts, J. D. (**1964**) Nitrogen-15 magnetic resonance spectroscopy. II. Coupling constants. *J. Am. Chem. Soc. 86*, 5564-5570.

(105) Bourn, A. J. R., and Randall, E. W. (**1964**) Proton-proton double resonance studies of formamide-^{15}N and N-methylformamide-^{15}N. *Mol. Phys. 8*, 567-579.

(106) Beinert, W.-D., Ruterjans, H., and Muller, F. (**1985**) Nuclear magnetic resonance studies of the old yellow enzyme. 1. ^{15}N NMR of the enzyme recombined with ^{15}N-labeled flavin mononucleotides. *Eur. J. Biochem. 152*, 573-579.

(107) Vervoort, J., and Muller, F. (**1986**) Bacterial Luciferase: A Carbon- 13, Nitrogen-15, and Phosphorus-31 Nuclear Magnetic Resonance Investigation. *Biochemistry 25*, 8067-8075.

(108) Chang, F.-C., and Swenson, R. P. (**1999**) The Midpoint Potentials for the Oxidized-Semiquinone Couple for Gly57 Mutants of the Clostridium beijerinckii

Flavodoxin Correlate with Changes in the Hydrogen-Bonding Interaction with the Proton on N(5) of the Reduced Flavin Mononucleotide Cofactor As Measured by NMR Chemical Shift Temperature Dependencies. *Biochemistry 38*, 7168-7176.

(109) Fleischmann, G., Lederer, F., Muller, F., Bacher, A., and Ruterjans, H. (**2000**) Flavin-protein interactions in flavocytochrome b2 as studied by NMR after reconstitution of the enzyme with 13C- and 15N-labelled flavin. *Eur. J. Biochem. 267*, 5156-5167.

(110) Kasim, M., Chen, H.-C., and Swenson, R. P. (**2009**) Functional Characterization of the re-Face Loop Spanning Residues 536 541 and Its Interactions with the Cofactor in the Flavin Mononucleotide-Binding Domain of Flavocytochrome P450 from *Bacillus megaterium*. *Biochemistry 48*, 5131-5142.

(111) Rothman, S. C., Johnston, J. B., Lee, S., Walker, J. R., and Poulter, C. D. (**2008**) Type II Isopentenyl Diphosphate Isomerase: Irreversible Inactivation by Covalent Modification of Flavin. *J. Am. Chem. Soc. 130*, 4906-4913.

(112) Sharma, N. K., Pan, J.-J., and Poulter, C. D. (**2010**) Type II Isopentenyl Diphosphate Isomerase: Probing the Mechanism with Alkyne/Allene Diphosphate Substrate Analogues. *Biochemistry 49*, in press.

(113) Griller, D., and Ingold, K. U. (**1980**) Free radical clocks. *Acc. Chem. Res. 13*, 317-323.

(114) Suga, T., Ohta, S., and Ohmoto, T. (**1987**) *J. Chem. Soc. Perkins Trans. 1 12*, 2845-2848.

(115) Schowen, K. B., and Schowen, R. L. (**1982**) Solvent isotope effects on enzyme systems. *Methods Enzymol. 87*, 551-606.

(116) Cerjan, C., and Barnett, R. E. (**1972**) Viscosity dependence of a putative diffusion-limited reaction. *J. Phys. Chem. 76*, 1192-1195.

(117) Nakatani, H., and Dunford, H. B. (**1979**) Meaning of diffusion-controlled association rate constants in enzymology. *J. Phys. Chem. 83*, 2662-2665.

(118) Brouwer, A. C., and Kirsch, J. F. (**1982**) Investigation of Diffusion-Limited Rates Viscosity Variation. *Biochemistry 21*, 1302-1307.

(119) St. Maurice, M., and Bearne, S. L. (**2002**) Kinetics and Thermodynamics of Mandelate Racemase Catalysis. *Biochemistry 41*, 4048-4058.

(120) Johnson, K. A., Simpson, Z. B., and Blom, T. (**2009**) Global Kinetic Explorer: A new computer program for dynamic simulation and fitting of kinetic data. *Anal. Biochem. 387*, 20-29.

(121) Johnson, K. A., Simpson, Z. B., and Blom, T. (**2009**) FitSpace Explorer: An algorithm to evaluate multi-dimensional parameter space in fitting kinetic data. *Anal. Biochem. 387*, 30-41.

(122) Thibodeaux, C. J., Chang, W.-c., and Liu, H. w. (**2010**) Linear Free Energy Relationships Demonstrate a Catalytic Role for the Flavin Mononucleotide Coenzyme of the Type II Isopentenyl Diphosphate:Dimethylallyl Diphosphate Isomerase. *J. Am. Chem. Soc. 132*, 9994-9996.

(123) Frey, C. M., and Stuehr, J. E. (**1972**) Interactions of Divalent Metal Ions with Inorganic and Nucleoside Phosphates. I. Thermodynamics. *J. Am. Chem. Soc. 94*, 8898-8904.

(124) Schowen, R. L. (**2007**) The use of solvent isotope effects in the pursuit of enzyme mechanisms. *J. Label. Comp. Radiopharm. 50*, 1052-1062.

(125) Mandel, J. (**1964**) *The statistical analysis of experimental data*, Interscience Publishers, New York.

(126) Cassidy, C. S., Lin, J., and Frey, P. A. (**1997**) A New Concept for the Mechanism of Action of Chymotrypsin: The Role of the Low-Barrier Hydrogen Bond. *Biochemistry 36*, 4576-4584.

(127) Markley, J. L., and Westler, W. M. (**1996**) Protonation-State Dependence of Hydrogen Bond Strengths and Exchange Rates in a Serine Protease Catalytic Triad: Bovine Chymotrypsinogen A. *Biochemistry 35*, 11092-11097.

(128) Toulokhonova, L., Metzler, W. J., Witmer, M. R., Copeland, R. A., and Marcinkeviciene, J. (**2003**) Kinetic Studies on β-Site Amyloid Precursor Protein-cleaving Enzyme (BACE). *J. Biol. Chem. 278*, 4582-4589.

(129) Branson, J. P., Nezic, M., Jitrapakdee, S., Wallace, J. C., and Attwood, P. V. (**2004**) Kinetic Characterization of Yeast Pyruvate Carboxylase Isozyme Pyc1 and the Pyc1 Mutant, C249A. *Biochemistry 43*, 1075-1081.

(130) Frey, P. A., Whitt, S. A., and Tobin, J. B. (**1994**) A low-barrier hydrogen bond in the catalytic triad of serine proteases. *Science 264*, 1927-1930.

(131) Kreevoy, M. M., and Liang, T. M. (**1980**) Structures and Isotopic Fractionation Factors of Complexes, $A_lHA_2^-$. *J. Am. Chem. Soc. 102*, 3315-3322.

(132) Cleland, W. W. (**1992**) Low-Barrier Hydrogen Bonds and Low Fractionation Factor Bases in Enzymatic Reactions. *Biochemistry 31*, 317-319.

(133) Cleland, W. W., and Kreevoy, M. M. (**1994**) Low-Barrier Hydrogen Bonds and Enzymic Catalysis. *Science 264*, 1887-1890.

(134) Gerlt, J. A., and Gassman, P. G. (**1993**) Understanding the Rates of Certain Enzyme-Catalyzed Reactions: Proton Abstraction from Carbon Acids, Acyl-Transfer Reactions, and Displacement Reactions of Phosphodiesterst. *Biochemistry 32*, 11943-11952.

(135) Grinnell, J., and Fornwalt, H. J. (**1936**) The viscosity of deuterium oxide and its mixtures with water at 25°. *J. Chem. Phys. 4*, 30-33.

(136) Hardy, L. W., and Kirsch, J. F. (**1984**) Diffusion-Limited Component of Reactions Catalyzed by Bacillus cereus β-Lactamase. *Biochemistry 23*, 1275-1282.

(137) Kurz, L. C., Weitkamp, E., and Frieden, C. (**1987**) Adenosine Deaminase: Viscosity Studies and the Mechanism of Binding of Substrate and of Ground- and Transition-State Analogue Inhibitors? *Biochemistry 26*, 3027-3032.

(138) Adams, J. A., and Taylor, S. S. (**1992**) Energetic Limits of Phosphotransfer in the Catalytic Subunit of CAMP Dependent Protein Kinase As Measured by Viscosity Experiments? *Biochemistry 31*, 8516-8522.

(139) Wood, B. M., Chan, K. K., Amyes, T. L., Richard, J. P., and Gerlt, J. A. (**2009**) Mechanism of the Orotidine 5'-Monophosphate Decarboxylase-Catalyzed Reaction: Effect of Solvent Viscosity on Kinetic Constants. *Biochemistry 48*, 5510.

(140) Raber, M. L., Freeman, M. F., and Townsend, C. A. (**2009**) Dissection of the Stepwise Mechanism to β-Lactam Formation and Elucidation of a Rate-determining Conformational Change in β-Lactam Synthetase. *J. Biol. Chem. 284*, 207-217.

(141) Francis, K., and Gadda, G. (**2006**) Probing the Chemical Steps of Nitroalkane Oxidation Catalyzed by 2 Nitropropane Dioxygenase with Solvent Viscosity, pH, and Substrate Kinetic Isotope Effects. *Biochemistry 45*, 13889-13898.

(142) Draper, N. R., and Smith, H. (**1998**) *Applied Refression Analysis*, 3rd ed., John Wiley & sons, New York.

(143) Hasford, J. J., and Rizzo, C. J. (**1998**) Linear free energy substituent effect in flavin redox chemistry. *J. Am. Chem. Soc. 120*, 2251-2255.

(144) Anslyn, E. V., and Dougherty, D. A. (**2006**) *Modern Pysical Organic Chemistry*, University Science Books, Sausalito, CA.

(145) Edmondson, D. E., and Ghisla, S. (**1999**) Electronic effects of 7 and 8 ring substituents as predictors of flavin oxidation-reduction potentials, in *Flavins and Flavoproteins 1999, Proceedings of the International Symposium, 13th, Konstanz, Germany* (Ghisla, S., Ed.) pp 71-76, Rudolf Weber, Agency for Scientific Publications, Berlin.

(146) Hansch, C., Leo, A., and Taft, R. W. (**1991**) A Survey of Hammett Substituent Constants and Resonance and Field Parameters. *Chem. Rev. 91*, 165-195.

(147) Perrin, D. D. (**1965**), Butterworths, London.

(148) Ghisla, S., Hartmann, U., Hemmerich, P., and Muller, F. (**1973**) Die reduktive Alkylierung des Flavinkerns 2); Struktur und Reaktivitat von Dihydroflavinen. *Liebigs Ann. Chem. 8*, 1388-1415.

(149) Hoshino, T., Tamegai, H., Kakinuma, K., and Eguchi, T. (**2006**) Inhibition of type 2 isopentenyl diphosphate isomerase from Methanocaldococcus jannaschii by a mechanism-based inhibitor of type 1 isopentenyl diphosphate isomerase. *Bioorg. Med. Chem. 14*, 6555-6559.

(150) Yu, Q., Schaub, P., Ghisla, S., Al-Babili, S., Krieger-Liszkay, A., and Beyer, P. (**2010**) The Lycopene Cyclase CrtY from *Pantoea ananatis* (Formerly *Erwinia uredovora*) Catalyzes an FADred-dependent Non-redox Reaction. *J. Biol. Chem. 285*, 12109-12120.

(151) Bruice, P. Y. (**1998**) *Organic Chemistry*, 2nd ed., Prentice-Hall, Upper Saddle River, NJ.

(152) Gebler, J. C., Woodside, A. B., and Poulter, C. D. (**1992**) Dimethylallyltryptophan synthase. An enzyme-catalyzed electrophilic aromatic substitution. *J. Am. Chem. Soc. 114*, 7354-7360.

(153) Kommoju, P.-R., Bruckner, R. C., Ferreira, P., and Jorns, M. S. (**2009**) Probing the Role of Active Site Residues in NikD, an Unusual Amino Acid Oxidase That

Catalyzes an Aromatization Reaction Important in Nikkomycin Biosynthesis. *Biochemistry 48*, 6951-6962.

(154) Rauch, G., Ehammer, H., Bornemann, S., and Macheroux, P. (**2007**) Mutagenic analysis of an invariant aspartate residue in chorismate synthase supports its role as an active site base. *Biochemistry 46*, 3768-3774.

(155) Edmondson, D. E., Mattevi, A., Binda, C., Li, M., and Hubalek, F. (**2004**) Structure and mechanism of monoamine oxidase. *Curr. Med. Chem. 11*, 1983-1993.

(156) Molla, G., Pilone, M. S., Pollegioni, L., and Ghisla, S. (**2002**) Studies on the elimination reaction of Rhodotorula gracilis D-amino acid oxidase with β-chloro-D-alanine., in *Flavins and Flavoproteins 2002: Proc. 14th Int. Symp., Cambridge, UK* (Chapman, S., Perham, R., and Scrutton, N., Eds.) pp 299-304, Agency for Scientific Publ., Berlin.

(157) Burroughs, L. F. (**1957**) 1-Aminocyclopropane-1-carboxylic acid: a new amino-acid in perry pears and cider apples. *Nature 179*, 360-361.

(158) Adams, D. O., and Yang, S. F. (**1979**) Ethylene biosynthesis: Identification of 1-aminocyclopropane-1-carboxylic acid as an intermediate in the conversion of methionine to ethylene. *Proc. Natl. Acad. Sci. USA 76*, 170-174.

(159) Kende, H. (**1993**) Ethylene biosynthesis. *Annu. Rev. Plant Physiol. Plant Mol. Biol. 44*, 283-307.

(160) Honma, M., and Shimomura, T. (**1978**) Metabolism of 1-aminocyclopropane-1-carboxylic acid. *Agric. Biol. Chem. 42*, 1825-1831.

(161) Klee, H. J., Hayford, M. B., Kretzmer, K. A., Barry, G. F., and Kishore, G. M. (**1991**) Control of Ethylene Synthesis by Expression of a Bacterial Enzyme in Transgenic Tomato Plants. *Plant Cell 3*, 1187-1193.

(162) Eliot, A. C., and Kirsch, J. F. (**2004**) Pyridoxal phosphate enzymes: Mechanistic, structural, and evolutionary considerations. *Annu. Rev. Biochem. 73*, 383-415.

(163) Dunathan, H. C. (**1966**) Conformation and reaction specificity in pyridoxal phosphate enzymes. *Proc. Natl. Acad. Sci. USA 55*, 712-716.

(164) Toney, M. D. (**2005**) Reaction specificity in pyridoxal phosphate enzymes. *Arch. Biochem. Biophys. 433*, 279-287.

(165) Matthews, R. B., and Drummond, J. T. (**1990**) Providing one-carbon units for biological methylations: mechanistic studies on serine hydroxymethyltransferase, methylenetetrahydrofolate reductase, and methyltetrahydrofolate-homocysteine methyltransferase. *Chem. Rev. 90*, 1275-1290.

(166) Schirch, V., and Szebenyi, D. M. E. (**2005**) Serine hydroxymethyltransferase revisited. *Curr. Opin. Chem. Biol. 9*, 482-487.

(167) Walsh, C. T., Pascal Jr., R. A., Johnston, M., Raines, R., Dikshit, D., Krantz, A., and Honma, M. (**1981**) Mechanistic studies on the pyridoxal phosphate enzyme 1-aminocyclopropane-1-carboxylate deaminse from *Pseudomonas* sp. *Biochemistry 20*, 7509-7519.

(168) Stewart, J. M., and Westberg, H. H. (**1965**) Nucleophilic ring-opening additions to 1,1-disubstituted cyclopropanes. *J. Org. Chem. 30*, 1951-1955.

(169) Yates, P., Helferty, P. H., and Mahler, P. (**1983**) Nucleophilic and acid-catalyzed cleavage of the cyclopropane rings of β,γ - unsaturated α - spirocyclopropyl ketones. *Can. J. Chem. 61*, 71-85.

(170) Danishefsky, S. (**1979**) Electrophilic cyclopropanes in organic synthesis. *Acc. Chem. Res. 12*, 66-72.

(171) Cleland, W. W. (**1982**) The use of pH studies to determine chemical mechanisms of enzyme-catalyzed reactions. *Methods Enzymol. 87*, 390-405.

(172) Walsh, C., Pascal, J., R.A., Johnston, M., Raines, R., Dikshit, D., Krantz, A., and Honma, M. (**1981**) Mechanistic Studies on the Pyridoxal Phosphate Enzyme 1 - Aminocyclopropane- 1 -carboxylate Deaminase from Pseudomonas sp. *Biochemistry 20*, 7509-7519.

(173) Battiste, M. A., and Coxon, J. M. (**1987**) Acidity and basicity of cyclopropanes, in *The chemistry of the cyclopropyl group Part 1* (Rappoport, Z., Ed.) pp 255-305, John Wiley & Sons, Chichester.

(174) Ramalingam, K., Lee, K.-M., Woodard, R. W., Bleecker, A. B., and Kende, H. (**1985**) Stereochemical course of the reaction catalyzed by the pyridoxal phosphate-dependent enzyme 1-aminocyclopropane-1-carboxylate synthase. *Proc. Natl. Acad. Sci. USA 82*, 7820-7824.

(175) Hill, R. K., Prakash, S. R., Wiesendanger, R., Angst, W., Martinoni, B., Arigoni, D., Liu, H.-w., and Walsh, C. T. (**1984**) Stereochemistry of the enzymatic ring opening of 1-aminocyclopropanecarboxylic acid. *J. Am. Chem. Soc. 106*, 795-796.

(176) Liu, H.-w., Auchus, R., and Walsh, C. T. (**1984**) Stereochemical studies on the reactions catalyzed by the PLP-dependent enzyme 1-aminocyclopropane-1-carboxylate deaminase. *J. Am. Chem. Soc. 106*, 5335-5348.

(177) Yao, M., Ose, T., Sugimoto, H., Horiuchi, A., Nakagawa, A., Wakatsuki, S., Yokoi, S., Murakami, T., Honma, M., and Tanaka, I. (**2000**) Crystal Structure of 1-Aminocyclopropane-1-carboxylate Deaminase from *Hansenula saturnus*. *J. Biol. Chem. 275*, 34557-34565.

(178) Ose, T., Fujino, A., Yao, M., Watanabe, N., Honma, M., and Tanaka, I. (**2003**) Reaction Intermediate Structures of 1-Aminocyclopropane-1-carboxylate Deaminase: Insight into PLP-dependent cyclopropane ring-opening reaction. *J. Biol. Chem. 278*, 41069-41076.

(179) Karthikeyan, S., Zhao, Z., Kao, C.-L., Zhou, Q., Tao, Z., Zhang, H., and Liu, H.-w. (**2004**) Structural Analysis of 1-Aminocyclopropane-1-Carboxylate Deaminase: Observation of an Aminyl Intermediate and Identification of Tyr 294 as the Active-Site Nucleophile. *Angew. Chem. Int. Ed. 43*, 3425-3429.

(180) Karthikeyan, S., Zhou, Q., Zhao, Z., Kao, C.-L., Tao, Z., Robinson, H., Liu, H.-w., and Zhang, H. (**2004**) Structural Analysis of Pseudomonas 1 Aminocyclopropane-1-carboxylate Deaminase Complexes: Insight into the Mechanism of a Unique Pyridoxal-5'-phosphate Dependent Cyclopropane Ring-Opening Reaction. *Biochemistry 43*, 13328-13339.

(181) Murakami, T., Kiuchi, M., Ito, H., Matsui, H., and Honma, M. (**1997**) Substitutions of alanine for cysteine at a reactive thiol site for lysine at a pyridoxal

phosphate binding site of 1-aminocyclopropane-1-carboxylate deaminase. *Biosci. Biotech. Biochem. 61*, 506-509.

(182) Zhao, Z., Chen, H., Li, K., Du, W., He, S., and Liu, H.-w. (**2003**) Reaction of 1-amino-2-methylenecyclopropane-1-carboxylate with 1-aminocyclopropane-1-carboxylate deaminase: Analysis and mechanistic implications. *Biochemistry 42*, 2089-2103.

(183) Thibblin, A., and Jencks, W. P. (**1979**) Unstable carbanions. General acid catalysis of the cleavage of 1-phenylcyclopropanol and 1-phenyl-2-arylcyclopropanol anions. *J. Am. Chem. Soc. 101*, 4963-4973.

(184) Wiberg, K. B., and Kass, S. R. (**1985**) Electrophilic cleavage of cyclopropanes. Acetolysis of alkylcyclopropanes. *J. Am. Chem. Soc. 107*, 988-995.

(185) Baird, R. L., and Aboderin, A. A. (**1964**) Concerning the Role of Protonated Cyclopropane Intermediates in Solvolytic Reactions. The Solvolysis of Cyclopropane in Deuteriosulfuric Acid. *J. Am. Chem. Soc. 86*, 252-255.

(186) McKinney, M. A., Smith, S. H., Hempelman, S., Gearen, M. M., and Pearson, L. (**1971**) Proteolytic cleavage of cyclopropanes: The structure of the transition state in the protonation of arylcyclopropanes. *Tetra. Lett.*, 3657-3660.

(187) McKinney, M. A., and So, E. C. (**1972**) Protolytic Cleavage of Cyclopropanes. The Two Mechanisms for the Acid-Catalyzed Cleavage of 1-Phenylcyclopropylmethyl Ether. *J. Org. Chem. 37*, 2818-2822.

(188) Bradford, M. M. (**1976**) A rapid and sensitive method for the quantitation of microgram quantities of protein utilizing the principle of protein-dye binding. *Anal. Biochem. 72*, 248-254.

(189) Eliot, A. C., and Kirsch, J. F. (**2002**) Modulation of the Internal Aldimine pKa's of 1 Aminocyclopropane-1-carboxylate Synthase and Aspartate Aminotransferase by Specific Active Site Residues. *Biochemistry 41*, 3836-3842.

(190) Singleton, D. A., and Thomas, A. A. (**1995**) High-precision simultaneous determination of multiple small kinetic isotope effects at natural abundance. *J. Am. Chem. Soc. 117*, 9357-9358.

(191) Northrop, D. B. (**1975**) Steady-State Analysis of Kinetic Isotope Effects in Enzymic Reactions. *Biochemistry 14*, 2644-2651.

(192) Simon, H., and Palm, D. (**1966**) Isotope Effects in Organic Chemistry and Biochemistry. *Angew. Chem. Int. Ed. Engl. 5*, 920-933.

(193) Cleland, W. W. (**2005**) The use of isotope effects to determine enzyme mechanisms. *Arch. Biochem. Biophys. 433*, 2-12.

(194) Yano, T., Kuramitsu, S., Tanase, S., Morino, Y., and Kagamiyama, H. (**1992**) Role of Asp222 in the catalytic mechanism of *Escherichia coli* aspartate aminotransferase: the amino acid residue which enhances the function of the enzyme-bound coenzyme pyridoxal 5'-phosphate. *Biochemistry 31*, 5878-5887.

(195) Yano, T., Hinoue, Y., Chen, V. J., Metzler, D. E., Miyahara, I., Hirotsu, K., and Kagamiyama, H. (**1993**) Role of an active site residue analyzed by combination of mutagenesis and coenzyme analog. *J. Mol. Biol. 234*, 1218-1229.

(196) Gong, J., Hunter, G. A., and Ferreira, G. C. (**1998**) Aspartate-279 in aminolevulinate synthase affects enzyme catalysis through enhancing the function of the pyridoxal 5'-phosphate cofactor. *Biochemistry 37*, 3509-3517.

(197) Momany, C., Levdikov, V., Blagova, L., Lima, S., and Phillips, R. S. (**2004**) Three-Dimensional Structure of Kynureninase from Pseudomonas fluorescens. *Biochemistry 43*, 1193-1203.

(198) Gong, J., Hunter, G. A., and Ferreira, G. C. (**1998**) Aspartate-279 in aminolevulinate synthase affects enzyme catalysis through enhancing the function of the pyridoxal 5'-phosphate cofactor. *Biochemistry 37*, 3509-3517.

(199) Demidkina, T. V., Faleev, N. G., Papisova, A. I., Bazhulina, N. P., Kulikova, V. V., Gollnick, P. D., and Phillips, R. S. (**2006**) Aspartic acid 214 in Citrobacter freundii tyrosine phenol-lyase ensures sufficient C-H-acidity of the external aldimine intermediate and proper orientation of the cofactor at the active site. *Biochim. Biophys. Acta 1764*, 1268-1276.

(200) Osterman, A. L., Kinch, L. N., Grishin, N. V., and Phillips, M. A. (**1995**) Acidic Residues Important for Substrate Binding and Cofactor Reactivity in Eukaryotic Ornithine Decarboxylase Identified by Alanine Scanning Mutagenesis. *J. Biol. Chem. 270*, 11797-11802.

(201) Li, Y., Feng, L., and Kirsch, J. F. (**1997**) Kinetic and spectroscopic investigations of wild-type and mutant forms of apple 1-aminocyclopropane-1-carboxylate synthase. *Biochemistry 36*, 15477-15488.

(202) Zhou, X., and Toney, M. D. (**1999**) pH Studies on the Mechanism of the Pyridoxal Phosphate-Dependent Dialkylglycine Decarboxylase. *Biochemistry 38*, 311-320.

(203) Osterman, A. L., Brooks, H. B., Rizo, J., and Phillips, M. A. (**1997**) Role of Arg-277 in the Binding of Pyridoxal 5'-Phosphate to Trypanosoma brucei Ornithine Decarboxylase. *Biochemistry 36*, 4558-4567.

(204) Hayashi, H., Mizuguchi, H., and Kagamiyama, H. (**1993**) Rat liver aromatic L-amino acid decarboxylase: Spectroscopic and kinetic analysis of the coenzyme and reaction intermediates. *Biochemistry 32*, 812-818.

(205) Metzler, C. M., Viswanath, R., and Metzler, D. E. (**1991**) Equilibria and absorption spectra of tryptophanase. *J. Biol. Chem. 266*, 9374-9381.

(206) Karsten, W. E., Ohshiro, T., Izumi, Y., and Cook, P. F. (**2005**) Reaction of serine-glyoxylate aminotransferase with the alternative substrate ketomalonate indicates rate-limiting protonation of a quinonoid intermediate. *Biochemistry 44*, 15930-15936.

(207) Karsten, W. E., Ohshiro, T., Izumi, Y., and Cook, P. F. (**2001**) Initial velocity, spectral, and pH studies of the serine-glyoxylate aminotransferase from *Hyphomicrobium methylovorum*. *Arch. Biochem. Biophys. 388*, 267-275.

(208) Kortemme, T., and Creighton, T. E. (**1995**) Ionisation of cysteine residues at the termini of model α-helical peptides. Relevance to unusual thiol pK_a values in proteins of the thioredoxin family. *J. Mol. Biol. 253*, 799-812.

(209) Snook, C. F., Tipton, P. A., and Beamer, L. J. (**2003**) Crystal structure of GDP-mannose dehydrogenase: A key enzyme of alginate biosynthesis in *P. aeruginosa*. *Biochemistry 42*, 4658-4668.

(210) Davies, C., Heath, R. J., White, S. W., and Rock, C. O. (**2000**) The 1.8 A crystal structure and active-site architecture of β-ketoacyl-acyl carrier protein synthase III (FabH) from *Escherichia coli*. *Structure 8*, 185-195.

(211) Scharschmidt, M., Fisher, M. A., and Cleland, W. W. (**1984**) Variation of Transition-State Structure as a Function of the Nucleotide in Reactions Catalyzed by Dehydrogenases. 1. Liver Alcohol Dehydrogenase with Benzyl Alcohol and Yeast Aldehyde Dehydrogenase with Benzaldehyde. *Biochemistry 23*, 5471-5478.

(212) Hess, R. A., Hengge, A. C., and Cleland, W. W. (**1998**) Isotope Effects on Enzyme-Catalyzed Acyl Transfer from p-Nitrophenyl Acetate: Concerted Mechanisms and Increased Hyperconjugation in the Transition State. *J. Am. Chem. Soc. 120*, 2703-2709.

(213) Lee, J. K., Bain, A. D., and Berti, P. J. (**2004**) Probing the Transition States of Four Glucoside Hydrolyses with 13C Kinetic Isotope Effects Measured at Natural Abundance by NMR Spectroscopy. *J. Am. Chem. Soc. 126*, 3769-3776.

(214) Swanson, T., Brooks, H. B., Osterman, A. L., O'Leary, M. H., and Phillips, M. A. (**1998**) Carbon-13 Isotope Effect Studies of Trypanosoma brucei Ornithine Decarboxylase. *Biochemistry 37*, 14943-14947.

(215) O'Leary, M. H. (**1988**) Transition-State Structures in Enzyme-Catalyzed Decarboxylations. *Acc. Chem. Res. 21*, 450-455.

(216) O'Leary, M. H., Richards, D. T., and Hendrickson, D. W. (**1970**) Carbon isotope effects on the enzymic decarboxylation of glutamic acid. *J. Am. Chem. Soc. 92*, 4435-4440.

(217) Erion, M. D., and Walsh, C. T. (**1987**) 1-Aminocyclopropanephosphonate: Time-dependent inactivation of 1-aminocyclopropanecarboxylate deaminase and *Bacillus stearothermophilus* alanine racemase by slow dissociation behavior. *Biochemistry 26*, 3417-3425.

(218) Woehl, E. U., Tai, C.-H., Dunn, M. F., and Cook, P. F. (**1996**) Formation of the α-aminoacrylate intermediate limits the overall reaction catalyzed by O-acetylserine sulfhydrylase. *Biochemistry 35*, 4776-4783.

(219) Tidwell, T. T. (**1987**) Conjugative and substitutive properties of the cyclopropyl group, in *The chemistry of the cyclopropyl group* (Rappoport, Z., Ed.) pp 565-632, John Wiley & Sons, New York.

(220) Li, K., Du, W., Que, N. L. S., and Liu, H.-w. (**1996**) Mechanistic Studies of 1-Aminocyclopropane-1-carboxylate Deaminase: Unique Covalent Catalysis by Coenzyme B6. *J. Am. Chem. Soc. 118*, 8763-8764.

Vita

Christopher J. Thibodeaux was born and raised in Sulphur, Louisiana, where he graduated valedictorian from Sulphur High School in 1998. He then graduated *Summa Cum Laude* and as valedictorian from Louisiana State Univeristy in 2002, with majors in Biochemistry and Plant Biology, and a minor in Chemistry. In 2003, he entered graduate school at the University of Texas, Asutin, where he joined the research group of Hung-wen Liu in the summer of 2004. During his graduate studies, his research has focused on studying the chemical mechanisms of enzyme-catalyzed reactions.

Permanent Address: 11160 Jollyville Rd., Austin, Texas, 78759

This manuscript was typed by the author.